

APPLICATIONS OF HYBRID DIFFUSE OPTICS FOR CLINICAL MANAGEMENT
OF ADULTS AFTER BRAIN INJURY

Meeri Nam Kim

A DISSERTATION

in

Physics and Astronomy

Presented to the Faculties of the University of Pennsylvania

in

Partial Fulfillment of the Requirements for the
Degree of Doctor of Philosophy

2013

Supervisor of Dissertation

Graduate Group Chairperson

Arjun G. Yodh
Professor of Physics and Astronomy

Alan T. Johnson
Professor of Physics and Astronomy

Dissertation committee:

Ravi Sheth, Professor of Physics

Masao Sako, Professor of Physics

Timothy Zhu, Professor of Radiology

Joel Karp, Professor of Radiology

APPLICATIONS OF HYBRID DIFFUSE OPTICS FOR CLINICAL MANAGEMENT

OF ADULTS AFTER BRAIN INJURY

COPYRIGHT

2013

Meeri Nam Kim

Acknowledgements

Well, it is finally the end of the "Road to Ph.D.", and I can hardly believe it. I've had such a great time at Penn (perhaps that's why I spent so many years here!), and I have a number of people to thank for their contributions to my graduate student career.

First and foremost, none of this would have been possible without my advisor, Arjun Yodh. He has been a wonderful source of support and generosity, and I can honestly say that I wouldn't have gotten to where I am today without his help. He pushed me to finish my degree while also allowing me the freedom to further my non-academic career, and for this I'll always be grateful.

Rickson Mesquita, a postdoc in Arjun's lab, served as a beacon of good advice and guidance – in matters of both lab and life – throughout my graduate career. Ever since he joined the lab, he has been a great friend and colleague. An earlier postdoc, Turgut Durduran, packed in an incredible amount of training in a very short time. His efficiency and work ethic rubbed off on me early, and I'm thankful for all he has taught me.

Working on such an interdisciplinary topic had wonderful perks, such as opportunities to collaborate with medical researchers. My closest collaborator has been neurologist Brian

Edlow, whom I've been working with since my first year in Arjun's lab. His upbeat energy and optimism helped push our projects forward. The wisdom of neurologists John Detre and Joel Greenberg has guided my research from the beginning. Their critical eyes made my work better, and I am grateful to them for their generosity of time and feedback.

Many thanks to the hard-working neurocritical care researchers at the Hospital of the University of Pennsylvania for their help and clinical expertise: nurses Suzanne Frangos and Eileen Maloney-Wilensky, anesthesiologist Andrew Kofke, neurologists Joshua Levine and Heather Moss, and radiologist Ronald Wolf.

My times spent with the ever-rotating members of Arjun's biomedical optics group have been some of the most memorable. The always entertaining Leonid Zubkov taught me bookloads of instrumentation and electrical engineering, and loved celebrating the end of the work day with a hard-earned piece of fruit. My friendship with Han Ban began modestly, when we first met during a NIST summer internship in 2005. It amazes me how far we have come, and through countless lunches, coffees, and "happy happs," he has truly become a friend-for-life.

Erin Buckley and I joined the lab at the same time, and supported each other through those tough early years with lots of laughter, gossip, and even a lab pet (R.I.P. JD). Wes Baker has frequently been generous with his time both in and out of the lab. Julien Menko always knew how to make me laugh while lending a helping hand with instrumentation. And Sophie Chung and I shared a love for cats (even though ours didn't get along!) and cupcakes.

Other members of Yodh group I would also like to acknowledge are Chao Zhou, Jiaming Liang, David Minkoff, David Busch, Regine Choe, Ashwin Parthasarathy, Dalton Hance, Steve Schenkel, Guoqiang Yu, Jenn Lynch, Frank Moscatelli, Saurav Pathak, Soren Konecky, Alper Corlu, Jonathan Fisher, Kijoon Lee, Hsing-Wen Wang, Ellen Foster, and Tiffany Aversa.

Also many thanks to: biostatistician Mary Putt, who elevated the quality of our research with her contributions; Arjun's assistants, Dot Coleman and Glenn Fechner, for helping me with all sorts of administrative issues; Nicolas Skuli and Amar Majmundar, who taught me it was possible to have fun cooped up in a mouse house for 12 hours; my collaborators on the Alps project (Matthew Sanborn, Mark Edsell, Chris Imray, Heng Yow); Mike and Bill from the Biomedical Machine Shop; and my dissertation committee members (Ravi Sheth, Joel Karp, Masao Sako, Timothy Zhu) for listening to me drone on.

In addition, I have met all sorts of people in Philadelphia outside of the physics department through internships and otherwise. They helped to give me a broader perspective on life, and I would like to thank them for making my life out of the lab meaningful and fun.

Finally, I'd like to acknowledge my family – my parents and sisters, Julie and Eree – who have cheered me on with their unconditional support throughout this entire process. I will look back on my graduate school years as much more than an academic experience, and I've learned so much about career and life satisfaction during my time in Philadelphia. Like much of life, my Ph.D. path did not go according to plan, and as a result, ended up exceeding my expectations in so many ways.

ABSTRACT

APPLICATIONS OF HYBRID DIFFUSE OPTICS FOR CLINICAL MANAGEMENT OF ADULTS AFTER BRAIN INJURY

Meeri Nam Kim

Arjun G. Yodh

Information about cerebral blood flow (CBF) is valuable for clinical management of patients after severe brain injury. Unfortunately, current modalities for monitoring brain are often limited by hurdles that include high cost, low throughput, exposure to ionizing radiation, probe invasiveness, and increased risk to critically ill patients when transportation out of their room or unit is required. A further limitation of current technologies is an inability to provide continuous bedside measurements that are often desirable for unstable patients.

Here we explore the clinical utility of diffuse correlation spectroscopy (DCS) as an alternative approach for bedside CBF monitoring. DCS uses the rapid intensity fluctuations of near-infrared light to derive a continuous measure of changes in blood flow without ionizing radiation or invasive probing. Concurrently, we employ another optical technique, called diffuse optical spectroscopy (DOS), to derive changes in cerebral oxyhemoglobin (HbO_2) and deoxyhemoglobin (Hb) concentrations. Our clinical studies integrate DCS with DOS into a single hybrid instrument that simultaneously monitors CBF and HbO_2/Hb in the injured adult brain.

The first parts of this dissertation present the motivations for monitoring blood flow in injured brain, as well as the theory underlying diffuse optics technology. The next section elaborates on details of the hybrid instrumentation. The final chapters describe four human subject studies carried out with these methods. Each of these studies investigates an aspect of the potential of the hybrid monitor in clinical applications involving adult brain. The studies include: (1) validation of DCS-measured CBF against xenon-enhanced computed tomography in brain-injured adults; (2) a study of the effects of age and gender on posture-change-induced CBF variation in healthy subjects; (3) a study of the efficacy of DCS/DOS for monitoring neurocritical care patients during various medical interventions such as head-of-bed manipulation and induced hyperoxia; and (4) a first feasibility study for using DCS to study hemodynamics at high altitudes.

The work presented in this dissertation thus further develops DCS/DOS technology and demonstrates its utility for monitoring the injured adult brain. It demonstrates the promise of this new clinical tool to help neurocritical care clinicians make more informed decisions and thereby improve patient outcome.

Contents

Acknowledgements	iii
Abstract	vi
Contents	viii
List of Tables	xiii
List of Figures	xvi
1 Introduction	1
1.1 Traumatic Brain Injury	2
1.2 Aneurysmal Subarachnoid Hemorrhage	4
1.3 Dangers of Secondary Injury	6
1.4 Imaging and Monitoring the Injured Adult Brain	9
1.4.1 Neuroimaging	11
1.4.2 Intracranial Pressure	13
1.4.3 Cerebral Perfusion Pressure	14

1.4.4	Cerebral Blood Flow	15
1.4.5	Cerebral Oxygenation	17
1.5	Potential Role of Hybrid Diffuse Optics	18
2	Theory of Diffuse Optics	21
2.1	Diffuse Optical Spectroscopy (DOS)	25
2.1.1	The Diffusion Approximation	25
2.1.2	Diffuse Photon Density Waves (DPDWs)	30
2.1.3	The Semi-Infinite Medium Solution	31
2.1.4	The Differential Pathlength Method	36
2.2	Diffuse Correlation Spectroscopy	40
2.2.1	Dynamic Light Scattering	41
2.2.2	The Correlation Diffusion Equation	44
2.2.3	Diffuse Correlation Spectroscopy	47
3	Hybrid Optical Instrumentation	53
3.1	The DOS Module	54
3.1.1	Basic DOS Module	54
3.1.2	Upgraded DOS Device ("SOJI")	59
3.1.3	DOS Module Quality Testing	62
3.2	The DCS Module	72
3.2.1	Lasers	72
3.2.2	Detectors	75

3.2.3	Correlator	77
3.2.4	Visual Basic Code	79
3.2.5	DCS Module Assembly	91
3.2.6	DCS Module Quality Testing	95
3.3	Multi-Wavelength DCS	102
3.3.1	DCS Multi-Wavelength Phantom Results	102
3.3.2	Initial Human Experiment	104
3.3.3	Ultra-Portable Multi-wavelength DCS Module	105
4	Validation of DCS in Brain-Injured Adults	109
4.1	Methods	112
4.1.1	DCS/DOS	113
4.1.2	Stable Xenon-Enhanced CT	114
4.1.3	Statistical Analysis	116
4.2	Results	118
4.2.1	Comparison of $rCBF_{XeCT}$ and $rCBF_{DCS}$ Data	121
4.2.2	Effects of Xenon Inhalation	124
4.3	Discussion	127
5	Effects of Posture Change on Healthy Adults	131
5.1	Methods	134
5.1.1	Optical Instrumentation	135
5.1.2	Monitoring of Systemic Vitals	136

5.1.3	Posture Change Protocol	137
5.1.4	Statistical Analysis	138
5.2	Results	141
5.2.1	Cerebral Hemodynamic Responses to Posture Change	143
5.2.2	Systemic Responses to Posture Change	150
5.2.3	Correlations Between Parameters	150
5.3	Discussion	151
5.4	Conclusion	162
6	Use of DOS/DCS in the Neurocritical Care Unit	164
6.1	Head-of-Bed Manipulation	167
6.1.1	Methods	169
6.1.2	Results	176
6.1.3	Discussion	183
6.2	Induced Hyperoxia	190
6.2.1	Methods	191
6.2.2	Results	194
6.2.3	Discussion	197
6.3	Conclusion	199
7	Use of DCS at High Altitudes	200
7.1	Effects of High Altitude	201
7.2	Hyperventilation as Possible Treatment	204

7.3	Study Motivation	205
7.4	Methods	206
7.4.1	Optical Instrumentation	207
7.4.2	Transcranial Doppler Ultrasound	208
7.4.3	Systemic Vitals	209
7.4.4	Hyperventilation Protocol	209
7.4.5	Statistical Analysis	211
7.5	Results	212
7.5.1	Effects of Altitude on Baseline Physiology	213
7.5.2	Effects of Altitude on Response to Hyperventilation	214
7.5.3	Correlations Between Parameters	216
7.6	Discussion	216
7.7	Conclusion	221
8	Conclusions and Future Work	223
	Bibliography	227

List of Tables

1.1	Glasgow Coma Scale	3
1.2	Hunt-Hess Scale	5
1.3	Fisher Scale	6
3.1	Results of experiment comparing two identical 808 nm lasers, one with TEC and the other without, in SOJI's DOS module.	62
3.2	Long-term stability (>16 hours) of amplitude and phase for all five wave- lengths of SOJI.	64
3.3	Comparison of instrument offset and signal stability for all detectors in four different DOS instruments.	65
3.4	Comparison of dynamic range for all detectors in four different DOS in- struments.	67
3.5	SPCM-AQ4C Power Supply Requirements.	76
3.6	SPCM-AQ4C Power Supplies Used.	76
3.7	VB Code Global Variables.	80
3.8	More VB Code Global Variables	81

3.9	USB Controls.	83
3.10	Summary of dynamic light scattering experiments using solutions of Intralipid and two different diameters of polystyrene spheres.	105
4.1	Patient clinical and study data.	119
4.2	ΔMAP , ΔCPP , CBF_{XeCT} , $r\text{CBF}_{\text{XeCT}}$, and $r\text{CBF}_{\text{DCS}}$	120
5.1	Demographic information and baseline characteristics of study population ($N = 60$). Data listed as mean \pm standard error.	142
5.2	Cerebral hemodynamic and systemic responses to posture change for all subjects ($N = 60$).	143
5.3	Cerebral hemodynamic and systemic responses to posture change, including gender effects ($N = 60$).	147
5.4	Comparisons between "young" cohorts in the present study, Mehagnoul-Schipper <i>et al</i> (2000) and Tachtsidis <i>et al</i> (2004).	156
6.1	Patient clinical characteristics.	175
6.2	Effects of head lowering on cerebral and systemic vitals in brain-injured cohort.	177
6.3	Effects of head lowering on systemic vitals in healthy cohort.	177
6.4	Effects of head lowering on $r\text{CBF}$, ΔHbO_2 , ΔHb and ΔTHC in brain-injured versus healthy cohorts.	178

6.5 Effects of induced hyperoxia on vitals and DCS/DOS parameters in brain-injured patients (n = 11). 195

7.1 Number of subjects included in each timepoint. 212

7.2 Baseline (resting) physiology at sea level, 2 days at altitude, and 7 days at altitude. 213

7.3 Effects of hyperventilation at sea level, 2 days at altitude, and 7 days at altitude. 214

List of Figures

1.1	Intracranial pressure-volume curve.	8
1.2	CT scans from an aneurysmal subarachnoid hemorrhage patient who had a decompressive craniotomy.	10
1.3	Example CBF maps from an SAH patient imaged with stable xenon-enhanced CT.	13
2.1	Absorption spectra of common biological tissue chromophores.	23
2.2	A semi-infinite medium geometry.	32
2.3	A diagram of the extrapolated boundary condition for a semi-infinite geometry.	35
2.4	Single-scattering dynamic light scattering setup.	42
2.5	Example autocorrelation function $g_2(\tau)$ fit to Brownian diffusion and random flow models.	48
2.6	Example autocorrelation function $g_2(\tau)$ from arm cuff occlusion experiment.	49
3.1	A schematic of the frequency-domain technique for DOS.	54
3.2	Diagram of a basic homodyne detection DOS system.	55

3.3	Photos of the old instrument and the upgraded SOJI.	60
3.4	Example results from testing temperature controlled lasers using the SOJI DOS module.	61
3.5	Example results of a long-term stability test using the SOJI DOS module. .	63
3.6	Example results of a linearity test using the SOJI DOS module.	66
3.7	Example results of an Intralipid titration test using the SOJI DOS module. .	68
3.8	Example results of an arm cuff test using the SOJI DOS module.	69
3.9	Example results of a breath hold test using the SOJI DOS module.	71
3.10	An example of a DCS laser with good output power stability.	75
3.11	Diagram of multi-tau correlation scheme.	79
3.12	Part 1 of the VB code.	85
3.13	Part 2 of the VB code.	87
3.14	Flow chart of Time in VB code.	88
3.15	Flow chart of ReadData from VB code.	90
3.16	Front and back panels of a standard 8-channel DCS module.	92
3.17	Inside views of a standard 8-channel DCS module.	93
3.18	Circuitry of power supplies to APDs.	94
3.19	Example result of intensity and β from an overnight stability test on a basic DCS module.	98
3.20	Example result of relative BFI from an overnight stability test.	99
3.21	Diagram of stirring test for DCS box.	100

3.22	Examples of $g_2(\tau)$ during stirring test, directly comparing curves during 8-channel versus 4-channel modes.	101
3.23	Relative blood flow (rBF) from blood pressure arm cuff testing.	101
3.24	Schematic of an initial dynamic light scattering experiment to test the effects of different wavelengths on DCS results.	103
3.25	Example g_1 data and linear fit from a dynamic light scattering experiment.	104
3.26	Example result from an arm cuff experiment on a human subject using multi-wavelength DCS.	106
3.27	Photo of the ultra-portable, 2-channel DCS module that was modified for multi-wavelength operation.	107
4.1	Schematic of optical probe.	114
4.2	Photo of DCS/XeCT experiment and timeline.	115
4.3	Example CT scans showing optical probes on the forehead.	117
4.4	Scatter and Bland-Altman plots of $rCBF_{DCS}$ versus $rCBF_{XeCT}$	122
4.5	Example DCS time-series during XeCT study.	123
4.6	Example of xenon-enhanced flow activation.	125
4.7	All individual patient results of xenon-enhanced flow activation.	126
5.1	Posture change protocol.	137
5.2	Bar graphs demonstrating the number of subjects in each age range, by decade.	142
5.3	Timeseries data of $rCBF$ for an example subject and entire study population.	144

5.4	Bar graphs for mean changes in $rCBF$, THC , HbO_2 , and Hb with each posture change for the entire population.	145
5.5	Effect of age on the supine-to-standing postural change in $rCBF$, THC , HbO_2 , and Hb	149
6.1	Protocol for head-of-bed manipulation.	172
6.2	Box plots showing $rCBF$ and ΔTHC cohort responses.	179
6.3	Box plots comparing TBI versus SAH patient responses to head-lowering.	181
6.4	Case example data from an SAH patient over three consecutive days.	182
6.5	Bar plot showing cohort-averaged responses to induced hyperoxia.	194
6.6	Example timeseries from a brain-injured patient during a hyperoxia intervention.	196
7.1	Effects of high altitude on humans.	202
7.2	Effects of hyperventilation on humans at sea level.	204
7.3	Hyperventilation protocol.	209
7.4	Study protocol.	210
7.5	Bar plot showing peripheral and cerebral oxygen saturation values.	215
7.6	Bar plot showing cerebral blood flow changes with hyperventilation.	216
7.7	Scatter plot of $rCBF$ versus rPSV.	217

Chapter 1

Introduction

The overarching goal of the research described in this dissertation is to investigate the feasibility of hybrid diffuse optics – a combination of diffuse optical spectroscopy (DOS) and diffuse correlation spectroscopy (DCS) – as a method to quantitatively measure cerebral hemodynamics in adults after severe brain injury. This introductory chapter will elaborate on two types of severe brain injury that affected the majority of patients in our clinical studies, and it will also describe the modalities currently employed for neuromonitoring. The remainder of the thesis includes a chapter on the theory of diffuse optics, i.e., DCS theory, and a chapter that details the instrumentation and quality testing. The final four chapters each describe successful studies in humans that explore and demonstrate the feasibility for using hybrid diffuse optics on adult brain in practice, with an emphasis in problems related to management of those with brain injury.

1.1 Traumatic Brain Injury

Traumatic brain injury (TBI) occurs when a sudden force on the head such as a bump, blow or jolt, causes damage to the brain. The majority of TBIs that occur are mild forms such as a concussion. The most common cause of TBI is falling, especially for children and the elderly. Falls cause 50% of all TBIs for children younger than 14 years of age, and 61% of all TBIs for those older than 65 [65]. Other causes include motor vehicle accidents, struck by/against events, assault/violence, and blast injuries.

According to a report by the Centers for Disease Control and Prevention [65], there are 1.7 million cases of TBI per year in the United States, with 275,000 requiring hospitalization, 80,000 causing permanent disabilities, and 52,000 causing death. The estimated direct medical and indirect costs of TBI total about \$60 billion dollars nationally (i.e., as measured in 2000 [232, 68]). Worldwide, injury due to falls and traffic accidents is ranked as the fourth-highest cause of life years lost due to both death and disability [162]. More men suffer from TBI than women in all age groups [65], and males comprise about 75% of all TBIs in young people [140].

TBI is classified by mechanism, clinical severity, and computed tomography (CT) assessment of structural damage. Mechanism includes whether the injury is closed, e.g., when the skull remains intact, or penetrating. Clinical severity is typically indicated by the patient's post-resuscitation Glasgow Coma Scale score. The Glasgow Coma Scale (GCS) was developed in 1974 by Graham Teasdale and Bryan Jennett, two professors of neurosurgery at the University of Glasgow [229]. It was developed to assess the depth and

Table 1.1: Glasgow Coma Scale

Eye opening		Motor response		Verbal response	
Spontaneous	4	Normal	6	Normal conversation	5
To voice	3	Localized to pain	5	Disoriented conversation	4
To pain	2	Withdraws to pain	4	Words, but not coherent	3
None	1	Decorticate posture	3	No words, only sounds	2
		Decerebrate	2	None	1
		None	1		

duration of impaired consciousness and coma, and it is currently used as the universal classification of TBI severity. However, the reader should be aware that a patient’s GCS score can be easily confounded by medical sedation, paralysis, or intoxication [9, 222].

The GCS score ranges from 3 (comatose) to 15 (normal), and it is divided into three independently measured aspects of behavior – eye opening, motor responsiveness, and verbal performance (see Table 1.1). Mild TBI (typically a concussion) includes a post-resuscitation GCS score of 13 to 15; even mild TBI has been found to cause longer term effects like persistent headaches and memory issues [188]. If a patient has a GCS score of 9 to 13, as is usually found in stuporous or lethargic conditions, then he or she would be classified as having suffered a moderate TBI. Lastly, severe TBI victims have a GCS of 3 to 8, and they are usually found comatose, i.e., unable to open their eyes or follow commands. For instance, one of the severe TBI patients we studied was an 18 year old male pedestrian who was hit by a car and thrown 100 ft; his GCS score at the scene of the accident was a 3, the worst possible score.

Damage from the initial insult commonly includes shearing of white-matter tracts (bundles of axons that connect different parts of the brain together), focal contusions (bruises that cause swelling, bleeding, and destruction of brain tissue), hematomas (an expanding

mass of blood in the brain), and torn blood vessels. Such injuries cause a cascade of reactions by the body, including neurotransmitter release and inflammation, and these reactions may inflict eventual secondary damage (see Section 1.3).

Thankfully, mortality from severe TBI has fallen drastically over the past 30 years [75]. In the 1970s, the mortality rate was at about 55%, and now it is at about 20 to 30%, in part due to the advent of critical care, routine CT scanning, and monitoring of intracranial pressure (ICP). Studies have shown that patient recovery typically depends on the severity of initial and injuries, treatment received, and patient's genotype [230].

1.2 Aneurysmal Subarachnoid Hemorrhage

Subarachnoid hemorrhage (SAH) is when bleeding occurs in the subarachnoid space of the brain. There are three membranes that envelop the central nervous system – the dura mater, the arachnoid mater, and the pia mater. The subarachnoid space is situated between the arachnoid and pia mater. Bleeding in this space may arise from a ruptured cerebral aneurysm or as a result of TBI, and is thus usually prefaced by "aneurysmal" or "traumatic." This section will focus on aneurysmal SAH only.

The vast majority of SAH – up to 85% – is caused by a ruptured saccular aneurysm at the base of the brain [237, 241, 117, 238]. An aneurysm occurs when there is a weakened area in a vessel wall that becomes a balloon-like structure. They develop in certain people over the course of life, but not others; reasons for this are unknown [237]. However, risk factors include hypertension, smoking, and alcohol abuse [231]. Also, women are 1.6 times

Table 1.2: Hunt-Hess Scale

Category	Criteria	% Dead
Grade I	Asymptomatic, or minimal headache and slight neck stiffness	7/61 = 11%
Grade II	Moderate to severe headache, neck stiffness, no neurological deficit other than cranial nerve palsy	23/88 = 26%
Grade III	Drowsiness, confusion, or mild neurological deficit	29/79 = 37%
Grade IV	Stupor, moderate to severe hemiparesis, possibly early decerebrate rigidity and vegetative disturbances	25/35 = 71%
Grade V	Deep coma, decerebrate rigidity, moribund appearance	12/12 = 100%

more susceptible to SAH as men [224].

Aneurysmal SAH has a high rate of death and complications. About 10% of deaths from SAH occur before the patient can even receive medical attention, and 25% occur within 24 hours of the initial rupture [21]. The fatality rate for SAH is approximately 51%, with 40% death within only one month of hospitalization, and one third of survivors needing lifelong care [100, 198, 175].

Several classification systems exist for SAH: GCS, the Hunt and Hess scale, and Fisher grade. GCS score (see Section 1.1), used for severe TBI, is also used to assess consciousness in SAH patients. The Hunt and Hess scale (see Table 1.2) was intended to gauge surgical risk and to decide the appropriate time after SAH at which the neurosurgeon should operate [194, 104]. It is commonly used by the neurocritical care community, although it has drawbacks, e.g., the terms used to define the grades are fairly vague and subjective. Table 1.2 also shows the percentage of patients that died at each grade from Hunt and Hess's original study [104].

The Fisher grade (see Table 1.3) classifies patients by the amount of subarachnoid blood detected by CT. Fisher *et al.* determined that the amount and distribution of subarachnoid

Table 1.3: Fisher Scale

Grade	CT Scan
1	No blood visualized
2	A diffuse deposition or thin layer with all vertical layers of blood < 1 mm thick
3	Localized clots and/or vertical layers of blood \geq 1 mm in thickness
4	Diffuse or no SAH blood, but with intracerebral or intraventricular clots

blood after aneurysm rupture strongly correlates with the later development of vasospasm, i.e., a condition in which blood vessels spasm and narrow [70]. The more blood, the higher the risk of developing cerebral vasospasm. The danger of vasospasm lies in that it causes the spasming artery to shut down, and the part of the brain supplied by that artery then can become ischemic and die. Cerebral vasospasm typically develops between days 4 and 12 after injury, and is most likely due to an inflammatory reaction in the blood-vessel wall [224].

1.3 Dangers of Secondary Injury

For both TBI and SAH patients, the secondary injury can be often as dangerous as the primary injury. The primary injury is the initial insult, such as when a hard object strikes the head for TBI or aneurysm bursting for SAH. The secondary injury evolves after the primary injury over hours and days, often while patients are under neurocritical care.

For TBI patients, complications usually arise due to brain swelling. It is the leading cause of in-hospital deaths, post-TBI [143]. Swelling occurs due to a cascade of reactions by the body after acute injuries, such as neurotransmitter release and inflammatory response. For those suffering from SAH, complications due to the initial hemorrhage, cere-

bral vasospasm and rebleeding are the biggest secondary injury dangers [163]. Vasospasm and rebleeding each directly cause almost a quarter of deaths due to SAH [216].

Hemorrhaging and brain swelling due to the initial insult cause ICP to increase. ICP is the pressure exerted by the cranium onto the brain tissue, cerebrospinal fluid and blood volume. Cerebral perfusion pressure (CPP), defined as the difference between mean arterial pressure (MAP) and ICP, is the net pressure driving flow of blood to the brain. When ICP rises due to the increase of fluid within the skull, CPP drops. Or in the case of cerebral vasospasm, the narrowing of the artery causes CPP to drop. This drop in CPP causes a drop in cerebral blood flow (CBF), which in turn decreases the blood supply to the brain, and can lead to ischemia and tissue death.

The main principles of ICP [6] are the following:

- The brain is enclosed in a non-expandable case of bone.
- The brain's grey and white matter is nearly (but not perfectly) incompressible.
- The volume of blood that can occupy the cranial cavity is nearly constant.
- Continuous outflow of venous blood from the cranial cavity is required to make room for continuous incoming blood.

A non-linear pressure-volume model describing the relationship between ICP and intracranial volume has been determined, pictured in Figure 1.1 [221]. In the flat regime, at lower intracranial volumes, ICP is low and stable with good compensatory reserve; in this scenario, some cerebrospinal fluid and intracranial blood are able to leave the cranium if

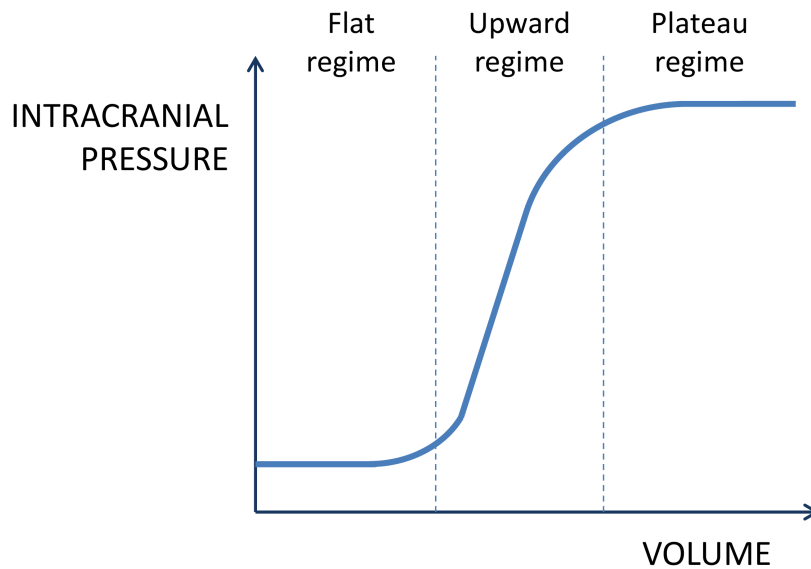


Figure 1.1: Intracranial pressure-volume curve. A normal intracranial pressure (ICP) ranges from 0-10 mmHg (flat regime) for an adult human, while 15-25 mmHg marks the point at which treatment should begin to reduce ICP (upward regime). Any higher than 25 mmHg marks the plateau regime where the cerebral arterial bed begins to collapse.

need be. This regime is the typical condition for a healthy individual at rest. The rapidly rising upward regime is where that compensatory reserve begins to be spent, resulting in a sharp rise in ICP even with a small increase in intracranial volume. Lastly, the curve plateaus at the so-called "critical pressure." In this regime, the compensatory reserve is completely spent, and at this point, the cerebral arterial bed will collapse and blood is unable to reach tissues. This last regime is the zone wherein most severely brain-injured patients reside, and this regime is a signal for increased danger due to secondary injury.

Methods for monitoring ICP are described in Section 1.4.2. A normal ICP ranges from 0-10 mmHg, while 15-25 mmHg marks the point at which treatment should begin to reduce ICP [75]. The first line of defense against high ICP is draining cerebrospinal fluid (CSF),

the fluid that occupies the subarachnoid space that acts as a cushion for the cortex. If draining isn't enough, clinicians will sometimes use hyperventilation. By increasing the patient's ventilator breath rate, hyperventilation will cause vasoconstriction, a drop in CBF, and thus lower ICP. However, there is a risk, in this case, of worsening ischemia. Another technique to manage high ICP is osmotherapy, which is a method of inducing dehydration usually via drugs, in order to reduce accumulated fluid in the brain. The last resort is decompressive craniotomy; this procedure involves removing a substantial portion of the cranium and opening the dura in order to allow the brain's volume to increase against "atmospheric pressure" and thus relieve pressure. Figure 1.2 shows CT scans from an SAH patient who participated in one of our studies that required a craniotomy. Notice the large portions of skull (bone shows up as white in CT) that are missing from the patient, suggesting that major intervention was required to prevent further crushed brain tissue.

1.4 Imaging and Monitoring the Injured Adult Brain

The patients residing in the neurocritical care unit have a wide range of injuries. Even within a single injury category, patient population can be very heterogenous. For instance, those with TBI have only one unifying factor among them, i.e., brain damage resulted from external forces. This reason is often cited for the numerous failed randomized clinical trials; none in the last 25 years has convincingly shown efficacy, as in they have shown no significant improvement in patient outcomes [164]. Even though standardized treatment protocols exist [19, 75], individualized approaches determined by monitoring are being

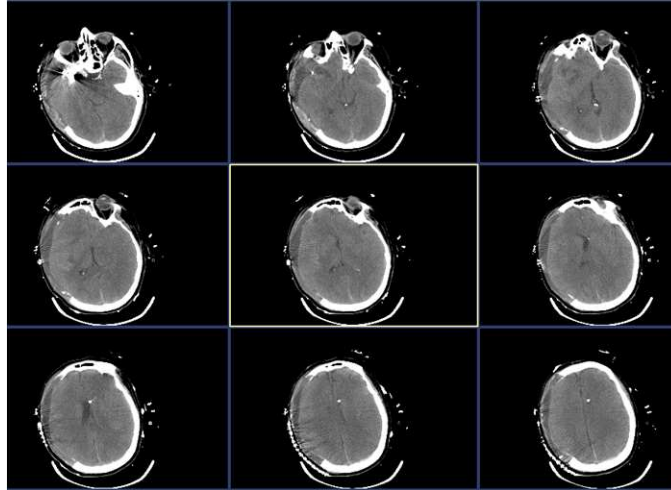


Figure 1.2: CT scans from an aneurysmal subarachnoid hemorrhage patient who had a decompressive craniotomy. Bone shows up as white in the CT, while brain tissue is a light grey. Note the large amount of skull that has to be removed in this case, suggesting that a major (and probably last resort) intervention was required to prevent crushed brain tissue from elevated ICP.

explored as a better alternative to improve outcomes [140].

Neuromonitoring of 30 or 40 years ago would generally only alert clinicians of a patient's deteriorating condition when it was irreversible. Today, clinicians know the broad strokes of management to try to prevent occurrences of high ICP, etc. Neuromonitoring of the future should be even more proactive and goal-oriented for each patient [247].

This section focuses on current neuromonitoring techniques used for those patients who have suffered from severe brain injury. I describe the most common modalities employed by clinicians in the neurocritical care unit, both to assess initial injury and for following the dynamic progression of a patient's condition. The section is divided into parameters measured, with details of the various options available under each subsection: neuroimaging for structural damage/changes, intracranial pressure, cerebral perfusion pressure, cerebral blood flow, and cerebral oxygenation.

1.4.1 Neuroimaging

The most common type of neuroimaging performed on brain-injured patients is structural, i.e., rather than functional. Structural imaging probes the morphological details of the structures of the brain, while functional imaging probes actual cerebral processes.

CT uses X-rays to produce high-resolution structural images of the body, with contrast provided by the degree of X-ray attenuation. Imaging with CT is quick and easy, both beneficial for scanning patients that are agitated and/or unstable [38]. CT scanning is typically one of the first studies performed on patients with severe TBI or suspected SAH. For TBI, patients that have been stabilized are typically examined by CT to identify mass lesions such as hematomas that need to be dealt with surgically. For example, the removal of such lesions soon after initial injury can have a profound improvement on mortality, thus reinforcing the importance of CT imaging [205, 91].

CT, however, cannot detect lesions at the microscopic level. For example, it cannot detect diffuse axonal injury (DAI). DAI is damage that has occurred over a widespread area due to shearing of tissues in the white matter. DAI thus affects the neuronal axons. Magnetic resonance imaging (MRI) can detect white matter abnormalities better than CT, but MRI is not commonly used in the acute phase due to various logistical complexity [38]. Repeated CT radiation exposure plagues CT, and is said to be responsible for 2% of all cancer cases in the United States [20]. Also, both MRI and most CT requires the patient to be taken from their room into an imaging suite, a process which puts the patient at additional risk [248].

CBF is the blood supply to the brain in a given time, and is typically given in units of *mL* per 100 g per minute. It can be measured with modified methods using MRI and CT, such as arterial spin-labeled perfusion MRI and stable xenon-enhanced CT (XeCT). Stable non-radioactive ^{131}Xe is radio-opaque, highly lipid-soluble, and diffusive tracer capable of traveling through the blood-brain barrier [176, 258]. It provides a quantitative measure of blood flow based on a modification of the Fick principle, which states that the amount of oxygen uptake of each unit of blood as it passes through the lungs is equal to the oxygen concentration difference between the arterial and mixed venous blood [119]. The patient inhales a xenon + oxygen mixture, and the increase seen in CT contrast relates to the increase of xenon concentration in the tissue, an effect which permits estimation of blood flow. End-tidal xenon concentration is assumed to be proportional to arterial concentration. The results are six CBF maps, each from a different slice of brain; Figure 1.3 shows two slices from the same patient, before and after a blood pressure manipulation that decreased perfusion. More details about XeCT can be found in Chapter 4, where we validate DCS against XeCT measurements of CBF.

All neuroimaging techniques have the prominent drawback of only capturing momentary snapshots of the patient's condition. Because severe brain injury is such a dynamically evolving process, it is desirable for clinicians to have continuous feedback in order to decide on the best methods of treatment. Thus, the term "multimodal monitoring" has gained traction in the neurocritical care community to describe continuous monitoring of numerous parameters and thus rapidly update and inform clinicians of the patient's evolving condi-

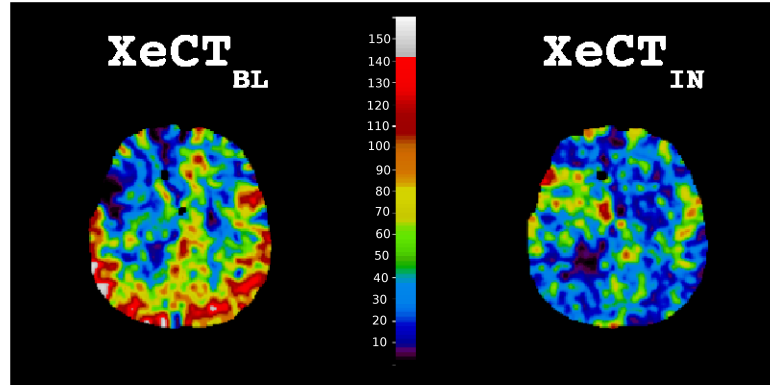


Figure 1.3: Example CBF maps from an SAH patient imaged with stable xenon-enhanced CT. A medication was given to increase blood pressure, and baseline (XeCT_{BL}) and post-intervention (XeCT_{IN}) scans showed an overall CBF decrease. A color scale showing level of absolute CBF is shown, with blue representing very low flow and red representing very high flow, quantified in $mL/100g/min$.

tion. The next sections describe a few of these parameters and techniques for monitoring them.

1.4.2 Intracranial Pressure

First used in the 1960s [136], ICP monitoring has since been the most universally accepted neuromonitoring technique by clinicians [53]. The gold standard method for measuring ICP is via intraventricular catheter. A small burr hole is drilled in the skull, and a catheter is passed into one of the lateral ventricles. The catheter is connected to an external pressure transducer. Ventriculostomy has the benefit of allowing for both monitoring and treatment. CSF can be drained as a first effort to relieve elevated ICP, as mentioned in Section 1.3, and also to acquire samples for metabolite analysis. It is also known as the most accurate, low-cost, and reliable method for measuring ICP [19].

The main drawback of the intraventricular catheter is the risk of infection or signifi-

cant hemorrhage. However, most clinicians believe that the benefits of ICP information outweigh the risks. Hematomas associated with ventriculostomy had an average incidence of 1.1% in a review of eight studies [19], while risk of infection in two other studies was found to be about 11% [146, 8].

Other methods for monitoring ICP include subdural, subarachnoid, and epidural probes. These may be less invasive than intraventricular probes, but they have proven themselves to be not as accurate.

1.4.3 Cerebral Perfusion Pressure

Monitoring ICP means CPP can be calculated as well. However, unlike ICP, no target thresholds for upper and lower limits of CPP have been agreed upon [7, 196]. Usually clinicians aim to increase CPP levels in order to increase perfusion, but this is only the case if cerebral autoregulation is damaged.

Cerebral autoregulation is a homeostatic phenomenon wherein blood vessels will dilate or constrict in order to keep CBF relatively constant despite changes in CPP, within the range of 50 to 150 mmHg [173]. Below or above this range, the relationship between CPP and CBF is linear. This linear behavior occurs when autoregulation is impaired, which often happens to brain-injured patients. Thus, an increase in CPP will only lead to an increase in CBF when CPP is either outside the autoregulatory range or when autoregulation is damaged.

1.4.4 Cerebral Blood Flow

Severe head injury leaves patients at risk of cerebral ischemia due to secondary injury as described in Section 1.3. Inadequate perfusion likely increases the probability of a poor outcome, but no standard method of directly measuring CBF has been widely accepted for use in neurocritical care. This could be due to the fact that thresholds for absolute CBF are unclear [221].

CBF may be measured by the so-called Kety-Schmidt technique [119], wherein the arterial and jugular venous concentrations of a contrast agent such as nitrous oxide are measured, and global CBF is calculated from the tissue uptake rate. However, the Kety-Schmidt technique can only give a measure of non-continuous global CBF.

Thermal diffusion and laser Doppler probes are both microsensor methods of continuously monitoring CBF. The thermal diffusion flowmetry (TDF) method is based on the temperature difference measured by a thermistor (heated to a few degrees above tissue temperature) and a temperature probe [235]. The temperature difference can be translated to a quantitative measurement of CBF. The probe is implanted through a burr hole either directly into the white matter or on the cortex; thus, TDF an invasive measure of microvascular blood flow [221].

Laser Doppler flowmetry (LDF) uses the Doppler shift of light – the frequency change that light undergoes when it reflects off of moving red blood cells – to measure flow in superficial volume under the probe [81]. It consists of a low power laser source and detector placed a small distance apart that penetrates only to a depth of about a millimeter. Thus to

measure cortical flow, it must be used in an invasive way.

Both TDF and LDF are invasive regional measures of CBF, and thus only a limited number of such probes may be implanted in patients. This means that only a small region of CBF may be measured in a single patient, and thus the diagnostic output may not be reflective of other areas of the injured brain. Although both techniques measure microvascular flow, they are also restricted to the white matter due to logistical issues with probe placement. While TDF can give an absolute measure of CBF, LDF only provides a relative measure [18]. However, presently neither of these techniques have become standard in the neurointensive care unit, most likely due to the substantial operator expertise required [247].

One technique that measures not flow, but cerebral blood flow velocity (the rate at which blood moves through a particular vessel), has increasingly become commonplace for neurocritical care clinicians: transcranial Doppler (TCD) ultrasound. An ultrasound probe emits a high-pitched sound wave that scatters, and the speed of the blood in relation to the probe causes a phase shift, which is then translated into blood velocity [219]. TCD has become a standard way to diagnose vasospasm after SAH, defined as a mean flow velocity of over 200 cm/s. Being non-invasive, it is often performed daily at the bedside to get a snapshot of the patient's flow velocities, but TCD is logistically challenging to implement continuously for days or even hours. It also does not involve any ionizing radiation or contrast agents.

However, efficient diagnosis with TCD requires much experience and skill, and it holds

the risk of being highly operator dependent [256]. The operator utilizes the thin portion of the skull as an acoustic window to permit penetration of ultrasound waves to the intracranial blood vessels. However, if the acoustic window is inadequate or not sufficiently transparent, that can limit TCD use in certain patients [182]. It also only measures macrovascular flow velocity, or blood flow velocity in the large vessels of the brain, which does not necessarily reflect microvascular perfusion in patients with cerebrovascular disease [184]. For this reason, any focal microvascular CBF impairments may still return a normal TCD diagnosis.

1.4.5 Cerebral Oxygenation

Similarly, just as invasive intracranial pressure monitoring to derive CBF is a routine part of patient care in the neurointensive care unit, many clinicians rely on invasive monitors for measurement of brain oxygen levels. The most commonly used method is jugular bulb oximetry. It involves sampling the blood of the jugular bulb, which is the cranial tip of the internal jugular vein that contains pure cerebrovenous blood [87]. The result is an invasive, global measurement of jugular venous oxygen saturation. This technique, however, has been critiqued as somewhat fraught with technical problems and non-reflective of regional cerebral metabolic changes [87, 42, 47, 249].

Some neurointensivists utilize invasive electrodes to measure the partial pressure of brain tissue oxygen (PbtO₂) [139, 239, 133]. This technique involves the intraparenchymal insertion of a Clark type electrode, which generates a current dependent on the amount of oxygen near the catheter tip. These monitors provide continuous monitoring of cerebrovas-

cular oxygenation, but they are also invasive, and their measurements are limited to a small ($\sim\text{mm}^3$) volume of white matter tissue.

1.5 Potential Role of Hybrid Diffuse Optics

In the work presented within this dissertation, we validate and explore hybrid diffuse optical monitoring – as in, the combination of DOS + DCS in a single instrument/probe setup – as a means to non-invasively and continuously measure microvascular CBF and blood oxygenation in a neurocritical care population. DOS measures tissue oxygen levels based on the different absorption properties of oxy- and deoxyhemoglobin [244, 96], while DCS measures CBF by using the intensity fluctuations of light scattered many times from moving red blood cells [13, 15, 177, 142]. Having both blood flow and oxygenation information can better elucidate the patient’s condition, as they can give correlated or uncorrelated trends.

DOS, more commonly called near-infrared spectroscopy (NIRS) by clinicians, has been studied previously in brain-injured patients. Specifically, DOS has been compared to invasive electrode monitors [123, 3, 98, 197, 22, 4], as a means of detecting intracranial hemorrhage and contusion [95, 220], as a surrogate approach to measure of CBF using tracers [118], and, more recently, as a measure of autoregulation in stroke patients [59, 88]. Thus far, DCS has been used to study autoregulatory function in stroke patients [59] and to study CBF in ill neonates [24, 23, 25, 191].

Hybrid diffuse optics holds potential to be a useful neuromonitoring tool for this pa-

tient population because of its continuous output, its non-invasive nature, its ability to put multiple probes on different locations on the head, and its lack of ionizing radiation. This dissertation further explores the feasibility and applications of DCS/DOS. Chapters 2 and 3 describe underlying theory in detail, as well as recent instrumentation advances. Both chapters are geared towards the application of DCS/DOS for monitoring adult brain. The basic hybrid diffuse optical device used in the experiments featured in this dissertation is also outlined in depth, particularly the DCS module.

Chapter 4 presents a validation study of DCS-measured CBF against a gold-standard technique that measures absolute CBF: stable xenon-enhanced CT. Importantly, this successful validation is performed on neurocritical care patients, since this injured population is of central interest to us here.

The next chapter (Chapter 5) appears to be a departure from the application of DCS/DOS in those with brain injury, in that we looked at healthy subjects across the age continuum during a posture change. However, it originally began as a way to quantify the normative response during head-of-bed manipulation – a common intervention in the neurocritical care unit. We found that age did not have an effect on CBF responses to posture change, but that the healthy response was clearly differentiated against the brain-injured population.

Chapter 6 investigated cerebral hemodynamics during head-of-bed manipulation in patients after severe brain injury. We chose head-of-bed manipulation because of its ease of implementation, as well as the fact that it is a commonly performed intervention in the neurocritical care unit. Not only did we find that the patient response differed significantly

from the normative response, but we also found that the heterogeneity of the patients revealed itself through a widely varying CBF response to head lowering. This result supports arguments for individualized patient management, and indicates how hybrid diffuse optics could add useful information to further guide clinicians and to customize treatment.

The final chapter (Chapter 7) studies humans at high altitude. While many people work at and are stationed at high altitudes, our understanding of cerebral hemodynamics in such an environment is quite limited. Cerebrovascular stress in the form of acute mountain sickness or the potentially fatal high altitude cerebral edema can put people who live above 2400 m at risk. Our investigation successfully implemented DCS at high altitude for the first time, and it measured changes in CBF during a hyperventilation task at high altitude.

The results in this dissertation have led to three publications [120, 61, 121], with another currently in preparation (based on results from Chapter 7). Notably, my validation publication [120] was the first paper featuring DCS in human brain studies to break through the clinical journal barrier (i.e., *Neurocritical Care* for neurosurgeons). At this stage, it is important for us to aim for clinical journals, because wider audience among doctors will help push DCS/DOS technology into the clinic. I am also a co-author on several other publications with members of this lab and our collaborators [24, 59, 58, 154, 212, 156, 141].

Chapter 2

Theory of Diffuse Optics

Diffuse optical methods can non-invasively measure tissue optical properties and tissue dynamics millimeters to centimeters below the surface of the skin. This chapter outlines the basic theory behind the two optical monitoring techniques we use to probe hemodynamics in the adult brain: diffuse optical spectroscopy (DOS) and diffuse correlation spectroscopy (DCS). Diffuse optical spectroscopy, also called near-infrared spectroscopy (NIRS), is used to probe slow variations in absorption and scattering of biological tissues due to changes in the concentrations of tissue chromophores. Diffuse correlation spectroscopy utilizes the fast intensity fluctuations of scattered light to characterize the movement of red blood cells, i.e., to provide a measure of relative blood flow.

Both techniques take advantage of the so-called "therapeutic window" of common biological tissue chromophores wherein the absorption of light is low [112]. This window (from about 650 nm to 900 nm) lies between the visible absorption bands of hemoglobin and the near-infrared absorption band of water. Figure 2.1 shows the full absorption spectra

of the main chromophores in tissue – oxyhemoglobin, deoxyhemoglobin, water, and lipid; it also shows a close-up of the therapeutic window optical range. $\mu_a(\lambda)$, the absorption coefficient, has units of cm^{-1} and is the reciprocal of the absorption length, or the typical distance traveled by a photon before it becomes absorbed. $\mu_a(\lambda)$ is a very important "optical property" that characterizes the tissue medium, since it depends on the concentrations of oxyhemoglobin, deoxyhemoglobin, water, and lipid.

The low absorption of hemoglobin, water, and lipid in this near-infrared window allow light to penetrate to deeper regions of tissue. When this discovery was made, it was then speculated that near-infrared light could non-invasively probe the workings of the brain through skull and scalp. While light can penetrate through the skull and into the brain, tissue is a highly scattering medium, and a model had to be derived to understand the process of photon propagation through such a turbid substance. It was found that light transport through such turbid media over longer distances can be well-approximated by a diffusive model. This model applies when light scattering dominates rather than absorption, i.e., the photon scattering length are much smaller than the absorption length. In this regime, one is able to separate out of the two effects.

The scattering equivalent to the absorption length, the wavelength-dependent scattering length is defined as the typical distance traveled by a photon before being scattered. The reciprocal of this distance is $\mu_s(\lambda)$, called the scattering coefficient. However, we typically use a different and arguably more important parameter to characterize scattering called the reduced scattering coefficient and denoted by $\mu'_s(\lambda)$. This reduced scattering coefficient is

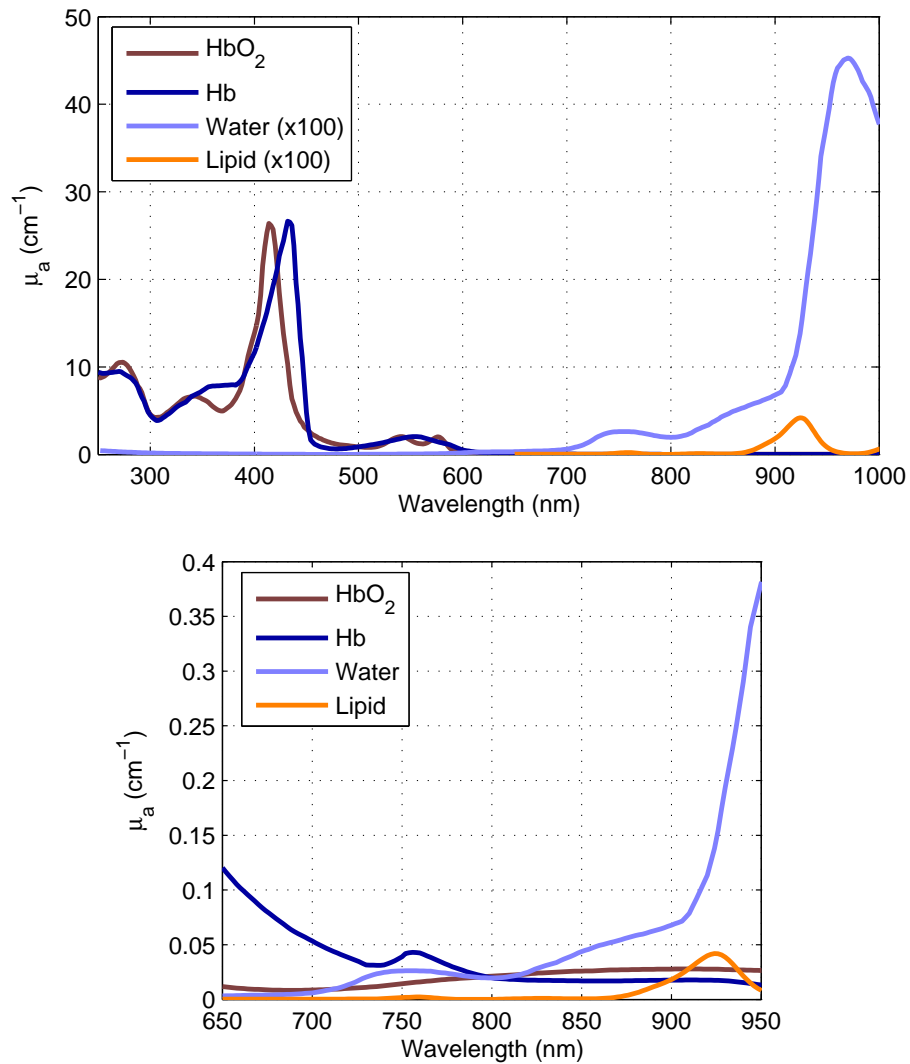


Figure 2.1: (top) Absorption spectra of common biological tissue chromophores in the range 250 to 1000 nm – oxygenated hemoglobin (HbO_2), deoxygenated hemoglobin (Hb), water, and lipid. Absorption is quantified by μ_a , the absorption coefficient. (bottom) Zoomed-in spectra, the so-called "therapeutic window" from 650 to 950 nm where the absorption of tissue chromophores is relatively low. This lack of absorption allows light within this window to penetrate up to centimeters deep into biological tissues to probe chromophore concentrations.

the reciprocal of one photon random walk step, or the distance a photon travels before its direction becomes randomized. It depends on both μ_s and the degree of forward scattering anisotropy of a typical scattering event. If the photon propagation is well-modeled, one can readily calculate the concentration changes of tissue chromophores in the brain such as oxy- and deoxyhemoglobin. This is the DOS technique that is oriented towards these concentration measurements.

The work in this dissertation focused not only on blood oxygenation, but also on blood flow. DCS is a technique that also uses the diffusive behavior of light in tissue, but tracks the fast fluctuations of light due to scattering off of moving red blood cells in order to derive a measure of flow. It shares the same advantages of DOS with respect to looking at deeper tissues, and so it is natural to use the two together to obtain information about blood hemodynamics in order to paint a fuller picture of brain physiology.

In this chapter, we will first outline the basic theory behind DOS, starting from the radiation transport equation and deriving the photon diffusion equation. Two different geometries will be discussed: the infinite medium and the semi-infinite medium. Much of the oxygenation work in this dissertation uses another analysis technique (i.e., an approximation of the diffusion approach) called the differential pathlength method; this approach will be explained. Lastly, we will outline DCS theory, i.e., going from single scattering to multiple scattering regimes, and finally deriving the correlation diffusion equation.

2.1 Diffuse Optical Spectroscopy (DOS)

2.1.1 The Diffusion Approximation

The derivation of the photon diffusion equation commonly begins with the photon transport equation [55]. It is derived from linear transport theory, which is itself an approximation of the complex light transport problem posed by the highly scattering media, that allows us to avoid fumbling with Maxwell's equations [28]. In most cases, diffraction and interference effects may be neglected, and geometrical analysis based on ray tracing or energy transport helps us understand and visualize the problem. In this approach, one can visualize the photons to propagate in straight lines between scattering events.

Light radiance, $L(\vec{r}, \hat{\Omega}, t)$, is defined as the power of light per unit area per solid angle traveling in the $\hat{\Omega}$ direction at position \vec{r} and time t in the sample; its units are $\text{W}/(\text{cm}^2 \cdot \text{sr})$. Photon fluence rate, denoted as $\Phi(\vec{r}, t)$, and photon flux or current density $\vec{J}(\vec{r}, t)$, both have units of W/cm^2 . They are defined as integrals of the radiance, i.e.,

$$\Phi(\vec{r}, t) = \int L(\vec{r}, \hat{\Omega}, t) d\hat{\Omega}, \quad (2.1)$$

and

$$\vec{J}(\vec{r}, t) = \int L(\vec{r}, \hat{\Omega}, t) \hat{\Omega} d\hat{\Omega}. \quad (2.2)$$

The photon fluence rate can be thought of as the total number of photons emerging from a small volume element per unit area per time, i.e., it is the total sum of the radiance emerging

from \vec{r} . The photon flux is a similar quantity, but it is directional, i.e., it is a vector sum of the radiance emerging at \vec{r} .

An initial radiance can have various processes affect it within an infinitesimal volume such as scattering, absorption, additional light scattered in, or light source emission. With a lot of work [46], one can derive a transport equation for the radiance:

$$\frac{1}{\nu} \frac{\partial L(\vec{r}, \hat{\Omega}, t)}{\partial t} + \nabla \cdot L(\vec{r}, \hat{\Omega}, t) \hat{\Omega} = -\mu_t L(\vec{r}, \hat{\Omega}, t) + \mu_s \int L(\vec{r}, \hat{\Omega}', t) f(\hat{\Omega}, \hat{\Omega}') d\hat{\Omega}' + S(\vec{r}, \hat{\Omega}, t). \quad (2.3)$$

Here $\nu = c/n$ is the speed of light in the medium, with n being the index of refraction of the medium. We define a transport coefficient $\mu_t = \mu_s + \mu_a$ that describes the rate (in cm^{-1}) that photons are lost through absorption or scattering. The second term on the right hand side accounts for photons scattered into the volume from other places via use of a normalized phase function, $f(\hat{\Omega}, \hat{\Omega}')$. This phase function gives the probability of a photon scattering from direction $\hat{\Omega}$ to $\hat{\Omega}'$. The last term is for photons generated by the light source. $S(\vec{r}, \hat{\Omega}, t)$ is the power per volume emitted; its units are $\text{W}/(\text{cm}^3 \cdot \text{sr})$. Equation (2.3) basically describes radiance conservation in each infinitesimal volume element within the sample [16].

To simplify the photon transport equation, we approximate Equation (2.3) by expanding the radiance and source terms using spherical harmonics ($Y_{l,m}(\hat{\Omega})$) with coefficients

$\phi_{l,m}(\vec{r}, t)$, and then we truncate the series at $l = N$, i.e.,

$$L(\vec{r}, \hat{\Omega}, t) = \sum_{l=0}^N \sum_{m=-l}^l \phi_{l,m}(\vec{r}, t) Y_{l,m}(\hat{\Omega}), \quad (2.4)$$

and

$$S(\vec{r}, \hat{\Omega}, t) = \sum_{l=0}^N \sum_{m=-l}^l q_{l,m}(\vec{r}, t) Y_{l,m}(\hat{\Omega}). \quad (2.5)$$

This analysis scheme is called the P_N approximation, and, for this dissertation, we will only retain terms with $l = 1$ or lower. This approximation is called the P_1 approximation. The P_1 approximation is only valid for radiance that is nearly isotropic, i.e., in situations wherein $\Phi(\vec{r}, t) \gg 3|\vec{J}(\vec{r}, t)|$. For this situation to occur, the medium must have $\mu_s \gg \mu_a$ and the positions of interest \vec{r} must be far from the light source. In the P_1 approximation, the radiance can be approximated as

$$L(\vec{r}, \hat{\Omega}, t) \approx \frac{1}{4\pi} \Phi(\vec{r}, t) + \frac{3}{4\pi} \vec{J}(\vec{r}, t) \cdot \hat{\Omega}, \quad (2.6)$$

and the source term is approximated as

$$S(\vec{r}, \hat{\Omega}, t) \approx \frac{1}{4\pi} S_0(\vec{r}, t) + \frac{3}{4\pi} \vec{S}_1(\vec{r}, t) \cdot \hat{\Omega}. \quad (2.7)$$

We also assume that the normalized phase function depends only on the cosine of the angle between the incident and outgoing wave vectors and not on the values of the angles themselves. This assumption implies that $f(\hat{\Omega}, \hat{\Omega}') = f(\hat{\Omega} \cdot \hat{\Omega}')$, and it is an acceptable

assumption when the scattering medium is isotropic.

If we insert these expression for the radiance and source into the photon transport equation (Equation (2.3)), we obtain [189]:

$$\begin{aligned}
& \frac{1}{\nu} \frac{\partial \Phi(\vec{r}, t)}{\partial t} + \frac{3}{\nu} \frac{\partial \vec{J}(\vec{r}, t)}{\partial t} \cdot \hat{\Omega} + \nabla \cdot \Phi(\vec{r}, t) \hat{\Omega} + 3 \nabla \cdot [\vec{J}(\vec{r}, t) \cdot \hat{\Omega}] \hat{\Omega} \\
& = -\mu_t \Phi(\vec{r}, t) - 3\mu_t [\vec{J}(\vec{r}, t) \cdot \hat{\Omega}] + \mu_s \int [\Phi(\vec{r}, t) + 3\vec{J}(\vec{r}, t) \cdot \hat{\Omega}] f(\hat{\Omega}, \hat{\Omega}') d\hat{\Omega}' \\
& \quad + S_0(\vec{r}, t) + 3\vec{S}_1(\vec{r}, \hat{\Omega}, t) \cdot \hat{\Omega}. \tag{2.8}
\end{aligned}$$

The anisotropy factor g conveys how much forward scattering is in each scattering event. It is defined as the average cosine of the scattering angle for a typical scattering event, i.e.,

$$g = \int f(\hat{\Omega} \cdot \hat{\Omega}') \hat{\Omega} \cdot \hat{\Omega}' d\hat{\Omega}' = \langle \cos \theta \rangle. \tag{2.9}$$

For our applications – human brain grey matter – we typically have values of $g = 0.88$ or larger; if $g = 1$, then photons are scattered completely in the forward direction [30].

We also define the reduced scattering coefficient $\mu'_s = \mu_s(1 - g)$, whose reciprocal is the so-called photon random walk step length.

Then multiplying Equation (2.8) by $\hat{\Omega}$ and integrating over $\hat{\Omega}$ gives

$$\frac{1}{\nu} \frac{\partial \vec{J}(\vec{r}, t)}{\partial t} + \frac{1}{3} \nabla \Phi(\vec{r}, t) + [\mu_a + \mu'_s] \vec{J}(\vec{r}, t) = \vec{S}_1(\vec{r}, t). \tag{2.10}$$

We next neglect the term containing $\frac{\partial \vec{J}(\vec{r}, t)}{\partial t}$ by assuming that variations in the diffuse total

flux are much slower than the mean time between scattering events [189, 55]. We also assume isotropic sources (i.e., $S(\vec{r}, \hat{\Omega}, t) = S(\vec{r}, t)$), so that all $l \neq 0$ terms of the source become zero. Usually this assumption can be justified by noting that collimated sources are simply isotropic sources displaced one transport mean free path away from the actual source location [16].

So then Equation (2.10) becomes

$$\nabla \Phi(\vec{r}, t) = -3 [\mu_a + \mu'_s] \vec{J}(\vec{r}, t), \quad (2.11)$$

which is known as Fick's law of diffusion, and defines the photon diffusion coefficient.

If we insert all of these approximations for the radiance and source (Equations (2.6) and (2.7)) into the photon transport equation (Equation (2.3)) and then integrate over $\hat{\Omega}$, we have

$$\frac{1}{\nu} \frac{\partial \Phi(\vec{r}, t)}{\partial t} + \nabla \cdot \vec{J}(\vec{r}, t) + \mu_a \Phi(\vec{r}, t) = S_0(\vec{r}, t). \quad (2.12)$$

Upon inserting Equation (2.11) into Equation (2.12), we retrieve the typical form for the photon diffusion equation in a homogeneous medium:

$$\frac{\partial \Phi(\vec{r}, t)}{\partial t} - D \nabla^2 \Phi(\vec{r}, t) + \nu \mu_a \Phi(\vec{r}, t) = \nu S_0(\vec{r}, t), \quad (2.13)$$

where the diffusion coefficient D is defined as

$$D = \frac{\nu}{3(\mu_a + \mu'_s)} \approx \frac{\nu}{3\mu'_s}. \quad (2.14)$$

2.1.2 Diffuse Photon Density Waves (DPDWs)

For the data presented in this thesis, we often used what is called the intensity-modulated or frequency-domain (FD) technique of DOS.¹ This technique involves modulating the light source at a specific frequency such as 70 MHz and then detecting the amplitude and phase changes of the "differential waves" as they pass through tissue. With that information, we can readily extract the optical properties (μ_a and μ'_s) of the medium. Specifically, when a light source is frequency-modulated, the photon fluence will oscillate at the same frequency, creating a macroscopic scalar disturbance, part of which is a wave called the diffuse photon density wave (DPDW) [71]. The DPDW is the AC component of the photon fluence rate, i.e., of

$$\begin{aligned}\Phi(\vec{r}, t) &= \Phi_{DC}(\vec{r}) + \Phi_{AC}(\vec{r}, t) \\ &= \Phi_{DC}(\vec{r}) + \Phi_{AC}(\vec{r})e^{-i\omega t},\end{aligned}\tag{2.15}$$

where $\omega = 2\pi f$, and f is the modulation frequency.

If we insert the AC component of Equation (2.15) into Equation (2.13), we can rewrite it in Helmholtz equation form:

$$(\nabla^2 + k_{AC}^2)\Phi_{AC}(\vec{r}) = -\frac{\nu}{D}S_0(\vec{r}),\tag{2.16}$$

¹As opposed to continuous-wave (CW), where the laser intensity remains constant over time), or time-resolved (TRS), where the laser is pulsed and one measures the broadened pulse shape as it propagates through tissue). We find FD to be a "happy medium" of sorts, in terms of greater information content than CW but not as complicated or expensive electronics as TRS.

where

$$k_{AC}^2 = \frac{i\omega - \nu\mu_a}{D} \quad (2.17)$$

is the complex wavenumber ($k_{AC} = k_r + ik_i$). The solution to Equation (2.16) for an infinite homogeneous medium is [71]:

$$\Phi_{AC}(\vec{r}, t) = \frac{\nu S_{AC}}{4\pi D r} e^{ikr - i\omega t}, \quad (2.18)$$

with S_{AC} as the source modulation amplitude, and $r = |\vec{r}|$. The DPDW is a spherical wave that must decay to zero at large distances from the light source ($k_i \geq 0$), and this restricts the real and imaginary parts of the wavenumber solution to be [131]:

$$k_r = \sqrt{\frac{\nu\mu_a}{2D}} \left[\sqrt{1 + \left(\frac{\omega}{\nu\mu_a}\right)^2} - 1 \right]^{1/2} \quad (2.19)$$

$$k_i = \sqrt{\frac{\nu\mu_a}{2D}} \left[\sqrt{1 + \left(\frac{\omega}{\nu\mu_a}\right)^2} + 1 \right]^{1/2}. \quad (2.20)$$

The amplitude of the DPDW is $A(r) = \nu S_0 e^{-k_i r} / (4\pi D r)$, and the phase is $\theta = k_r r$.

DPDWs demonstrate many familiar wave-like properties such as refraction [169], diffraction [14], interference [201], and dispersion [233].

2.1.3 The Semi-Infinite Medium Solution

The simplest geometry that approximates source and detector optical fibers on a tissue surface is the homogeneous, semi-infinite medium (see Figure 2.2). In this geometry, there

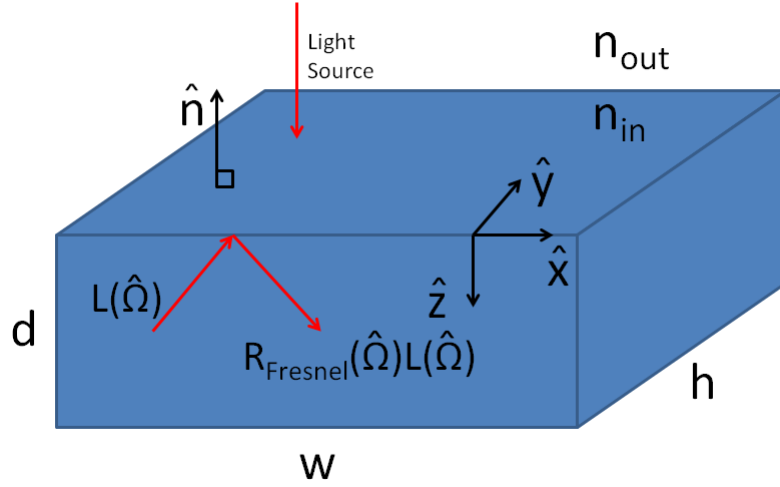


Figure 2.2: A semi-infinite medium geometry, with planar boundary between a homogeneous turbid medium (index of refraction n_{in}) and non-scattering medium (index of refraction n_{out}). w , h , and d go to infinity, and the medium is azimuthally symmetric about the z -axis. The unit vector \hat{n} points from inside the tissue perpendicularly outwards. The diagram also shows the radiance $L(\hat{\Omega})$ incident upon the boundary and reflecting back inside the turbid medium with Fresnel coefficient $R_{Fresnel}(\hat{\Omega})$.

exists a planar boundary at $z = 0$ with a homogeneous turbid medium at $z < 0$ and a non-scattering medium at $z > 0$. Given the case where the indices of refraction match and the boundary is then perfectly transmitting, any light passing from the scattering medium through to the non-scattering medium will not return back to the scattering medium [92]. Thus, a discontinuity in the radiance $L(\vec{r}, \hat{\Omega}, t)$ arises when $\hat{\Omega}$ points into tissue from air. This is a violation of the diffusion approximation expressed in Equation (2.6), which stated that the radiance is primarily isotropic.

However, in the case of mismatched indices of refraction, much of the radiance incident upon the boundary from the turbid medium will be reflected back inside. This allows us to avoid the discontinuity in radiance found with a perfectly transmitting boundary.

We start by setting the irradiance, or total inward radiance, at the boundary equal to the integral of the reflected radiance:

$$\begin{aligned}
E_{in} &= \int_{\hat{\Omega} \cdot \hat{n} < 0} L(\hat{\Omega}) \hat{\Omega} \cdot (-\hat{n}) d\Omega \\
&= \int_{\hat{\Omega} \cdot \hat{n} < 0} R_{Fresnel}(\hat{\Omega}) L(\hat{\Omega}) \hat{\Omega} \cdot \hat{n} d\Omega
\end{aligned} \tag{2.21}$$

where $\hat{n} = -\hat{z}$ is the outward normal unit vector (see Figure 2.2) and $R_{Fresnel}(\hat{\Omega})$ is the Fresnel reflection coefficient for light incident upon the boundary at angle $\hat{\Omega}$ from within the turbid medium.

From here, we can substitute in Equation (2.6) for L and the equation for the Fresnel reflection coefficient for unpolarized light to get to the partial-flux boundary condition valid at $z = 0$ [92]:

$$\Phi = z_b \hat{n} \cdot \nabla \Phi \tag{2.22}$$

where $z_b = 2D \frac{1+R_{eff}}{(1-R_{eff})}$, and R_{eff} is the effective reflection coefficient to take into account the index of refraction mismatch. For instance, tissue has $n_{in} = 1.4$ and air has $n_{out} = 1.0$.

Unfortunately, the partial-flux boundary condition, while exact, is difficult to use in practice. A simpler boundary condition is typically used, called the extrapolated-zero boundary condition, which is a good approximation to the partial-flux boundary condition even though there is no strict physical implication behind it [131]. It is a convenient mathematical device to simplify the analysis. The extrapolated-zero boundary condition involves having the fluence rate fall to zero at a point on the air side of the boundary, which

we will say is at a distance z_b outwards from the boundary:

$$\Phi(z = -z_b) = 0. \quad (2.23)$$

The fluence rate is extrapolated into the non-scattering medium with a straight line with the same slope found at the boundary. Thus, the fluence rate on the air side of the boundary can be given by

$$\Phi(z) = \frac{\partial\Phi(\vec{r})}{\partial z}\Big|_{z=0}z + \Phi(z = 0). \quad (2.24)$$

Setting Equation (2.24) equal to zero, we find that $z_b = 2/3\mu'_s$.

We can use the method of images to obtain the solution of a DPDW for a homogeneous semi-infinite turbid medium, made up of a superposition of a DPDW in an infinite medium and a DPDW of a negative image source outside of the turbid medium on the air side. They are symmetric to one another with respect to the extrapolated boundary.

Figure 2.3 shows a diagram of this extrapolated boundary situation. A collimated source at the air-tissue boundary can be well-approximated as an isotropic light source a distance of one transport mean free path ($\ell_{tr} = 1/\mu'_s$) into the medium. The negative image source is placed at $-(\ell_{tr} + 2z_b)$. Then for a detector at (r, z) , the solution of the diffusion equation is

$$\Phi(r, z) = \frac{\nu S_0}{4\pi D} \left[\frac{e^{ikr_1}}{r_1} - \frac{e^{ikr_2}}{r_2} \right], \quad (2.25)$$

with $r_1 = \sqrt{r^2 + (z - \ell_{tr})^2}$ and $r_2 = \sqrt{r^2 + (z + \ell_{tr} + 2z_b)^2}$. And in the limit $r \gg$

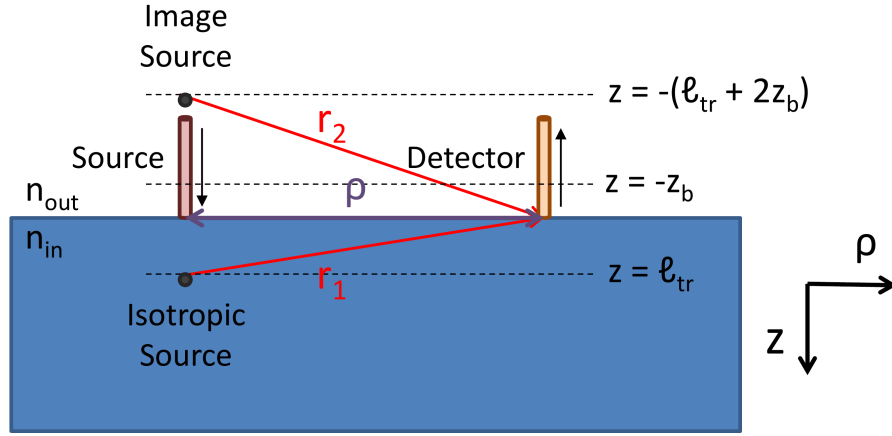


Figure 2.3: A diagram of the extrapolated boundary condition for a semi-infinite geometry. There exists a planar boundary between a homogeneous turbid medium (index of refraction n_{in}) and non-scattering medium (index of refraction n_{out}). Source and detector fibers are shown, with separation ρ between them. There is an isotropic source one transport mean free path ($z = \ell_{tr}$) into the turbid medium, and a negative image source located at $z = -(\ell_{tr} + 2z_b)$.

($\ell_{tr} + 2z_b$), Equation (2.25) simplifies for r on the surface to

$$\begin{aligned}
 \Phi_{semiinf}(r, z = 0) &\approx \frac{\nu S_0}{4\pi D} \frac{e^{-k_r r}}{r^2} [2k(\ell_{tr} z_b + z_b^2)] \\
 &= A_0 \frac{e^{-k_r r}}{r^2} e^{i(-k_i r + \theta_0)} \\
 &= A(r) e^{i\theta(r)},
 \end{aligned} \tag{2.26}$$

Conveniently, these can be written as

$$\ln[r^2 A(r)] = -k_r r + \ln A_0 \tag{2.27}$$

$$\theta(r) = -k_i r + \theta_0, \tag{2.28}$$

making it easy to use multiple (at least two, but preferable more) source-detector distances to linearly fit for slopes k_i and k_r . For instance, a titration test to characterize a DOS module typically uses an automated translation stage to measure amplitude and phase at many different distances over a range of ~ 1 cm to 10 cm (see Section 3.1.3). Both amplitude and phase will vary linearly (within a certain range) with respect to source-detector separation. The slopes of the amplitude and phase plots are equal to k_r and k_i , respectively.

Lastly, the optical properties of interest, μ_a and μ'_s , may be solved for using the following equations:

$$\begin{aligned}\mu_a &= \frac{\omega}{2\nu} \left[\frac{k_i}{k_r} - \frac{k_r}{k_i} \right] \\ \mu'_s &= \frac{2\nu}{3\omega} k_i k_r.\end{aligned}\tag{2.29}$$

2.1.4 The Differential Pathlength Method

Out of convenience, much of the optical property data in this dissertation was measured by a simpler method called the differential pathlength approach. In this case, only one source-detector distance is required to find temporal changes in tissue optical properties, which permits for much more compact probes and instrumentation. In this case, we use only the intensity of detected light at different wavelengths to calculate changes in absorption.

Derivation of the differential pathlength method begins with the Beer-Lambert law, which relates absorption of light to the properties (concentration and thickness) of an opti-

cally thin sample material through which different wavelengths (λ) of light travel:

$$OD(\lambda) = -\ln\left(\frac{I(\lambda)}{I_0(\lambda)}\right) = -\mu_a(\lambda)L. \quad (2.30)$$

Here $OD(\lambda)$ is called the optical density of the sample, $I_0(\lambda)$ is the intensity of the light incident on the sample, $I(\lambda)$ is the transmitted intensity, $\mu_a(\lambda)$ is the absorption coefficient, and L is the sample thickness or light pathlength.

By extracting values of $\mu_a(\lambda)$ from Equation (2.30), we can then calculate the concentration of chromophores in the sample. In order to back-calculate N chromophore concentration *changes*, one requires at least N wavelengths of light. Using elementary optical absorption theory, we use the following relation between the absorption coefficient and chromophore concentration

$$\mu_a(\lambda) = \sum_i \epsilon_i(\lambda)C_i. \quad (2.31)$$

Here C_i is the concentration of the i th chromophore in the sample, and their corresponding wavelength-dependent extinction coefficients are ϵ_i . If we are only interested in looking at the *changes* in absorption, then we have

$$\Delta\mu_a(\lambda) = \sum_i \epsilon_i(\lambda)\Delta C_i. \quad (2.32)$$

One of the conditions for the Beer-Lambert law (Equation (2.30)) to hold, however, is that the material must not scatter the light. Biological tissue is highly scattering. In turbid media, both scattering and absorption attenuate the intensity, and furthermore, there is a

distribution of photon pathlengths from source to detector rather than a single pathlength. Hence, for our applications we use the so-called modified Beer-Lambert law (MBLL), which effectively accounts for changes due to light scattering and absorption [48]. The method is primarily useful for deriving "changes" in chromophore concentrations from "changes" in light transmission. It is thus a differential method.

Given a turbid medium with baseline optical properties $\mu_{a0}(\lambda)$ and $\mu'_{s0}(\lambda)$, the baseline optical density is $OD(\mu_{a0}(\lambda), \mu'_{s0}(\lambda))$. Changes in those optical properties are signified by $\Delta\mu_a(\lambda)$ and $\Delta\mu'_s(\lambda)$. The MBLL is derived from a first-order Taylor expansion of the optical density [39, 17, 23]:

$$\begin{aligned}
OD[\mu_{a0}(\lambda) + \Delta\mu_a(\lambda), \mu'_{s0}(\lambda) + \Delta\mu'_s(\lambda)] &\approx OD[\mu_{a0}(\lambda), \mu'_{s0}(\lambda)] \\
&+ \frac{\partial OD[\mu_{a0}(\lambda), \mu'_{s0}(\lambda)]}{\partial \mu_a(\lambda)} \Delta\mu_a(\lambda) + \frac{\partial OD[\mu_{a0}(\lambda), \mu'_{s0}(\lambda)]}{\partial \mu'_s(\lambda)} \Delta\mu'_s(\lambda) \\
&= OD[\mu_{a0}(\lambda), \mu'_{s0}(\lambda)] + d_A \Delta\mu_a(\lambda) + d_S \Delta\mu'_s(\lambda), \tag{2.33}
\end{aligned}$$

with $d_A = \frac{\partial OD[\mu_{a0}(\lambda), \mu'_{s0}(\lambda)]}{\partial \mu_a(\lambda)}$ and $d_S = \frac{\partial OD[\mu_{a0}(\lambda), \mu'_{s0}(\lambda)]}{\partial \mu'_s(\lambda)}$. We call these the absorption and scattering differential pathlengths, respectively.

In studies of brain hemodynamics, we typically assume scattering changes are small, i.e., $\Delta\mu'_s \approx 0$, and that $d_A = L\ell_{DPF}(\lambda)$. $\ell_{DPF}(\lambda)$ is the so-called differential pathlength factor (DPF). This wavelength-dependent factor, which is unitless, takes into account the increased distance that the light must travel from source to detector because of scattering and absorption effects. With no scattering, $\ell_{DPF}(\lambda) = 1$.

Inserting these two approximations into Equation (2.1.4) and looking only at changes in OD , we reach the typical form of the MBLL

$$\Delta OD(\lambda) = \Delta\mu_a(\lambda)L\ell_{DPF}(\lambda), \quad (2.34)$$

where $\Delta OD(\lambda)$ is the change in optical density at a given wavelength, $\Delta\mu_a(\lambda, t)$ is the change in absorption coefficient, L is the source-detector separation, and $\ell_{DPF}(\lambda)$ is the differential pathlength factor.

In the case of brain tissue, the main chromophores that absorb light are oxy- and deoxyhemoglobin (ΔHbO_2 , ΔHb). In this case, the MBLL can be written as follows:

$$\Delta OD(\lambda) = [\epsilon_{HbO_2}(\lambda)\Delta HbO_2 + \epsilon_{Hb}(\lambda)\Delta Hb] L\ell_{DPF}(\lambda). \quad (2.35)$$

$\epsilon_{HbO_2}(\lambda)$ and $\epsilon_{Hb}(\lambda)$ are the wavelength-dependent extinction coefficients for oxy- and deoxyhemoglobin.

For instance, to calculate changes in oxy- and deoxyhemoglobin concentrations using two wavelengths (λ_1, λ_2), we may use the following equations:

$$\begin{aligned} \Delta HbO_2 &= \frac{\epsilon_{Hb}(\lambda_1)\Delta\mu_a(\lambda_2) - \epsilon_{Hb}(\lambda_2)\Delta\mu_a(\lambda_1)}{\epsilon_{Hb}(\lambda_1)\epsilon_{HbO_2}(\lambda_2) - \epsilon_{HbO_2}(\lambda_1)\epsilon_{Hb}(\lambda_2)} \\ \Delta Hb &= \frac{\epsilon_{HbO_2}(\lambda_2)\Delta\mu_a(\lambda_1) - \epsilon_{HbO_2}(\lambda_1)\Delta\mu_a(\lambda_2)}{\epsilon_{Hb}(\lambda_1)\epsilon_{HbO_2}(\lambda_2) - \epsilon_{HbO_2}(\lambda_1)\epsilon_{Hb}(\lambda_2)}. \end{aligned} \quad (2.36)$$

These can be combined for a measure of total hemoglobin concentration change (ΔTHC):

$$\Delta THC = \Delta HbO_2 + \Delta Hb. \quad (2.37)$$

Values of differential pathlength factor depend on source-detector separation, tissue geometry, baseline optical properties, and wavelength of light. When we used the MBLL in this dissertation, values were taken from the literature for adult brain. These values were adjusted for age and also interpolated for wavelengths that were not reported [52]. As a warning, the MBLL is not accurate for when changes in μ_a and μ'_s are large compared to baseline values, or when changes are localized [17, 223].

2.2 Diffuse Correlation Spectroscopy

Light scattering can provide information about the motions of small objects such as red blood cells via tracking speckle fluctuations. Similarly, diffuse correlation spectroscopy derives changes in blood flow using the speckle fluctuations of light that is multiply scattered in biological tissue [13, 15]. This is done by measuring the time dependence of detected light intensity and computing the temporal intensity autocorrelation function. The decay rate of this autocorrelation function is related to the motions of scatterers, and in tissue the most prominent moving scatterers are red blood cells. What is unique about DCS (as opposed to laser Doppler flowmetry, for instance) is its ability to probe the dynamics of deeper tissues (>1 cm below the surface). DCS exploits the fact that the behavior of the

intensity and electric field correlation functions in a highly scattering medium can also be approximated with a diffusion equation.

This section will discuss single scattering and multiple scattering; then it outlines a derivation of the photon correlation diffusion equation, and describes various DCS blood flow validation studies.

2.2.1 Dynamic Light Scattering

In the classic single scattering version of the "dynamic light scattering" (DLS) experiment, a laser beam is pointed at a solution of dilute particles and a point-like photon detector collects light (Figure 2.4, top). The sample solution is sufficiently dilute so that light is scattered either once off a particle or not at all. As seen in Figure 2.4, bottom, the incident light electric field (with wavevector \vec{k}_{in}) induces oscillating dipole moments in the particles, which in turn radiate light fields in all directions (with wavevector \vec{k}_{out}). Momentum transfer is denoted by $\vec{q} = \vec{k}_{out} - \vec{k}_{in}$, where $q = |\vec{q}| = 2k_0 \sin \frac{\theta}{2}$. The magnitude of the wavevector is $k_0 = |\vec{k}_{in}| = |\vec{k}_{out}| = \frac{2\pi n}{\lambda}$, and θ is the scattering angle. The motion of the particles and the resulting scattered light phases cause constructive and destructive interference at the detector that manifest as a flickering of light intensity over time.

These fluctuations are recorded, and the unnormalized light intensity autocorrelation function (G_2) is calculated by a hardware correlator:

$$G_2(\tau) = \langle I(t)I(t + \tau) \rangle \quad (2.38)$$

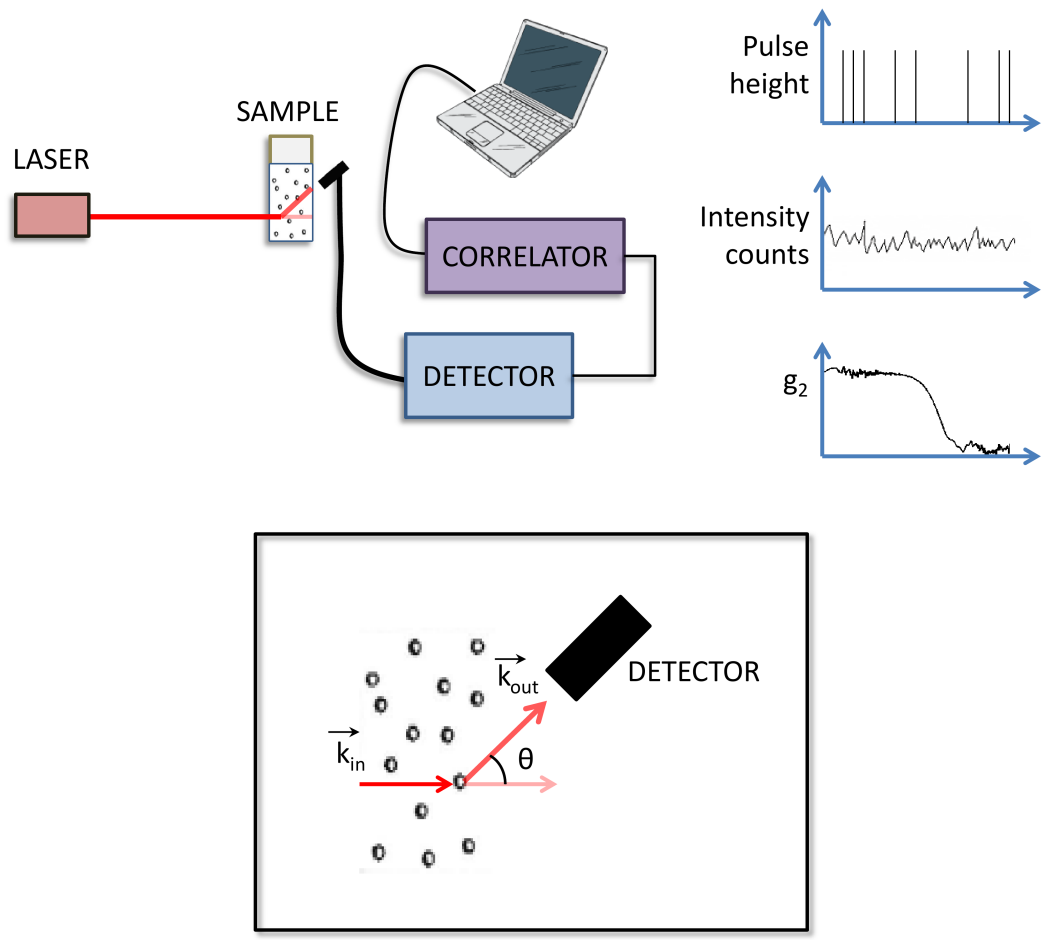


Figure 2.4: Single-scattering dynamic light scattering (DLS) setup. Light is incident (with wavevector \vec{k}_{in}) upon a very dilute solution of particles, and a detector is placed at scattering angle θ . The light scatters once off of the particle and the resulting field has wavevector \vec{k}_{out} . The electric field at the detector is a superposition of scattered fields from all particles in the sample.

with τ being the autocorrelation delay time and intensity $I(t) = |\vec{E}(t)|^2$. The brackets denote an ensemble average (for calculations), and for an ergodic system, this is equal to a time average². Figure 2.4, right, shows the trail of photon pulses over time for every instance that the photon-counting detector is triggered by a photon. These pulses are binned to get a time series of intensity counts, and this time series is autocorrelated and normalized to calculate the normalized intensity autocorrelation function $g_2(\tau)$:

$$g_2(\tau) = \frac{\langle I(t)I(t + \tau) \rangle}{\langle I(t) \rangle^2}. \quad (2.39)$$

$g_2(\tau)$ is related to the normalized temporal electric field autocorrelation function ($g_1(\tau)$)

$$g_1(\tau) = \frac{\langle \vec{E}(t) \cdot \vec{E}^*(t + \tau) \rangle}{\langle \vec{E}(t) \cdot \vec{E}^*(t) \rangle} \quad (2.40)$$

(where $\vec{E}(t)$ is the scattered electric field) by way of the Siegert relation [186]:

$$g_2(\tau) = 1 + \beta |g_1(\tau)|^2. \quad (2.41)$$

The Siegert relation is valid for Gaussian sources, and while direct laser output is not Gaussian, the superposition of all the randomly scattered fields is. β depends on detection optics and is inversely proportional to the number of detected speckles or modes. It is also affected by the coherence length and stability of the laser, and ambient light, with an ideal experimental setup having $\beta = 1$.

²In experiments, time averages are measured.

In DLS, after calculating the field autocorrelation function g_1 , dynamics of the sample can be determined by the following relation [16, 263]:

$$g_1^s(\tau) = e^{i2\pi f\tau} e^{-\frac{1}{6}q^2\langle\Delta r^2(\tau)\rangle}, \quad (2.42)$$

where f is the frequency of incident light, and $\langle\Delta r^2(\tau)\rangle$ is the mean squared displacement of the scatterers in the sample in time τ . For Brownian motion, $\langle\Delta r^2(\tau)\rangle = 6D_B\tau$ where D_B is the particle diffusion coefficient.

2.2.2 The Correlation Diffusion Equation

Since biological tissue is a turbid medium where photons multiply scatter, using DLS is not an option. We must take into account each of many scattering events that contribute to the phase shift of the emerging light fields. Physically, we can envision the detected field as comprised of light rays traveling along many photon pathways, and the total temporal electric field autocorrelation function as the weighted sum of these individual photon paths' electric field autocorrelation functions.

Another approach is to develop an analogous linear transport equation for electric field

correlation³ [1, 16], i.e.,

$$\nabla \cdot G_1^T(\vec{r}, \hat{\Omega}, \tau) \hat{\Omega} + \mu_t G_1^T(\vec{r}, \hat{\Omega}, \tau) = S(\vec{r}, \hat{\Omega}) + \mu_s \int G_1^T(\vec{r}, \hat{\Omega}', \tau) g_1^s(\hat{\Omega}, \hat{\Omega}', \tau) f(\hat{\Omega}, \hat{\Omega}') d\Omega', \quad (2.43)$$

where

$$G_1^T(\vec{r}, \hat{\Omega}, \tau) = \langle \vec{E}^*(\vec{r}, \hat{\Omega}, t) \cdot \vec{E}(\vec{r}, \hat{\Omega}, t + \tau) \rangle \quad (2.44)$$

is the unnormalized field autocorrelation function for the electric field $\vec{E}(\vec{r}, \hat{\Omega}, t)$ at position \vec{r} and time t propagating in the $\hat{\Omega}$ direction. $g_1^s(\hat{\Omega}, \hat{\Omega}', \tau)$ is a correlation scattering function for each single scattering event, i.e., derived from Equation (2.42) for single scattering. $f(\hat{\Omega}, \hat{\Omega}')$ is the normalized differential single scattering cross-section, and $S(\vec{r}, \hat{\Omega})$ is again the source distribution. Note that at $\tau = 0$, there is no field decorrelation, and Equation (2.43) reduces to the familiar photon transport equation, i.e., Equation (2.3). The correlation transport equation is applicable from single scattering to multiple scattering systems, but like the photon transport equation, it is difficult to implement in practice.

To simplify things, one can again make a P_1 approximation and ultimately derive the field correlation analogue to the photon diffusion equation (Equation (2.13)) [16, 55], i.e.,

$$\left(D\nabla^2 - \nu\mu_a - \frac{1}{3}\alpha\nu\mu'_s k_0^2 \langle \Delta r^2(\tau) \rangle \right) G_1(\vec{r}, \tau) = -\nu S(\vec{r}). \quad (2.45)$$

Here $G_1(\vec{r}, \tau)$ is the unnormalized field correlation function at \vec{r} and integrated over all an-

³Time dependence has been left out of the correlation transport equation because we only consider measurements with CW sources in steady state systems. In biological tissue, the dynamics are in a quasi-steady state, since the scatterer dynamics are not changing over the time scale of the measurement.

gles; $S(\vec{r})$ is the isotropic light source term; $D \approx \nu/3\mu'_s$ is the photon diffusion coefficient, and $k_0 = 2\pi/\lambda$ is the wavenumber of the incident CW light. α represents the fraction of total photon scattering events from moving scatterers. As in Equation (2.13), ν is the speed of light in the medium, μ_a is the absorption coefficient, and μ'_s is the reduced scattering coefficient. A step-by-step derivation of Equation (2.45) can be found in Appendix A.2 of David Boas's dissertation [16, 13, 15].

The assumptions required for Equation (2.45) are as follows: the medium is highly scattering, the scattering phase function and single scattering temporal autocorrelation function depend only on the scattering angle (i.e. randomly oriented scatterers and isotropic dynamics), and the photon random walk step length is much smaller than the dimensions of the sample and the photon absorption length. Strictly speaking, we also assume that the correlation time τ is much smaller than the time it takes for a scatterer to move a wavelength of light (i.e., $\kappa_0^2 \langle \Delta r^2(\tau) \rangle \ll 1$). In biological tissue, the capillary network is serpentine enough that red blood cell motions can be approximated as isotropic. Also, as is the case with DOS, the DCS signal will be weighted towards the capillary network, since larger vessels that have more directional flow will be highly absorbing.

For a homogeneous semi-infinite medium, the standard extrapolated-zero boundary condition is used (see Section 2.1.3):

$$G_1(z = -z_b, \tau) = 0. \quad (2.46)$$

The field correlation function on the inside of the medium is well-modeled with the bound-

ary condition that the function drops to zero at a distance $z_b = \frac{2}{3\mu'_s}$ outside of the turbid medium. Then the method of images is readily implemented to obtain a solution for $G_1(\tau)$.

Predictably, the solution to Equation (2.45) is of a similar form as the semi-infinite medium solution to the photon diffusion equation (Equation (2.25)):

$$G_1(r, z, \tau) = \frac{\nu}{4\pi D} \left[\frac{e^{-K(\tau)r_1}}{r_1} - \frac{e^{-K(\tau)r_2}}{r_2} \right] \quad (2.47)$$

for a detector at (r, z) , but the "wavevector" depends on τ , i.e.,

$$K(\tau) = \sqrt{\frac{\nu}{D} \left[\mu_a + \frac{1}{3}\alpha\mu'_s k_0^2 \langle r^2(\tau) \rangle \right]}. \quad (2.48)$$

Again, $r_1 = \sqrt{r^2 + (z - \ell_{tr})^2}$, $r_2 = \sqrt{r^2 + (z + \ell_{tr} + 2z_b)^2}$, and $\ell_{tr} = 1/\mu'_s$ is the transport mean free path. Importantly, the term $\frac{1}{3}\alpha\mu'_s k_0^2 \langle r^2(\tau) \rangle$ is a loss term, akin to μ_a , that represents the "absorption" of correlation due to dynamic processes [16].

2.2.3 Diffuse Correlation Spectroscopy

When implementing diffuse correlation spectroscopy in practice, we have found over a wide range of biological tissues that the Brownian diffusion model (i.e., $\langle \Delta r^2(\tau) \rangle = 6D_{BT}$) mentioned in Section 2.2.1 fits our correlation curves better than other models such as random ballistic flow ($\langle \Delta r^2(\tau) \rangle = \langle V^2 \rangle \tau^2$, where $\langle V^2 \rangle$ is the second moment of the particle speed distribution) [34, 54, 263]. This general effect is demonstrated in Figure 2.5, where an intensity autocorrelation function from human arm muscle is fit to both Brownian

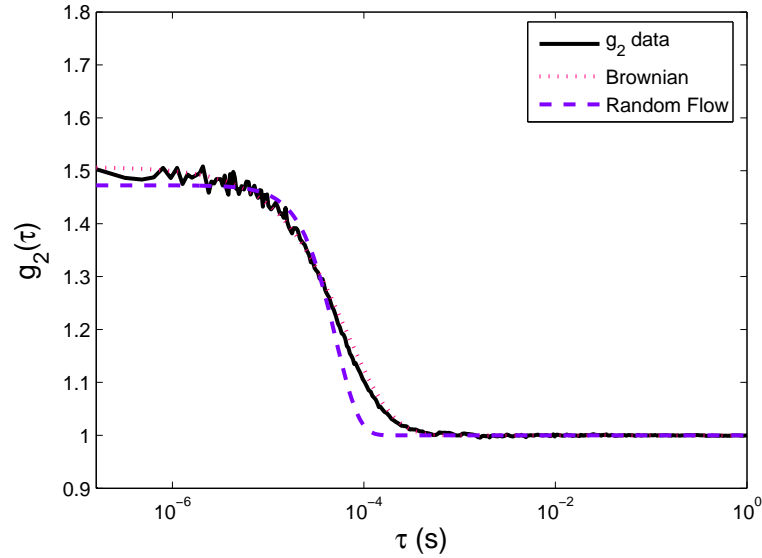


Figure 2.5: Measured normalized intensity autocorrelation function $g_2(\tau)$ plotted against delay time τ measured from human arm muscle with source-detector separation of 2.5 cm, fit to both Brownian diffusion and random flow models. We typically fit $g_2(\tau)$ to a Brownian model, which as seen from the figure, fits much better than a random flow model.

diffusion and random flow models. The exact reason why the Brownian model fits so well is still not fully understood. In general, red blood cells in the microvasculature experience rolling, tumbling, and translating rather than straightforward ballistic flow, but apparently these effects can be lumped into a diffusion coefficient.

Thus, in our analysis using Equation (2.47), we set $\langle \Delta r^2(\tau) \rangle = 6D_B\tau$, and we can fit our $g_2(\tau)$ data for the quantity that we define as the blood flow index ($BFI = \alpha D_B$). BFI has units of cm^2/s , while true blood flow should have units of cm^3/s . Thus, BFI is not an absolute measure of blood flow. Interestingly, a few studies have found good correlation between BFI and absolute blood flow [24, 261, 191], and BFI has been found to accurately track *relative changes* in blood flow in most systems studied, including in this

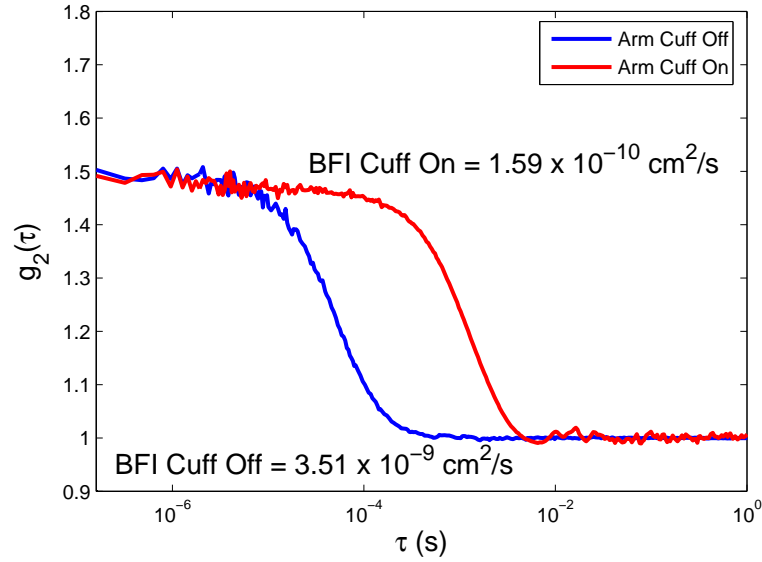


Figure 2.6: Normalized intensity autocorrelation functions ($g_2(\tau)$) plotted against delay time τ from an arm cuff occlusion experiment. One curve shows $g_2(\tau)$ during baseline, when the arm cuff is "off" or uninflated. When the arm cuff is "on" or inflated, the decay of $g_2(\tau)$ becomes much slower due to less blood flow in the arm muscle due to artery occlusion. The source-detector separation was 2.5 cm.

thesis (see Chapter 4). Thus, we often report the percent change from baseline of blood flow, or what we call relative blood flow (rBF):

$$rBF = \frac{BFI - BFI_0}{BFI_0} \times 100\%, \quad (2.49)$$

where BFI_0 is the baseline value of the blood flow index. Ultimately, calibration of BFI may also be possible using DCS in conjunction with an absolute blood flow technique; this problem is an area of active research in the field.

Figure 2.6 shows raw data from an arm cuff occlusion, an experiment frequently used to test whether a new DCS module is properly able to measure changes in blood flow.

The stark difference in g_2 decay with and without the occlusion reflects the difference in muscle blood flow while the arm cuff is uninflated versus when it is inflated. The arm cuff being tightened around the arm provides sufficient artery occlusion to significantly lower the blood flow, and thus we see a much slower decay in the autocorrelation function. This is quantified by an order of magnitude change in BFI ($BFI_{CuffOff} = 3.51 \times 10^{-9}$ cm²/s versus $BFI_{CuffOn} = 1.59 \times 10^{-10}$ cm²/s).

Also notice in Figure 2.6 that the normalized autocorrelation curves have an intercept of approximately 1.5 as the delay time approaches zero. From Equation (2.41), we see that this means $\beta = 0.5$, which is a typical value for our experimental setup for human brain measurements too. As mentioned in Section 2.2.1, β is dependent on source coherence, detection optics, ambient light, and other factors, with an ideal setup having $\beta = 1$. We also noted that β is inversely proportional to the number of detected speckles or modes. Since the experiments on human brain performed in this dissertation use single mode detection fibers that allow transmission of two orthogonal polarization modes, a β of 0.5 is reasonable [263, 23].

The "detection volume" of cortical tissue from which diffuse optical measurements are recorded depends on the source-detector separation [74, 37] and the optical properties of the tissue (i.e. the number and density of photon scatterers and absorbers). In the investigations of adult brain described in this dissertation, the detection volume was standardized by utilizing a DCS/DOS source-detector separation of 2.5 cm for all subjects. A 2.5 cm source-detector separation corresponds to a penetration depth of about 1.25 to 1.5 cm. Al-

though larger source-detector distances have been used for some DOS studies [149, 226], a separation distance of 2.5 cm has been utilized effectively in several DOS studies of the brain [57, 59, 130, 120] and provides a better signal for transcranial DCS than larger distances. Since the light path of DCS is approximately the same as that of DOS, due to the similar wavelengths that are utilized, both methods sample essentially the same tissue volume.

With regard to the DCS detection volume, thus far five published studies have quantitatively examined the penetration of DCS signals into the brain at the 2.5 cm source-detector separation. In a study by Durduran [54], a human skull was used to verify experimentally that DCS penetrates the skull and interrogates the properties of an underlying medium. In this same paper, hypercapnia-induced changes in intracranial blood flow were also detected and were shown to be distinct from concurrent laser Doppler flowmetry measurements of scalp blood flow. Li *et al* [130] produced experimentally similar findings to Durduran [54] using a three-layer model of the skull. Lastly, Gagnon *et al* [73] utilized analytic two-layer solutions, Monte Carlo simulations derived from segmented MRI images and experiments on layered phantoms to verify that DCS is able to penetrate through the scalp and skull using a source-detector separation of approximately 2.5 cm.

A fourth study (Chapter 4 in this dissertation) validated DCS measurements of $rCBF$ using a 2.5 cm source-detector separation with concurrent Xenon-CT measurements of $rCBF$ in patients (mean age 48, range 18-82) with traumatic brain injury, aneurysmal subarachnoid hemorrhage, and acute ischemic stroke [120]. This clinical study provided direct

validation of DCS against an established diagnostic modality for measuring cerebral blood flow. Finally, a 2.5 cm source-detector separation has also been used in a clinical study that utilized DCS to characterize autoregulatory impairment in acute, ischemic stroke patients and to investigate cerebral autoregulation in subjects with vascular risk factors such as hypertension and diabetes [59]. While the research described above clearly indicates that light from the DCS probe penetrates through the skull and into the cortex, we have already begun current studies using probes with both small and large source-detector separations in order to more definitively account for scalp and skull signals.

DCS has been successfully validated by numerous studies on animals [150, 54, 260, 225, 264, 27, 156, 50] and some studies on humans [261, 24, 191, 58, 120, 265, 25, 155, 56]. These investigations have explored a wide range of tissue types, perturbations, and comparison modalities. With each study, we gather more evidence that DCS indeed measures a quantity that trends with blood flow, and our lab also continues to develop DCS theory, instrumentation, and probes further with every application.

Chapter 3

Hybrid Optical Instrumentation

This chapter will review details involved in the hybrid implementation of DCS/DOS. In Section 3.1, I will first describe the standard homodyne frequency-domain device ("Joel's Instrument", so-called because it was typically stored in the lab of our frequent collaborator Dr. Joel Greenberg) used in most of the dissertation experiments. In Section 3.1.2, I will describe the changes in the next iteration of "Joel's Instrument," called "Small Optical Joel's Instrument (SOJI)." SOJI is an upgraded version of Joel's Instrument, with significant improvements implemented. Then I move on to describing the DCS modules. First, I start with describing the basic 8-channel DCS device, both how to build and test it. Then I move onto the next iteration of DCS devices, of using multiple wavelengths to extract oxygenation information simultaneously. Lastly, I describe an ultra-portable DCS-only instrument that was modified specifically for a study at high altitudes (see Chapter 7).

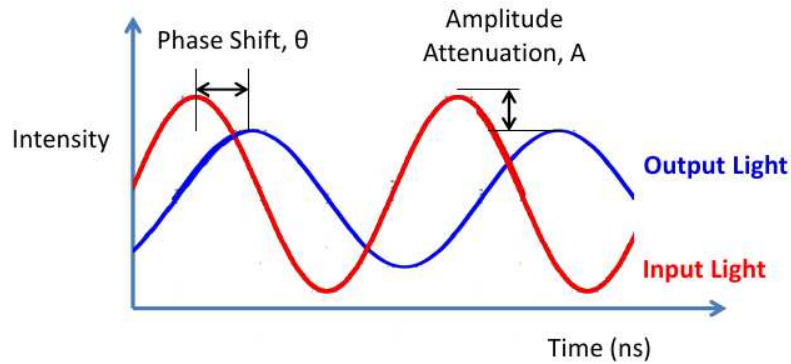


Figure 3.1: A schematic of the intensity-modulated or frequency-domain technique for DOS. Input light is sinusoidally modulated, and the subsequent amplitude attenuation and phase shift of the detected light is used to extract information about the medium’s optical properties.

3.1 The DOS Module

What follows is a brief description of both a basic DOS module as well as an upgraded version. The basic DOS module has been described previously [263], and is the same one that we have used for numerous experiments on human brain in the last few years [61, 56, 120, 59]. I will start with the homodyne frequency-domain DOS module, providing information about its parts and characterization of the device. Then I will describe important details about the 8-channel DCS module, i.e., its parts and characterization.

3.1.1 Basic DOS Module

Out of the three DOS schemes described in Section 2.1.2, Joel’s Instrument employs the frequency-domain (FD) technique, where the light source intensity is modulated with a radio-frequency (RF) sinusoidal signal. We extract information about the turbid medium

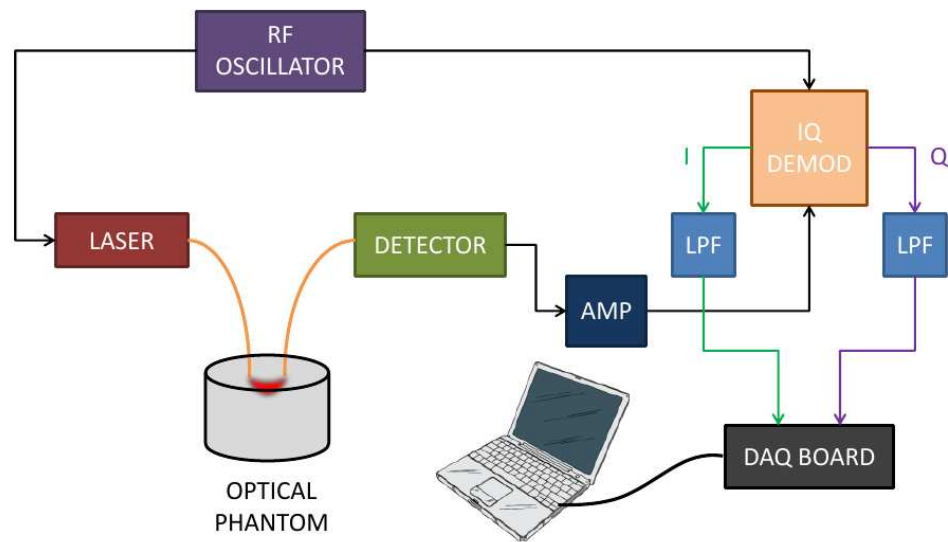


Figure 3.2: Diagram of a basic homodyne detection DOS system. The oscillator provides a reference signal to the laser and IQ demodulator. The light from the laser goes to, say, an optical phantom, and is detected and amplified before being transformed by the IQ demodulator to I and Q signals. Those then go through low pass filters (LPF) before being transmitted to a computer through a data acquisition (DAQ) board.

from both the amplitude attenuation and phase shift of the input light versus the detected light (see Figure 3.1). Our DOS module uses what is called a homodyne detection technique. Light is detected, translated into an electronic signal by the detector, then amplified and sent to an in-phase/in-quadrature (IQ) demodulator. The outputs of the IQ demodulator, i.e., the in-phase and in-quadrature parts, are respectively the sine and cosine components of the signal.

A diagram of a basic homodyne detection technique is shown in Figure 3.2. The RF oscillator provides a sinusoidal reference signal for both the laser diode and IQ demodulator on the detection side. On the source side, this intensity-modulated light is transmitted to a turbid medium through a multimode optical fiber. Light that has traveled through the

medium and reaches the detector, typically a photomultiplier tube (PMT) or avalanche photodiode (APD), is then amplified and put through the IQ demodulator.

In the IQ demodulator, both the reference signal from the oscillator ($A_{ref} \sin \omega t$) and the signal from the detector ($A_{det} \sin(\omega t + \theta)$, where θ is the phase shift with respect to the reference) are split in two. One of the reference signal arms is shifted by 90° , the other is not. Neither of the detected signal arms is phase-shifted. The non-shifted reference and detector signals are multiplied for the in-phase component:

$$\begin{aligned} I(t) &= \frac{1}{2} A_{ref} \sin \omega t \cdot A_{det} \sin(\omega t + \theta) + I_{off} \\ &= \frac{1}{8} A_{ref} A_{det} [\cos \theta - \cos(2\omega t + \theta)] + I_{off}, \end{aligned} \quad (3.1)$$

where I_{off} is the in-phase DC offset term. Similarly, when the 90° -shifted reference and detector signals are multiplied, they create the in-quadrature component:

$$\begin{aligned} Q(t) &= \frac{1}{2} A_{ref} \cos \omega t \cdot A_{det} \sin(\omega t + \theta) + Q_{off} \\ &= \frac{1}{8} A_{ref} A_{det} [\sin \theta + \sin(2\omega t + \theta)] + Q_{off}, \end{aligned} \quad (3.2)$$

where Q_{off} is the in-quadrature DC offset term.

The purpose of the low pass filters (LPF) after the IQ demodulator (see Figure 3.2) is to remove the high frequency components of the signal (the $2\omega t$ terms in Equations (3.1)

and (3.2)), resulting in two DC signals

$$\begin{aligned} I_{DC} &= A \cos \theta + I_{off} \\ Q_{DC} &= A \sin \theta + Q_{off} \end{aligned} \quad (3.3)$$

where $A = \frac{1}{8}A_{ref}A_{det}$. I_{DC} and Q_{DC} then travel by RF-shielded cables to a digital-to-analog data acquisition (DAQ) board to be then recorded by a computer.

We then can calculate the amplitude (A) and phase (θ) of the detected signal from I_{DC} and Q_{DC} and their DC offsets for each frame of data using our analysis software:

$$\begin{aligned} A &= \sqrt{[I_{DC} - I_{off}]^2 + [Q_{DC} - Q_{off}]^2} \\ \theta &= \arctan \left[\frac{Q_{DC} - Q_{off}}{I_{DC} - I_{off}} \right]. \end{aligned} \quad (3.4)$$

I_{off} and Q_{off} are measured by obtaining values of I_{DC} and Q_{DC} while blocking input light. Typically it is best to have values of offset for every frame of data, since the levels may change over the course of an experiment. A and θ can subsequently be used to obtain optical properties of the medium via the methods described in Chapter 2.

In Joel's Instrument, we use a modulation frequency of 70 MHz from an oscillator whose output goes into an RF splitter. From there, the RF signal goes into each source and detector circuit of the homodyne system. The instrument uses three different wavelengths of near-infrared light for sources: 685 nm (ML1413R; Mitsubishi Electric, Japan), 785 nm (DL-4140-001S; Sanyo Electric, Japan), and 830 nm (DL-8032-001; Sanyo Electric,

Japan). Each laser diode is driven sinusoidally at 70 MHz by a driving circuit; the RF signal is combined with the DC component responsible for CW operation using a bias-tee (ZFBT-4R2G+; Mini-Circuits, NY). And as stated earlier, the 70 MHz output from the oscillator also provides a reference signal for the IQ demodulator (MIQY-70D; Mini-Circuits, NY) in the detection circuit.

We mount components individually in modular nuclear instrument bins (NIM-BIN; Mech-Tronics, IL) for sufficient RF shielding. This approach also makes connecting power supplies to each component much simpler, since wiring is built into the larger frame that houses the modules. NIM-BINs come in different widths, and we typically use 1"- or 2"-wide modules. Also high-quality RF-shielded coaxial cables (RF Connection, Inc., CA) are used between NIM-BINs that house the oscillator and those containing the laser and detection circuits.

Joel's Instrument has four DOS detectors each in their own NIM-BIN, two PMTs (R928; Hamamatsu, Japan) and two APDs (C5331-01; Hamamatsu, Japan). APDs are typically used when we detect "a lot" of light, i.e. such as experiments with small source-detector separations; APDs in this case employ gains of ~ 100 . PMTs have higher gains, about 10^7 , with almost no additional noise; they are used for applications which require low light level detection. For instance, we use the PMTs to detect signal from human cortex through scalp and skull for our DOS brain applications.

The detection circuit involves a series of components. Briefly, the detected light is converted to an electronic signal by the PMT, then bandpass filtered at 70 ± 7 MHz (SBP-

70; Mini-Circuits, NY). The output is amplified by 24 dB (ZFL-500LN; Mini-Circuits, NY) and then by 19 dB (ZFL-500HLN; Mini-Circuits, NY). This signal is sent to the IQ demodulator, along with the reference signal from the RF oscillator. Lastly, I and Q are low-pass filtered (SLP-30; Mini-Circuits, NY) to remove the high-frequency components, and the final output signals go through 100 kHz low-pass filters [23] and then into the analog inputs of a DAQ board (PCI-6032E; National Instruments, TX).

In order to deliver light to multiple locations or probes, we use a 4×8 optical switch (Piezosystem Jena, Germany) capable of cycling through all three wavelengths plus a DCS source, if needed, to 8 different source fiber positions. The switching time is roughly 2 ms, and input light will experience a loss of around 1.4 dB. Digital signals from a DAQ board hooked up to a computer are used to control the switching.

3.1.2 Upgraded DOS Device (“SOJI”)

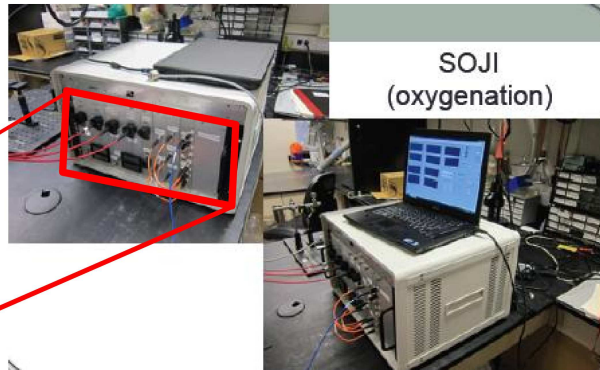
Since Joel’s Instrument was built some years ago, we upgraded the device in virtually all aspects. The result is an instrument we call SOJI, or Small Optical Joel’s Instrument. As we will show in this section, and in Section 3.1.3, that the DOS module of SOJI improves on almost every aspect of modules we had previously been using in our lab (which were described in the previous section).

SOJI’s frequency-domain DOS device also employs a homodyne detection technique. Figure 3.3 shows photos of the unwieldy old instrument compared to SOJI; SOJI has a far smaller footprint and overall size (less than half the volume), even while containing

old Joel's instrument



new Joel's Instrument



So much smaller!

Figure 3.3: Photos of the old instrument and the upgraded Small Optical Joel's Instrument (SOJI). Note that SOJI packs more lasers and detectors into less than half the space of the older instrument.

more lasers and detectors. SOJI contains a total of 6 detectors (4 PMTs, 2 APDs) and 5 lasers (685, 705, 808, 830, and 850 nm). We have assembled smaller circuitry for the laser drivers, so that we can pack 5 lasers in two 1" NIM-BINs. Joel's Instrument used three 2" NIM-BINs for only 3 lasers. The smaller laser drivers have also improved output stability dramatically (see Section 3.1.3).

An issue with past instruments has been laser warm-up time. Even though they are already quite stable, the lasers in SOJI are in the process of being fitted with thermoelectric cooling (TEC), so that we will no longer have to wait up to 1 hour for the laser output to stabilize. Each laser will sit on a thermoelectric cooler (CP1.0-31-06L; Melcor Corp., NJ) driven by a high efficiency TEC controller chip (TEC5V6A-D; Analog Technologies, CA). This feature is useful especially for human stroke studies, where clinical experiments tend to pop up spontaneously and with little prior notice.

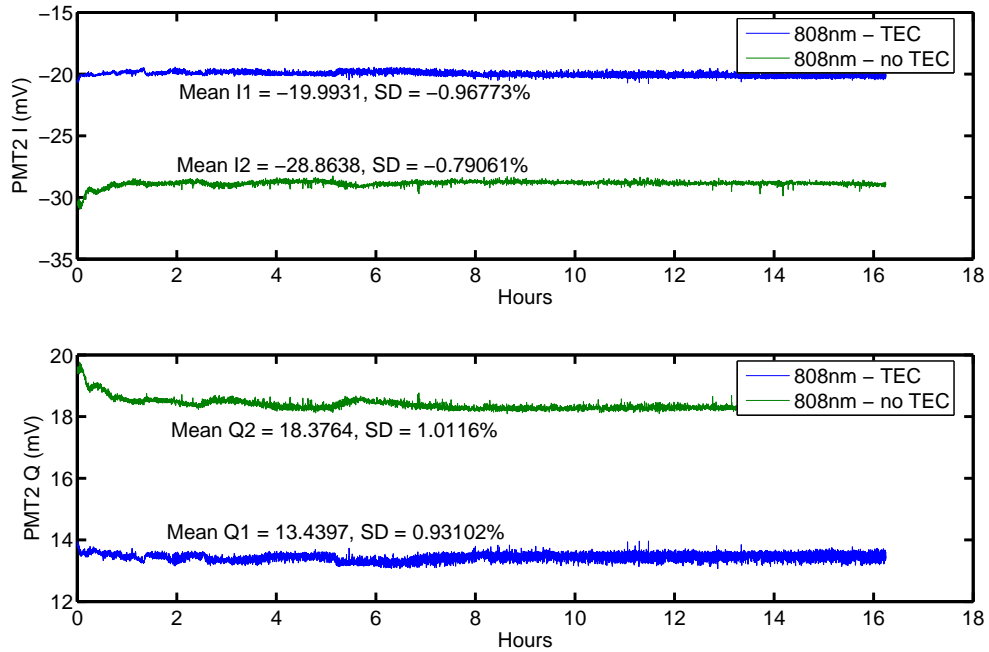


Figure 3.4: Example results from testing temperature controlled lasers using the SOJI DOS module. Data shows long-time stability of I and Q from two identical 808 nm lasers: one with TEC and one without. Note that the laser without TEC takes ≈ 1 hour to warm up and stabilize in the beginning.

We tested the temperature control using two identical 808 nm lasers (DL-8141-035; Sanyo Electric, Japan): one with TEC and the other without. They both went to a solid phantom, and for detection we used one of SOJI's PMTs. SOJI started out "cold." Figure 3.4 shows results of this test. We recorded I and Q values overnight from both lasers simultaneously; notice that the laser without TEC takes ≈ 1 hour to warm up and stabilize at the beginning of the experiment. Over a long period of time, the two lasers behaved more or less the same, but the first hour clearly reveals that TEC helps with initial amplitude drift (see Table 3.1). Also, apparently phase is not strongly affected by temperature-related instability.

Table 3.1: Results of experiment comparing two identical 808 nm lasers, one with TEC and the other without, in SOJI’s DOS module.

Quantity	No TEC	TEC
Amplitude Error, Whole Period, %	0.83	0.93
Amplitude Error, 1st Hour, %	1.7	0.71
Phase Error, Whole Period, degrees	0.12	0.13
Phase Error, 1st Hour, degrees	0.09	0.10

We have also upgraded the optical switch to a 5×8 microelectromechanical systems (MEMS) switch (DiCon Fiberoptics Inc., CA). It has improved transmission and stability, and does not require an additional driver circuit. Also, we have found smaller and more stable AC-DC power supplies (Acopian Technical Company, PA) for the detection and source circuits. Improvements in stability and linearity are quantified in the following section.

3.1.3 DOS Module Quality Testing

Before being used for human and animal experiments, DOS modules were thoroughly tested for stability and accuracy. Its range of viability must be characterized so that we know its limits of operation. This section describes the tests we need to do for any DOS module.

Quality checking of DOS lasers involves investigating their modulation depth and long-term stability. Modulation depth is defined as the modulation amplitude, or half the peak-to-peak value, divided by the mean value. With a PIN diode, the modulation depth of a given laser can be easily checked with an oscilloscope. Manipulating the DC operating current of the driver and strength of RF modulation permits adjustment of modulation depth

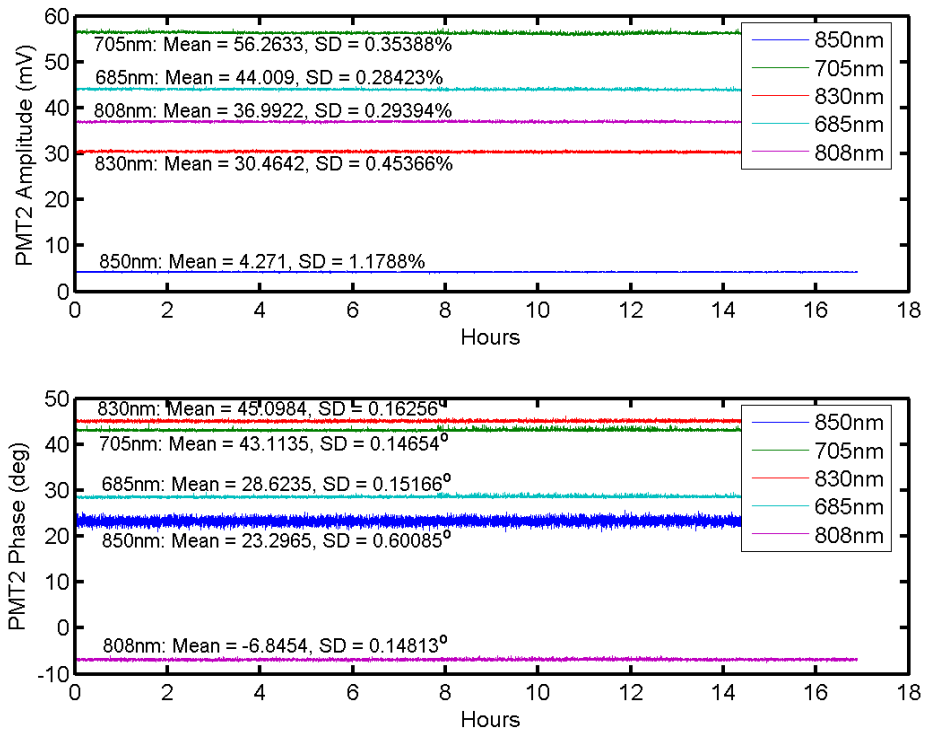


Figure 3.5: Example results of a long-term stability test using the SOJI DOS module. Data shows little variation in AC amplitude (in mV) and phase (in degrees) from all five wavelengths over a period of over 16 hours on a solid optical tissue phantom. Mean and standard deviation values from each laser are noted.

to a desired $\sim 100\%$. Typical values for our lasers range from 80-90%.

Long-term stability is important, because we do not want changes in amplitude or phase due to laser instability to be mistaken for physiological occurrences during a clinical experiment. Typically an overnight stability test is performed for about 15 hours on an optical tissue phantom. All lasers can be measured at once by going through the optical switch, and offset stability can be checked by capping one source position in the switch.

An example stability plot from SOJI is shown in Figure 3.5. Amplitude must not have jumps and its percentage standard deviation should remain below 2%. The standard devia-

Table 3.2: Long-term stability (>16 hours) of amplitude and phase for all five wavelengths of SOJI.

Laser	Mean Amplitude <i>mV</i>	Amplitude Error %	Phase Error <i>degrees</i>
850 nm	4.3	1.2	0.60
705 nm	56.3	0.35	0.15
830 nm	30.5	0.45	0.16
685 nm	44.0	0.28	0.15
808 nm	37.0	0.29	0.15

tion of phase must remain below 2° . Stability details for each of the five lasers¹ are shown in Table 3.2.

It should be noted that these minimum requirements have been barely maintained, if at all, by past instruments built in our lab [23, 263]. SOJI, on the other hand, shows greater stability in this respect than any other instrument currently in use by our lab, including the commercial ISS ImagentTM heterodyne device. A comparison of SOJI to past devices can be found in Table 3.3. The stability of the basic DOS module found in the old instrument (see Section 3.1.1) is closest to that of the Homodyne device values.

The dynamic range of the DOS module, including all electronic and optical components, is investigated with a linearity test [36]. This is important because when calculating changes in optical properties from the output of the module, we assume that the changes we are seeing are proportional to the light detected, i.e., that intensity variations will translate to a proportional change in light detected by our system. If we are outside of the linear range, such as below the noise floor or in saturation mode of the detector, this assumption will prove false.

Figure 3.6 (top) shows a diagram of how we investigate the dynamic range. Experimen-

¹Data is from PMT 2, but the other five detectors showed similar results.

Table 3.3: Comparison of instrument offset and signal stability for all detectors in four different DOS instruments: Homodyne, Heterodyne, ISS Imagent™, and SOJI. Data from the former three devices are taken from Erin M. Buckley’s dissertation [23].

Instrument	Detector	Amplitude Error	Phase Error
Homodyne	PMT 1	1.0%	0.5°
	PMT 2	2.4%	1.5°
	APD 1	1.8%	0.7°
	APD 2	2.3%	1.3°
Heterodyne	PMT 1	1.0%	0.4°
	PMT 2	1.5%	0.7°
ISS Imagent™	PMT 1	1.0%	0.8°
	PMT 2	1.0%	1.5°
SOJI	PMT 1	0.7%	0.1°
	PMT 2	0.3%	0.2°
	PMT 3	0.4%	0.2°
	PMT 4	0.1%	0.1°
	APD 1	0.5%	0.7°
	APD 2	0.3%	0.1°

tally, we connect a mechanical attenuator that can be tuned to block off a certain amount of light directly to one of the lasers in our system. Then, that light is split into two beams with a 90-10 fiber splitter, i.e., 90% of the light goes to a solid phantom and 10% goes to an optical power meter. A detector fiber is placed a fixed distance away from the source fiber on the phantom, with the other end going to the detector of interest. Then the power of the laser is attenuated in 1 dB steps from below the noise floor to above the saturation point to fully characterize the instrument’s linear range. This procedure is repeated for all detectors.

We plot input power (in dBmW) versus output voltage (in dBmV) to discover the voltage range to stay within during measurements (see Figure 3.6), bottom). In this range, power and voltage have a linear relationship, slope is close to 2, and phase is fairly constant. Table 3.4 shows the dynamic ranges of all detectors in SOJI in comparison to other

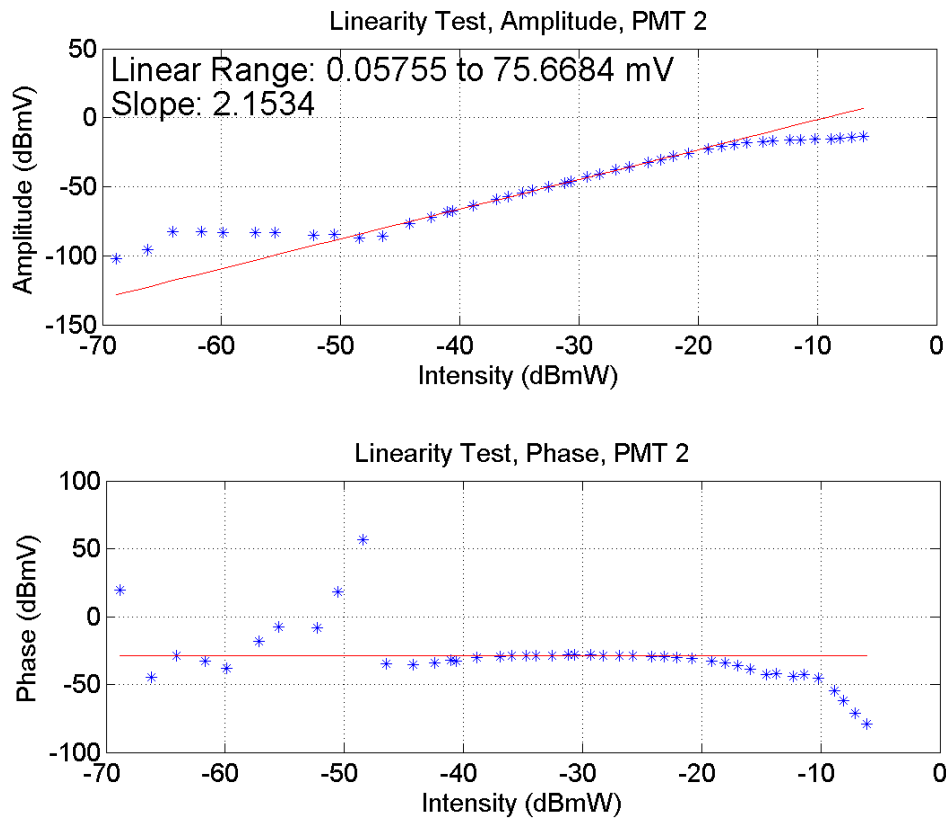
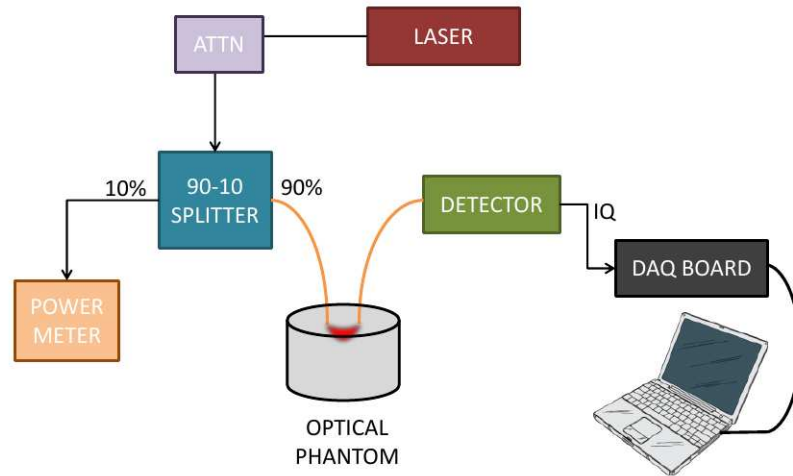


Figure 3.6: (top) Diagram of a linearity test to find the dynamic range of DOS instrument detectors. The laser output goes into a variable optical attenuator, which is used to change the power fed into the 90-10 splitter. The 10% portion goes into a power meter, while the 90% goes to an optical phantom. (bottom) Example results of a linearity test using the SOJI DOS module. This test used the 808 nm laser to find the dynamic range of PMT 2. Note that the slope of the amplitude versus intensity plot is close to 2, as it should be, and the phase is constant within a wide range of intensities.

Table 3.4: Comparison of dynamic range for all detectors in four different DOS instruments: Homodyne, Heterodyne, ISS ImagentTM, and SOJI. Data from the former three devices are taken from Erin M. Buckley’s dissertation [23].

Instrument	Detector	Dynamic Range (dB)
Homodyne	PMT 1	51.3
	PMT 2	31.6
	APD 1	53.3
	APD 2	41.7
Heterodyne	PMT 1	55.3
	PMT 2	48.1
ISS Imagent TM	PMT 1	45.1
	PMT 2	46.0
SOJI	PMT 1	79.6
	PMT 2	62.0
	PMT 3	67.3
	PMT 4	63.6
	APD 1	82.4
	APD 2	71.1

instruments currently used in our lab. All PMT bias voltages were fixed at 700 V, and we used the linear range of phase (within 1°) to fit for the amplitude linear range. Again, SOJI has a much larger dynamic range than the others, making it more suitable for a wide range of light levels and source-detector separations.

Next, we test the instrument’s ability to extract accurate optical properties. This is done using a liquid tissue phantom, and we gradually vary the absorption and scattering in a range that we might typically see in a clinical experiment. To vary scattering, we use Intralipid, a fat emulsion often used to make solutions that closely mimic the response of biological tissue. To vary absorption, we add small concentrations of either India ink or nigrosin. Detailed recipes and instructions for tissue phantoms can be found in Regine Choe’s dissertation [36].

Figure 3.7 shows an example Intralipid titration plot to test SOJI’s ability to extract

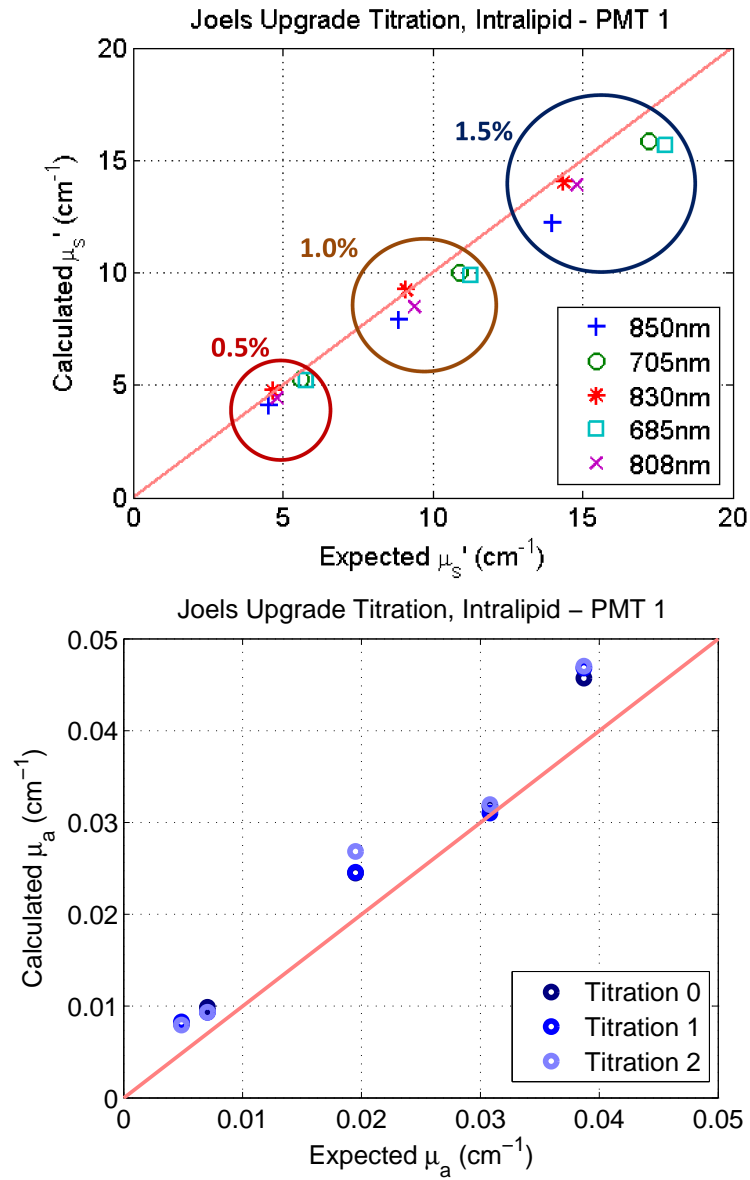


Figure 3.7: Example results of an Intralipid titration test using the SOJI DOS module. The plot on the left shows expected μ'_s for all five wavelengths versus the experimentally derived μ'_s . This titration used Intralipid concentrations of 0.5, 1.0, and 1.5%. The plot on the right shows expected versus experimentally derived μ_a values for the five different wavelengths. In both plots, the red line is unity.

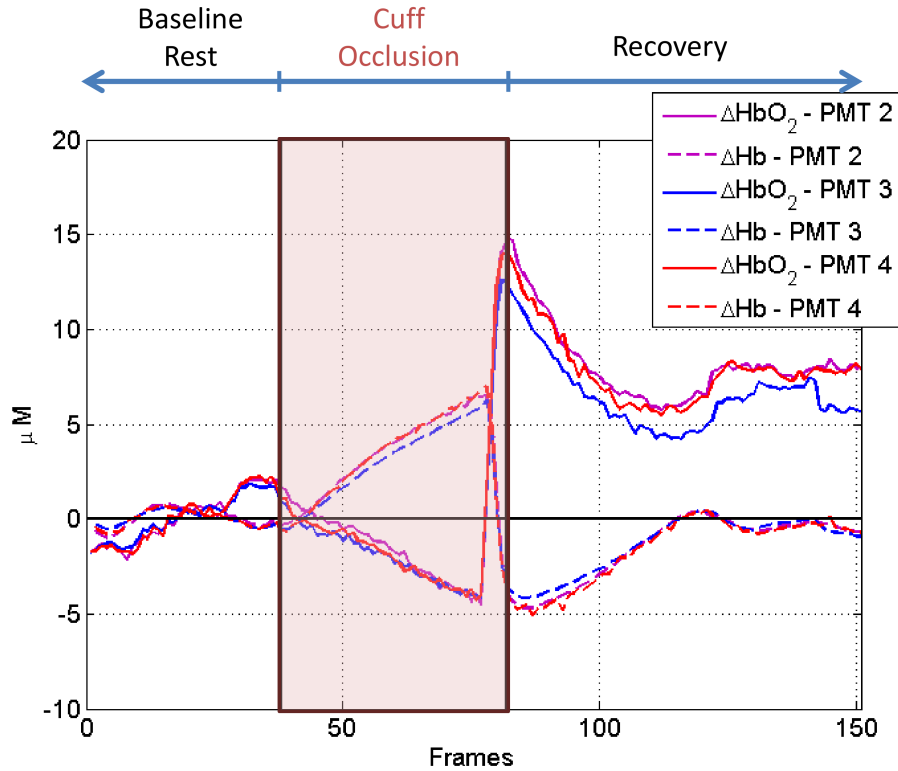


Figure 3.8: Example results of an arm cuff test using the SOJI DOS module. The timeline above the plot shows the arm cuff occlusion protocol used. The subject first rested for several minutes with the probe on his arm. Then the cuff was then occluded, then released for end recovery period. The shaded maroon area marks when the cuff was occluded. Three PMTs were used at the same source-detector separation of 2.5 cm.

scattering properties. Experimentally, we used a large (≈ 18 L) fish tank in order to model the infinite geometry, and we employed an automated translation stage to enable the source fiber to move smoothly and in fixed steps to accurately measure at a wide range of source-detector separations (usually < 1 cm to > 9 cm). PMT bias voltage were kept at 700 V, and the Intralipid concentration levels varied around 0.5, 1.0, and 1.5%. No absorption agent was added, so the solution's μ_a levels were similar to those of water.

Lastly, the DOS device was tested on a human subject. For this purpose, we typically

carry out an arm cuff occlusion experiment, placing the optical probe on the inner forearm muscle. An inflatable blood pressure cuff is used to occlude blood flow to the lower part of the arm. This prevents new oxygenated blood from coming in, while the muscle uses up the oxygen contained in the blood already in the lower arm. The experimental result we expect is a slow decrease in oxyhemoglobin and a mirrored slow increase in deoxyhemoglobin. Then when the cuff is released, we expect and see an overshoot of oxyhemoglobin as the oxygenated blood floods back into the lower arm.

An example arm cuff experiment result from SOJI is shown in Figure 3.8. Three PMTs were used at the same source-detector separation of 2.5 cm, and all gave the correct trend and magnitude of change for Hb and HbO_2 concentrations. Analysis was completed with the modified Beer-Lambert law using all five wavelengths of SOJI.

We also performed an experiment for testing human brain applications using a breath-holding task. A probe is adhered to one side of the forehead, with a source-detector separation of 2.5 cm. The subject sits in a chair quietly for 2 minutes to use as baseline data, then he or she holds breath for 20 seconds, and then there is a recovery period of 3 minutes. The breath hold task is repeated 3 times, with results averaged over the 3 events.

Figure 3.9 shows an example result from SOJI's breath hold experiment. The trends of Hb and HbO_2 are as expected – both increase over the period of breath holding, and then drop once the subject has started to breath normally again. This is due to the increase in CBF as the body tries to deliver more oxygen to the brain.

These simple and straightforward human experiments are also used to test DCS mod-

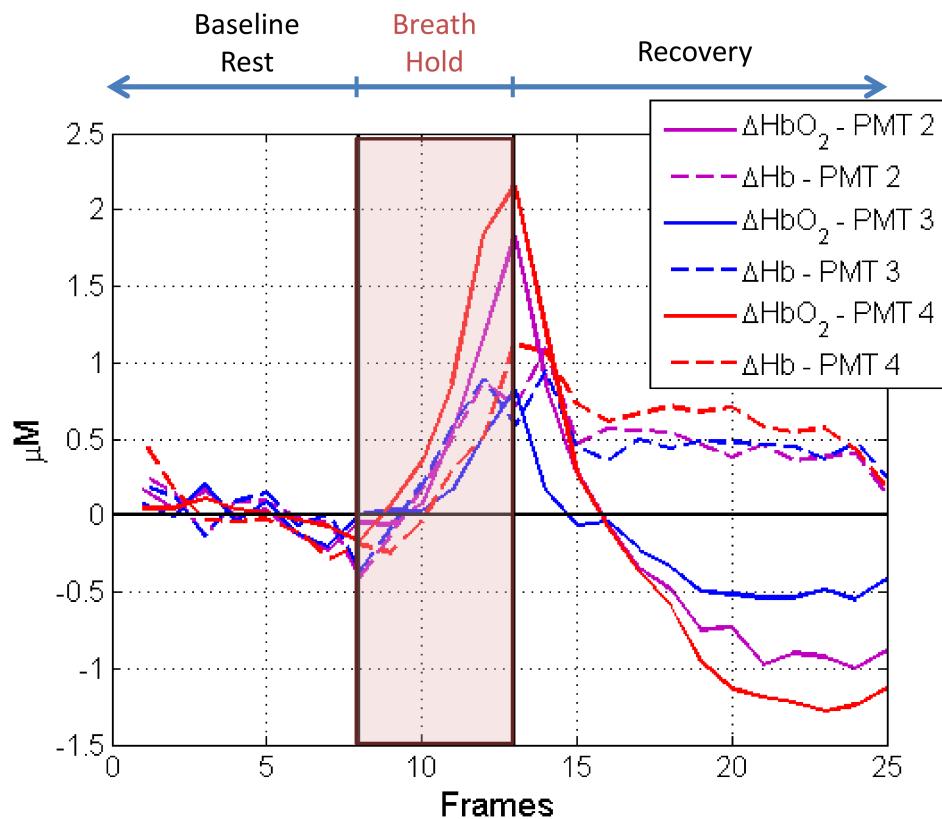


Figure 3.9: Example results of a breath hold test using the SOJI DOS module. The timeline above shows the breath hold protocol used – a baseline rest period of several minutes, then the subject held his breath until the last possible moment, then started breathing again during the recovery period. The maroon shaded area shows when the actual breath hold period took place. Three PMTs were used at the same source-detector separation of 2.5 cm.

ules (see Section 3.2.6). Usually once the instrument has both DOS and DCS modules completed and individually tested, they will be placed on a cart together with a computer and human experiments will be performed before taking the hybrid device to the clinic.

3.2 The DCS Module

This section focuses on the basic DCS module that can be found on many of our lab's hybrid DOS/DCS devices. This basic module was used to take the majority of the DCS data in this dissertation. I will describe each of its components, including how to properly wire them together, and I will describe the tests we employ to be done to characterize the device once it is built.

3.2.1 Lasers

The requirements for a DCS laser include: a long coherence length to preserve the coherence between fields from both the shortest and longest pathlengths through the tissue; sufficient power for a fairly clean correlation curve; a near-infrared wavelength to probe through deep tissue; and compactness so it can be inserted easily into a portable device. Our current best model is a CW, single longitudinal mode (SLM), 785 nm laser from CrystaLaser Inc. (DL785-100-SO, CrystaLaser Inc., NV). This laser has a coherence length of > 50 m (and a corresponding very narrow linewidth, < 0.00001 nm). The laser is available in different power outputs (maximum available in SLM: 120 mW), and we have found that the 100 mW output works well for most of our experiments. The downside of having too

much power is the danger of burning the skin of a patient. Of course, it is easy to attenuate power, and thus far 100 mW has not posed an issue for any of the adult brain studies featured in this thesis. Also, the 785 nm wavelength has traditionally been used in our lab out of convenience and availability, but other wavelengths can be used as well (see Section 3.3).

Application of this laser to DCS requires three custom options that the company provides on request. The first is the placement of an optical isolator in front of the beam. This is a device that transmits light traveling in one direction while blocking light traveling in the opposite direction. An optical isolator is necessary for DCS because any light that reflects backwards from, say, an optical fiber tip will disrupt the laser and can degrade its coherence. Unfortunately, an optical isolator effectively takes output power away from the laser. Just to give you an idea, for a 100 mW laser, after the optical isolator, the power will have dropped to ~ 85 mW. The second option is fiber coupling out of the laser with a 65 μm multi-mode fiber terminated with an Fiber Connector [ferrule] (FC) end. This option also reduces transmission, for example, the 100 mW laser after the optical isolator and fiber coupling will have a power of ~ 72 mW. Lastly, the third option enables TTL modulation to turn the laser on and off. This is useful for the hybrid instrumentation, so that during DOS acquisition you can turn the DCS laser off directly rather than having it go through another optical switch and lose more light.

One bit of soldering required early on is to make a TTL output cable for each laser in your module. There is a plug that looks like a phone jack plug on the back of the laser

power supply with two pieces of exposed wire, one black and one red, and then a looped wire. Solder the black wire to another long piece of black wire (about a foot and a half long), and same with the red wire to a long red wire. Then solder those pieces to a female BNC end, with the black wire going to ground and the red wire going to signal.

These lasers have good output stability, listed by the manufacturer as $< 1\%$ over 24 hours. However, one should always test laser stability with a power meter before starting to wire up the DCS components. It is best to do so when you first receive the lasers because if there is a stability issue, it can often take months for the company to make repairs.

Use the following quick checklist for testing the DCS laser upon arrival from the company:

- Test power straight out of the laser output, and make sure it is close to specifications. If the power is much lower, then send back to CrystaLaser.
- Test power through the company-provided $65\ \mu\text{m}$ FC-FC fiber; make sure power is close to specifications.
- Connect laser to DAQ digital output and make sure a TTL pulse can turn the laser on and off (HIGH turns laser on, LOW turns laser off).
- Test power straight out of the laser output when TTL is low, to ensure that the power is only few μW or less. This leakage has been an issue, and if the power is not low enough, then send back to CrystaLaser for adjustment.
- Configure to record analog output from power meter and leave on at least overnight

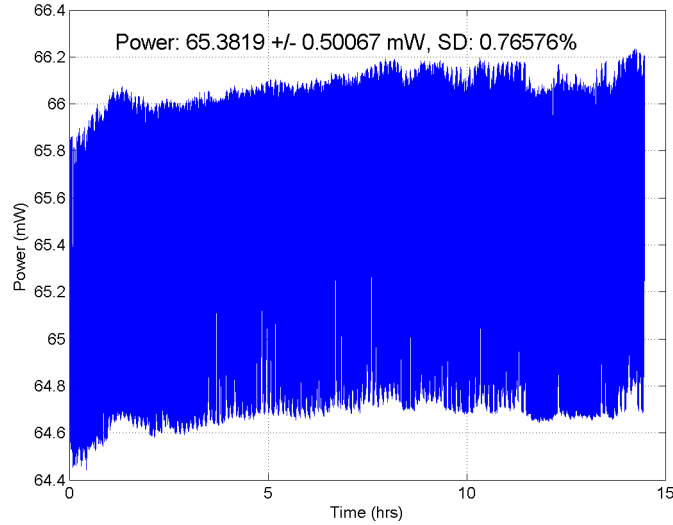


Figure 3.10: An example of a DCS laser with good output power stability.

(~ 15 hours). Stability over this period should be <1%.

Figure 3.10 shows an example of a good result from an overnight stability test. The output power is roughly what it should be, the percent standard deviation is <1%, and there are no large jumps in power.

3.2.2 Detectors

For detection, the DCS module uses arrays of single-photon counting avalanche photodiodes (APD). DCS requirements on the detection side include: good photon detection efficiency in the near-infrared range; single-photon detection capability; and compactness. We have found that PerkinElmer meets these requirements with their 4-channel APD arrays (SPCM-AQ4C, PerkinElmer Inc., Quebec, CA) and interface boards (SPCM-AQ4C-IO, PerkinElmer Inc., Quebec, CA). One interface board goes with every single APD array, and it is used to facilitate power and signal connections to the APD array. The photon

Table 3.5: SPCM-AQ4C Power Supply Requirements.

Voltage	Min. Voltage	Max. Voltage	Typical Current	Max. Current	Power (for 2 Arrays)
+2 V	1.95 V	2.05 V	1.0 A	4.0 A	$2 \times 6 \text{ W} = 12 \text{ W}$
+5 V	4.75 V	5.25 V	0.20 A	1.0 A	$2 \times 5 \text{ W} = 10 \text{ W}$
+30 V	29 V	31 V	0.01 A	0.04 A	$2 \times 1.2 \text{ W} = 2.4 \text{ W}$

Table 3.6: SPCM-AQ4C Power Supplies Used.

Model	Voltage	Max. Current	Ripple Noise	Voltage Range
Astec LPT81	+3.3 V	8 A	50 mV p-p	1.8 - 3.5 V
Murata DMS-PS1-CM	+5 V	1 A	40 mV p-p	5 V
Lambda HSB-28-1.0	+28 V	1 A	< 3 mV p-p	26.6 - 29.4 V

detection efficiency at 785 nm is $\sim 50\%$.

The array requires three different voltages to run: +2 V, +5 V, and +30 V. Table 3.5 summarizes the SPCM-AQ4C power requirements. PerkinElmer recommends that the power supplies be well-regulated and low ripple noise (< 50 mV p-p).

The +2 V power supply is for cooling the APDs. As count rates increase, the card will heat up, which will cause the cooler circuit to compensate by transferring heat from the detector to a heatsink. The number of counts we typically see (< 500 kHz) will not be high enough to disturb operation significantly (occurs at counts > 2 MHz). However, because these are the most expensive components of the DCS module, precautions should be taken regardless. For instance, PerkinElmer suggests usage of 18 wire gauge size or larger for the +2 V connections, because when the coolers can draw over 4 A.

The +5 V power supply is for the TTL pulses. PerkinElmer recommends that the +5 V and +30 V grounds should be connected all at a single point, while the +2 V grounds should be connected to each other, but not to the +5 V and +30 V grounds. Details of the power supplies we found to suit our eight-channel DCS module are listed in Table 3.6.

The interface card has two rows of 4 BNC connectors each. The top row (further from the board) is a gate input, for controlling APD function via digital input. With no gate signal or floating gate inputs, the APDs will be ready to count photons. An applied TTL HIGH signal will gate the channels off. Jumpers on the board can be configured to either control each detector individually, or one digital signal to turn them all on or off simultaneously. We have not applied this gate input feature of the SPCM-AQ4C yet, and we only control the APD power by toggle switch within the circuit. However, using software controls instead would be useful for future work.

The bottom row (closer to the board) of BNC connectors are TTL signal output of photon counts from the APDs. These outputs get directly connected to the hardware correlator.

3.2.3 Correlator

We use a hardware multi-tau correlator (Correlator.com, Bridgewater, NJ) that takes TTL signal output for each photon from the APDs and then calculates various parameters that it then outputs via USB connection to a computer. The hardware approaches were developed more than 40 years ago and are still the method of choice. The schemes are ingenious.

To experimentally perform the photon correlation measurement, the correlator hardware must perform four basic tasks:

1. Count the arrival of input pulses over sampling intervals spaced on a grid defined by the sampling time Δt_o .
2. Delay the count sequence for some lag time τ , say $k\Delta t_o$ (k being number of chan-

nels), and store this sequence.

3. Multiply the two count sequences.
4. Accumulate the products, or calculate their sum.

Efficiency is important – steps 2-4 is done in parallel for k channels that correspond to different lag times. In our case, we use what is called a "multiple-tau" scheme, in which data is processed at many different sample times simultaneously. Experimentally we aim to carry all of these steps out in real time.

"Multiple-tau" or "multi-tau" correlation refers to the multiple samples times (taus) that are processed simultaneously by the correlator. This approach greatly reduces the computation load, and permits experimenters to access both small τ and large τ . For example, a 8-channel correlator with multi-tau capability would have the layout shown in Figure 3.11:

- First tier: Registers 1-16 have bin width $t_o = 200$ ns
- Second tier: Next 8 registers have $t_o = 400$ ns (bin width doubles every 16 registers)
- Third tier: Next 8 registers have $t_o = 800$ ns
- ... and so on.

At the start of a measurement, the digital counter reports photon counts within each bin time of the first register. Those values in the first register shift to the next register as a new value comes in from left. This goes on until all registers are filled. Before each shift, temporal autocorrelation functions (G_2) are calculated, e.g., $G_2(\tau_i) = \langle n_i \cdot n_o \rangle$, where n_i

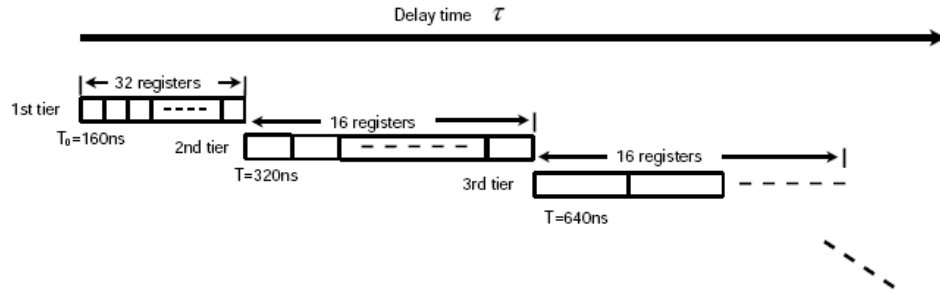


Figure 3.11: Diagram of multi-tau correlation scheme from [263].

is the photon count in i^{th} register, n_o is the photon count in the register for zero delay time ($\tau = 0$), and τ_i is the delay time between n_i and n_o . The autocorrelation functions are then normalized in a separate register to create the normalized temporal autocorrelation function g_2 . An average of these g_2 traces are calculated over the entire duration t (which is preset by the user, usually about 2.5 s) to produce a final, averaged g_2 curve. This then is a single data point in time, of which we use a continuous stream of, to then calculate relative flow.

3.2.4 Visual Basic Code

We use a Visual Basic code to manipulate the correlator (start, stop, update), to change duration time, to plot the normalized autocorrelation functions, and to log the data into files for analysis. What follows is a detailed interpretation of the code.

Initializing: The first part of the code is for defining the variables that will be used throughout the code, for loading the graphical user interface (GUI) form and its components, and for initializing the correlator. First we define the data type, and in some cases the dimension or value of the global variables. Because the 4 vs. 8 channel modes dif-

Table 3.7: VB Code Global Variables.

Variable Name	Data Type	4CH Value	8CH Value
TIMEFLEX	Double	47.18592 ms	104.8576 ms
FIRSTDELAY	Double	40 ns	200 ns
CHANTOT	Double	512	256
NumFirstRegister	Integer	32	16
NumNextRegister	Integer	16	8
NumRegisterGroups	Integer	30	30
Variable Name	Data Type	4CH Size	8CH Size
CORRELATORcorr	Single	0 to 2048	0 to 2048
CORRELATORtraceA	Single	0 to 2048	0 to 2048
CORRELATORDelayTime	Single	0 to 512	0 to 256
CORRELATORCounts	Single	0 to 3	0 to 7

fer in correlator bin size and other factors, some of these global variables have different values depending on the mode in which we choose to run the flow box. For instance, the smallest bin size (called FIRSTDELAY in the code) is 40 ns for 4 channel mode, but 200 ns in 8 channel mode. Table 3.7 shows the variable name, data type, and 4 vs. 8 channel values/dimensions. Following the table are definitions of the variables.

- TIMEFLEX: Time interval in which correlator returns data, in seconds.
- FIRSTDELAY: Bin width of first register, in seconds.
- CHANTOT: Total number of bins across all registers in a single channel.
- NumFirstRegister: Number of bins in first register, with lag time FIRSTDELAY.
- NumNextRegister: Lag time keeps doubling after this register interval.
- NumRegisterGroups: Total number of registers (not including the first).
- CORRELATORcorr: Contains normalized, averaged g_2 data for all channels.

Table 3.8: More VB Code Global Variables

Variable Name	Data Type
State	Integer
newlabel	Single
Tau	Single
SequenceCounter	Integer
CORRELATOROk	Boolean
CORRELATORElapsedTime	Single
CORRELATORTraceCount	Integer
CORRELATORDuration	Double
CORRELATORTimeleft	Double
CORRELATORDataToPlot	Variant

- `CORRELATORtraceA`: Contains photon counts for all channels. With each `TIMEFLEX`, the counts are accumulated until the end of duration time.
- `CORRELATORDelayTime`: Array of lag times τ , calculated in the code.
- `CORRELATORCounts`: Intensity values (in photon counts per second) for all channels.

Other variables are defined in the global area (Table 3.8), many having to do with the duration time that G_2 is averaged over or the correlation initialization. One important variable is `State`, which plays a large part in the `Timer` function in Visual Basic; `Timer` will check the value of `State` at a pre-defined time interval and cause actions to be performed according to its value.

- `State`: For the sub `Timer`. Value of `State` is checked in every pre-defined time interval, and actions are performed (defined in sub `Timer`) according to its value.
- `newlabel`: Only used in 8CH mode. Needed because correlator in 4CH mode takes first four outputs as 1-4, but in 8CH mode alternates as 1-3-5-7 as first four outputs.

`newlabel` used to detangle them to right order.

- `Tau`: A shorthand way to calculate relative changes of flow, calculated by taking the time for g_2 to decay $1/e$. When baseline button is clicked, use that particular frame's `Tau` as baseline and values thereafter as relative changes.
- `SequenceCounter`: Number keeps track of each completed logged file/frame, as in g_2 logged of full duration time.
- `CORRELATOROk`: Will be "True" if correlator initializes correctly, otherwise will be "False".
- `CORRELATORElapsedTime`: Returned by correlator, how much time correlator has been averaging for between when USB told to start and stop.
- `CORRELATORTraceCount`: How many G_2 traces have been generated so far.
- `CORRELATORDuration`: Duration time, G_2 traces accumulated during this time will be averaged for final G_2 .
- `CORRELORTimeleft`: Difference in time of `CORRELATORDuration` and `CORRELATORElapsedTime`. How much time left to average over.
- `CORRELATORDataToPlot`: `CORRELATORcorr` reshaped into g_2 for each channel; gets plotted against `DelaysToPlot`.

Also in the global section of the code is the definition of two subs (subroutines) and two functions that involve communication with the correlator via USB 2.0 port. These four

Table 3.9: USB Controls.

Sub Name	Type	Argument Variables	Return Variables
USBInitialize	Function	none	USBInitialize as Byte
USBStart	Sub	none	none
USBStop	Sub	none	none
USBUpdate	Function	ElapsedTime as Single TraceCount as Any corr1 as Single TraceA as Single	USBUpdate as Byte

controls access the appropriate .dll file². Details about each control are seen in Table 3.9.

There is an additional sub `USBFree` that is defined, but never used in the code.

- `USBInitialize`: Will return a value of zero if correlator not initializing correctly; otherwise will be non-zero. Often non-zero if correlator not connected, or driver not installed properly.
- `USBStart`: Begin acquiring data from correlator, start `CORRELATORElapsedTime` at zero.
- `USBStop`: Stop acquiring data from correlator, stop updating `CORRELATORElapsedTime`.
- `USBUpdate`: Returns new data values. `ElapsedTime` is amount of time passed while averaging the correlation curve, total time being the duration t . `TraceCount` is the number of correlation curve traces averaged for the final curve. `corr1` is the normalized and averaged correlation curve data. `TraceA` is the current individual trace.

Here ends the global heading of the code. The bulk of the code is made up of many

²There are .dll files specific to 4 (`flex05-4chPascal.dll`) or 8 channel (`flex05oem8chautoPASCAL.dll`) mode.

public subs. A flow chart (Figure 3.12) shows the preliminary section of the code, beginning from defining the variables that we have just discussed to various initial procedures done before taking a measurement.

During the `FormLoad` sub, the number of sources and detectors being used are defined (`NUMSOURCES`, `NUMDETS`) and the dimensions of `CORRELATORCounts` and `Tau` are altered accordingly. The number of channels (detectors) is fixed at 8 by default, but it can be changed to 4 with a click of a button once the form fully loads.

Next is the initialization process, which involves filling `CORRELATORDelayTime` with the lag times (τ) corresponding to 8 channel mode. It is important to know that in the code we must calculate the values of τ based on the configuration of the correlator, and the numbers are not automatically fed into the computer by the correlator:

```
For i = 0 To NumFirstRegister
    CORRELATOR_DelayTime(i) = i * FIRSTDELAY
Next i

For j = 1 To NumRegisterGroups
    For i = 0 To NumNextRegister
        CORRELATOR_DelayTime(i + (j - 1) * NumNextRegister
            + NumFirstRegister) = CORRELATOR_DelayTime((j - 1)
            * NumNextRegister + NumFirstRegister + i - 1)
            + FIRSTDELAY * 2 ^ j
    Next i
Next j
```

After creating the lag times, the correlator is checked by checking the value returned by `USBInitialize`. Remember that if the correlator is not initializing properly because it

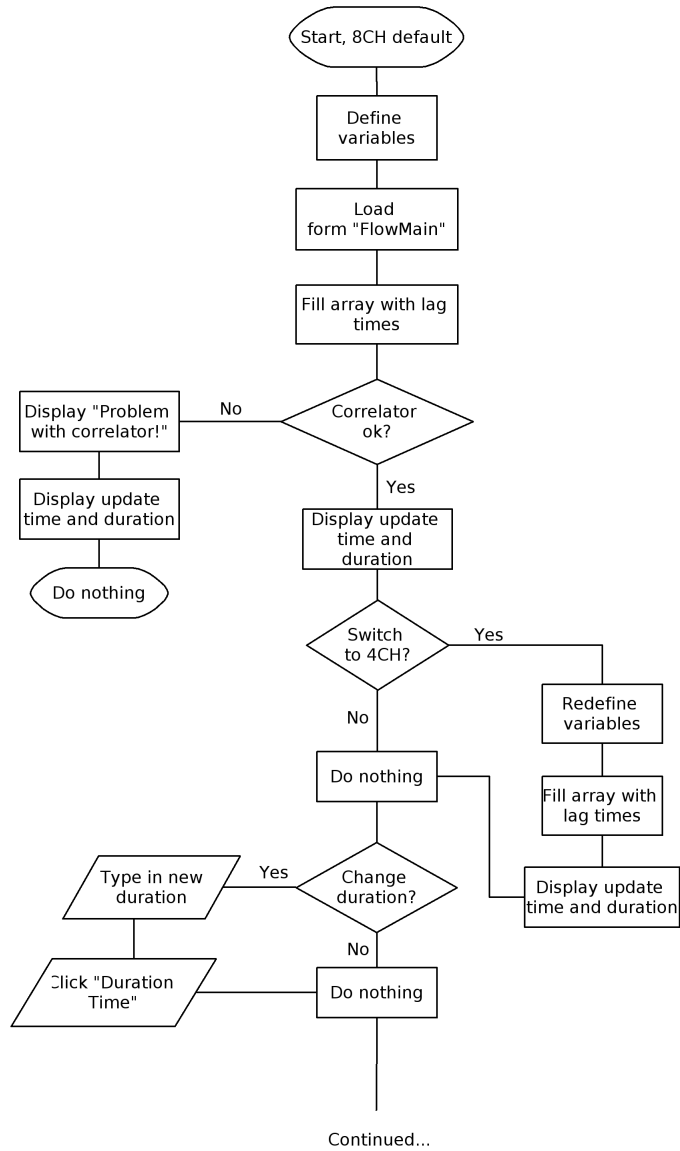


Figure 3.12: Part 1 of the VB code: Preliminary actions such as defining variables, checking on correlator, creating lag times.

is not plugged in or there is a driver issue, then it will return as zero. If there is a problem, as seen in Figure 3.12, it will display an error message but still show the default update time (TIMEFLEX) and duration (CORRELATORDuration) before it rests. If there is no problem, it will show the times without an error message. Next the code defines the timer interval as the default update time. At this point, if we want to switch to 4 channel mode, we can click the "4CH" button where it will redefine certain 4 channel specific variables, refill the lag time array, and display the new update time and duration. Changing update time or duration requires only typing the time in and clicking the appropriate button.

Taking Data: Now the program is ready for its job—reading g_2 data from the correlator and logging it into files for further analysis. There are two options for scan type:

- Single scan: Take a single frame of data, or a single g_2 curve for each channel at one time point.
- Sequence scan: Keep taking continuous frames of data every duration time interval for each channel until the "Stop" button is clicked.

We can choose which scan type we want by clicking the corresponding button. Essentially the same chain of events occurs, except for single scan it only loops one time, and for sequence scan it continues looping until the user presses "Stop" (Figure 3.13).

The use of buttons gets turned off, and the time left on the correlator (CORRELATORTimeleft) is reset to the duration time. Then the state of the timer is specified, and this is where single scan and sequence scan differ. Then the USB function is started, the elapsed time on the correlator starts counting, and the events governed by the

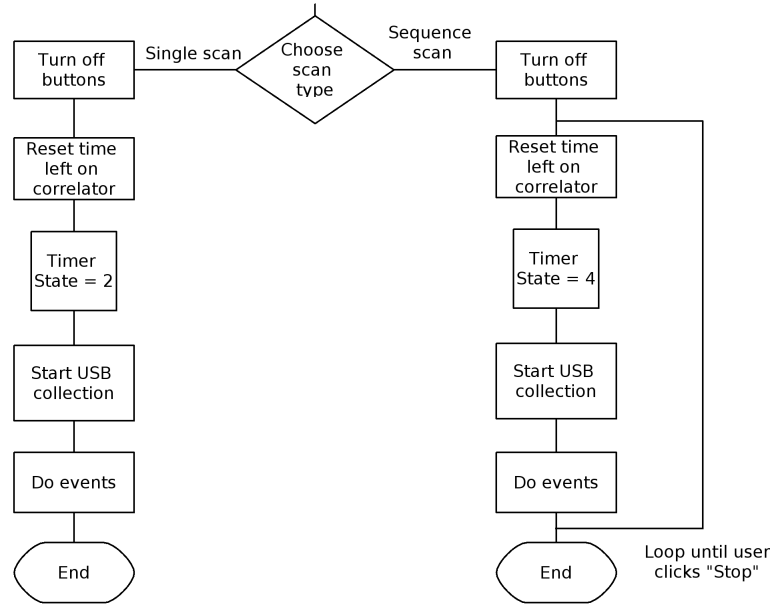


Figure 3.13: Part 2 of the VB code: Taking data, choose either single scan or sequence scan.

timer begin to take place. The timer is not always exact, and so sometimes the duration countdown will go negative. When it stops, the use of buttons returns.

The details of each state of the timer is given in Figure 3.14. There are four timer states that are used throughout the program (States 0, 2, 4 and 100), and two that are defined but never used (States 1 and 3). Essentially the timer works as follows: at every pre-defined interval time, the timer will check the state (i.e., value of `State` variable) and according to the value, perform the appropriate actions under the specific state that are dictated in the timer sub.

During the initialization process that occurs when the form is loading, the timer interval is set as the correlator update time (`TIMEFLEX`):

```
Timer1.Interval = TIME_FLEX * 1000.
```

This is because we assume that there is no need to check the state any faster than the

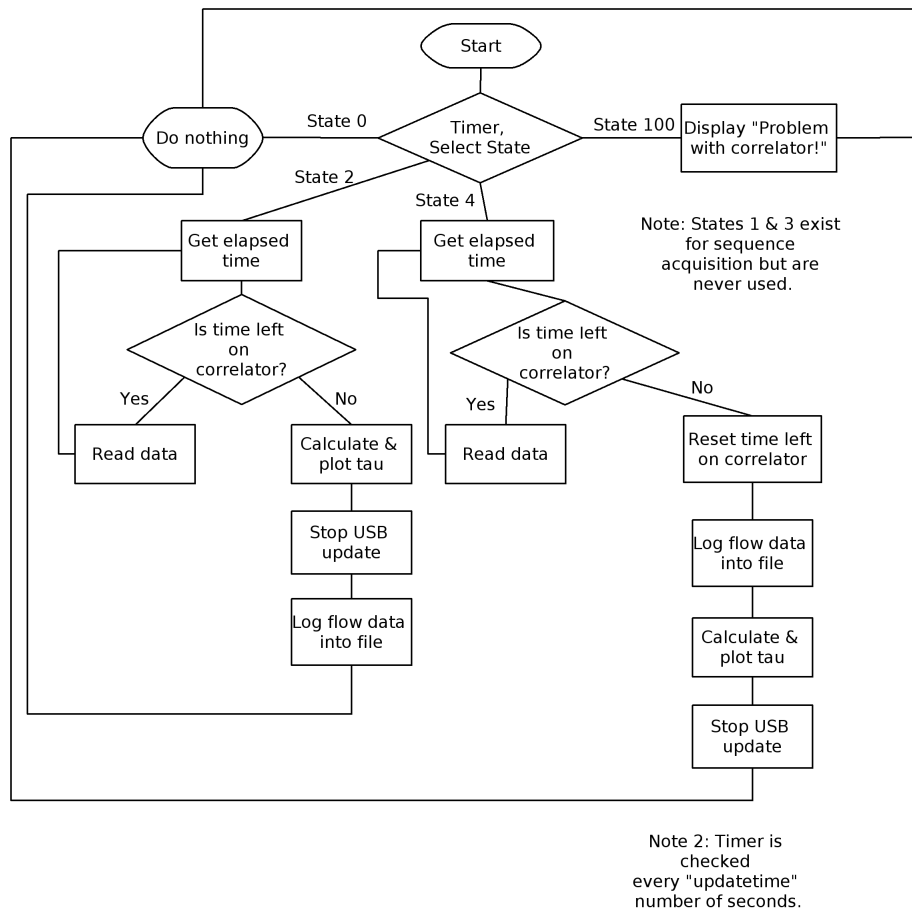


Figure 3.14: Timer: In VB, this will check the state value at a pre-defined interval and do the following actions accordingly.

correlator itself can update and produce a new trace. The four cases perform actions as follows:

- `Case 0`: Do nothing.
- `Case 2`: For single acquisition. First checks if the elapsed time on the correlation matches the duration, as in if it is done averaging g_2 . If not, then it keeps reading the data (in sub `ReadData`); if so, then it plots a rough estimate of rCBF, stops the USB data acquisition, and logs the data into a file.
- `Case 4`: For sequence acquisition. The only difference here is that this case will reset the time left on the correlator before plotting and logging the data. This causes the scan to keep looping.
- `Case 100`: If there is a problem with the correlator, it displays a message ("Problem with correlator!") and then does nothing (`Case 0`).

The last part of the code needed is the essential sub `ReadData`, which actually gets the data from the correlator, plots the normalized data, and puts it into variables that will later be logged into files. The flow chart is documented in Figure 3.15. First it checks if data is already being read, if not it then checks if the correlator is returning nonzero values through `USBUpdate`. If they are nonzero, the time is updated on the correlator and an array of total counts is created. The total counts is converted into average counts per second and the correlation curve plot is updated with a new g_2 . This is looped until the elapsed time is equal to the preset duration time.

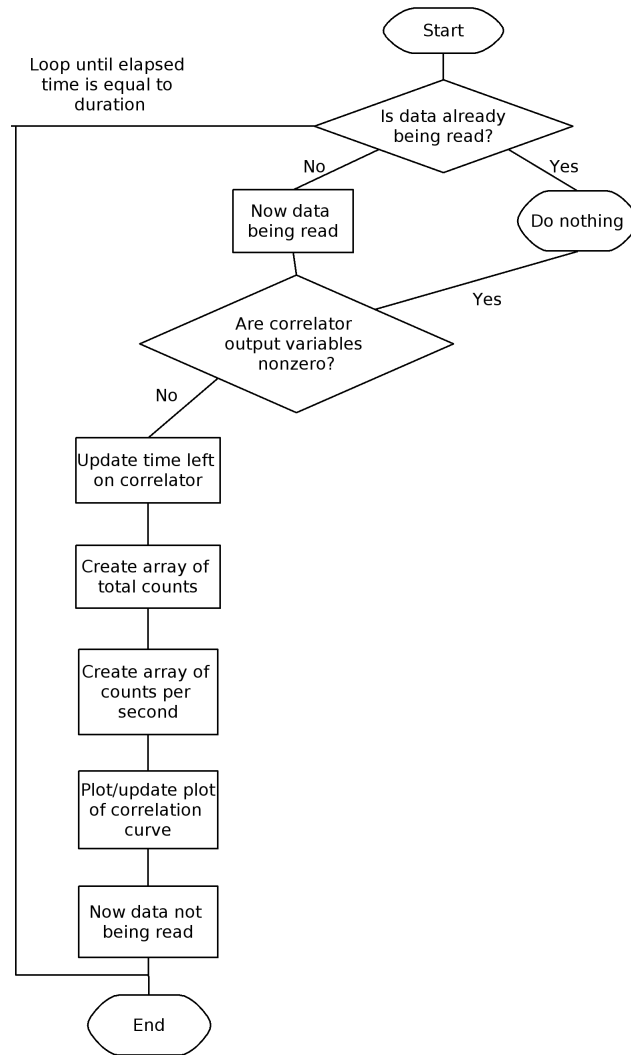


Figure 3.15: ReadData: This sub takes the data from the correlator, updates/averages G_2 , and calculates average count rate for each detector.

Logging the Data: The last part of the code deals with logging data such as our final averaged, normalized g_2 and counts per second into files to be analyzed by MATLAB. The code does this by first printing a header containing the duration time used for taking the data and counts per second for each channel used. Then another sub is used to print columns of data that include the delay times and the corresponding g_2 value for each time for all channels. Lastly, the final row of the file is designated for marks—whether the user pressed the "Mark" button to indicate an event occurring. It logs "1" for a particular file with mark pressed, or "0" for no mark.

3.2.5 DCS Module Assembly

A basic 2-laser, 8-channel DCS module contains:

- Two 100mW, CW, long coherence length (> 50 m), 785 nm lasers (CrystaLaser Inc.), \$7000.00 each
- Two APD 4-channel SPCM arrays + Two SPCM AQ4C cards (PerkinElmer Inc.), \$9000.00 each array + \$265.00 each card
- One 8-channel multi-tau digital correlator (Correlator.com), \$7000.00 each
- One Murata +5 V power supply, \$54.00 each
- One Lambda +28 V power supply, \$41.16 each
- One ASTEC +2 V power supply, \$194.00 each



Figure 3.16: Front and back panels of a standard 8-channel DCS module.

- One box enclosure, \$330.54 each (Bud Industries)
- One power module with switch/fuse, \$15.95 each (Tyco)
- One square AC fan, \$22.00 each
- One square nickel-plated fan guard, \$1.00 each
- Two red LED indicator lights, \$2.249 each (Lumex)
- Two 4PDT ON-NONE-ON toggle switches, \$22.90 each (Electroswitch)
- Two BNC female-to-female adapters, \$7.56 each (Pomona Electronics)
- Two 309 Ohm .125W resistors, \$0.137 each
- Five 50 Ohm 3W resistors, \$1.218 each

It is, of course, possible to vary certain components. For instance, one could reduce the number of channels to four or choose to use low power lasers instead, but the basics remain the same. The basic 8-channel DCS module is shown in Figures 3.16 and 3.17. The



Figure 3.17: Inside views of a standard 8-channel DCS module.

front panel (Figure 3.16, left) shows the inputs for the lasers in the upper left, their power supplies in the bottom left, and the two 4-channel APD arrays on the right. In between them are toggle switches for channels 1-4, and 5-8 with their respective indicator lights. Notice that with this arrangement, one must turn on channels 1-4 and 5-8 together – each channel cannot be turned on individually.

The back panel (Figure 3.16, right) has BNC inputs used for turning the lasers on and off with a TTL pulse, a USB cable that powers and allows communication with the correlator (silver cord), and the power switch. Not shown is the fan attached to the top of the box.

Figure 3.18 shows the electrical connections one must make from the APD cables to the power supplies. The grounds of the power supplies connect directly to the APDs, but the voltages must go through the toggle switch. The toggle switch also controls the indicator light (powered by 5 V power supply).

In addition to the wiring of the APDs, you also must connect the fan directly to the N and L pins of the power entry module so that it powers up as the switch is turned on.

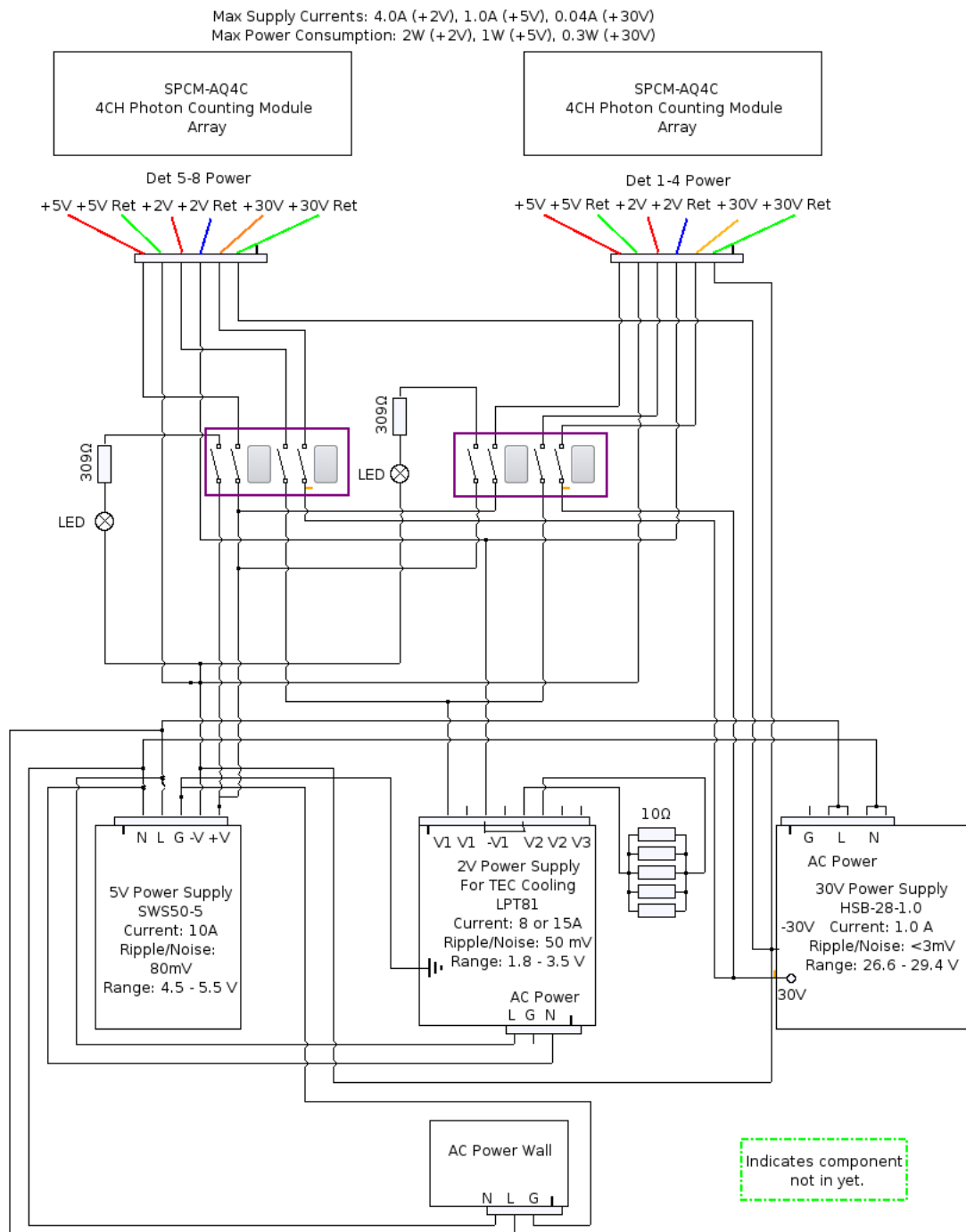


Figure 3.18: Circuitry of power supplies to APDs.

BNC cables connect the correlator to the APDs, and then a USB cable (male B to male A) connects the correlator to the computer.

3.2.6 DCS Module Quality Testing

Before going into the clinic, the DCS module must be tested thoroughly for quality, in a fashion similar to the DOS module (see Section 3.1.3). After assembly and soldering, the wired connections must be checked. Then the device has to be tested for stability and accuracy.

Before turning the device on, it must be verified that the parts and power supplies are correctly connected. Then, each component must be powered up, i.e., after confirming that they are receiving the right voltages. The following list details this procedure step-by-step:

1. Make sure AC power is unplugged, and the power switch is OFF. Unplug the power to both sets of APDs. Also unplug power to both lasers, making sure that the lasers are switched OFF.
2. Get a multimeter and turn dial to the beeping thing. (Have circuit diagram alongside you as you check that all appropriate connections are made.)
3. Make sure no connections exist where there shouldn't be any by using the voltmeter.
4. Now plug in AC power. Remember that power to APDs should still be disconnected.
Turn power switch ON.

5. First thing you should notice: fan starts spinning. If it is spinning, then you have wired the fan correctly.
6. Pick up your multimeter again, but this time turn the dial to measure AC voltage. Use this setting to test the voltage going to the lasers, as well as the fan (if it is not spinning). BE CAREFUL! You could easily shock yourself, or cause a short circuit. Watch where you put those test pins.
7. Check that the AC voltages coming into the power supplies is correct (check N, G and L pins).
8. Test that the AC voltages coming into both lasers is correct. If they are, turn off the power switch and plug the laser power cords in.
9. Turn ON the power switches of both lasers. Turn the key of Laser 1 and place a piece of white paper in front of the output. You should see a red spot. Repeat for Laser 2.
10. Switch your multimeter to measure DC voltage. Start with the power supplies, putting one test pin on +V and the other on -V. You should get a value very close to 2 V, 5 V and 30 V for the respective power supplies.
11. Now turn your attention to the wires you disconnected from the APDs. Use jumper wires to test that the +V and +V return pins are receiving the appropriate voltages (2 V, 5 V or 30 V). Repeat for both sets of wires.
12. Congratulations! Now you can turn on the device with everything connected. Even close the lid if you want.

As with the DOS module, the laser stability of the DCS module must be confirmed. As stated in Section 3.2.1, stability for all lasers should be checked with a power meter overnight as soon as they arrive from the company. Then, once the DCS module is completely wired up, and the connections are tested, then the stability of the device as a whole must be verified. Typically a probe is made to hold optical fibers at multiple source-detector separations. Then the probe is held so it is just touching the surface of a liquid Intralipid phantom, so as to mimic a semi-infinite medium geometry. Data is recorded overnight.

First we must check intensity (i.e. photon counts per second) over time, which is outputted in kHz by the correlator. Figure 3.19, top, shows an example intensity plot from a successful stability test. Notice that percent standard deviation is small ($<2\%$), and there are no large jumps in the data. Even though intensity values are not used explicitly in calculating BFI , they can be an indication of good laser performance. A laser that has large jumps in intensity could be unstable in coherence as well, which would affect the stability of BFI .

Next we observe the stability of β over time. Again, this is a feature of the correlation curve that may not affect values of BFI directly, but can give insight into whether there are issues with laser coherence or other mishaps with experimental setup. Figure 3.19, bottom, shows an example plot of β from an overnight stability test. The values should be close to 0.5 with no abrupt changes in value.

Figure 3.20 shows a plot of relative BFI versus time for a DCS module during an overnight stability test. For analysis, we used the first 50 or so frames as baseline BFI ,

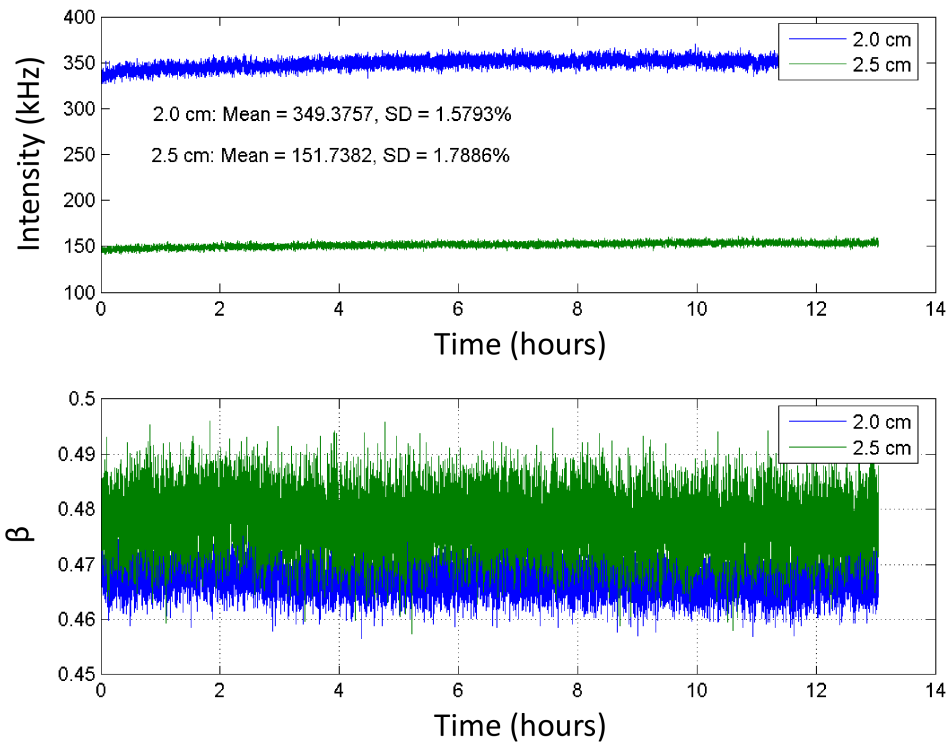


Figure 3.19: Example result of intensity and β from an overnight stability test on a basic DCS module. Intensity values are returned by the correlator in photon counts per second, or kHz. Note that percent standard deviation over ~ 13 hours is $< 2\%$. β should be close to 0.5 and with no large jumps, as seen in the second plot.

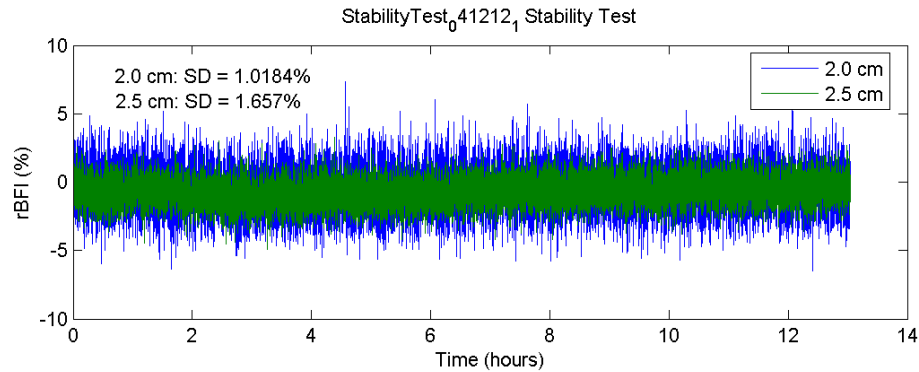


Figure 3.20: Example result of relative BFI from an overnight stability test. BFI was derived from fitting a correlation diffusion model to g_2 curves obtained from a liquid phantoms. The first 50 frames (integration time 3 s) were used as baseline.

then the remainder of the timeseries is normalized to this baseline to find relative BFI in terms of percent change. This is to see how large the variations of relative BFI are (acceptable would be $<2\%$), and to ensure that there are no abrupt jumps. Also, individual frames of g_2 data and their fitted curves should be plotted. In some cases, such as when the source-detector separation is small and we are on the edge of the diffusion approximation, or when a brain-injured patient has an injury that affects blood flow strangely, the model will produce badly fit curves. In these instances, corresponding data should most likely be left out of analysis.

A method to test whether the DCS module is able to distinguish changes in flow is to use a liquid phantom with a magnetic stirrer (see Figure 3.21). The speeds depend on what is available on the stirrer, but we went from having the stirrer completely off to the stirrer on at low speed. This scheme was used to make sure the same correlation curves were being produced for both 8-channel and 4-channel modes (see Figure 3.22). This test is carried out to confirm that the two modes are working correctly, retrieving the same BFI values,

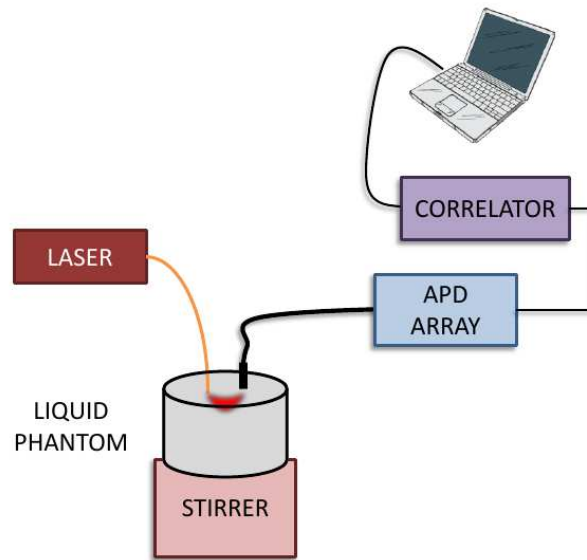


Figure 3.21: Diagram of stirring test. A liquid phantom is placed on top of a magnetic stirrer that is capable of different stirring speeds. Optical fibers go to the laser source and detectors (an array of APDs), which take data to the correlator and laptop. This test is to enable that the DCS box is capable of distinguishing changes in flow.

and that 4-channel mode has increased sensitivity and higher resolution.

As with the DOS module, we must advance our DCS device from testing on tissue phantoms to real human subjects. The arm cuff experiment described in Section 3.1.3 is typically performed after the DOS/DCS hybrid device has been fully compiled on the cart. Figure 3.23 is an example result from a basic DCS module during an arm cuff occlusion and release. After an initial stable baseline period, blood flow should sharply drop to about 80% of baseline during occlusion (typically at a pressure of 180 mmHg). Then there will be a rapid overshoot as the blood rushes back into the forearm. Lastly, the blood flow should slowly stabilize back to its baseline value.

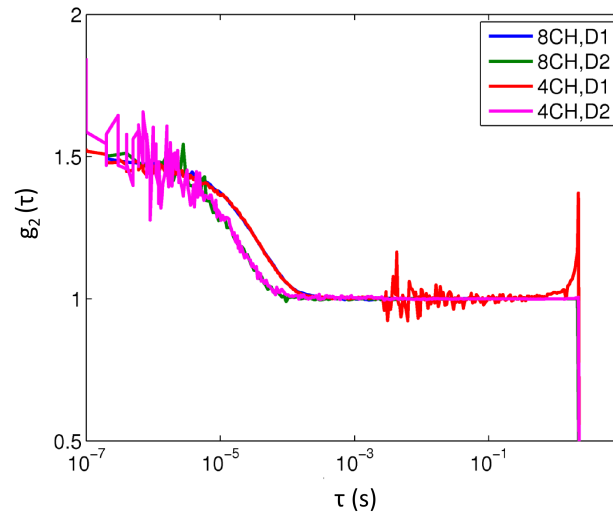


Figure 3.22: Examples of $g_2(\tau)$ during stirring test, directly comparing curves during 8-channel versus 4-channel modes. Notice how $g_2(\tau)$ in 4-channel mode is noisier, because it has a higher resolution and smaller bins to enable less smoothing of the correlation curve. Also the 4-channel $g_2(\tau)$ is able to retrieve more of the initial part of the curve, since the first delay time is smaller.

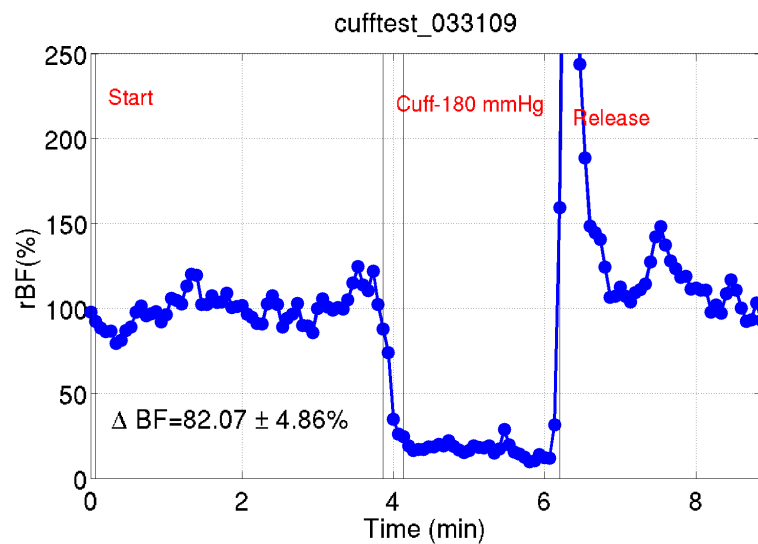


Figure 3.23: Relative blood flow (rBF) from blood pressure arm cuff testing. When arm is cuffed, rBF drops sharply to about 80% of initial baseline value. Then when cuff is released, an overshoot occurs initially, then rBF slowly returns to baseline level.

3.3 Multi-Wavelength DCS

For the DCS module in SOJI, we decided to add multi-wavelength capability. This capability was added so that we might potentially use as a standalone DCS device that will also be able to take oxygenation data using the differential pathlength method described in Section 2.1.4. We wished to explore how easy it might be to extract absorption properties with DCS CW lasers. Some preliminary experiments were performed to ensure that different wavelengths of laser could be employed to take *BFI* data (i.e., in addition to our usual 785 nm laser) with the hope that reasonable *changes* in oxygenation could be measured simultaneously.

We added two additional lasers: a 50 mW, 690 nm laser (DL690-050-SO; CrystaLaser Inc., NV) and a 100 mW, 830 nm laser (DL830-100-SO; CrystaLaser Inc., NV). This adds one more wavelength to a previously published study [208], wherein the authors refer to multi-wavelength DCS as "DCS flow oximetry."

3.3.1 DCS Multi-Wavelength Phantom Results

To investigate whether or not there is any discrepancy in DCS using different wavelengths, we decided on a simple single scattering experiment to start with (see Section 2.2.1). We used a dynamic light scattering setup (see Figure 3.24) to determine the average size of both spherical "particles" Intralipid and in monodisperse polystyrene colloids. All three lasers were fed into a 3×1 optical switch, whose output was then put through a collimator, a lens to focus the beam, and a polarizer. The cuvette containing the sample solution was

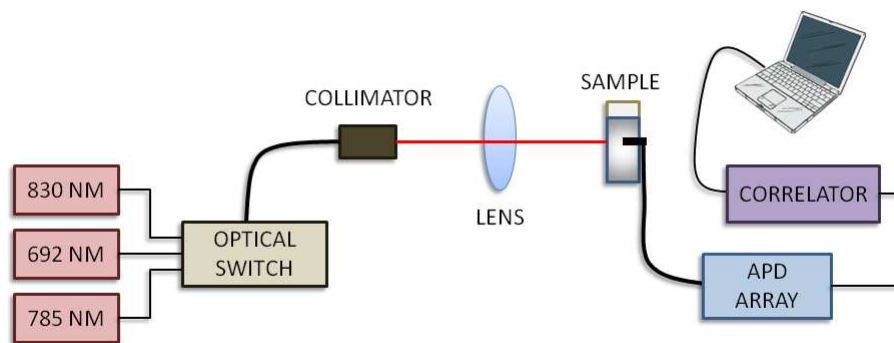


Figure 3.24: Schematic of an initial dynamic light scattering experiment to test the effects of different wavelengths on DCS results. The sample contained a solution of either Intralipid or monodisperse polystyrene spheres.

placed at the focal point of the lens. Then a single-mode detection fiber was placed at 90° from the beam path, split, and sent to the 4 photon-counting APDs.

We can obtain the translational diffusion coefficient, D , for the particles in the samples from the measured correlation curve. Then, using the standard Stokes-Einstein theory, we can calculate the particle radius. The particles were assumed to be spherical. The electric field correlation function will have the form $g_1(\tau) = e^{-\Gamma\tau}$, where $\Gamma = DK^2$. For non-interacting Brownian particles in a homogeneous solvent, $D = k_B T / f$, where k_B is Boltzmann's constant, T is the temperature, and f is the frictional coefficient of the particle. For spherical particles, $f = 6\pi\eta R_H$. η is the solvent viscosity and R_H is the hydrodynamic radius of the particle.

Figure 3.25 shows example data and linear fit of g_1 versus τ from a dynamic light scattering experiment with a solution containing polystyrene spheres. Table 3.10 summarizes results from using Intralipid (0.03 to 0.4 μm) [240] and two different diameters of

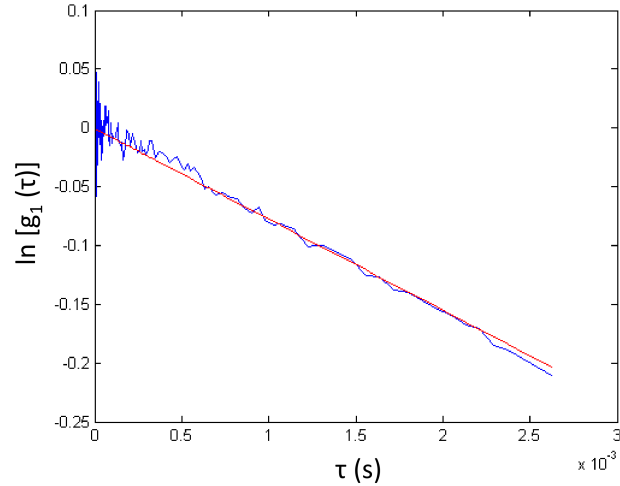


Figure 3.25: Example g_1 data and linear fit from a dynamic light scattering experiment with a solution containing polystyrene spheres.

polystyrene spheres (0.5 and 1.0 μm). Note that while the percentage error in predicting particle size is sometimes larger than desired, the value of diameter given by the three different wavelengths are always within error of one another. We conclude that using different wavelengths for DLS does not have a significant effect on measuring particle size properties.

3.3.2 Initial Human Experiment

Of course, we also want to determine how well multi-wavelength DCS works in practice with a real human subject. To this end, we performed the arm cuff experiment described at the end of Sections 3.1.3 and 3.2.6.

Figure 3.26 shows an example result from an arm cuff occlusion experiment using our multi-wavelength DCS setup. The top figure shows relative blood flow changes for all three wavelengths during the test. All show the correct trends that we look for during arm

Table 3.10: Summary of dynamic light scattering experiments using solutions of Intralipid and two different diameters of polystyrene spheres. No error is listed for Intralipid because there is a wide distribution of particle sizes, but our measurements were well within that range.

Solution	Quantity	830 nm	692 nm	785 nm
Intralipid, 0.03 - 0.4 μm	Diameter, μm	0.33	0.31	0.33
	SD Diameter, μm	0.01	0.01	0.01
	Error, %	N/A	N/A	N/A
Polystyrene, 0.5 μm	Diameter, μm	0.53	0.63	0.57
	SD Diameter, μm	0.04	0.09	0.05
	Error, %	6%	26%	14%
Polystyrene, 1.0 μm	Diameter, μm	0.82	0.90	0.88
	SD Diameter, μm	0.05	0.06	0.04
	Error, %	18%	10%	12%

cuff occlusion and release, and, more importantly, the timeseries from all wavelengths are equivalent to one another. This information tells us that the values of relative blood flow given by DCS does not depend on the wavelength of the source laser, as long as we take the differing optical properties into account during analysis.

Figure 3.26, bottom, compares calculated changes in oxyhemoglobin (ΔHbO_2) and deoxyhemoglobin (ΔHb) from multi-wavelength DCS and SOJI. The resulting timeseries from DCS is noisier and with lower time resolution than SOJI's, but the trends and magnitude of overshoot (in μM) match relatively well.

3.3.3 Ultra-Portable Multi-wavelength DCS Module

For the requirements of a study performed at high-altitude (Chapter 7), we had to modify a 2-channel DCS module [263]. Because the device had to travel across an ocean and up a mountain, we had to make it ultra-portable as well as we had to add multi-wavelength DOS capability to the DCS-only device. To do this, an 830 nm long-coherence

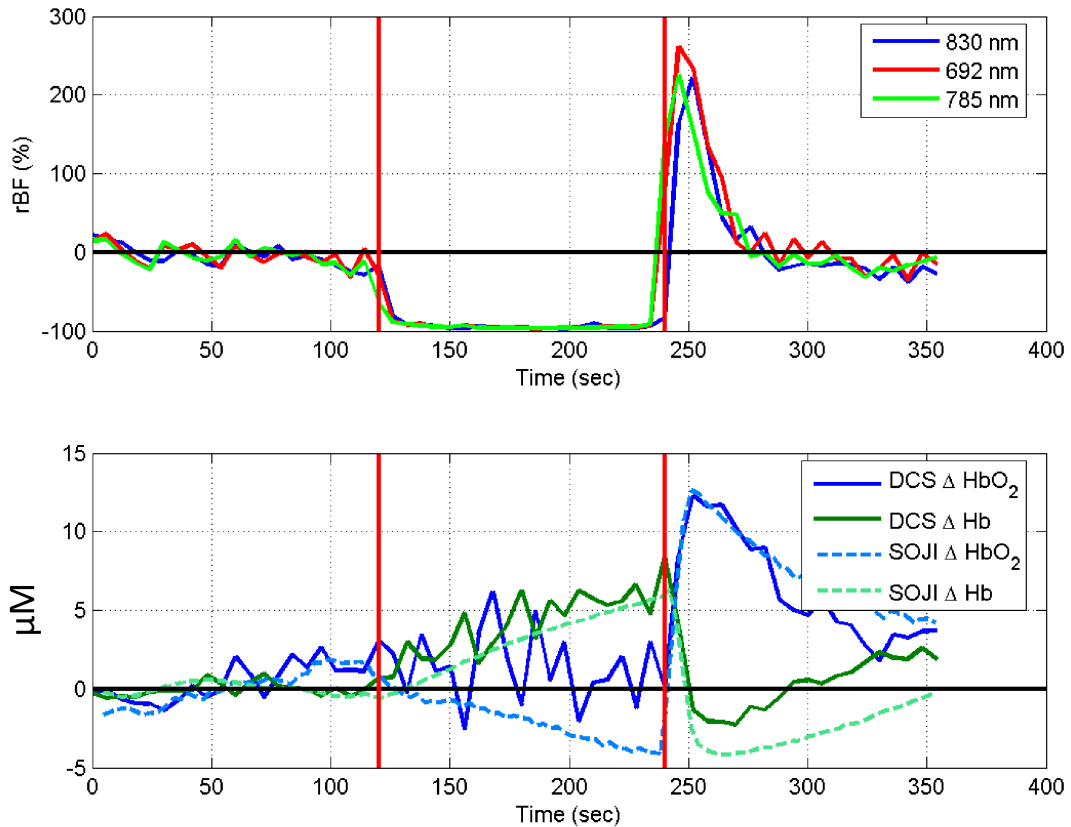


Figure 3.26: Example result from an arm cuff experiment on a human subject using multi-wavelength DCS, with the red lines marking occlusion and release. The top figure shows a relative blood flow (rBF) timeseries from each of the three different wavelengths, giving an equivalent and correct result. The bottom figure shows the calculated changes in oxyhemoglobin (ΔHbO_2) and deoxyhemoglobin (ΔHb) both from the multi-wavelength DCS and SOJI. While the DCS result is noisier with a lower time resolution, it matches the trends seen by SOJI.

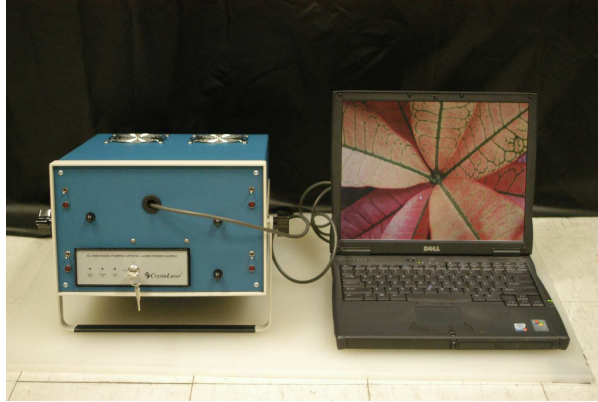


Figure 3.27: Photo of the ultra-portable, 2-channel DCS module that was modified for multi-wavelength operation.

length, continuous-wave laser was added so that we could extract hemoglobin concentration changes with the differential pathlength method (see Section 2.1.4).

The original DCS module, seen in Figure 3.27, contained a 785 nm laser, two individual APDs, and a 2-channel multi-tau correlator. To modify it into an ultra-portable multi-wavelength DCS module, we added an 830 nm laser, a compact DAQ board for switching between lasers using TTL pulses, and a Labview code was created that displayed oxygenation changes along with laser intensities, correlation curves, etc. The graphical interface also was made more user-friendly, since large parts of the study would be operated completely by doctors lacking DCS expertise.

The idea behind the multi-wavelength DCS was that the wavelengths would switch off using the DAQ board, so intensity timeseries would be recorded and used to extract oxygenation information, while each would still be taking g_2 data at every frame. This allows the device to be ultra-portable and still gather both blood flow and oxygenation data. However, the oxygenation data will have distinct disadvantages from even a basic FD-DOS

device as described in Section 3.1.1. For instance, the data may be affected by room light, since the detected light is not filtered for a certain frequency. Also, only changes in Hb and HbO_2 can be observed, not absolute values. In a less extreme situation where such a compact setup is not needed, a traditional hybrid DOS/DCS instrument should be utilized.

Chapter 4

Validation of DCS in Brain-Injured

Adults

This chapter is based on work I have published in clinical journal *Neurocritical Care* [120]. The most important result is that changes in cerebral blood flow (CBF) measured by diffuse correlation spectroscopy (DCS) are well-correlated with changes in CBF as measured by xenon-enhanced computed tomography.

Measurement of CBF provides valuable information for clinical management of neurocritical care patients, but current modalities for monitoring CBF are often limited by practical and technological hurdles. Such hurdles include cost, exposure to ionizing radiation, and the logistical challenges and increased risk to critically ill patients when transportation out of the neurointensive care unit is required [248]. Furthermore, standard radiological modalities such as CT, PET, and MRI cannot provide continuous measures of CBF that

may be required in clinically unstable patients. Bedside techniques for monitoring CBF include transcranial Doppler (TCD) ultrasonography [63], and thermal diffusion [235] and laser Doppler flowmetries [124]. However, TCD ultrasonography is limited to observations of large vessel flow velocities, which do not necessarily reflect microvascular perfusion in patients with cerebrovascular disease [184], and both thermal diffusion and laser Doppler flowmetries are invasive.

Diffuse correlation spectroscopy is a novel noninvasive optical technique with potential as an alternative approach for bedside CBF monitoring. DCS uses near-infrared light within the therapeutic spectral window (i.e., wavelengths from ~ 650 to ~ 950 nm) to provide a continuous, transcranial measure of blood flow. Changes in blood flow are obtained from DCS by measuring the decay rate of the detected light intensity autocorrelation function (g_2) [13, 142, 177]. At present, quantitative absolute measurements of CBF with DCS are difficult to obtain, and thus we typically derive microvascular relative CBF ($rCBF_{DCS}$), i.e., blood flow changes relative to some baseline period. Diffuse optical spectroscopy (DOS), otherwise known as near-infrared spectroscopy, is a more widely known optical monitoring technique that derives concentration changes of oxy- and deoxyhemoglobin (ΔHbO_2 , ΔHb) [244, 96]. In this study, we have integrated DCS with DOS in a hybrid optical instrument that simultaneously monitors CBF and oxy- and deoxyhemoglobin concentrations. The instrument thus facilitates monitoring both CBF and oxygen metabolism in neurocritical care patients. The continuous and noninvasive nature of these optical techniques may lead to new clinical tools in the neurointensive care unit.

DOS and, more recently, DCS have been employed to measure tissue perfusion and oxygenation in human populations. For example, DCS/DOS has detected changes in autoregulatory function associated with ischemic stroke [59] and healthy aging [61]. $rCBF_{DCS}$ measurements also have been validated against fluorescent microspheres in brain-injured piglets [264]. This study is the first to evaluate $rCBF_{DCS}$ in an adult neurocritical care population.

In the study, we assessed the feasibility of DCS as a continuous monitor of CBF in neurocritical care patients by comparing DCS measurements of CBF with a more established technique, stable xenon-enhanced CT (XeCT) [176, 258]. XeCT is a diffusible tracer technique that provides quantitative CBF by administering xenon via inhalation and using the time-dependent concentration of xenon in tissue as a measure of perfusion. XeCT CBF calculations are based on the modified Kety-Schmidt equation, which describes the relationship of CBF to the tracer blood/brain partition coefficient and tracer concentration in the brain and arterial blood [119]. We performed continuous bedside DCS/DOS with two serial concurrent XeCT measurements in a cohort of patients in whom pharmacological or physiological interventions aimed at altering CBF were administered. We hypothesized that $rCBF_{DCS}$ would correlate with CBF measured by XeCT in co-registered spatial regions of the injured brain, and that correlations would also exist between CBF measured by both techniques and DOS parameters.

4.1 Methods

Patients were considered eligible for study enrollment if they were ≥ 18 years old and were receiving care in the Hospital of the University of Pennsylvania neurointensive care unit for aneurysmal subarachnoid hemorrhage, traumatic brain injury, or ischemic stroke. Patients were recruited through the Department of Neurology and the Neurosurgery Clinical Research Division under a research protocol for the study of portable xenon-enhanced CT. Written consent for both the XeCT and optical monitoring portions of the study was provided by the subject (if able) or by a legally authorized representative. All studies were conducted in the patient's room, following protocols approved by the University of Pennsylvania Institutional Review Board.

As part of routine neurocritical care, a variety of physiologic parameters were monitored throughout the duration of the study. Intracranial pressure (ICP) was monitored either by an external ventricular device or a fiberoptic intraparenchymal catheter (Camino-MPM1; Integra NeuroSciences, Plainsboro, NJ). Cerebral perfusion pressure (CPP) was calculated from the difference between mean arterial pressure (MAP), measured by an arterial line, and ICP. Peripheral oxygen saturation (SpO_2) was measured by a pulse oximeter, and when available, partial pressure of brain tissue oxygenation ($PbtO_2$) was monitored (Licox®CMP; Integra LifeSciences, Plainsboro, NJ). The $PbtO_2$ monitor consisted of a polarographic Clark-type electrode inserted into cerebral white matter.

4.1.1 DCS/DOS

The hybrid diffuse optical device used in this study contains both DCS and DOS modules. The DCS module uses two long-coherence-length, continuous-wave 785 nm lasers (CrystaLaser Inc., Reno, NV) for sources, eight photon-counting fast avalanche photodiodes (Perkin Elmer, Canada) for detection, and two 4-channel autocorrelator boards (Correlator.com, Bridgewater, NJ) to compute g_2 . The DOS module employs three wavelengths of amplitude-modulated near-infrared light (685, 785, and 830 nm) for sources, and two photomultiplier tubes for detection. The probe held four optical fibers (one source and detector each for DCS/DOS) at a fixed configuration (Figure 4.1) to permit the two optical modalities to measure nearly concurrent changes in approximately the same volume of tissue. The source-detector separation was 2.5 cm, and the depth of penetration of light into tissue was approximately 1.25-1.5 cm. As shown in Figure 4.1, perturbations from voxels within the darkest banana-shaped region (about 1.25 cm deep) have the greatest influence on the detected optical signal, with lighter regions having progressively less influence. This penetration depth permits the near-infrared light to interrogate microvasculature within the surface region of adult cerebral cortex [57].

Optical probes were positioned on both sides of the forehead, over the left and right frontal poles. $rCBF_{DCS}$, ΔHbO_2 , ΔHb , and ΔTHC for each hemisphere were updated every 7 s. Positioning and shielding of the probes were adjusted until adequate signal was confirmed prior to data collection. In one instance, optical data could not be obtained; this patient had traumatic epidural and subdural hematomas along the anterior bifrontal

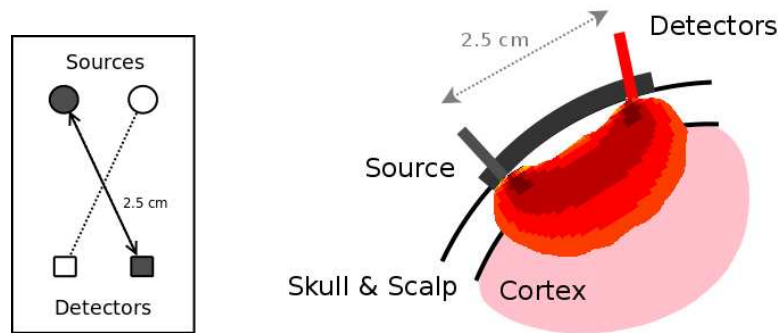


Figure 4.1: Right: Schematic of the source-detector separation of the optical probe. The resulting area of highest probability signal origin is shown as dark gray, with the lighter areas having lower probability of signal. Left: Schematic of optical probe, with DCS/DOS source-detector pairs in crossed configuration at a fixed separation of 2.5 cm to measure approximately same volume of tissue.

convexities. These particular hematomas prevented sufficient photon transmission through the cortex due to excessive absorption by the concentrated blood.

DCS data analysis used a Brownian diffusion model to characterize relative blood flow [142, 177], along with a semi-infinite, homogeneous medium model for the optical properties of the head to fit the measured autocorrelation functions [16]. Decay curves that failed to fit the model produced low confidence results and were omitted from the analysis. A modified Beer-Lambert law was used for DOS analysis [52]. Details of both DCS and DOS analyses have been published previously [15, 34].

4.1.2 Stable Xenon-Enhanced CT

Xenon CT studies were performed with a portable CT scanner (Neurologica Ceretom®), seen in Figure 4.2, left) and a stable xenon delivery circuit using the following parameters: inhalation of 28% xenon mixed with oxygen, 100 kV/5-6 mA CT parameters, low

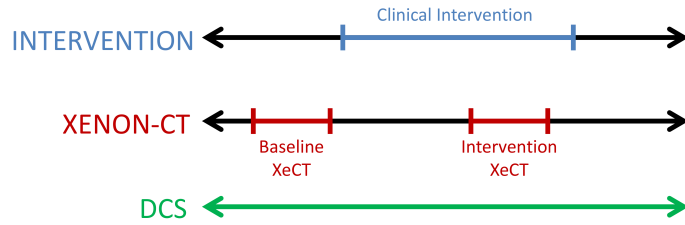


Figure 4.2: Right: Timeline of the DCS/XeCT validation study. Two XeCT scans were performed, baseline and post-intervention scans. A clinical intervention – either blood pressure alteration or hyperventilation – was administered in between the two scans. DCS/DOS monitored the patient continuously throughout. Left: A photo of a patient during the DCS/XeCT study. A black cloth covers the optical probes on the patient’s forehead, and the portable XeCT scanner is shown.

dose resolution (2 s scan), 8 time points (2 during baseline and 6 during xenon administration), 6 imaging locations (two 1 cm images per 2 s scan), and estimated dose CTDI_w = 120 mGy (CereTom portable CT scanner, Neurologica, Danvers, MA). Six adjacent 10-mm-thick axial quantitative CBF maps (along with their respective confidence maps) were generated using product software (Xenon-CT System 2, Diversified Diagnostic Products Inc, Houston, TX) to derive blood flow (ml/100 g brain/min) for each voxel of the CT image [258, 83, 165, 158].

The XeCT scans were used clinically to evaluate the effect of a physiological intervention on CBF, e.g., manipulation of MAP or arterial partial pressure of carbon dioxide. The specific intervention performed was at the discretion of the attending neurointensivist and varied depending on the particular clinical scenario. For example, if regions of oligemia were observed on the baseline XeCT, then MAP was increased by approximately 20% by

administering increased doses of vasopressors. If regions of hyperemia were observed, then vasopressor dose was lowered, antihypertensive medications were administered, or ventilation rate was increased. A second XeCT scan was then performed after a minimum of 10 min to re-evaluate CBF after the intervention. DCS/DOS monitoring was continuous throughout the scans. A timeline schematic of the study is shown in Figure 4.2, right.

Regions-of-interest (ROIs) of approximately 6-8 ml from the CBF_{XeCT} images, corresponding to the regions of cerebral cortex under the optical probes, were chosen by a physician blinded to the optical results. Figure 4.3 shows a representative noncontrast CT image slice where optical probes can be seen on the forehead, with outlined ROIs on the corresponding CBF map. ROIs with greater than 30% of pixels having motion artifact or beam-hardening artifact, e.g., due to surgical staples or monitoring equipment, were identified by visual inspection and excluded from the analysis [262].

4.1.3 Statistical Analysis

For each ROI, the change in relative CBF_{XeCT} ($rCBF_{XeCT}$) was calculated as the percentage change from the baseline scan:

$$rCBF_{XeCT} = (CBF_{XeCT,IN} - CBF_{XeCT,BL})/CBF_{XeCT,BL}. \quad (4.1)$$

Here $CBF_{XeCT,IN}$ refers to absolute CBF_{XeCT} measured after intervention from the second scan, and $CBF_{XeCT,BL}$ is absolute CBF_{XeCT} from the baseline scan. All continuous time-series data (DCS/DOS/MAP) were computed using the average ($\langle \rangle$) of the 2-min pe-

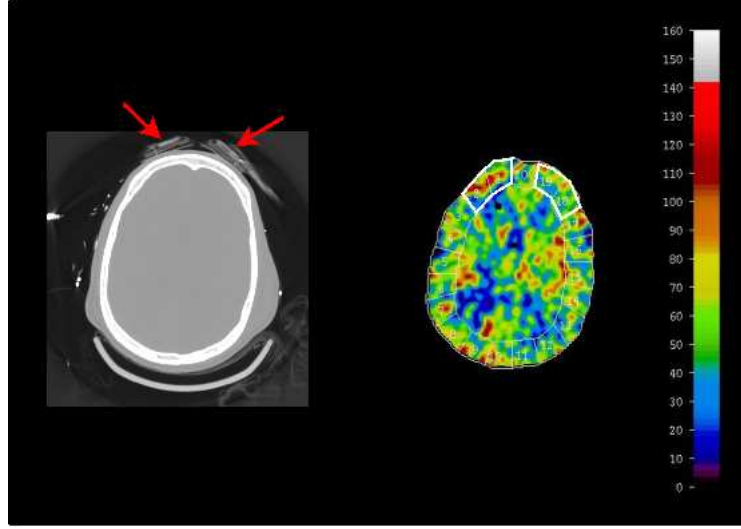


Figure 4.3: Left: Representative axial slice from bone-windowed, non-contrast CT scan (Pt. 7) showing optical probes on both sides of the forehead (red arrows). Right: CBF map from XeCT baseline scan of the same axial slice with ROIs under DCS/DOS probes outlined. Color scale shows absolute blood flow in $mL/100g/min$.

rior to xenon administration for both baseline (Δt_{BL}) and intervention (Δt_{IN}) XeCT scans:

$$rCBF_{DCS} = \frac{\langle rCBF_{DCS}(\Delta t_{IN}) \rangle - \langle rCBF_{DCS}(\Delta t_{BL}) \rangle}{\langle rCBF_{DCS}(\Delta t_{BL}) \rangle}. \quad (4.2)$$

The changes in DOS parameters and vitals were defined as

$$\Delta Y = \langle Y(\Delta t_{IN}) \rangle - \langle Y(\Delta t_{BL}) \rangle, \quad (4.3)$$

with Y representing the parameter of interest. The period prior to xenon administration was used to exclude the possible effects of hemodynamic change due to pharmacological effects of xenon gas [44].

Spearman's rank coefficients were used to assess various correlations between $rCBF_{XeCT}$,

$rCBF_{DCS}$, ΔHbO_2 , ΔHb , and ΔTHC . To analyze the effects of xenon wash-in on CBF, a paired Student's t-test was used to compare population-averaged CBF from the minute before xenon inhalation had begun to population-averaged CBF at the time that xenon had fully washed in (6 min after start of inhalation).

4.2 Results

Clinical and study data for the 10 episodes of measurement are provided in Table 4.1. The eight patients (five males/ three females) had a mean age of 48 years (range, 18 to 82 years). The Glasgow Coma Score (GCS) ranged from 3 to 15 on admission, and from 3 to 9 on the day of measurement, while study timing ranged from ICU day 2 to 9. Interventions included decrease in vasopressor medication dose (four patients), increase in vasopressor medication dose (two patients), increase in ventilator respiratory rate (one patient), and increase in antihypertensive medication dose (one patient). Pharmacological and physiological interventions are summarized in Table 4.1.

Comparisons between XeCT and DCS/DOS parameters were performed using at least one ROI from seven patients (due to poor XeCT confidence, thus exclusion, for both ROIs in Pt. 5), while comparisons between DOS and DCS parameters were performed using data from all eight patients. Changes in blood pressures, CBF_{XeCT} , and DCS data for baseline and intervention measurements with sufficient confidence are in Table 4.2.

Table 4.1: Patient clinical and study data.

No.	Gender	Age	Injury	Initial GCS	Study GCS	Intervention
1	F	62	SAH	15	8	Phenylephrine ↓
2	M	18	TBI	3	7	Ventilator respiratory rate ↑
3	M	23	AIS	7	3	Labetalol ↑
4	M	46	SAH	14-15	6	Norepinephrine ↑
5	M	38	SAH	15	9	Phenylephrine ↑
6	M	82	TBI	11	6	Norepinephrine ↓
7-1	F	50	SAH	3	3	Norepinephrine ↓, Phenylephrine ↓
7-2					3	Norepinephrine ↓
8-1	F	55	SAH	14	3	Norepinephrine ↓, Phenylephrine ↓
8-2					3	Vasopressin ↓

GCS, Glasgow Coma Score; SAH, subarachnoid hemorrhage; TBI, traumatic brain injury; AIS, acute ischemic stroke.

Table 4.2: Δ MAP, Δ CPP, CBF_{XeCT} , $rCBF_{XeCT}$, and $rCBF_{DCS}$.

No.	Blood Pressure, mmHg		Left CBF_{XeCT} , mL/100g/min		Right CBF_{XeCT} , mL/100g/min		Left $rCBF$, %		Right $rCBF$, %	
	Δ MAP	Δ CPP	CBF_{BL}	CBF_{IN}	CBF_{BL}	CBF_{IN}	XeCT	DCS	XeCT	DCS
1	-35	-33	53.5	32.2	63.2	45.1	-39.8	-41.6	-28.7	-14.7
2	-7	-9	57.6	54.2	47.0	46.5	-18.4	4.1	-14.2	-5.5
3	-22	-17	57.1	45.0	**	**	-21.1	-45.0	**	-36.9
4	25	23	38.5	25.9	18.3	27.7	-32.8	-15.4	51.1	**
5	19	20	**	**	**	**	**	-11.2	**	-38.0
6	-17	-18	25.5	21.4	37.9	28.6	-15.8	-21.1	-24.7	-22.2
7-1	-28	-30	60.1	64.0	**	**	6.5	**	**	18.5
7-2	-10	-14	**	**	38.6	35.1	**	39.9	-9.1	20.2
8-1	-17	-10	61.6	64.2	67.5	65.7	4.1	3.2	-2.7	13.9
8-2	-8	-2	86.5	76.7	**	**	-11.3	-5.9	**	7.7

** XeCT or DCS data were not of acceptable confidence for use

4.2.1 Comparison of $rCBF_{XeCT}$ and $rCBF_{DCS}$ Data

Changes in CBF measured by DCS and XeCT correlated well and were in good agreement, as shown in Figure 4.4. Figure 4.4, top, shows the observed correlation between $rCBF_{XeCT}$ and $rCBF_{DCS}$ ($R_S = 0.73$, $P = 0.010$), indicating a positive and significant association between the two quantities. The linear fit by simple regression has a slope equal to 1.1, with an offset of 9.3%.

Figure 4.4, bottom, is the Bland-Altman plot that defines agreement between two techniques measuring the same parameter [12]. The difference of the two quantities is plotted versus the average, and all but one data point is within two standard deviations of the difference mean, meaning relatively good agreement.

ΔHbO_2 was moderately correlated with $rCBF_{XeCT}$ and bordered on significance ($R_S = 0.57$, $P = 0.053$). Correlation was not found for either ΔHb ($R_S = -0.51$, $P = 0.087$) or ΔTHC ($R_S = 0.41$, $P = 0.193$).

Detailed results follow for a subarachnoid hemorrhage patient (Pt. 1), a 62-year-old female with a ruptured aneurysm at the middle cerebral artery bifurcation. We studied her on the 9th day after aneurysm rupture, which was clipped on the 2nd day. After the baseline XeCT scan, the phenylephrine drip rate was gradually lowered by 274 $\mu\text{g}/\text{min}$, and a decrease in CBF was observed by both modalities for the post-intervention scan. A timeline of scans and drip rate changes is shown in Figure 4.5, corresponding to the continuous time-series of $rCBF_{DCS}$ monitored throughout the study. In this case, clinicians decided to decrease the phenylephrine level after seeing the post-intervention scan because they felt

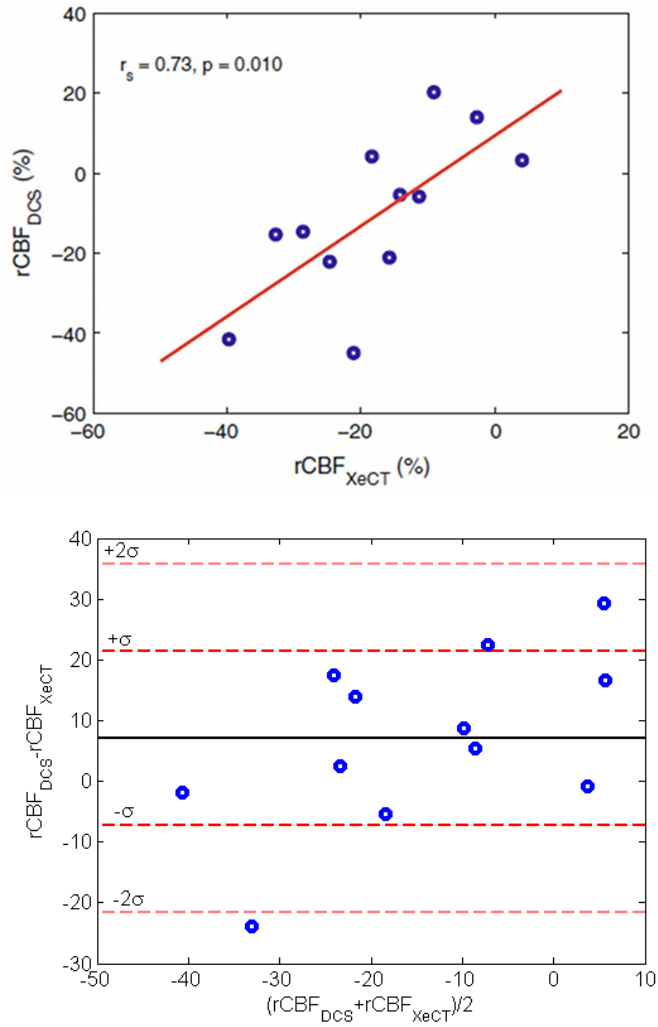


Figure 4.4: Scatter plot (top) and Bland-Altman plot (bottom) illustrating the correlation and agreement, respectively, between $rCBF_{DCS}$ and $rCBF_{XeCT}$ calculated from ROIs located on the frontal poles of each patient, under the optical probes. The fit line has a slope of 1.1 and an offset of 9.3%. All but one data point is within two standard deviations of the difference between $rCBF_{DCS}$ versus $rCBF_{XeCT}$.

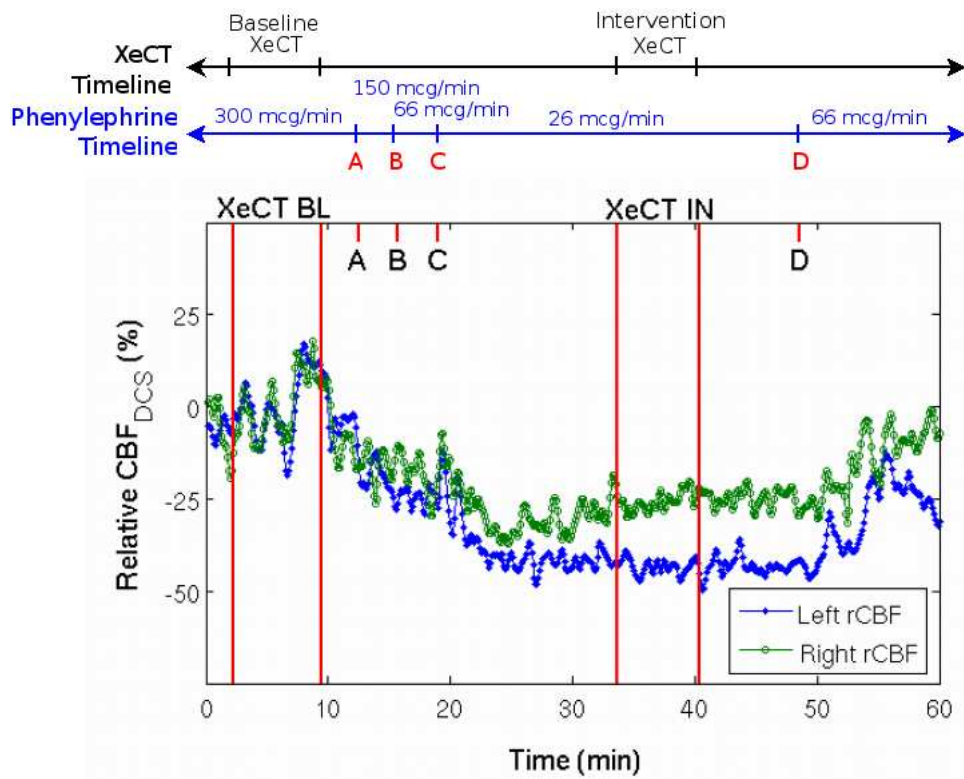


Figure 4.5: Time-series of continuous rCBFDCS from an example patient (Pt. 1) during concurrent validation with XeCT with timeline showing phenylephrine levels. Letters A-D indicate alterations of phenylephrine drip rate. Vertical lines for baseline (BL) and post-intervention (IN) XeCT scans indicate beginning and end of scan. Phenylephrine at baseline was 300 mcg/min, then lowered to (A) 150 mcg/min, (B) 66 mcg/min, (C) 26 mcg/min. Level at post-intervention scan was 26 mcg/min. Clinical decision made to raise drip rate after scans to (D) 66 mcg/min.

that CBF was too high. High CBF can be dangerous because of increased ICP as well as a potential higher chance of aneurysm rebleed. Thus, phenylephrine, and subsequently CBF, was lowered to a more moderate level.

Comparing the relative changes in CBF from both modalities, $rCBF_{XeCT}$ fell -39.8% and -28.7% for left and right ROIs respectively, while $rCBF_{DCS}$ fell -41.6% and -14.7%. MAP showed a decrease of 35 mmHg. Agreement was very good in this patient, in the sign and magnitude of the CBF changes, as well as in hemispheric disparity.

4.2.2 Effects of Xenon Inhalation

Figure 4.6 illustrates one patient's reaction to xenon inhalation. $rCBF_{DCS}$ and ΔTHC changed by 10.9% and 2.1 μM , respectively, in the left frontal cortex and 6.4% and 1.3 μM , respectively, in the right frontal cortex, while MAP increased by 16 mmHg. Such responses observed among the cohort were heterogeneous, and, as a result, they were not significant in the population as a whole ($2.6\% \pm 11.5\%$, $P = 0.191$) with a range of -21.3% to +29.2% relative to baseline. ΔHbO_2 ($0.1 \mu M \pm 1.9 \mu M$, $P = 0.853$) and ΔTHC ($0.4 \mu M \pm 1.4 \mu M$, $P = 0.089$) varied similarly, while ΔHb increased ($0.4 \mu M \pm 1.0 \mu M$, $P = 0.035$).

Figure 4.7 shows the spread in individual patient responses in both optical parameters and vitals. Many times, even left and right probes in the same patient behaved in an opposite manner. This is undoubtedly due to the heterogeneity of patients' injuries and degree of impaired autoregulation.

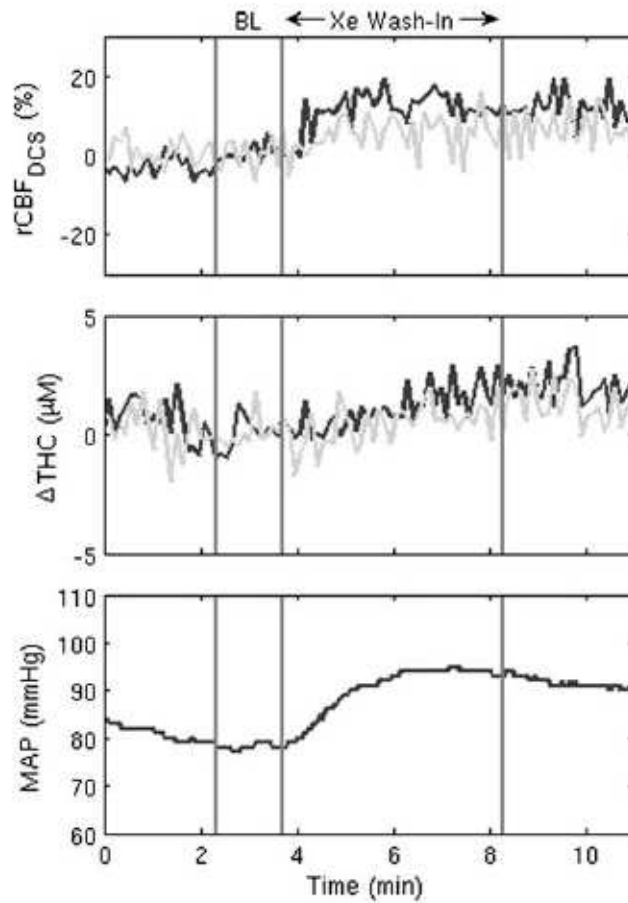


Figure 4.6: Example of xenon-enhanced flow activation. Vertical lines indicate the following marks: beginning of baseline CT scan (BL), xenon gas washing in, and lastly end of xenon-CT scan. Measurements from the left and right frontal optical probes are indicated by light gray and dark gray lines, respectively. Once xenon begins to wash in, $rCBF_{DCS}$ in both hemispheres begins to increase (top panel) and elevated CBF is maintained throughout the duration of the scan. ΔTHC increases in both cerebral hemispheres during the scan (middle panel), with a concurrent rise in MAP (bottom panel).

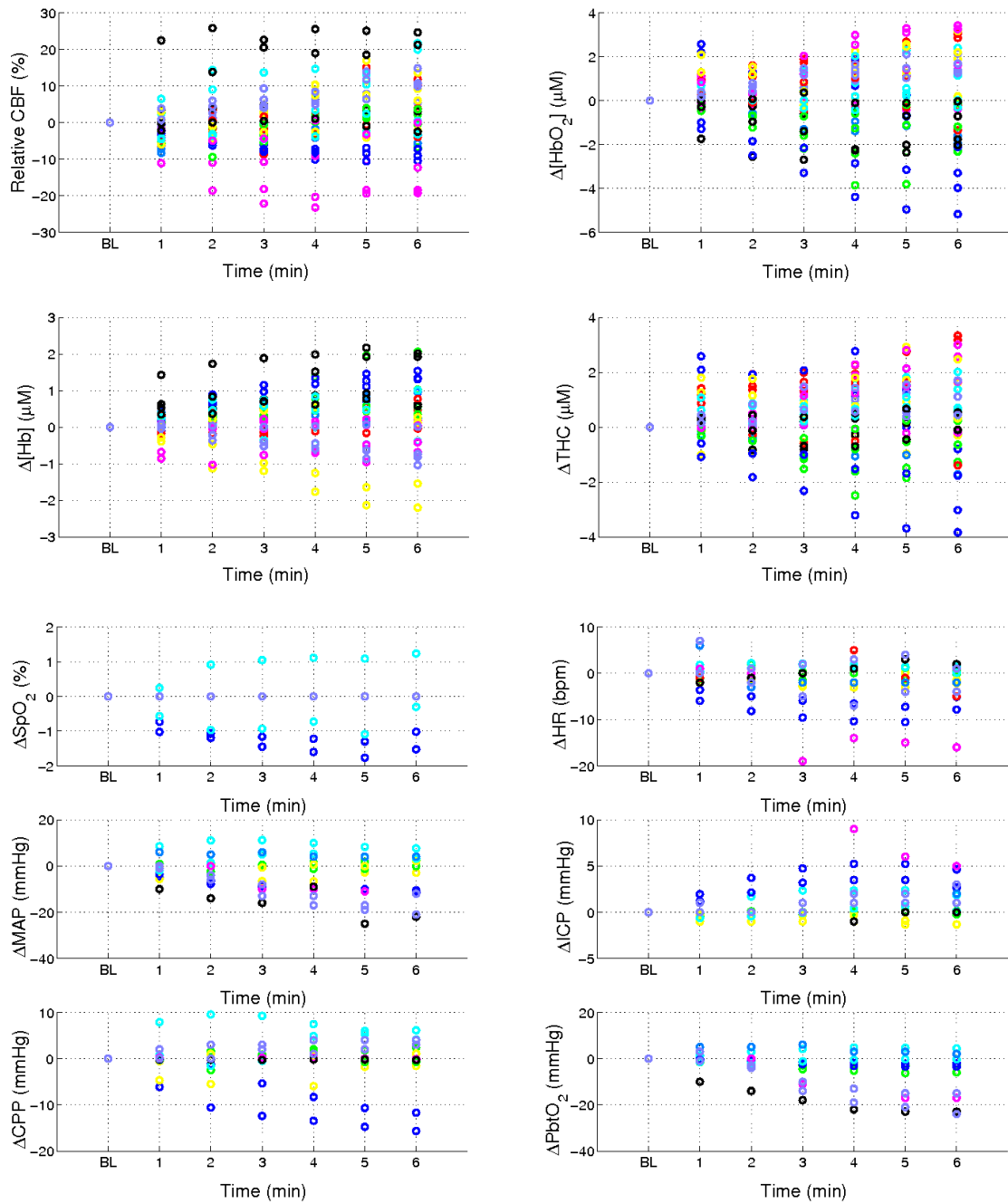


Figure 4.7: All individual patient results of xenon-enhanced flow activation. The first point indicates baseline (BL), and the following points are the number of minutes that pass after xenon gas begins to wash in. At minute 5, the xenon has stopped. Each color represents a different episode of measurement, where two scans occurred per episode. Note the heterogeneity of patient responses.

4.3 Discussion

In this preliminary study, the feasibility for non-invasive continuous bedside CBF and oxygenation monitoring in the neurocritical care unit using a hybrid optical device was demonstrated. Importantly, DCS/DOS monitoring of frontal cortical microvascular hemodynamics was performed non-invasively across a range of patients without requiring transport outside the neurointensive care unit. Only frontal epidural or subdural hemorrhages with large enough absorbance to prevent photon detection posed a barrier to the optical signal. DCS measurements of changes in relative CBF correlated well with changes in CBF measured by a well-established, low-throughput technique: stable xenon-enhanced CT. In addition, significant correlations between DCS measurements of $rCBF$ and DOS measurements of ΔHbO_2 and ΔTHC were demonstrated. The association between ΔHbO_2 and $rCBF_{XeCT}$ only bordered significance ($P = 0.053$), while no correlation was found for ΔTHC or ΔHb with $rCBF_{XeCT}$.

DCS has not been previously validated in critically brain-injured patients. XeCT is one method used to assess CBF in these patients, with the advantage of providing quantitative CBF measurements and coverage through much of brain parenchyma. However, XeCT requires exposure to ionizing radiation and cannot provide continuous or even frequent CBF measurements. The good correlation between DCS- and XeCT-measured CBF in this study suggests that DCS may therefore complement existing perfusion imaging techniques by providing continuous, bedside monitoring of CBF in specific cortical ROIs.

As a secondary aim, we examined the correlations between changes in DOS parame-

ters (ΔHbO_2 , ΔHb , and ΔTHC) and changes in CBF, as determined by both DCS and XeCT. DOS assessment of ΔHbO_2 is sometimes used as a surrogate of CBF. In this study, we found moderate correlation with $rCBF_{DCS}$ but not with $rCBF_{XeCT}$. One explanation for this finding is simply that more data were available to compare DCS to DOS than to compare XeCT to DOS (due to low confidence images from XeCT). The small number of patients was the main limitation of the study, and may have introduced a bias. However, perturbations in cortical metabolic rate, ICP, arterial inflow, or venous drainage may also complicate the relationship between ΔHbO_2 and CBF in neurocritical care patients. Our findings suggest that direct measurements of CBF using DCS are superior to DOS surrogates and will enhance the diagnostic specificity of transcranial optical monitoring.

Both DCS and DOS detected the effects of xenon inhalation on CBF and oxygenation. This well-documented phenomenon ("xenon-enhanced flow activation") occurs with the inhalation of stable xenon. As an inert gas, xenon is an anesthetic in high concentrations (70%) [44]. Horn et al. [101] observed xenon-enhanced flow activation in a brain-injured population (using thermal diffusion flowmetry) and demonstrated variability in the magnitude of CBF response (-29% to +44% relative to baseline) that was similar to the variability detected by DCS (-21.3% to +29.2% relative to baseline). Studies by Giller et al. and Hartmann et al. recorded a heterogeneous response in blood velocity and flow even in a healthy cohort [90, 77]. To our knowledge, there are no prior studies employing optics to investigate the effects of xenon inhalation on oxygenation. Examination of the full time-course of CBF throughout XeCT scans could improve the accuracy of the CBF map, but calculations

of a simulated 3545% CBF increase due to xenon-enhanced flow activation yield only a minor 35% enhancement in calculated flow as most of the calculations are completed prior to the onset of flow activation [166, 78]. Thus, despite inducing changes in CBF during xenon gas inhalation, the resulting enhancement or reduction in calculated CBF is small compared to errors due to CT noise, motion artifacts, etc.

Like DOS, DCS has several clinical limits. Light penetration depth is only a few centimeters due to light attenuation by tissue. In the present application, flow measurements were limited to near the surface of the cerebral cortex. In addition, optical data could not be resolved in the presence of underlying extra-axial hemorrhage. Edema directly beneath the optical probes may also prevent signal detection when light absorption is high. Furthermore, since DCS detects changes in CBF more reliably than absolute blood flow. Thus, measurements during a baseline period must be obtained prior to longterm monitoring. Development of an absolute measure of CBF_{DCS} is an area of active research, although arguably, trends in CBF may be more clinically relevant since absolute healthy/ischemic thresholds remain unclear [217, 221, 79].

DCS is also limited by the fact that it is a local measure of CBF, and each sourcedetector pair is only able to probe a region of several cubic centimeters in size. However, multiple probe pairs could be strategically placed with the guidance of CT or MRI to provide continuous monitoring of the most clinically relevant areas of the brain. Continuous noninvasive CBF measurements in multiple regions could be generated using DCS with significantly less morbidity than using multiple intracerebral monitors.

The good correlation between DCS and XeCT observed in this pilot study provides support for further evaluation of the clinical utility of DCS. Given the dynamic, evolving, and heterogeneous nature of intracranial pathology in brain-injured patients, continuous CBF monitoring may provide the neurointensivist with an important tool for early detection of secondary injury. Since CBF reductions often precede the onset of new clinical symptoms and infarction, DCS monitoring has the potential to detect changes in cerebrovascular physiology while ischemic changes are still reversible. In addition, the configuration of hybrid instrumentation with DOS would provide comprehensive assessment of cortical blood flow and oxygenation using a single device and the same probes. Additional studies are warranted to assess the utility of DCS/DOS for neurocritical care, such as by correlating long-term DCS/DOS measurements of cerebrovascular hemodynamics with patient outcome.

Chapter 5

Effects of Posture Change on Healthy

Adults

Posture change evokes hemodynamic responses in the cerebral and systemic vasculature aimed at maintaining cerebral perfusion. Venous return of blood flow to the heart is altered, leading to dynamic changes in vascular tone and the initiation of the systemic baroreceptor reflex. These cerebral and systemic hemodynamic responses occur in close temporal relation to maintain cerebral blood flow (CBF) across a mean arterial pressure (MAP) range of approximately 60-160 mmHg in normotensive people. Studies of healthy subjects have demonstrated that the systemic response to postural change, the baroreceptor reflex, is impaired with aging [80]. In addition, aging is associated with lower baseline blood flow velocities in the anterior cerebral artery (ACA), middle cerebral artery (MCA) and posterior cerebral artery (PCA) [126], as well as lower baseline CBF [145] and an increased

incidence of orthostatic hypotension [210]. The effect of healthy aging on cerebrovascular autoregulation (CA), however, has yet to be fully elucidated.

The most commonly used modality for assessing the effect of aging on CA has been transcranial Doppler (TCD) ultrasonography. TCD experiments have demonstrated that healthy elderly subjects maintain adequate autoregulatory function under both dynamic [26, 132, 218] and static conditions [26, 132, 257]. These TCD findings may be explained by a pronounced vasodilatory response to decreased cerebral perfusion pressures in elderly subjects during acute orthostatic stress [218]. However, while TCD studies have generally yielded consistent results about the absence of an aging effect in CA, these studies rely on an assumption that macrovascular CBF velocity is indicative of microvascular CBF.

The application of diffuse correlation spectroscopy (DOS), otherwise known as near-infrared spectroscopy (NIRS), to CA studies has provided an opportunity to evaluate this key assumption. Studies of healthy subjects using TCD and DOS concurrently have generally validated the correlation between macrovascular CBF velocity and microvascular oxygenation during steady-state conditions [184], during alterations in end-tidal CO₂ (EtCO₂) [213] and during orthostatic stress [125]. However, data from several DOS studies have conflicted with TCD data regarding the effect of healthy aging on autoregulatory function. For example, Mehagnoul-Schipper *et al* [149] found that elderly (mean age 74 years), but not young (mean age 27 years) subjects experienced significant declines in frontal cortical blood oxygenation and blood volume during supine-to-standing posture change. This finding was reproduced in a follow-up experiment in which serial DOS measurements were

performed in elderly subjects (mean age 75 years) during orthostatic stress [148]. Hunt *et al* [103] studied ten healthy subjects of mean age 60 years and demonstrated a significant postural decline in the ratio of oxygenated hemoglobin to total tissue hemoglobin concentration. The lack of concordance between TCD and DOS data in autoregulation studies may reflect differences in measured parameters and underscores the importance of developing a modality that can directly measure microvascular CBF to more completely characterize autoregulatory function.

We thought instead of using diffuse correlation spectroscopy (DCS) to provide direct measurements of microvascular relative CBF ($rCBF$) instead of the surrogate measures of CBF provided by DOS – total hemoglobin concentration (THC), oxyhemoglobin concentration (HbO_2) and deoxyhemoglobin concentration (Hb). These measurements are only accurate markers of CBF if arterial oxygen content and cerebral metabolic rate remain constant.

In this prospective observational study, we aimed to explore the effects of healthy aging on cerebral hemodynamic responses to posture change by utilizing hybrid diffuse optics for comprehensive cerebrovascular hemodynamic monitoring. We studied a large cohort of subjects across the age continuum, rather than examining cerebral hemodynamics at the extremes of age. We also examined the correlation between DCS and DOS measurements in order to assess whether hybrid diffuse optics can provide additional information about cerebral hemodynamics that cannot be obtained by DOS alone. Finally, by defining the normative response of cerebral hemodynamics to posture change across the age continuum, we

aimed to establish a control data set for comparison with clinical brain-injured populations, such as those with ischemic/hemorrhagic stroke or traumatic brain injury. Note that this chapter is based on work I have published in *Physiological Measurement* [61].

5.1 Methods

This study was conducted at the Hospital of the University of Pennsylvania. The study protocol was approved by the Institutional Review Board at the University of Pennsylvania. Written informed consent was provided by all subjects, who were recruited by posting fliers in the Hospital of the University of Pennsylvania and from a database maintained by the Center for Cognitive Neuroimaging at the University of Pennsylvania.

Subjects were excluded from the study if they had a history of hypertension, diabetes mellitus, hyperlipidemia, atrial fibrillation, congestive heart failure, coronary artery disease, previous myocardial infarction, previous stroke, previous transient ischemic attack, carotid artery disease, current smoking, previous smoking within 5 years, pulmonary disease, renal disease, or recent administration of vasoactive medications. The target enrollment was 60 subjects. Subjects were enrolled across the age continuum, with a minimum age of 18 years old. The National Institutes of Health Stroke Scale (NIHSS), a tool used by clinicians to objectively quantify impairment due to stroke, was performed prior to study initiation for all subjects.

5.1.1 Optical Instrumentation

A portable, custom-built instrument (see Section 3.1.1) was used to measure $rCBF$, THC , HbO_2 and Hb using DCS and DOS [54]. Two optical probes were secured on both sides of the forehead with medical grade adhesive materials and a head strap. The probes were covered with a loose-fitting black cloth to minimize ambient light interference with the optical signal. The regions of frontal cortical tissue investigated by each probe were approximately 4 to 5 cm apart. Each probe consisted of one light source and two detectors – one for DCS detection and the other for DOS detection. The distance between the light source and detectors was 2.5 cm.

Four high-speed, high-sensitivity avalanche photodiodes were used as photon counting detectors for DCS. Data output from these photodiodes were sent to a multi-tau hardware correlator for calculation of autocorrelation functions in real time. We then extract a blood flow index (BFI) by fitting the autocorrelation function to a semi-infinite homogeneous model (see Section 2.2.2). The correlator produces an independent autocorrelation curve every 0.04 seconds. However, we used an averaging time of 3 seconds for each of the two probes, allowing for one frame of DCS data to be acquired every 6 seconds. This 6-second DCS data acquisition interval was followed by a 1-second DOS data acquisition interval for both probes. Thus, a new set of DCS and DOS cerebral hemodynamic data was acquired every 7 seconds.

The DCS light source consisted of a long coherence length, continuous wave laser (785 nm). Concurrent DOS data were obtained using three lasers (690, 785, and 830 nm), whose

intensities were modulated at 70 MHz. A modified Beer-Lambert law (see Section 2.1.4) was used for DOS analysis, with a differential pathlength factor (DPF) of 5.86 and 6.51 for wavelengths of 830 nm and 690 nm, respectively [52].

5.1.2 Monitoring of Systemic Vitals

Blood pressure and heart rate (HR) were measured by a BpTRUVital Signs Monitor (VSM MedTech Devices Inc., model BPM-300; Brooklyn, NY) prior to study initiation with subjects resting in the seated position. A FinaPres (FINger Arterial PRESSure, Finapres Medical Systems, Finometer Pro Model 1 with BeatScope PC-based software; Amsterdam, The Netherlands) device was then secured non-invasively on the right third finger for continuous beat-to-beat measurement of HR, mean arterial pressure (MAP), systolic blood pressure (SBP) and diastolic blood pressure (DBP). Imholz *et al* [105] have comprehensively reviewed the FinaPres technology and its validation with intra-arterial blood pressure measurement.

An adjustable armrest was used to keep the subject's right third finger at the level of the right atrium (fourth intercostal space, mid-axillary line) throughout the study. Finger position was confirmed using the FinaPres automated height monitor, after zeroing the finger to the level of the right atrium at the beginning of the study. The FinaPres device factors finger height into its hemodynamic measurements to correct for any hand movements that may occur with respect to the heart level. A loose-fitting, black piece of cloth was placed over the patient's right hand in order to minimize ambient light interference with the FinaPres

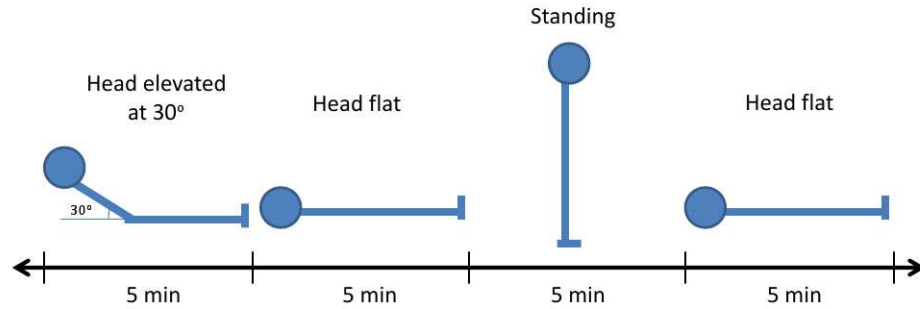


Figure 5.1: Posture change protocol. Subjects were monitored for 5 minutes each at four positions: Head-of-bed 30°, initial (baseline) supine, standing, and recovery supine.

signal.

A disposable rubber mouthpiece was placed in the subject's mouth with an EtCO₂ monitor attached to the opening of the mouthpiece (Micro-Capnograph CI240, Columbus Instruments; Columbus, OH). A nose clip was placed over the nares to prevent nose breathing. The capnograph was used to record EtCO₂ continuously. A pulse oximeter (Nellcor; Boulder, CO) was placed on the index finger of the patient's right hand to record peripheral arterial oxygen saturation (SpO₂).

5.1.3 Posture Change Protocol

Measurements were performed in a quiet room with dim light at room temperature. The optical probes were placed securely on the forehead and a stable FinaPres signal was obtained. Cerebral hemodynamics, systemic hemodynamics, SpO₂ and EtCO₂ were then monitored for 5 minutes each at the following postures (see Figure 5.1) head-of-bed angle 30°, supine (initial supine), standing, and supine (recovery supine).

The supine and standing positions were chosen for the protocol so that healthy sub-

jects would be evaluated in natural postures. The head-of-bed 30° position was included to provide normative, control data for future studies of clinical populations since this is a posture at which many stroke and neurointensive care patients are kept to minimize aspiration risk or decrease intracranial pressure. The head of the hospital bed was lowered from a 30° to a 0° angle during the transition to the initial supine position, and then the subject was asked to stand up and lie back down for the subsequent transitions to the standing and recovery supine positions. Confirmation of optical probe placement, FinaPres finger level and EtCO₂ monitor placement was performed at the time of all posture changes, which occurred over the span of 5 to 10 seconds for the transition from head-of-bed 30° to initial supine and 30 seconds to 1 minute for the transitions from initial supine to standing and standing to recovery supine. Subjects fasted and avoided caffeine intake for 3 hours before the study and were also asked to void urine prior to study initiation.

5.1.4 Statistical Analysis

Analyses were carried out using `library(nlme)` and `library(gregmisc)` in R version 2.8.1 [228]. Two-sided hypothesis tests were carried out with a type I error rate of 0.05. For each subject, the outcome of interest for $rCBF$ was quantified relative to BFI at the initial (baseline) supine position (BL), as follows:

$$rCBF_i = (BFI_i - BFI_{BL})/BFI_{BL} \quad (5.1)$$

where BFI_i is BFI measured at the i th position ($i = \text{head-of-bed } 30^\circ, \text{ standing, or recovery supine}$). The outcomes of interest for all other cerebral and systemic hemodynamic parameters ($THC, HbO_2, Hb, MAP, SBP, DBP, HR, SpO_2$ and $EtCO_2$) were normalized as follows:

$$\Delta Y_i = Y_i - Y_{BL}, \quad (5.2)$$

where Y is the parameter of interest measured at the i th position.

A running Gaussian filter was used to smooth the DCS/DOS time series data, with a window size of 4. At each body position, the DCS/DOS, FinaPres, SpO_2 and $EtCO_2$ data were then averaged over the 5 min period. The beginning and ending timepoints of the transitions between each posture were marked on both the FinaPres and optical data. The cerebral and systemic hemodynamic data acquired during these transitions between postures are not reported because the study aimed to examine postural cerebral hemodynamic changes, not dynamic autoregulatory changes.

Our study yielded repeated measures data on individual subjects. To account for, and take advantage of the correlation between repeated measures on the same individual, a linear mixed effects model was used to estimate the effect of body posture and age on changes in the outcomes of interest [178]. The linear mixed effects model allowed for heterogeneity in the variance of the outcome at each position. As there was no significant hemispheric difference in any of the cerebral hemodynamic parameters at any of the body positions, hemisphere (left or right) was not included as a covariate in the model. Rather, measurements from the different hemispheres were analyzed as repeated measurements at

each body position. Model fit was assessed using residuals.

We assessed the overall effect of body position on each hemodynamic parameter. We then built models that included postural effects as well as both age and gender effects that were allowed to vary by position. There was no a priori hypothesis regarding an effect of gender on postural changes in cerebrovascular hemodynamics, but gender was included in the model as a possible confounder. We used a global likelihood ratio test to ask whether postural changes associated with age or gender were significant, by comparing the full model to a reduced model without the term of interest. If the global likelihood ratio test showed either strict ($P < 0.05$) or marginal ($P < 0.10$) evidence of statistical significance, a Wald test was used to determine which specific postures might be associated with changes from the initial supine posture. Specifically, we tested for nonzero age or gender effects at each posture. This approach of comparing specific body postures to the initial supine posture only if there was evidence of a global effect meant that a small number of statistical tests were conducted, hence reducing the possibility of spurious false positive findings.

In order to account for other potential confounders, the correlation of age with body mass index (BMI), baseline hemodynamics and baseline EtCO₂ in the study population was assessed using a Pearson's correlation coefficient. There was no evidence of a significant association of age with the baseline hemodynamics or baseline EtCO₂ ($P > 0.05$ for all variables), but there was a trend toward an association between increasing age and increasing BMI ($P < 0.10$). We therefore included BMI as a covariate in our models to explore the possibility that age effects were confounded by BMI. However, inclusion of

BMI in the models had little impact on the significance of the age effect, so results from the models that included BMI as a covariate are not reported.

Associations between postural changes in DCS measurements of $rCBF$ and DOS measurements of THC , HbO_2 , Hb and $HbDiff$ were explored using Pearson's correlation coefficient. $HbDiff$ is calculated as $HbO_2 - Hb$ and has been shown to be a better indicator of regional CBF than THC when SpO_2 is kept constant [234]. We also investigated associations between the supine-to-standing changes in systemic and cerebral hemodynamics using Pearson's correlation coefficient. These correlation analyses excluded six subjects whose DOS data were not analyzed because of poor optical fiber-to-detector connection in the DOS instrument. Three subjects had poor quality $EtCO_2$ data due to capnograph malfunction, and two had poor quality systemic hemodynamic data due to low $FinaPres$ signal. These subjects were excluded from the analyses of body posture effects on $EtCO_2$ and systemic hemodynamics, respectively.

5.2 Results

The demographic and baseline hemodynamic characteristics of the 60 healthy subjects are presented in Table 5.1. Age ranged from 20 to 78 years old (see Figure 5.2), with a mean of 42.3 years. The mean BMI was 24.7 kg/m^2 , with a baseline BP of 115.4/74.5 mmHg and HR of 71.3 beats per minute. None of the subjects experienced syncope or reported pre-syncope symptoms during the study.

Table 5.1: Demographic information and baseline characteristics of study population ($N = 60$). Data listed as mean \pm standard error.

Variable	Mean \pm SE
Male:Female	28:32
Age, years	42.3 (range 20-78)
BMI, kg/m^2	24.7 \pm 0.5
SBP, $mmHg$	115.4 \pm 1.9
DBP, $mmHg$	74.5 \pm 1.4
HR, bpm	71.3 \pm 1.4
EtCO ₂ , $mmHg$	39.4 \pm 0.5
NIHSS	All subjects scored 0

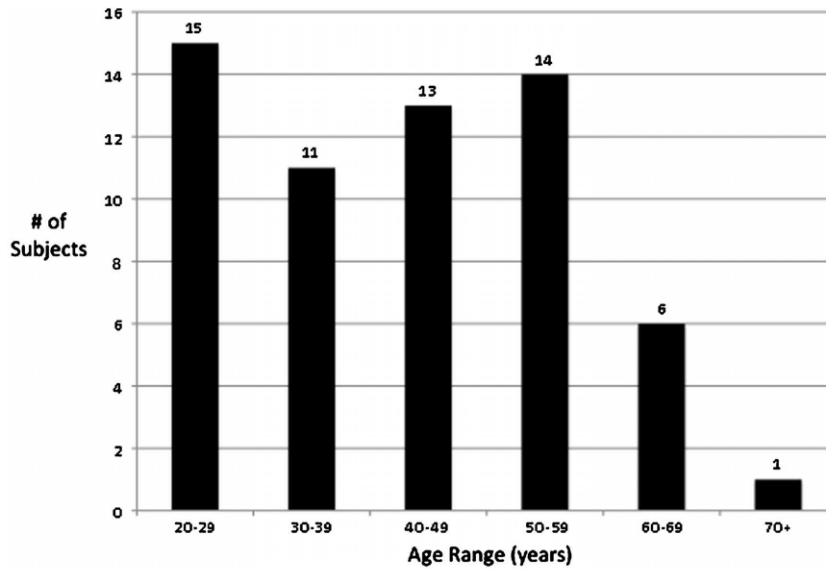


Figure 5.2: Bar graphs demonstrating the number of subjects in each age range, by decade. Note the few number of subjects at the upper (60+ years) range of ages – an inherent weakness of the study.

Table 5.2: Cerebral hemodynamic and systemic responses to posture change for all subjects ($N = 60$).

Parameter	Head-of-Bed 30° to supine	Supine to stand	Initial supine to recovery supine
$rCBF$, %	18.2 ± 1.5 *	-25.9 ± 1.5 *	9.7 ± 1.8 *
ΔTHC , μM	1.9 ± 0.3 *	-2.6 ± 0.4 *	1.6 ± 0.4 *
ΔHbO_2 , μM	2.0 ± 0.3 *	-3.4 ± 0.3 *	1.4 ± 0.3 *
ΔHb , μM	-0.07 ± 0.1	0.8 ± 0.1 *	0.2 ± 0.1
ΔMAP , mmHg	-0.9 ± 0.8	5.4 ± 1.0 *	6.3 ± 0.7 *
ΔSBP , mmHg	0.2 ± 1.0	1.3 ± 1.3	7.9 ± 1.0 *
ΔDBP , mmHg	-1.3 ± 0.7	8.6 ± 0.8 *	4.2 ± 0.6 *
ΔHR , bpm	-0.2 ± 1.4	12.4 ± 0.9 *	-2.2 ± 0.3 *
ΔSpO_2 , %	-0.1 ± 0.1	0.8 ± 0.2 *	0.0 ± 0.1
$\Delta EtCO_2$, mmHg	-0.1 ± 0.2	-2.0 ± 0.3 *	0.0 ± 0.2

Data are expressed as mean ± standard error.

* Significant change with new posture, $P < 0.01$.

5.2.1 Cerebral Hemodynamic Responses to Posture Change

Figure 5.3 (top) displays DCS timeseries data of $rCBF$ from a sample subject. Figure 5.3 (bottom) displays DCS timeseries data of $rCBF$ averaged over the entire study population on a minute-by-minute basis. Table 5.2 shows the mean changes in $rCBF$, THC , HbO_2 and Hb that occurred with each posture change across all subjects.

All cerebral hemodynamic parameters varied significantly with body posture ($P < 0.0001$). Supine-to-standing posture change led to significant decreases in $rCBF$, THC and HbO_2 , as well as a significant increase in Hb , across the age continuum ($P < 0.01$). Changes in $rCBF$, THC and HbO_2 were also significant during the transition from head-of-bed 30° position to supine position. All of the cerebral hemodynamic parameters except Hb differed significantly between the initial supine position (after transition from head-of-bed 30°) and the recovery supine position (after transition from standing, $P < 0.01$ for each parameter). Figure 5.4 provides bar graphs for average changes in $rCBF$, THC , HbO_2

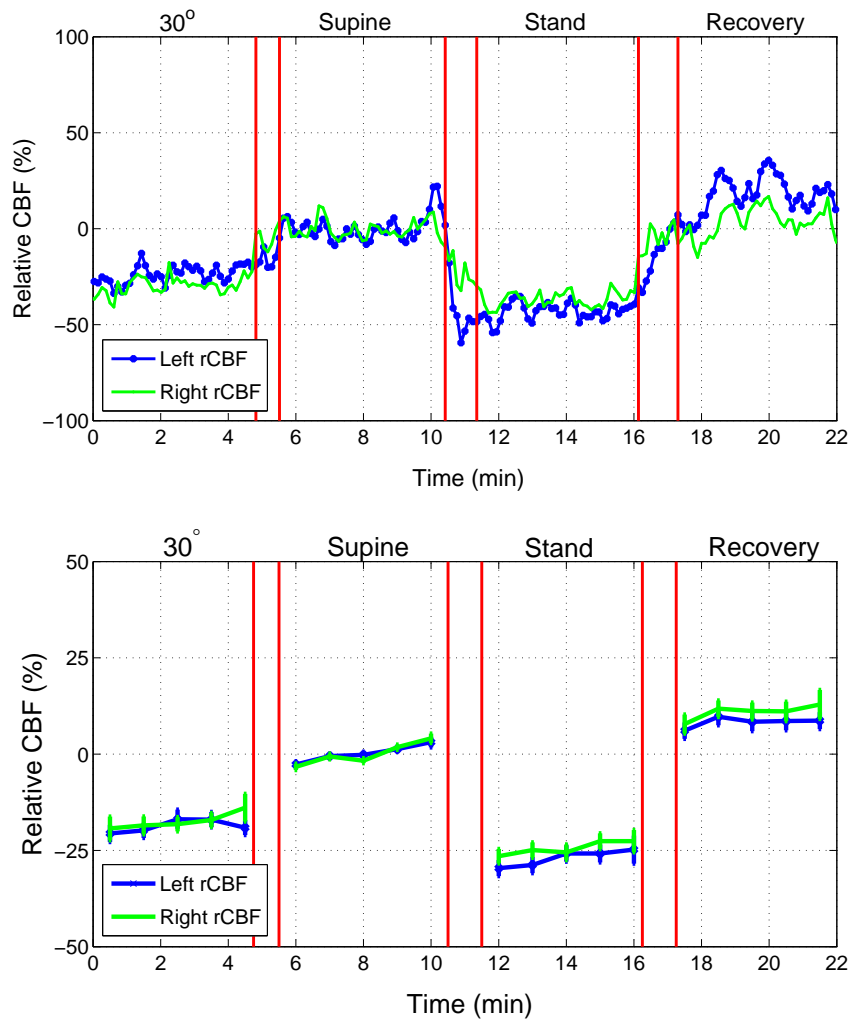


Figure 5.3: (Top) Timeseries data of $rCBF$ for an example subject. (Bottom) Timeseries data of $rCBF$ averaged at 1 minute intervals for the entire study population ($N = 60$). Standard error bars are provided at each 1 minute interval. The red vertical lines between each posture represent the transition periods between body postures. Data within these lines was excluded from data analysis.

and Hb with each posture change for the entire study population.

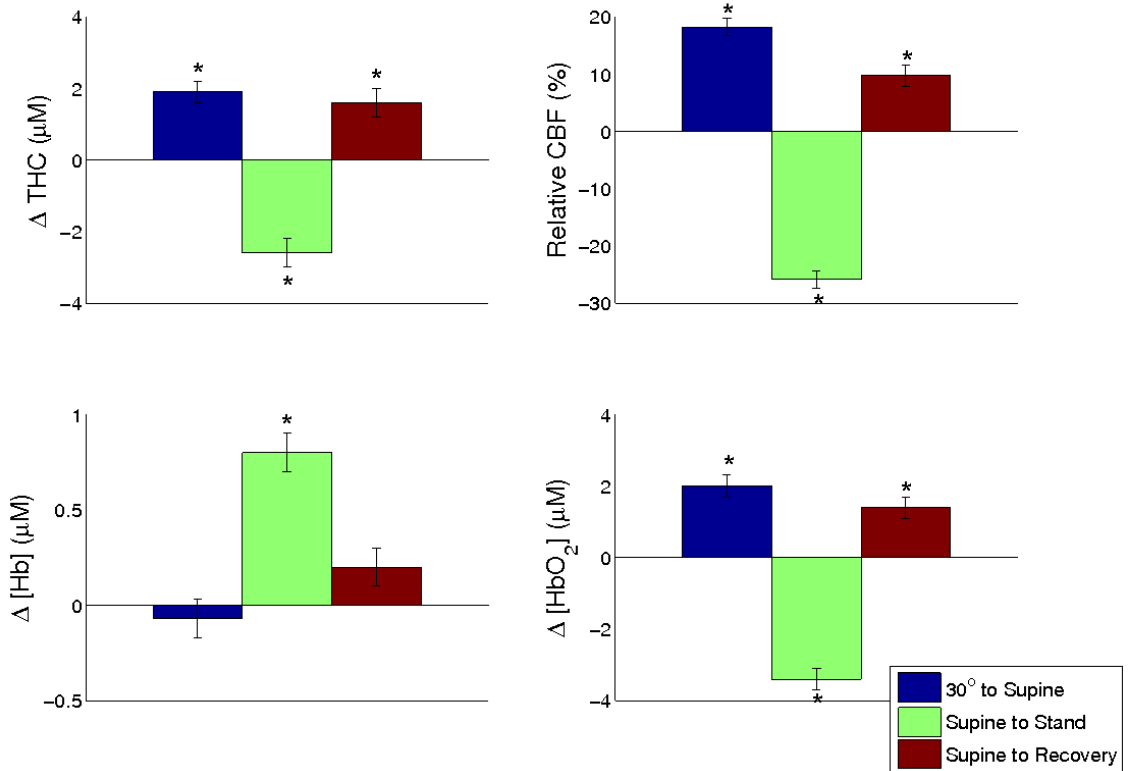


Figure 5.4: Bar graphs for mean changes in $rCBF$, THC , HbO_2 , and Hb with each posture change for the entire population. Error bars show standard error from the mean. Asterisk (*) indicates a significant change from the initial (baseline) supine value.

Among the four cerebral hemodynamic parameters considered, age did not significantly alter the magnitude of postural changes in $rCBF$ ($P = 0.25$), THC ($P = 0.34$) or Hb ($P = 0.60$) in an initial global likelihood ratio test. This test, however, provided evidence of a trend toward significance for age-related HbO_2 postural responses ($P = 0.058$). Subsequent investigations of specific postural changes indicated a significant association between age and HbO_2 change during supine-to-standing posture change ($P = 0.01$). Specifically, the magnitude of decline in HbO_2 during the supine-to-standing posture change decreased

significantly with age.

Table 5.3: Cerebral hemodynamic and systemic responses to posture change, including gender effects ($N = 60$).

Parameter	Head-of-Bed 30° to supine		Supine to stand		Initial supine to recovery supine		Gender effect <i>p</i> -value
	M	F	M	F	M	F	
$rCBF$, %	-21.3 ± 2.1 †	-15.2 ± 2.0 †	-28.8 ± 2.1	-23.8 ± 2.0	14.0 ± 2.6 †	5.8 ± 2.4 †	<0.01
ΔTHC , μM	-2.9 ± 0.4 †	-1.3 ± 0.4 †	-3.2 ± 0.6	-2.4 ± 0.5	2.6 ± 0.5 †	0.9 ± 0.5 †	<0.01
ΔHbO_2 , μM	-2.7 ± 0.4 †	-1.5 ± 0.3 †	-4.0 ± 0.5	-3.2 ± 0.4	2.3 ± 0.4 *	0.7 ± 0.4 *	<0.01
ΔHb , μM	-0.1 ± 0.1 †	0.2 ± 0.1 †	0.8 ± 0.2	0.8 ± 0.2	0.3 ± 0.2	0.1 ± 0.1	0.09
ΔMAP , $mmHg$	2.0 ± 1.2	0.2 ± 1.1	6.8 ± 1.4	4.5 ± 1.3	6.0 ± 1.1	6.4 ± 1.0	0.40
ΔSBP , $mmHg$	0.9 ± 1.5	-0.9 ± 1.4	2.2 ± 2.0	0.5 ± 1.8	7.0 ± 1.4	8.2 ± 1.3	0.50
ΔDBP , $mmHg$	2.2 ± 1.0	0.7 ± 0.9	10.5 ± 1.2	7.4 ± 1.1	4.5 ± 0.8	4.0 ± 0.8	0.23
ΔHR , <i>bpm</i>	0.5 ± 0.6	0.2 ± 0.4	15.2 ± 1.1 *	12.4 ± 0.9 *	-2.0 ± 0.5	-2.2 ± 0.3	0.03
ΔSpO_2 , %	-0.007 ± 0.2	0.2 ± 0.2	0.7 ± 0.2	0.7 ± 0.2	-1.7 ± 0.2 *	0.4 ± 0.2 *	<0.01
$\Delta EtCO_2$, $mmHg$	-0.3 ± 0.3	0.4 ± 0.3	-2.7 ± 0.4	-1.7 ± 0.4	-0.1 ± 0.3	0.2 ± 0.2	0.18

Data are expressed as mean \pm standard error.

Values are for the average 40-year-old male (M) versus the average 40-year-old female (F) based on the fit of the linear mixed effects model.

† Significant gender effect on postural change, $P < 0.05$. * Significant gender effect on postural change, $P < 0.01$.

Gender was associated with significant differences in overall postural changes in $rCBF$, THC , and HbO_2 ($P < 0.01$) and showed a trend toward an effect on postural changes in Hb ($P < 0.10$) (see Table 5.3). Subsequent investigations of specific postural changes did not demonstrate differences between males and females in the supine-to-standing postural changes for any cerebral hemodynamic parameter. However, females experienced a smaller magnitude of postural change in $rCBF$, THC and HbO_2 during the transition from head-of-bed 30° to supine ($P < 0.05$ for the gender effect on all parameters) and during the transition from initial supine to recovery supine ($P < 0.05$ for the gender effect on $rCBF$ and THC , $P < 0.01$ for the gender effect on HbO_2).

Figure 5.5 provides scatter plots of the data with fitted lines representing the mean supine-to-standing postural changes in each cerebral hemodynamic parameter for both genders, as predicted from the fitted models. The y-intercepts indicate the mean postural hemodynamic changes for a subject of age 20, while the slopes represent age effects. As discussed above, gender effects were not statistically significant for the supine-to-standing postural changes in any cerebral hemodynamic parameter but were included here so that the models would be consistent for all postural changes. For HbO_2 , supine-to-standing postural declines were substantially larger for younger than for older subjects. For example, at age 30, the linear model predicted a mean HbO_2 change for males and females of $-4.59 \mu\text{M}$ and $-3.75 \mu\text{M}$, respectively, while at age 60 the model predicted values of $-2.85 \mu\text{M}$ and $-2.01 \mu\text{M}$.

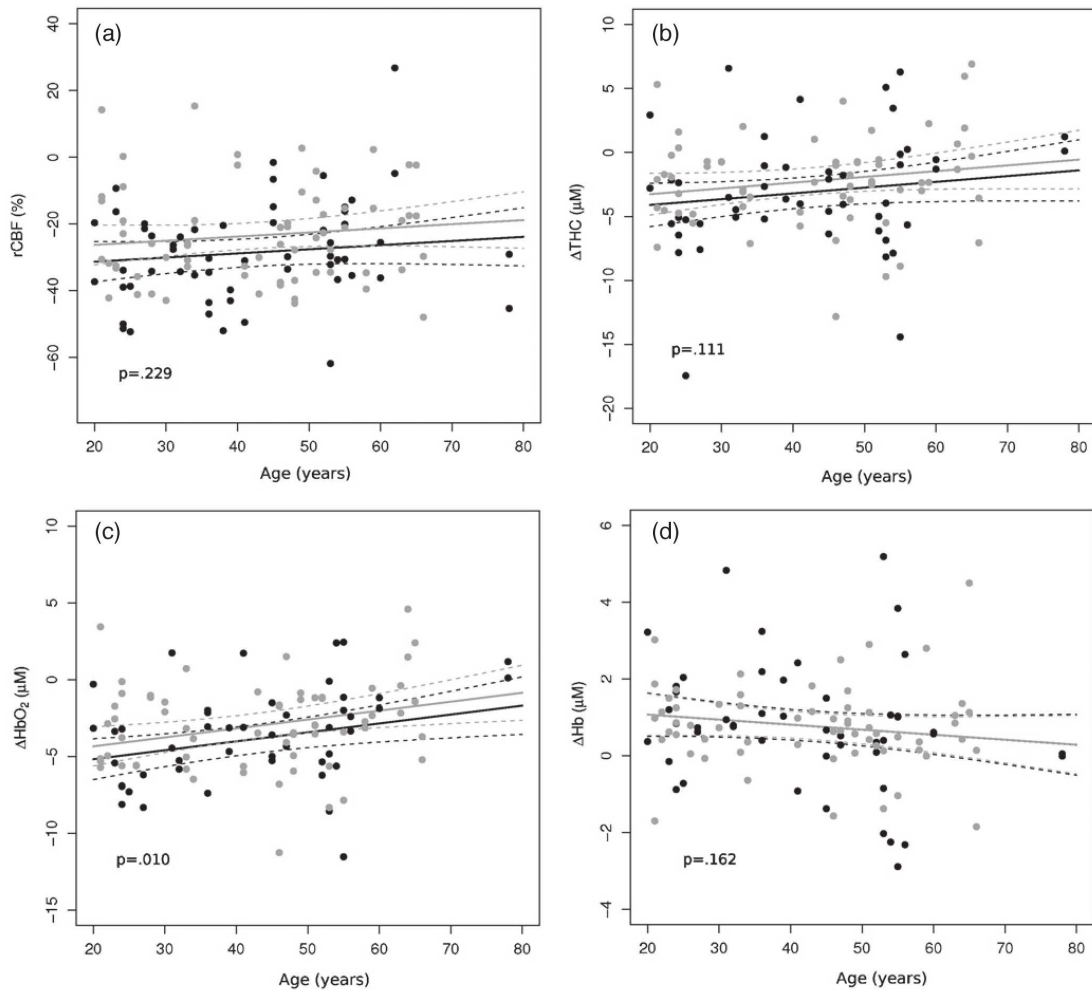


Figure 5.5: Effect of age on the supine-to-standing postural change in $rCBF$, THC , HbO_2 , and Hb . All data are presented for males (black) and females (gray). Left and right hemisphere values for each subject are shown as separate points. Lines represent the predicted value of a given cerebral hemodynamic parameter as a function of age for males (black) and females (gray). 95% confidence intervals based on our model are shown as dashed lines for males (black) and females (gray), along with P-values for the association between age and supine-to-standing posture change. The age effect is only significant for supine-to-standing on HbO_2 ($P = 0.01$). No significant gender effect was observed for any supine-to-standing postural hemodynamic changes ($P > 0.05$).

5.2.2 Systemic Responses to Posture Change

Table 5.2 shows the changes in MAP, SBP, DBP, HR, SpO₂ and EtCO₂ that occurred with each posture change. All systemic hemodynamic parameters varied significantly with body posture ($P < 0.0001$). No significant changes occurred in the transition from head-of-bed 30° to supine position, but during the supine-to-standing posture change subjects across the age continuum experienced a significant increase in MAP, DBP, HR and SpO₂ ($P < 0.01$). EtCO₂ decreased significantly with transition from supine-to-standing posture across the age continuum ($P < 0.01$). MAP, SBP, DBP and HR all differed significantly between the initial supine position and the recovery supine position ($P < 0.01$).

Age significantly altered the postural changes in HR ($P = 0.002$) and EtCO₂ ($P = 0.01$), but not the postural changes in MAP, SBP, DBP or SpO₂. Older subjects experienced smaller magnitudes of change in HR and EtCO₂ during the supine-to-standing posture change. Gender was associated with significant alterations in the magnitude of postural change in HR and SpO₂, with females having a smaller increase in HR during the supine-to-standing posture change ($P < 0.01$) and a small increase, rather than a decline, in SpO₂ at the recovery supine position, as compared to the initial supine position ($P < 0.01$) (see Table 5.3).

5.2.3 Correlations Between Parameters

DCS measurements of *rCBF* correlated weakly, but highly significantly, with DOS measurements of *THC* ($R = 0.25$, $P = 0.008$), *HbO₂* ($R = 0.30$, $P = 0.002$) and *HbDiff* (R

= 0.30, $P = 0.002$) during the supine-to-standing posture change. DCS measurements of $rCBF$ did not correlate with DOS measurements of Hb ($R = 0.045$, $P = 0.64$).

Mean supine-to-standing changes in $rCBF$ were significantly associated with mean changes in SBP ($R = 0.30$, $P = 0.02$). Postural changes in frontal cortical $rCBF$, THC , HbO_2 , and Hb were not associated with any of the other systemic hemodynamic parameters during the supine-to-standing position change.

5.3 Discussion

This study provides new insights into the effects of healthy aging on cerebral hemodynamic responses to posture change. The main finding of the study is that healthy aging alters the magnitude of change in frontal cortical HbO_2 , but not $rCBF$, THC , or Hb during supine-to-standing posture change. This age effect was found to be continuous, not one that only becomes significant at the extremes of age. We also demonstrated that posture change significantly alters frontal cortical $rCBF$, THC , HbO_2 , and Hb across the age continuum. This study also provides the largest cohort of normative optical data on postural hemodynamic changes in a healthy population, which can serve as a reference for comparative analysis in clinical, particularly brain-injured, populations.

The absence of an age-related effect on the magnitude of postural changes in $rCBF$ suggests that aging is not associated with a decline in global autoregulatory function, or more specifically, a decline in the autoregulatory capacity of the anterior cerebrovascular circulation. However, we did demonstrate that aging attenuates the magnitude of frontal

cortical HbO_2 decline during supine-to-standing position change, a finding that is consistent with DOS measurements of postural HbO_2 changes from a recent CA aging study by Kim *et al* [122]. The incongruity between age-related postural changes in $rCBF$ and HbO_2 may be partly explained by considering prior studies that demonstrate an age-dependent decrease in baseline CBF [145, 126]. Although our optical instrument does not measure absolute changes in CBF, our observation that there is no age effect on postural changes in relative CBF, when considered in the context of a higher baseline CBF in younger subjects, suggests that there are age-dependent changes in absolute CBF with posture change. Specifically, one would expect a larger absolute decline in CBF during supine-to-standing posture change in younger as compared to older subjects. Assuming no change in frontal cortical oxygen metabolism with posture change [170], a larger magnitude of decline in absolute frontal CBF during supine-to-standing posture change may be expected to cause a statistically significant, but clinically insignificant, increase in the magnitude of decline in frontal HbO_2 in young subjects.

Another possible explanation for the incongruity between age-related postural changes in $rCBF$ and HbO_2 is that there are age-dependent effects on shunting of blood around the circle of Willis during posture change. Indeed, a redistribution of cerebral perfusion to the posterior circulation during supine-to-head-up tilt posture change has been demonstrated across the age spectrum [246]. Furthermore, there is TCD evidence that posterior circulation, but not anterior circulation, autoregulatory function is compromised in older subjects [93, 218], suggesting that older subjects may be less able to redirect perfusion from the

anterior to the posterior circulation during posture change.

Other potential explanations for the difference between age-related postural changes in $rCBF$ and HbO_2 , such as age-related postural changes in frontal cortical metabolic rate or arterial oxygen saturation, are less likely. With regard to the former, there is no evidence to suggest that frontal cortical metabolic rate is altered by posture change even independent of age. Rather, positron emission tomography experiments have shown that increased metabolism occurs primarily in the cerebellum, visual cortex and midbrain in subjects standing still with eyes open, not in the frontal lobe cortex [170]. Indeed, we might have expected to observe an age effect on postural changes in Hb , independent of any change in THC , if there were an age-related postural change in frontal cortical metabolic rate. By contrast, we observed statistically significant declines in THC and increases in Hb during the supine-to-standing posture change that were similar for all subjects across the age continuum. With regard to the possibility of age-related changes in arterial oxygen saturation, our pulse oximetry data did not demonstrate any age-related effect on postural changes in SpO_2 ($P = 0.44$).

An implication of the observed incongruity between age-related postural changes in $rCBF$ and HbO_2 is that the hybrid diffuse optical technique provides an advantage over using DOS alone for cerebral hemodynamic monitoring because DOS measurements of HbO_2 are not adequate surrogates for DCS measurements of $rCBF$. This point is underscored by our correlation analyses, which demonstrated that $rCBF$ only weakly correlated with changes in HbO_2 ($R = 0.30$, $P = 0.002$), $HbDiff$ ($R = 0.30$, $P = 0.002$) and THC

($R = 0.25$, $P = 0.008$) during the supine-to-standing posture change. Although these correlations were statistically significant, the relatively low R -values indicate that microvascular $rCBF$ responses are only partially explained by HbO_2 and THC responses. Similar findings were observed in a recent study by Schytz *et al* [204] in which calculation of a blood flow index using continuous wave DOS in conjunction with an intravenous tracer did not correlate with ^{133}Xe -SPECT measurements of CBF in a healthy population ($R = 0.133$, $P = 0.732$).

The physiological basis for the weak correlations between DCS and DOS measurements in healthy populations is not completely clear, but discrepancies are certainly expected in clinical populations for whom perturbations in cortical metabolic rate, intracranial pressure, arterial inflow, or venous drainage complicate the relationship between CBF and oxygenation. Indeed, absent or weak correlations between postural changes in frontal cortical $rCBF$ and THC have previously been demonstrated in acute ischemic stroke patients ($R = 0.11$, $P = 0.3$) [59], as well as traumatic brain injury and aneurysmal subarachnoid hemorrhage patients ($R = 0.3$, $P = 0.01$) [120]. These data suggest that DCS measurements of microvascular $rCBF$ cannot be predicted by DOS measurements of microvascular THC or HbO_2 in either healthy or clinical populations. The DCS/DOS hybrid optical technique thus may provide a more comprehensive assessment of cerebral microvascular hemodynamics than can be obtained by using DOS alone.

An unexpected finding in this study was the relatively large magnitude of the mean decline in $rCBF$ during supine-to-standing posture change across the age continuum (25.9%

$\pm 1.5\%$). Notably, none of our subjects experienced pre-syncopal symptoms upon standing, and the 95% confidence interval of the postural $rCBF$ decline (23.3 to 28.8%) does not approach the 40% threshold that is associated with onset of pre-syncopal symptoms in healthy young and healthy old subjects [69]. While there are no prior DCS studies of healthy subjects to which our data can be compared, TCD studies have found declines in MCA CBF velocity ranging from 15 to 20% in healthy subjects during orthostatic stress [26, 132, 218].

In addition, Kim *et al* [122] observed an MCA blood flow velocity decline of 16 to 29% immediately following a supine-to-standing posture change, though this decline was attenuated to 6 to 15% after 5 minutes of standing. Alperin *et al* [5] observed a 12% average decline in global CBF using a vertical gap MRI during supine-to-sitting posture change in ten healthy subjects (average age 39 years old). Though this magnitude of CBF change is smaller than the supine-to-standing $rCBF$ change observed in our study, one would expect that standing causes a larger CBF decline than sitting since venous return of blood to the heart is more compromised in the standing position. It should also be highlighted that our data pertain only to frontal cortical CBF, and there may be regional variations in CBF that contribute differently to the overall effects of posture on global perfusion. Finally, the magnitudes of frontal cortical HbO_2 change ($-3.4 \mu\text{M} \pm 0.3 \mu\text{M}$) and Hb change ($0.8 \mu\text{M} \pm 0.1 \mu\text{M}$) during supine-to-standing posture change found in our DOS measurements are consistent with data from prior DOS studies [149, 148], suggesting that our optical instrumentation protocol was not systematically flawed.

Table 5.4: Comparisons between "young" cohorts in the present study, Mehagnoul-Schipper *et al* (2000) and Tachtsidis *et al* (2004).

Variable	Study cohort	Mehagnoul-Schipper <i>et al</i> (2000)	Tachtsidis <i>et al</i> (2004)
<i>Baseline characteristics and systemic hemodynamics</i>			
<i>N</i>	10	10	10
Gender	4M, 6F	4M, 6F	8M, 2F
Age, <i>years</i>	27.1 ± 7.2	27.1 ± 6.9	24 ± 6
Age range, <i>years</i>	22 to 45	22 to 45	Not provided
BMI, <i>kg/m²</i>	23.4 ± 3.2	21.9 ± 3.2	Not provided
SBP, <i>mmHg</i>	110 ± 15	118 ± 7	Not provided
DBP, <i>mmHg</i>	70 ± 10	77 ± 6	Not provided
HR, <i>bpm</i>	71 ± 13	61 ± 7	Not provided
<i>Supine-to-standing changes in DOS measurements</i>			
ΔTHC , μM	-3.1 ± 1.3	0.2 ± 4.9	1.0 ± 2.93
ΔHbO_2 , μM	-3.9 ± 1.1	-1.2 ± 5.4	-0.57 ± 1.96
ΔHb , μM	0.7 ± 0.3	1.4 ± 2.4	Not provided

In order to further evaluate the validity of our optical instrumentation, we performed a post hoc comparative analysis of our DOS measurements with those of two prior DOS studies. We selected the ten "young" subjects from our study population whose average age (27.1 years) and age distribution (22 to 45 years) best match the ages of the young cohorts in the Mehagnoul-Schipper *et al* [149] and Tachtsidis *et al* [226] studies. The cohorts from the three studies had similar average BMI (21.9-23.4 kg/m²), SBP (110-118 mmHg), DBP (70-77 mmHg) and HR (61-71 bpm). The supine-to-standing postural changes in the DOS measurements of ΔTHC , ΔHbO_2 , and ΔHb in our study had distributions that were broadly overlapping with all of the DOS measurements performed in the other two studies except for the ΔHbO_2 changes found by Tachtsidis *et al* [226] (see Table 5.4). While the results from our study are generally consistent with these prior DOS data, two possible explanations for the small differences may be that the duration of time at each posture varied between the studies, and the source-detector separation for our study was 2.5 cm,

whereas Mehagnoul-Schipper *et al* [149] and Tachtsidis *et al* [226] utilized source-detector separations of 5.5 cm and 5 cm, respectively.

The observed 25.9% decline in $rCBF$ is partly attributable to the significant decline in $EtCO_2$ that was found with postural change across the age spectrum, consistent with previous studies of $EtCO_2$ changes during orthostatic stress [26]. Assuming that CBF changes by approximately 2-4% for every mmHg change in $EtCO_2$ [215], an $rCBF$ change of 4-8% would be expected from the $2.0 \text{ mmHg} \pm 0.3 \text{ mmHg}$ mean decline in $EtCO_2$ that was found in our study population. Also contributing to the large postural decline in $rCBF$ is the presumed decline in cerebral perfusion pressure, despite the increase in MAP that was measured at the level of the heart. As demonstrated by Harms *et al* [89], even when MAP measured at the level of the heart remains constant or increases slightly in healthy subjects during supine-to-standing posture change, the calculated MAP at the level of the MCA declines by an average of 19 mmHg after 1 minute, and 14 mmHg after 5 minutes. Meanwhile, the postural decline in intracranial pressure is likely smaller [5], suggesting that the overall effect of supine-to-standing posture change in healthy subjects is a decrease in cerebral perfusion pressure.

We also found significant differences between all cerebral and systemic hemodynamic parameters, except Hb , SpO_2 and $EtCO_2$, at the initial supine position as compared to the recovery supine position. In a post hoc analysis we examined the Pearson's correlation between cerebral hemodynamic parameters at the two supine positions. This analysis indicated strong correlations ($R = 0.67-0.76$, $P < 0.05$) for all of the cerebral hemodynamic

parameters at the two supine positions, suggesting good reproducibility of the DCS/DOS measurements. These strong correlations are expected given that the light paths of DCS and DOS are similar. Durduran *et al* [59] recently found a similarly high degree of reproducibility in repeated measurements at the supine position in a population of acute ischemic stroke patients using the same DCS/DOS apparatus. The significant differences in cerebral hemodynamics at the two supine positions are therefore likely physiological in nature, not due to instrument error. A plausible physiological mechanism that explains these findings is an "overshoot phenomenon," whereby cerebral perfusion, blood volume and oxygenation all increase transiently when the subject transitions to the supine position from standing. It is likely that if we had observed our subjects for longer than 5 minutes at the recovery supine position, $rCBF$, THC and HbO_2 would have ultimately trended down to the levels observed at the initial supine position.

The systemic hemodynamic responses to posture change observed in this study are in general agreement with previous studies showing that aging significantly alters changes in HR, but not MAP, DBP or SBP, during posture change [111, 149]. Our finding that only SBP correlated strongly with changes in $rCBF$ during the supine-to-standing posture change differed from the correlations between postural changes in HbO_2 and Hb , and DBP and HR, found by Mehagnoul-Schipper *et al* [149]. A possible explanation for this difference is that the standard error of the mean was quite low for the baseline SBP of our study population, suggesting that our older subjects may have been healthier than the older subjects in the Mehagnoul-Schipper *et al* [149] cohort. Additionally, whereas Mehagnoul-

Schipper compared 18 subjects over 70 years old to 10 subjects under 45 years old, our study included only one subject over 70 years of age.

The observed gender effect on several of the cerebral and systemic hemodynamic parameters was a finding for which we did not generate an a priori hypothesis. We included gender effects in our statistical model in order to ensure that any effects we observed for age were independent of gender effects. We are not aware of prior studies of the effect of gender on cerebral hemodynamic postural changes in a healthy population. It is possible that differences in behavior between the men and women in our study population, such as frequency of exercise, may have affected our cerebral and systemic hemodynamic measurements. We consider our observation of gender effects on postural hemodynamic responses to be a finding that may form the basis for hypothesis generation in future investigations of cerebral hemodynamics.

An important technical consideration relating to our optical instrumentation protocol is that we used the same DPF value in DOS measurements for all subjects. Prior DOS aging studies have similarly utilized an age-independent DPF [149, 148, 226], yet Duncan *et al* [52] have shown that the DPF may change as a function of age. We therefore performed a post hoc analysis to determine whether the utilization of age-specific DPFs from the Duncan *et al* [52] study would alter our results. For our youngest subject (20 years old), DPFs of 6.06 and 5.39 were used for the 690 nm and 830 nm wavelength calculations. For our oldest subject (78 years old), DPFs of 7.62 and 6.87 were used. The postural changes in HbO_2 and Hb that were calculated for our oldest and youngest subject using these age-

specific DPFs all had error bars that included the postural changes that were calculated with our standard DPFs of 6.51 (at 690 nm) and 5.86 (at 830 nm). It therefore appears that the utilization of age-specific DPF values would have had little substantive effect on our results and would have made it difficult to compare our findings with prior DOS studies that used age-independent DPF values.

Another technical consideration in optical studies of cerebral hemodynamics is variability in skull thickness and cerebrospinal fluid (CSF) layer thickness between subjects. Okada and Delpy [168] demonstrated with a Monte Carlo simulation model that variations in skull thickness and CSF layer thickness may alter the DOS detection volume. In analyzing our results to derive physiological property variations, we have assumed that the interrogated brain tissue volumes are determined solely by tissue optical properties and are not age or gender dependent. We do not believe that skull thickness is a factor for our measurements or conclusions. Skull thickness has been shown to vary randomly between subjects in an age-independent and gender-independent manner [137] and would not therefore be expected to confound an analysis of age-related postural changes in the optical signal. On the other hand, cerebral cortex thickness has been shown to decrease [199, 185] and CSF layer thickness to increase [161, 84] as a function of age-related cerebral atrophy. Similarly, gender may also affect the scalp-to-brain distance, with women being found to have smaller age-related changes in intracranial CSF volume and left hemispheric atrophy than men [84]. Finally, intracranial CSF volume may change during posture changes [5].

From an experimental standpoint, serial radiological imaging of all subjects at different

postures to determine inter-subject or postural variations in skull and CSF layer thickness is impractical. Thus, it is extremely difficult to discern whether a substantive systematic error in our study could have been introduced by these age-, gender- or posture-related detection volume physiological changes. Nevertheless, we expect the effects of these potential methodological errors to be ameliorated by the fact that each subject effectively acted as his or her own control. The importance of absolute detection volume is reduced because we are probing the relative changes in cerebral hemodynamics in the same volumes at different postures. As a result, many of the random physiological effects that modify the absolute optical signals are self-normalized. We therefore believe that the present study, as with other optical studies, is accurate to within the methodological limitations of diffuse optics [96].

Another consideration in optical measurements of cerebral hemodynamics is the possibility of extracranial blood flow influencing the optical signal. Our analysis implicitly assumes that measured differential signals are due only to cortical tissue responses. With our present probe-pad configuration, we believe that there is substantial evidence to suggest that the potential effects of scalp blood flow are minimal. Previous studies performed by our laboratory with the same probe apparatus and source-detector separation have validated DCS measurements of $rCBF$ in critically ill adults using an established tool for measuring CBF, Xenon-CT [120], and have demonstrated in acute stroke patients that postural changes in $rCBF$ differ significantly between the infarcted and non-infarcted cerebral hemispheres [59]. Postural changes in scalp blood flow, which would be expected to be similar on

the left and right sides of the head, cannot account for this observed association between the presence of infarction and unilateral alterations in postural $rCBF$ changes. Together, these studies performed in clinical populations indicate that DCS investigates cortical CBF despite potential confounding by scalp blood flow changes.

It should also be noted that our optical instrumentation protocol was designed to provide an assessment of postural changes in cerebral hemodynamics, not an assessment of static or dynamic CA. Static CA is measured by comparing CBF at two steady states after an isolated change in MAP. Dynamic CA has been quantified using a variety of different methodologies, such as by measuring the degree to which acute manipulations in MAP impact CBF, the speed with which CBF returns to baseline after a change in MAP, or the transfer function between spontaneous oscillations in MAP and oscillations in CBF [236]. In contrast to static CA or dynamic CA protocols, our posture change protocol produced additional physiological changes in HR, SpO₂, and EtCO₂, not just changes in MAP. We chose this protocol because posture change is an intervention that is commonly performed to alter cerebral perfusion in the clinical setting, and we specifically aimed to provide a normative data set for comparative studies between healthy populations and clinical populations.

5.4 Conclusion

In summary, this study suggests that healthy subjects across the age spectrum experience significant postural declines in frontal cortical $rCBF$ but that aging does not alter the

magnitude of this postural $rCBF$ decline. We demonstrated that hybrid diffuse optics can be readily used for studying healthy populations in natural postures, and that DCS provides cerebral hemodynamic data that cannot be obtained from DOS measurements alone. Our optical data also provide normative values of frontal cortical microvascular hemodynamics across the age spectrum, to which pathological values can be compared in future studies of brain-injured populations.

Chapter 6

Use of DOS/DCS in the Neurocritical Care Unit

Severe brain injury can profoundly disturb cerebrovascular autoregulation and neuronal metabolism [242, 45, 214, 49, 97]. Over 17% of the estimated 1.5 million people who sustain a traumatic brain injury (TBI) each year in the United States are hospitalized, and the direct and indirect costs for TBI patients totaled approximately 60 billion dollars in 2000 [128, 68]. In addition, more than 27,000 people in the United States suffer aneurysmal subarachnoid hemorrhage (SAH) each year, and about 40% of hospitalized patients die within 1 month of admission [107, 175, 198].

Importantly, the extent of secondary injury, more so than that of the primary injury, can play a crucial role in ultimately determining outcome [32, 31, 114, 40, 82]. After the initial ictus, patients are susceptible to secondary injuries whose pathophysiology often involves

disturbed autoregulation. Thus, cerebral oxygenation and intracranial pressure monitoring is commonly performed in neurointensive care units to facilitate diagnosis and treatment of secondary injuries in severely brain-injured patients.

In TBI patients, post-traumatic edema and contusion expansion often leads to intracranial hypertension and a subsequent drop in cerebral blood flow (CBF); SAH patients are at risk of rebleeding and vasospasm, both of which can lead to cerebral ischemia, edema, and intracranial hypertension [203, 179, 108, 227, 11]. Current modalities for continuous monitoring of intracranial pressure (ICP) and cerebral perfusion pressure (CPP) require invasive introduction of pressure transducers into the brain parenchyma or lateral ventricles. Though these invasive ICP monitors provide a surrogate measurement of CBF, non-invasive continuous bedside monitors of CBF are lacking. Existing techniques for measuring CBF in patients include [¹⁵O]-PET, single photon emission computed tomography (SPECT), gadolinium-enhanced perfusion magnetic resonance imaging (MRI), and arterial spin labeled bolus tracking perfusion MRI (ASL-MRI). All of these techniques require the patient to be transported within the hospital, an activity which can be difficult or even dangerous to the patient [221, 134, 256].

Xenon-enhanced computed tomography (Xenon-CT) has recently become more transportable to patient rooms, but is not a continuous CBF measure [256, 35, 51]. Two more portable techniques are currently used to monitor CBF continuously at the bedside. Transcranial Doppler (TCD) ultrasonography is a valuable tool, but its capabilities are limited to observing large vessel behavior, which is not always an accurate surrogate for microvas-

cular perfusion [221, 159]. Thermal diffusion flowmetry (TDF) has also been gaining popularity in neuro-intensive care units [235, 195, 211]. The drawback of TDF is that, like intracranial pressure monitors, it is an invasive tool that needs to be placed into the brain parenchyma. Thus, a continuous, non-invasive monitor of microvascular cerebral blood flow is still lacking in the neuro-intensive care unit.

In this study, we evaluated the clinical utility of DOS and DCS in patients with severe brain injury by validating DCS measurements of CBF with Xenon-CT, and DOS measurements of cerebral oxygenation with invasive Licox monitors. We hypothesized that changes in CBF and oxy-/deoxyhemoglobin concentration during head-of-bed manipulations, induced hyperoxia, and pressor administration would be non-invasively detected by our hybrid DCS/DOS optical instrument, and that DCS/DOS measurements would correlate with simultaneous measurements of CBF, PbtO₂ or ICP by other techniques.

Brain-injured patients are a particularly challenging clinical population because of their heterogeneous condition and susceptibility to secondary injury. To support the use of our hybrid diffuse optical monitor for such a population, we have included in this paper a study of validation against xenon-CT during a blood pressure challenge. After comparison with xenon-CT, we began assessment of the applicability of the optical instrument to measure changes in CBF and oxygenation in patients during change of head elevation and during induced hyperoxia. These two interventions are commonly used in the critical care unit, often invoking a large response in patient hemodynamics as seen by current invasive monitors. Throughout the study, we hypothesize that the novel diffuse optical devices will

provide continuous, non-invasive CBF and oxygenation information for this population at the bedside.

6.1 Head-of-Bed Manipulation

It is common clinical practice in the neurocritical care unit to manipulate patient head-of-bed angle as a strategy for altering intracranial pressure (ICP) and cerebral perfusion [60, 64]. The efficacy of head-of-bed manipulation for improving cerebral blood flow (CBF), however, is not well-understood. Reduction of ICP does not always lead to an increase in cerebral perfusion pressure (CPP) [60, 255, 193, 160, 67], and even when CPP increases with head elevation, the link between CPP and CBF can depend on head-of-bed-position [160] and cerebrovascular resistance [43]. This complex relationship between ICP, CPP and CBF may explain why no single optimal CPP has been defined for the severely brain-injured patient [243], and why ICP- and CPP-targeted interventions sometimes fail to improve outcome [115, 33, 41]. Since recovery of neurological function may depend more directly on tissue perfusion [171] than on ICP or CPP, it is desirable to develop new tools that directly measure CBF in the neurocritical care unit.

The current lack of understanding about the relationship between head-of-bed position and CBF is largely attributable to the absence of an effective and convenient method for measuring CBF at the bedside. Conventional imaging techniques capable of measuring perfusion such as computed tomography (CT), positron emission tomography (PET), and magnetic resonance imaging (MRI), are mainly suited for imaging in prone or supine

positions, do not offer the possibility for continuous measurement of CBF, and are often unfeasible for single time-point perfusion measurements in clinically unstable patients. Similarly, current "bedside" techniques for monitoring CBF, which include transcranial Doppler (TCD) ultrasonography [63], thermal diffusion [235], and laser Doppler flowmetry [124], have significant limitations. TCD ultrasonography measures large vessel flow velocities that do not necessarily reflect microvascular perfusion [184], and although thermal diffusion and laser Doppler flowmetry monitor microvascular perfusion, routine use of these techniques is limited by their invasive nature.

Diffuse correlation spectroscopy (DCS) is a novel optical technique for probing continuous changes in regional microvascular blood flow. DCS utilizes non-invasive near-infrared light sources and detectors to track rapid temporal fluctuations of light intensity in brain tissue that arise when light is scattered by moving red blood cells. The method derives a blood flow index (*BFI*) from these intensity fluctuations whose trends have been shown to correlate well with blood flow in both animals [150, 54, 260, 225, 264, 27, 156] and humans [120, 24, 191, 58, 261, 265]. This *BFI* is readily used to calculate relative CBF (*rCBF*), i.e. blood flow variation relative to a baseline measurement. Validation of DCS-measured *rCBF* in adult patients with severe brain injury has been carried out with concurrent xenon-enhanced CT during induced manipulations of blood pressure and arterial CO_2 [120]. In addition, CBF responses during head-of-bed manipulation have been studied with DCS in both healthy [61] and ischemic stroke populations [59, 155]. In these early studies, DCS was combined with a more established optical technique called near-

infrared spectroscopy (NIRS), also known as diffuse optical spectroscopy (DOS). DOS uses wavelength-dependent light attenuation to measure concentration changes in oxyhemoglobin (ΔHbO_2), deoxyhemoglobin (ΔHb), and total hemoglobin (ΔTHC) concentrations. Our hybrid optical instrument employs both techniques concurrently.

The primary aim of the present study is to use DCS/DOS to measure cerebral hemodynamic changes in severely brain-injured patients during a simple clinical intervention: head-of-bed lowering. Importantly, this patient group is different from those in the previous clinical studies of head-of-bed positioning described above. We compare postural CBF responses in brain-injured patients to those of healthy subjects, and we assess posture-induced correlations of DCS-measured $rCBF$ and DOS-measured ΔHbO_2 , ΔHb , and ΔTHC versus other measured parameters such as ICP and CPP. Among other expectations, we hypothesized that continuous optical monitoring during head-of-bed lowering would reveal differences in postural $rCBF$ in the brain-injured patients versus the controls. Note that this section is based on a paper that has been accepted for publication in clinical journal *Neurocritical Care* [121].

6.1.1 Methods

All subjects in the brain-injured cohort were adults (≥ 18 years) receiving care in the neurointensive care unit at the Hospital of the University of Pennsylvania for subarachnoid hemorrhage or traumatic brain injury. Each study was performed at the patient bedside using protocols approved by the Institutional Review Board at the University of Pennsylvania.

Written consent was provided by the subject (if able) or by a surrogate.

Comparison data in healthy controls was obtained from a previous study that included optical monitoring of head of bed positioning on 60 healthy volunteers [61]. Adult subjects were included in the healthy cohort if they had no history of hypertension, diabetes mellitus, hyperlipidemia, atrial fibrillation, congestive heart failure, coronary artery disease, previous myocardial infarction, prior stroke or transient ischemic attack, carotid artery disease, smoking within the past 5 years, pulmonary disease, renal disease, or recent administration of vasoactive medications. Subjects were chosen to be gender-matched, since we previously found gender (but not age) to have an effect on frontal cortical hemodynamics during posture change [61]. Written informed consent was provided by all control subjects, and the controls were studied at the Hospital of the University of Pennsylvania with protocols approved by the Institutional Review Board.

Optical Instrumentation. The optical instrument was a custom-built, hybrid device containing both DCS and DOS modules (see Section 3.1.1). The DCS module uses two long-coherence-length, continuous-wave 785 nm lasers (CrystaLaser Inc., Reno, NV), two 4-channel avalanche photodiode arrays (Perkin Elmer, Canada) for single-photon detection, and an 8-channel multi-tau autocorrelator board (Correlator.com, Bridgewater, NJ) to compute the temporal intensity autocorrelation functions. The homodyne, frequency-domain DOS module employs three laser sources with wavelengths 685, 785, 830 nm, as well as two photomultiplier tubes for light detection. A single frame of DCS data was acquired every 6 s, followed by a 1 s DOS data collection interval. The data acquisition

rate was therefore one frame of DCS + DOS every 7 s. Both modalities employ optical fibers that affix to a black foam probe pad with source-detector separations of 2.5 cm. This separation distance ensures that light can penetrate to depths below the tissue surface of approximately 1.0 to 1.5 cm, a depth sufficient for light to reach the surface region of the adult human cortex [120, 57]. Further theoretical and technical details about diffuse optics can be found in recent reviews [55, 154, 157].

DCS data analysis employs a physical model to extract an index of local, microvascular relative blood flow and has been previously described [142, 177, 16]. All optical data were reviewed for motion artifacts prior to analysis, and epochs of data were excluded from further analysis, if excessive noise produced low-confidence values of the *BFI*. For DOS analysis, changes in ΔHbO_2 , ΔHb , and ΔTHC were calculated using a modified Beer-Lambert law that utilized changes in signal amplitude attenuation at each wavelength, as well as the subject's age-dependent differential path length factor [52]. Complete details about DCS and DOS analyses have been previously published [15, 34].

Optical Protocol during Head-of-Bed Manipulation. Most often, two optical probes were affixed to both sides of the forehead equidistant from the midline, in order to measure hemodynamic changes in the frontal poles of the left and right hemispheres. Note, two of the early patients provided unilateral data only as a result of restrictions in optical probe size; later versions were more compact, and thus bilateral probes were used. For the unilateral measurements, a probe was placed on either the left or the right side of the forehead.

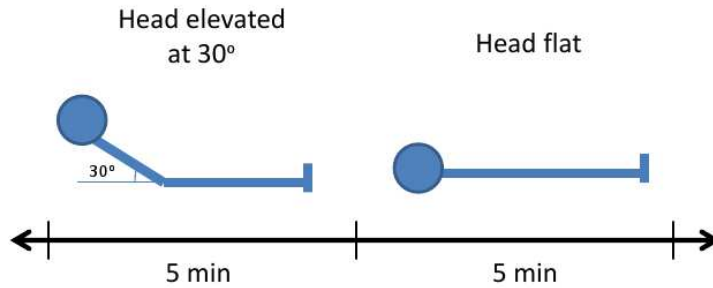


Figure 6.1: Protocol for head-of-bed manipulation. The subject starts at a baseline head-of-bed elevation of 30° for 5 minutes. Then the head-of-bed is lowered flat over a period of 30 seconds, and the subject rests supine for another 5 minutes.

During the measurements, a black opaque cloth was placed over the probes to shield them from ambient light. Once adequate optical signal was confirmed, continuous measurements of $rCBF$, ΔHbO_2 , ΔHb , and ΔTHC were made. The head-of-bed intervention protocol is depicted in Figure 6.1. The subject was initially positioned at a baseline head-of-bed elevation of 30° , wherein he/she rested quietly and still for 5 minutes. The head-of-bed was then lowered to the supine position (0°) over a period of 30 seconds, and the subject rested there for another 5 minutes. For the brain-injured patients, this intervention was repeated consecutively up to three times, and in order to examine longitudinal changes in frontal lobe hemodynamic response, for up to three measurement episodes usually on consecutive days. Data from these multiple days were averaged. The healthy subjects were monitored on a single day, all bilaterally, with the 30° -to- 0° protocol performed once.

Monitoring of ICP, CPP and PbtO₂ in Brain-Injured Patients. Cerebral and systemic physiological parameters were monitored as part of routine care for patients in the neurocritical care unit. ICP was monitored either by an external ventricular device or using

a fiberoptic intraparenchymal catheter (Camino-MPM1; Integra LifeSciences, Plainsboro, NJ). ICP transducers were zeroed at the level of the tragus. CPP was then calculated as the difference between mean arterial pressure (MAP) and ICP. Prior to study enrollment, select patients underwent placement of a continuous brain tissue oxygen partial pressure (PbtO₂) monitor (Licox®CMP; Integra LifeSciences, Plainsboro, NJ) at the discretion of the treating clinician. The PbtO₂ monitor consisted of a polarographic Clark-type electrode inserted into cerebral white matter.

Monitoring of MAP and Heart Rate (HR) in Brain-Injured and Control Subjects. In brain-injured subjects, MAP and HR were measured continuously via a radial arterial-line that was zeroed at the phlebostatic axis throughout the study. In healthy controls, continuous measurements of MAP and HR were monitored using a non-invasive plethysmographic device (Finapres Medical Systems, Finometer Pro Model 1; Amsterdam, The Netherlands) whose probe was secured to each subject's right third finger. An adjustable armrest was used to keep the subject's right third finger at the level of the heart at each head-of-bed position.

Statistical Analysis. Mean changes in each cerebral and systemic physiological parameter due to head lowering were computed from continuous time-series data by taking the average ($\langle \rangle$) during the 5-minute time period (t_{30°) at head-of-bed 30° as baseline for comparison against the 5-minute supine time period (t_{0°). Periods were defined as those data measured after the optical signal had stabilized, with all data during the head-of-bed transition and all motion artifacts excluded from the analysis. Differential values for DOS data

(ΔHbO_2 , ΔHb , ΔTHC) as well as for systemic vitals (HR, MAP, ICP, etc.) were defined as

$$\Delta Y = \langle Y(t_{0^\circ}) \rangle - \langle Y(t_{30^\circ}) \rangle, \quad (6.1)$$

with Y representing the parameter of interest. For DCS data, a percentage change from baseline was employed to compute $rCBF$:

$$rCBF = \frac{\langle rCBF(t_{0^\circ}) \rangle - \langle rCBF(t_{30^\circ}) \rangle}{\langle rCBF(t_{30^\circ}) \rangle}. \quad (6.2)$$

A two-tailed Student's t-test was used to determine whether the observed changes were different from zero, and a one-way ANOVA was used to test whether the cerebral hemodynamic responses of brain-injured patients differed from those of healthy subjects. When both left and right frontal pole data were available, a Pearson's coefficient was used to assess correlations between bilateral measurements of $rCBF$, ΔHbO_2 , ΔHb , ΔTHC . A Pearson's coefficient was also used to assess correlations between $rCBF$, CPP, and ICP. P-values less than 0.05 were considered to indicate statistical significance.

Table 6.1: Patient clinical characteristics.

No.	Gender	Age	Injury	SAH Severity	Study Day(s)	Admission GCS	Study GCS	Imaging Findings
1	M	28	ICH + SAH	N/A	2,3	7	7,8	Arteriovenous malformation-associated left temporal ICH with SAH
2	M	58	TBI	N/A	11,13	15	3,5	Acute traumatic SAH, left subdural hemorrhage, and hemorrhagic contusion
3	F	52	SAH	HH2/F3+4	12,13	14	10,11	Left PCA aneurysm, diffuse vasospasm
4	M	40	SAH	HH3/F4	8,9,10	7	7,7,3	ACOMM aneurysm, intraventricular hemorrhage, left MCA/ACA vasospasm
5	M	60	TBI	N/A	2,3	3	3,4	Bilateral frontal and temporal contusions, multiple frontoparietal parenchymal hemorrhages
6	M	51	TBI	N/A	4,6	14	6,7	Contusions in bilateral frontal and left temporal lobes, traumatic SAH, parenchymal hemorrhage in frontal lobes
7	F	62	SAH	HH1/F3	9	15	8	Right MCA aneurysm, bilateral ACA and right MCA vasospasm
8	M	18	TBI	N/A	2	3	7	SAH along right cerebral convexity, subdural hemorrhages along bilateral frontal convexities
9	M	46	SAH	HH1/F3+4	9	14	6	ACA and left anterior choroidal artery aneurysms, diffuse vasospasm (right > left hemisphere)
10	F	44	SAH	HH4/F3+4	8	4	10	Posterior inferior cerebellar artery aneurysm, vasospasm of distal vertebral arteries bilaterally

ICH, intracerebral hemorrhage; TBI, traumatic brain injury; SAH, subarachnoid hemorrhage; GCS, Glasgow Coma Score; HH, Hunt-Hess Score; F, Fisher Grade; N/A, not applicable; MCA, middle cerebral artery; ACA, anterior cerebral artery; PCA, posterior cerebral artery; ACOMM, anterior communicating artery

6.1.2 Results

Patient and Control Characteristics. Table 6.1 summarizes all clinical and study data for the brain-injured cohort. A total of ten patients (seven males/ three females) were included in the study, with a mean age of 46 years (range, 18-62 years). Five patients were admitted for subarachnoid hemorrhage (SAH) due to ruptured aneurysm, four for traumatic brain injury (TBI), and one for an arteriovenous malformation (AVM)-associated intracerebral hemorrhage (ICH) and SAH. For the TBI patients, the median admission Glasgow Coma Scale (GCS) [229] score was 9 (range, 3-15), while the median study day GCS score was 5 (range, 3-7). For the aneurysmal SAH patients, the Hunt Hess classification grade [104] was 1 (n=2), 2 (n=1), 3 (n=1), or 4 (n=1). The timing of optical data acquisition for the patient cohort ranged from post-injury day 2 to 12 and the GCS score for patients on the day of data acquisition ranged from 3 to 11. One patient was studied on 3 separate occasions, five patients on 2 occasions, and four patients were studied once. Data from all episodes of measurements were included in analysis. ICP was monitored for all patients (seven via external ventricular drain, three via intraparenchymal catheter), and eight patients had a brain tissue oxygen monitor in place during the study. The mean age for the ten healthy controls was 39 years (range, 24-55 years; seven males/ three females).

Physiologic Responses to Head-of-Bed Manipulation. For the brain-injured cohort, ICP changed significantly ($P = 0.002$) as the head-of-bed was lowered from 30° (11.2 ± 4.3 mmHg) to 0° (16.8 ± 9.5 mmHg), but CPP, PbtO₂, MAP and HR did not. Measurements of ICP, CPP, PbtO₂, MAP and HR in the brain-injured cohort at each head-of-bed position

Table 6.2: Effects of head lowering on cerebral and systemic vitals in brain-injured cohort.

Parameter	Head-of-Bed Position		Change from 30° to 0°	P-value
	30°	0°		
ICP, <i>mmHg</i>	11.2 ± 4.3 (3.8 to 19.5)	16.8 ± 9.5 (3.3 to 49.7)	5.6 ± 8.1 (-8.1 to 30.2)	0.002
CPP, <i>mmHg</i>	95.1 ± 22.8 (59.9 to 136.6)	88.2 ± 25.5 (42.0 to 137.8)	-6.9 ± 12.9 (-44.5 to 23.3)	0.218
PbtO ₂ , <i>mmHg</i>	47.5 ± 35.0 (8.5 to 196.5)	37.1 ± 19.8 (19.4 to 101.6)	-10.4 ± 18.0 (-94.9 to 11.5)	0.142
MAP, <i>mmHg</i>	106.7 ± 23.4 (67.8 to 151.0)	105.0 ± 23.3 (64.0 to 144.3)	-1.8 ± 8.3 (-15.5 to 26.9)	0.738
HR, <i>bpm</i>	84.3 ± 19.5 (54.2 to 118.4)	85.9 ± 18.7 (56.0 to 121.0)	1.6 ± 4.2 (-6.0 to 15.9)	0.712

Values listed as mean ± SD, with range in parentheses; P-values from one-way ANOVA test.

Table 6.3: Effects of head lowering on systemic vitals in healthy cohort.

Parameter	Head-of-Bed Position		Change from 30° to 0°	P-value
	30°	0°		
SYS, <i>mmHg</i>	137.4 ± 11.4 (117.8 to 157.3)	134.6 ± 10.5 (113.3 to 144.9)	-2.8 ± 8.0 (-13.7 to 13.4)	0.581
DIA, <i>mmHg</i>	78.9 ± 9.9 (63.5 to 93.7)	75.8 ± 10.0 (58.5 to 86.7)	-3.0 ± 6.8 (-14.7 to 11.1)	0.505
MAP, <i>mmHg</i>	102.4 ± 9.8 (88.5 to 119.3)	99.4 ± 10.4 (83.9 to 112.2)	-3.0 ± 7.0 (-13.9 to 11.1)	0.513
HR, <i>bpm</i>	68.8 ± 9.6 (53.3 to 82.7)	68.5 ± 10.6 (50.9 to 82.2)	-0.2 ± 3.1 (-4.1 to 7.6)	0.957

Values listed as mean ± SD, with range in parentheses; P-values from one-way ANOVA test.

Table 6.4: Effects of head lowering on $rCBF$, ΔHbO_2 , ΔHb and ΔTHC in brain-injured versus healthy cohorts.

Parameter	Brain-Injured (n = 10)	Healthy (n = 10)	P-value [†] , Brain-Injured	P-value [†] , Healthy	Difference b/w Groups ^{††}
$rCBF$, %	0.3 ± 28.2 (-49.2 to 90.0)	18.6 ± 9.4 (2.1 to 34.0)	0.938	<0.001	0.006
ΔHbO_2 , μM	5.0 ± 4.5 (-6.3 to 14.2)	2.3 ± 1.8 (-0.2 to 5.3)	<0.001	<0.001	0.010
ΔHb , μM	1.3 ± 1.8 (-3.0 to 7.1)	0.5 ± 0.7 (-0.6 to 2.1)	<0.001	0.005	0.059
ΔTHC , μM	6.3 ± 6.0 (-9.3 to 20.4)	2.8 ± 2.0 (-0.2 to 7.4)	<0.001	<0.001	0.012

Values listed as mean ± SD, with range in parentheses; [†]P-values from two-tailed Student's t-test; ^{††}P-values from one-way ANOVA test.

are summarized in Table 6.2. None of the systemic vital signs, including HR and MAP, changed significantly for the healthy controls (Table 6.3).

The population-averaged DCS and DOS results for the healthy and brain-injured cohorts are reported in Table 6.4. Positional changes in $rCBF$ ($18.6\% \pm 9.4\%$, $P < 0.001$), ΔHbO_2 ($2.3 \mu M \pm 1.8 \mu M$, $P < 0.001$), ΔHb ($0.5 \mu M \pm 0.7 \mu M$, $P = 0.005$), and ΔTHC ($2.8 \mu M \pm 2.0 \mu M$, $P < 0.001$) all reached significance for the healthy controls, with head-of-bed lowering causing an increase in each physiological parameter. ΔHbO_2 , ΔHb and ΔTHC increased for the brain-injured group as well ($P < 0.001$); however, no net change in $rCBF$ was observed, and there was a large inter-subject variance ($0.3\% \pm 28.2\%$, $P = 0.938$). Figure 6.2 shows box plots comparing postural changes in $rCBF$ and ΔTHC between the two groups.

All optical parameters except for ΔHb showed a significantly different postural response between the patient and healthy groups ($P < 0.02$). The most marked difference was seen for CBF responses ($P = 0.006$). Correlation analysis of left versus right hemisphere

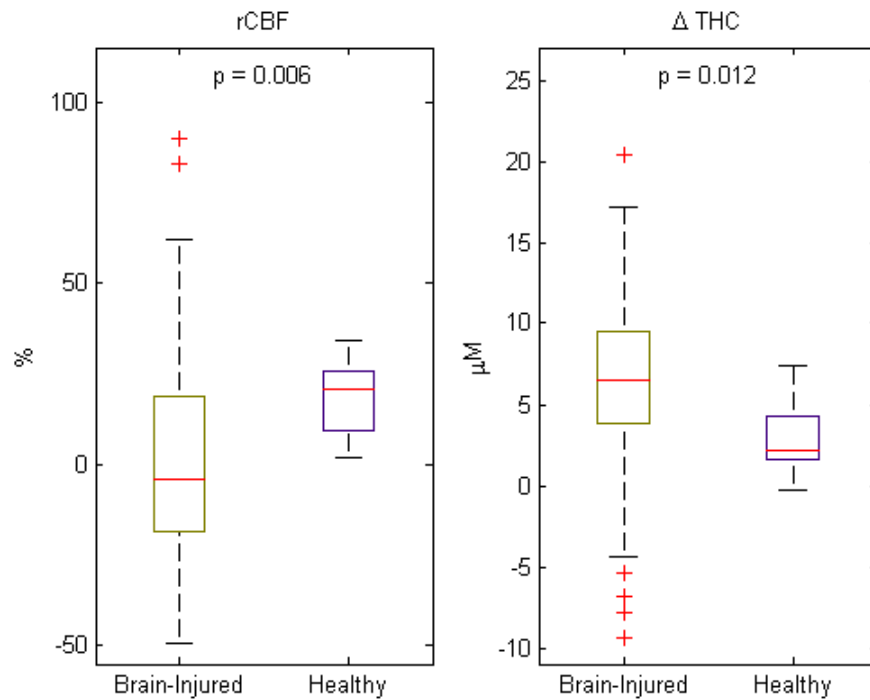


Figure 6.2: Box plots showing (left) DCS-measured relative cerebral blood flow ($rCBF$) and (right) DOS-measured total hemoglobin concentration changes (ΔTHC) in a group of brain-injured patients versus gender-matched healthy controls during a head-of-bed lowering. Note, the large spread of values around zero for the patient group is qualitatively different than the group response of the healthy subjects, e.g. a slight CBF increase. THC increases in both groups, with the patients' response again exhibiting significantly larger variance, and, on average, a greater magnitude.

responses to postural change also revealed a difference between the cohorts. Specifically, left and right frontal cortex measurements showed strong correlation in healthy subjects for $rCBF$ ($R = 0.94$, $P < 0.001$), ΔHbO_2 ($R = 0.85$, $P = 0.002$), and ΔTHC ($R = 0.75$, $P = 0.013$). In contrast, optical measurements in the left and right frontal lobe cortices did not correlate significantly for the brain-injured cohort ($rCBF$: $R = 0.27$, $P = 0.146$; ΔHbO_2 : $R = 0.22$, $P = 0.249$; ΔHb : $R = -0.04$, $P = 0.817$; ΔTHC : $R = 0.09$, $P = 0.639$).

We also observed a moderate but significant correlation ($R = 0.40$, $P < 0.001$) between change in CPP and $rCBF$, but no correlation with $rCBF$ was seen for ICP ($R = -0.15$, $P = 0.213$). Also, $PbtO_2$ did not correlate with any DOS parameters. While the magnitude (i.e. absolute value, disregarding sign) of $rCBF$ change was found to have a negative association with patient GCS score on the day studied ($R = -0.42$, $P < 0.001$), this was not the case for the DOS parameters (ΔHbO_2 : $R = -0.19$, $P = 0.118$; ΔHb : $R = -0.01$, $P = 0.907$; ΔTHC : $R = -0.18$, $P = 0.152$).

Similarly, as seen in Figure 6.3, $rCBF$ was the only parameter that could differentiate between SAH and TBI patients ($P = 0.008$). For patients with SAH (including the one with AVM), there was a difference between $rCBF$ responses measured on the side of ruptured aneurysm versus the contralateral side ($P < 0.001$). In comparison, there was no difference when comparing left and right $rCBF$ responses for TBI patients. Also, the number of days after injury inversely correlated with the absolute magnitude of $rCBF$ change with head lowering ($R = -0.30$, $P = 0.012$), but not with DOS parameters.

We present one case example of a 40-year-old male SAH patient (No. 4) studied over

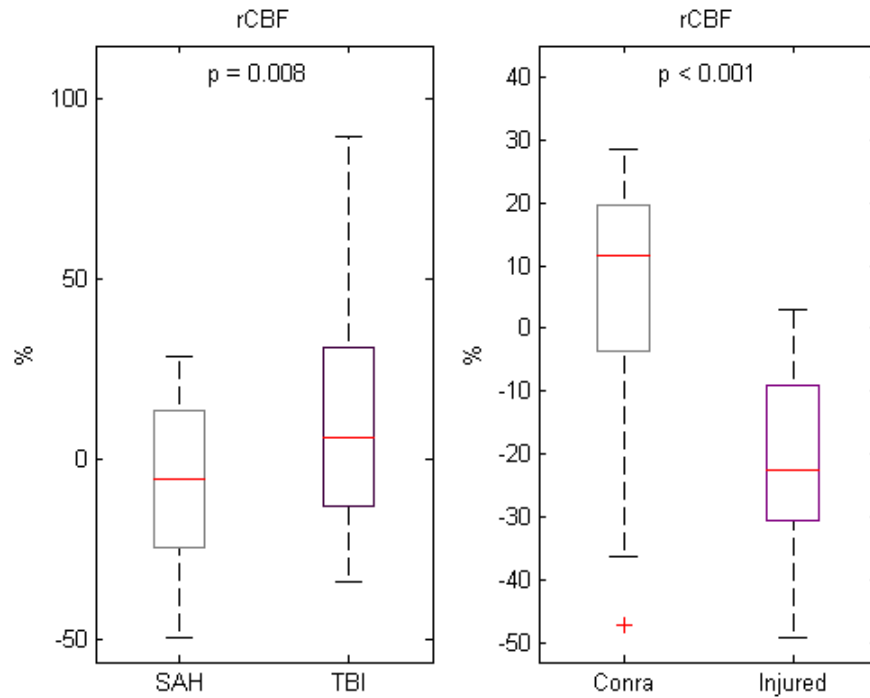


Figure 6.3: Box plots comparing relative cerebral blood flow (*rCBF*) response of (left) TBI versus SAH patients and (right) SAH patients' hemisphere of aneurysm rupture versus contralateral hemisphere. *rCBF* differed significantly between both sets of measurements, but DOS-measured oxygenation parameters did not distinguish either.

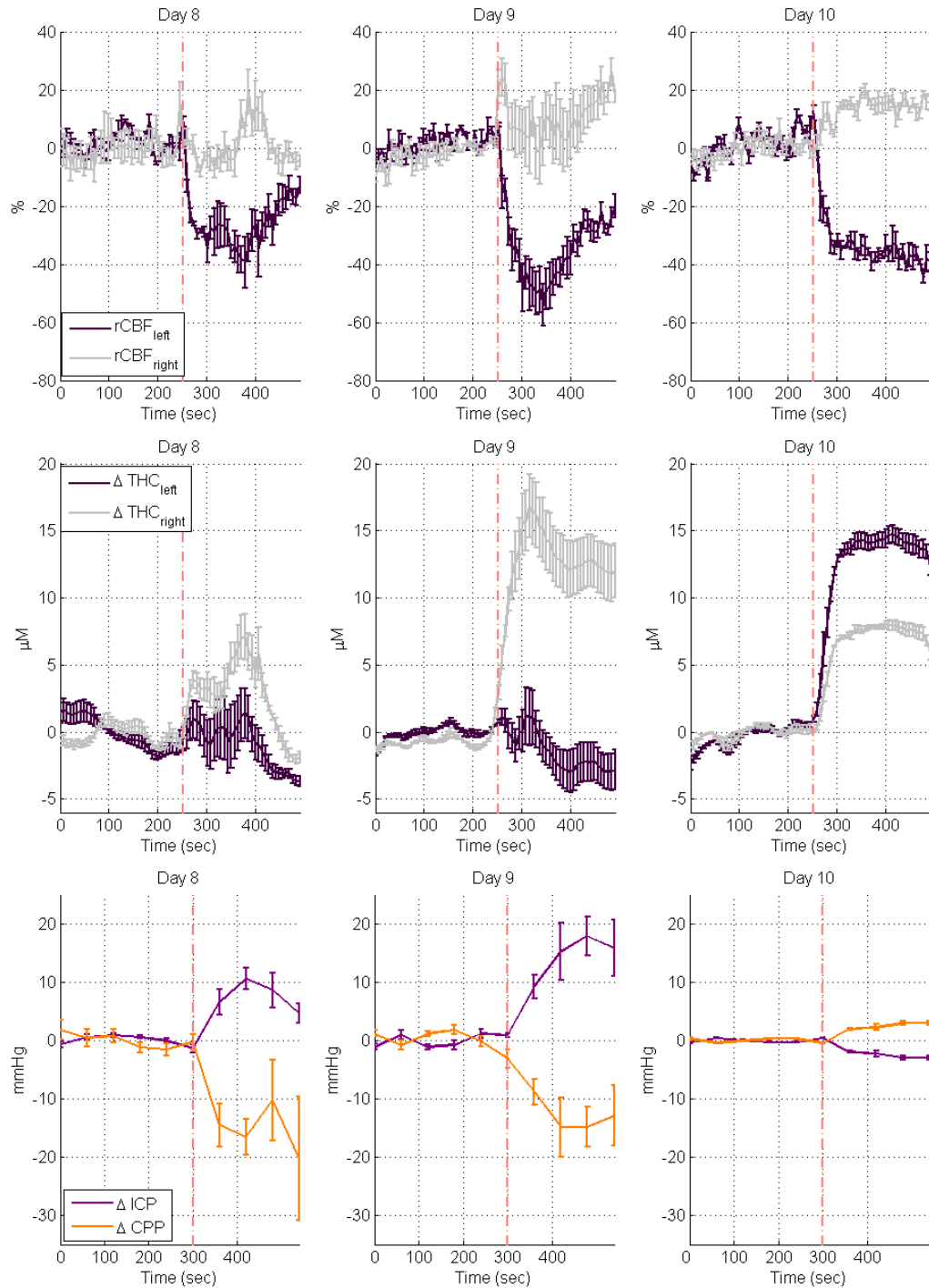


Figure 6.4: Case example data over three consecutive days (8, 9, and 10 days after injury) for a 40-year-old male subarachnoid hemorrhage patient (No. 4) who suffered a ruptured aneurysm in his anterior communicating artery. The vertical dotted line indicates the moment at which the patient’s bed was lowered from 30 degrees to flat. The Glasgow Coma Scale was 7 on days 8 and 9, and 3 on day 10. Each figure shows the averaged result of time-series data from three head lowering interventions for (a) $rCBF$, (b) ΔTHC , and (c) changes in ICP and CPP.

three consecutive days. Cerebral angiography identified a ruptured aneurysm in his anterior communicating artery that was clipped on post-bleed day 1. Figure 6.4 shows time-series results, averaged over three head-of-bed lowering events on each day, for three consecutive days (days 8, 9 and 10). The patient's GCS was 7 on days 8 and 9, and 3 on day 10. On day 7, the patient had moderate right middle cerebral artery (MCA) and basilar artery vasospasm, as well as mild left MCA vasospasm. On days 8 and 9, the patient had moderate right MCA vasospasm and mild-to-moderate bilateral carotid siphon vasospasm. On day 9, the patient also had mild bilateral posterior cerebral artery (PCA) vasospasm. $rCBF$ (Figure 6.4a) in the left hemisphere decreased with position change to supine on all three days, while $rCBF$ in the right hemisphere did not change on days 8 and 9, and then increased on day 10. Left frontal ΔTHC (Figure 6.4b), on the other hand, showed no change or even a decrease on days 8 and 9, but then sharply increased on day 10. These THC findings are in contrast to the right frontal cortex, in which ΔTHC increased with head-of-bed lowering on all three days. Figure 6.4c shows ICP and CPP data for this case, with an ICP increase and CPP decrease on days 8 and 9, and an ICP decrease and CPP decrease of reduced magnitude on day 10.

6.1.3 Discussion

In this study, we employed a novel optical methodology that combines DCS and DOS to measure cerebral hemodynamic changes during an intervention commonly performed in the neurocritical care unit: head-of-bed manipulation. Our findings suggest that the effect

of head-of-bed lowering on microvascular $rCBF$ differs in brain-injured patients as compared to healthy adults. Whereas frontal cortical $rCBF$ consistently increased in healthy subjects when lowering the head-of-bed from 30° to 0° , we found significant heterogeneity in cerebral hemodynamic responses to posture change in patients with severe brain injury.

In addition, we observed substantial variation in hemispheric responses to posture change in the brain-injured cohort, possibly due to the spatial heterogeneity in their disease. This intersubject and intrasubject (i.e. hemispheric) variability in $rCBF$ responses to posture change suggests that optimization of cerebral perfusion for patients in the neurocritical care unit may require an individualized approach to CBF management. Our results provide also preliminary evidence that the DCS/DOS hybrid device is well-suited to provide non-invasive, continuous hemodynamic monitoring that has the potential to optimize cerebral perfusion on an individualized basis.

The observed difference between positional $rCBF$ changes in the brain-injured versus healthy cohorts is consistent with prior studies of cerebral hemodynamics that have demonstrated impaired cerebrovascular autoregulation in severely brain-injured patients [172, 62, 45, 109, 127, 183]. Furthermore, the variability in frontal cortical cerebrovascular responses to posture change observed in the brain-injured cohort is consistent with similarly heterogeneous results in prior studies that examined the effect of head-of-bed position on CBF.

Shenkin et al. measured absolute CBF via the Kety-Schmidt N_2O technique at both 0° and 20° in six patients with elevated ICP due to brain tumors, finding that CBF was lower

at 20° by an average of 30% [209]. These findings suggested that the head-up position was detrimental because of decreased cerebral perfusion. In contrast, Feldman et al. recorded absolute CBF (also employing the Kety-Schmidt N_2O technique), CPP, and ICP in 22 head-injured patients at 0° and 30°, and found significantly lower ICP at head-of-bed 30° but no overall change in CPP and CBF [67]. As in our study, they established that head-of-bed angle did not have a significant effect on group-averaged CBF (47.8 ± 16.9 ml/100 g/min at 30°, 48.9 ± 20.4 ml/100 g/min at 0°), and their subjects experienced heterogeneous CBF responses ranging from increased to decreased perfusion. Specifically, five patients had values of supine CBF that were 5 ml/100 g/min or more greater than their CBF at 30°, and this subgroup had significantly different changes in CBF, cerebral metabolic rate of oxygen, and cerebrovascular resistance than the other seventeen patients.

Lastly, Moraine et al. measured CBF with the continuous thermodilution method, CPP, and ICP in thirty-seven comatose patients at head-of-bed angles 0°, 15°, 30°, and 45° [160]. CBF was higher at 0° (46.3 ± 4.8 ml/100 g/min) than at 30° (32.4 ± 2.8 ml/100 g/min), which constituted a relative difference of 43%. ICP also decreased with raised head-of-bed, but again with no change in CPP. Our study thus adds to prior evidence and suggests that there may not be a single head-of-bed position that is optimal for maximizing cerebral perfusion in brain-injured subjects in the neurocritical care unit. With regard to the healthy cohort findings, several prior studies have similarly observed that CBF and cerebral blood flow velocity via transcranial Doppler increase as the head of a healthy individual is lowered [59, 26, 5].

The heterogeneous frontal cortical $rCBF$ responses to postural changes observed in the patients in this study are also consistent with a prior DCS/DOS study in which patients with acute ischemic stroke were found to experience variable changes in frontal cortical $rCBF$ during posture change [59]. In this prior study, a $rCBF$ reduction after head-of-bed lowering occurred in four out of seventeen acute stroke patients – a “paradoxical response” for which a definitive pathophysiological mechanism could not be determined.

One possible explanation for $rCBF$ reduction after head-of-bed lowering is increased ICP, but in the present study, we did not find a significant correlation between changes in ICP and $rCBF$ response. CPP changes, however, were moderately correlated with $rCBF$ responses. This observation is consistent with prior studies showing that CPP-guided management may be more effective than ICP-guided management at promoting tissue perfusion, and thus improving clinical outcomes [259]. Yet the absence of a strong correlation between CPP and frontal cortical CBF underscores the difficulty in predicting CBF from CPP measurements and reinforces the need for direct monitoring of microvascular CBF to guide therapies in the neurocritical care unit.

Similar to our study, Moraine et al. demonstrated that the correlation between CPP and CBF is not always strong, but rather varies depending on head-of-bed position [160]. The authors found that the slope of absolute CBF versus CPP calculated with least-squares linear regression analysis changed from 1.71 at 0° to 0.76 at 30° . Ultimately, determination of which patients might experience predictable versus unpredictable changes in microvascular CBF during head-of-bed related CPP changes could be an important factor for optimizing

cerebral perfusion in individual patients.

In considering the individualized nature of $rCBF$ responses to posture change, it is also notable that the DOS-derived parameters for cerebral tissue oxygenation – HbO_2 , Hb , and THC – did not display the heterogeneous responses seen in $rCBF$. Rather, HbO_2 , Hb , and THC all significantly increased in the brain-injured cohort ($P < 0.001$) with head-of-bed lowering. The observed increases may be the result of passive venous pooling that increases cerebral blood volume when the head is lowered to the supine position. Because of impaired autoregulation in some patients, this increase in cerebral blood volume could contribute to an increase in ICP, and thus a decline in CBF. The fact that DCS and DOS results differed considerably in our study again highlights the advantage of hybrid DCS/DOS instrumentation over DOS monitoring alone.

Spatial resolution remains a major limitation of the current DCS/DOS approach, since measurements of $rCBF$, ΔHbO_2 , ΔHb , and ΔTHC are limited to approximately one cubic centimeter of cerebral tissue under the optical probes. This limitation could possibly explain any deviation from previous results in the literature, since CBF measurement techniques such as those used in Moraine et al. [160] and Feldman et al. [67] measured CBF more globally.

In addition, interfacing the optical probes to the patient's head can be challenging and can be hampered by hair or hair follicles; overcoming these technical barriers is an area of active research. In the present application, flow measurements were limited to near the surface of the frontal cortex due to placement of the optical probes on the forehead. However,

most other bedside monitoring methods have similar limitations, and brain-injured patients often have diffuse pathophysiological processes for which such measures remain useful. Another challenge in optical monitoring of cerebral physiology is accurate localization of signal changes measured by transcranial probes, which potentially detect signals from the scalp and other intervening tissues as well as the brain. Recent findings suggest the likelihood of some scalp contamination that can be suppressed by increasing probe pressure.

There are several further limitations of our study. First, timing of optical data acquisition ranged from day 2 to day 13 post-injury. As a result, patients were likely in different stages of their disease processes, during which cerebrovascular autoregulatory function may vary. For example, the data from the case example spanning three consecutive days demonstrated a change in cerebral hemodynamic responses to posture change from day 9 to day 10 post-injury. These longitudinal changes in $rCBF$ were associated with changes in GCS and postural changes in cerebral perfusion pressure.

Second, our cohort included three different types of brain injury: TBI, aneurysmal SAH, and AVM with associated ICH and SAH. Even within one of these injury categories, there is large variability with regards to the severity and neuroanatomic distribution of injury. Although our sample size was too small to determine the mechanisms that cause variability in CBF responses to posture change, our preliminary observations suggest that CBF responses may differ due to severity of injury (e.g. GCS score on day of study). We found that GCS on the day of study was negatively correlated with $rCBF$, indicating that as consciousness was more severely altered, postural changes in CBF were more pronounced.

Also, preliminary analysis may suggest that CBF responses may differ according to type of injury, hemisphere of aneurysm rupture, and number of days after injury. When patients were grouped by type of injury, $rCBF$ response differed between the SAH (n = 6) and TBI (n = 4) cohorts. This observation may be attributed to the diffuse hemodynamic effects of traumatic brain injury as compared to the potentially more focal hemodynamic effects of cerebral vasospasm after aneurysmal SAH [187, 181]. In addition, what may superficially be called the "injured hemisphere" (defined as the hemisphere containing the aneurysm or the AVM) had a significant effect on postural $rCBF$ changes in the patients with SAH. The number of days after injury inversely correlated with absolute magnitude of $rCBF$ response with head lowering, saying that perhaps autoregulation was more impaired earlier in the recovery stage, leading to greater changes in $rCBF$.

Finally, while studying individual patients on multiple days allowed for longitudinal analyses, such measurements could introduce bias towards data from these patients who were measured on more than one occasion. Nevertheless, the heterogeneity in our methods suggests that the DCS/DOS protocol utilized in this study may be generalizable to multiple patient populations within the neurocritical care unit, with the potential to improve patient care by providing clinicians with the capability to monitor cerebrovascular hemodynamics longitudinally at the bedside.

In conclusion, this study provides preliminary evidence that continuous, non-invasive bedside monitoring DCS/DOS can be used to detect differences in cerebral hemodynamic responses of brain-injured patients to posture change in the neurocritical care unit. These

cerebrovascular responses are not easily predicted by postural ICP and CPP changes, highlighting the potential value of direct measurement of microvascular perfusion. The observed variability in postural CBF responses also suggests that there may not be a single head-of-bed position that optimizes cerebral perfusion in all patients. Larger studies are needed to reproduce these findings, to further validate transcranial monitoring of cerebral perfusion and metabolism with diffuse optics, and to test whether bedside monitoring with DCS/DOS can be used to optimize head-of-bed positioning for maximizing cerebral perfusion in individual patients.

6.2 Induced Hyperoxia

After severe TBI, ischemia and subsequent lowered levels of oxygen delivery can have dire consequences such as mitochondrial dysfunction and hypometabolism [192]. The injured brain has been found to develop diffusion barriers to the cellular delivery of oxygen that prevents an increase in oxygen extraction that normally follows hypoperfusion, or lowered CBF [151].

Hyperoxia, or excess oxygen, has been explored as a method of therapy for brain-injured patients. Because patients are typically already intubated and on a respirator, increasing the fraction of inspired oxygen (FiO_2) to 100% at normobaric pressure is a simple way to induce hyperoxia. It is known to increase partial pressure of brain tissue oxygen [152]. For therapeutic uses, patients are typically put on 100% FiO_2 for a duration of hours [192].

Short-term induced hyperoxia (for ~ 2 minutes) is a commonly used intervention in the neurocritical care unit. For instance, after suctioning and clearing the patient's airway from a blockage, the nurse will give 2 minutes of oxygen. It may also be used in times of hemodynamic compromise, or as a simple way of testing the brain tissue oxygen partial pressure monitor. In this study, we wanted to again test whether our hybrid DCS/DOS monitor would be able to distinguish hemodynamic changes due to this simple intervention. Also, we hypothesized that we would see similar trends between our non-invasive DOS measurements and the invasive brain tissue oxygen monitor.

6.2.1 Methods

Patient Enrollment. Patients with traumatic brain injury or aneurysmal subarachnoid hemorrhage were recruited at the Hospital of the University of Pennsylvania (HUP) through the Department of Neurology and the Neurosurgery Clinical Research Division. Written consent was obtained by the subject or a legally authorized representative. Patients eligible for enrollment included severe head trauma patients with post-resuscitation GCS scores between 3 and 8, or those with aneurysmal subarachnoid hemorrhage with clinical Hunt-Hess classification grades III, IV, or V. All studies occurred in the patient's hospital room, following protocols approved by the University of Pennsylvania Institutional Review Board.

Patient Monitoring. A continuous brain tissue oxygen partial pressure (P_{btO_2}) monitor (Licox®CMP; Integra NeuroSciences, Plainsboro, NJ, USA) was placed on most study patients prior to enrollment. The Licox sensor consists of a polarographic Clark-type elec-

trode placed into the white matter. A ventriculostomy was performed on many study patients to continuously measure ICP and to drain cerebrospinal fluid, if necessary; for patients without an intraventricular drain, ICP was monitored by a fiberoptic intraparenchymal catheter (Camino-MPM1; Integra NeuroSciences, Plainsboro, NJ, USA). CPP data was calculated from the difference between mean arterial pressure (MAP) and ICP. For some patients, a multi-modality monitoring system (Mobius™; Integra NeuroSciences, Plainsboro, NJ, USA) was used to continuously record PbtO₂, ICP and CPP for analysis. Before the introduction of this new technology, the variables were typed once per minute into a spreadsheet by study staff.

The diffuse optical instrument (Joel's Instrument, see Section 3.1.1) was placed unobtrusively outside the patient's room. The optical fibers extended from the instrument to the patient's forehead and were held in place at the probe end with a rectangular piece of black foam. A source-detector separation of 2.5 cm was used for this study. A similar sized disposable Duoderm was used to secure the probe and the surrounding foam to the subject's forehead. Two optical probes were positioned on each side of the forehead, in front of the poles of the left and right frontal lobes. A black cloth rested on top of the probes to shield ambient light and improve signal-to-noise ratio. Once adequate signal was confirmed, the study began with induced hyperoxia interventions. Neurointensive care physicians reviewed all study interventions and confirmed their safety on a case-by-case basis prior to study initiation.

Study Protocol. Subjects began the hyperoxia protocol in the typical position at which

most neuro-ICU patients are kept, with head elevated at 30° . Baseline FiO_2 level was recorded at this head-of-bed position. FiO_2 was then increased to 100% for 2 minutes, followed by recovery for 5 minutes at baseline FiO_2 level. This intervention was repeated up to three times for each patient.

Data Analysis and Statistics. We used a portable hybrid DCS/DOS instrument that was built in our lab (see Section 3.1.1). DCS employs a narrowband continuous-wave laser (785 nm, 40 mW), four photon-counting fast avalanche photodiodes, and an four-channel autocorrelator board. Temporal autocorrelation functions of the reflected light were used to derive relative CBF.

For DOS, 3 mW of light from amplitude-modulated (70 MHz) lasers operating at 690, 785, and 830 nm were fiber-coupled onto the tissue surface. Photons transmitted into the brain were detected in reflection at the surface of the scalp. These wavelength-dependent photon reflections were used to determine the oxy- and deoxyhemoglobin concentrations by near-infrared (NIR) spectroscopic analysis.

DCS/DOS data was treated the same as described in Section 6.1. To assess the significance of changes in parameters due to the induced hyperoxia intervention, we utilized a linear mixed effects model. We used the library nlme in statistical software R (<http://www.rproject.org>). The threshold for significance was a p-value less than 0.05.

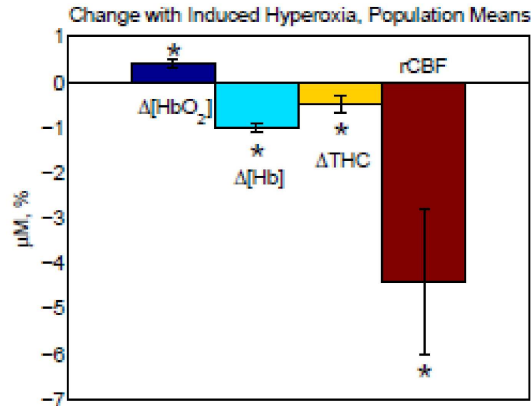


Figure 6.5: Bar plot showing cohort-averaged response of DOS/DCS quantities to induced hyperoxia. ΔHbO_2 and ΔHb changes were in opposite directions, but overall THC saw a decrease that is in agreement with the trend of $rCBF$.

6.2.2 Results

We induced hyperoxia in eleven brain-injured patients. Nine of the eleven patients possessed a continuous brain tissue oxygen partial pressure ($PbtO_2$) monitor, while the remainder did not have any $PbtO_2$ device.

Population-averaged results from DOS/DCS are shown in a bar plot in Figure 6.5, with means and standard errors listed in Table 4. All DOS/DCS-measured quantities showed a significant change with induced hyperoxia intervention. ΔHbO_2 and ΔHb changes were in opposite directions, and $rCBF$ and ΔTHC saw decreases.

Table 4 outlines changes of all quantities, including Licox-measured $PbtO_2$ and systemic vitals, with significant changes identified. Induced hyperoxia caused significant changes in heart rate, $PbtO_2$, respiration rate, and arterial oxygen saturation as measured by pulse oximetry.

Continuous timeseries from Patient 8, an 18-year-old male pedestrian hit by a car, is

Table 6.5: Effects of induced hyperoxia on vitals and DCS/DOS parameters in brain-injured patients (n = 11).

Parameter	Mean \pm SD	P-value
SYS, <i>mmHg</i>	-2.0 \pm 5.0	0.202
DIA, <i>mmHg</i>	-0.04 \pm 2.3	0.957
MAP, <i>mmHg</i>	-0.8 \pm 4.0	0.529
HR, <i>bpm</i>	-1.2 \pm 1.7	0.018
PbtO ₂ , <i>mmHg</i>	15.7 \pm 17.9	0.004
RESP, <i>bpm</i>	-1.8 \pm 3.3	0.070
ICP, <i>mmHg</i>	-0.4 \pm 3.0	0.642
CPP, <i>mmHg</i>	0.07 \pm 2.7	0.928
SpO ₂ , %	1.1 \pm 2.0	0.074
<i>rCBF</i> , %	-4.4 \pm 5.3	0.007
ΔHbO_2 , μM	0.4 \pm 0.3	0.006
ΔHb , μM	-1.0 \pm 0.3	<0.001
ΔTHC , μM	-0.5 \pm 0.7	0.009

Values listed as mean \pm SD, with range in parentheses; P-values from two-tailed Student's t-test

shown in Figure 6.6. He suffered from a TBI and had small evolving subarachnoid hemorrhaging in the right frontal lobe as a result. The patient also had subdural hemorrhage along both frontal convexities and the interhemispheric fissure. Figure 6.6(a) shows changes in the DOS-measured oxy- and deoxyhemoglobin concentrations against changes in the Licox-measured PbtO₂ during hyperoxia. ΔHbO_2 and PbtO₂ both begin to increase after 100% oxygen is administered, although temporally ΔHbO_2 seems to increase and reach a peak faster than PbtO₂. Trends of ΔHb and PbtO₂ show stronger temporal (negative) correlation. With the increase in fraction of inspired oxygen, it follows that blood and tissue oxygenation both increase as expected. Relative CBF measured during the same hyperoxia event is shown in Figure 6.6(b). The intervention leads to steady decreases in CBF of roughly 10% and THC of 2 μM in this patient.

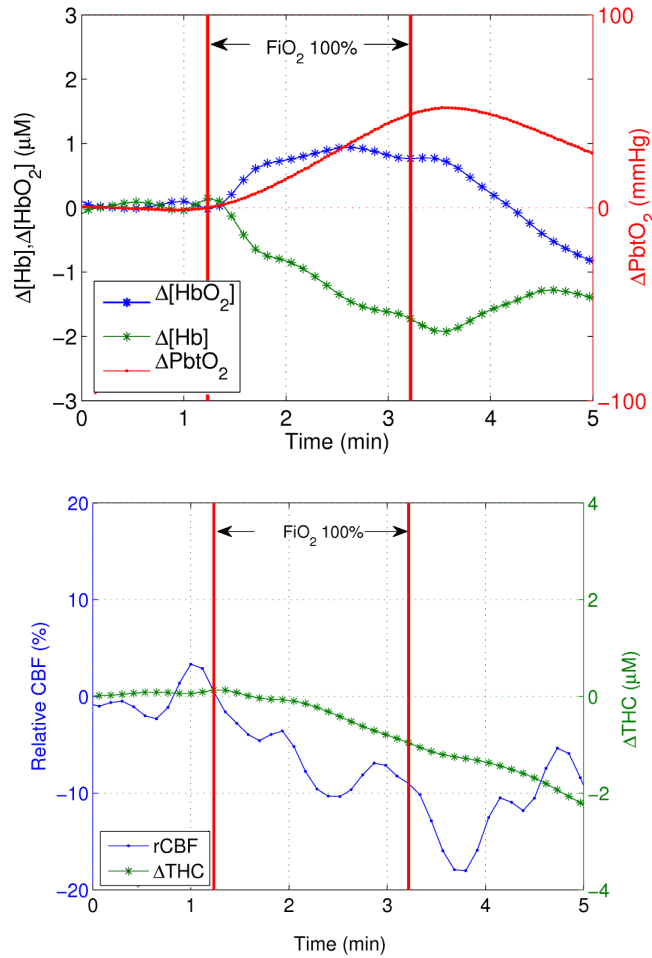


Figure 6.6: (top) Changes in ΔHbO_2 , ΔHb (from DOS, left hemisphere probe shown) and PbtO_2 (from Licox® monitor) during induced hyperoxia event. Fraction of inspired oxygen (FiO_2) was set at 100% for the 2-minute interval shown between the bars. Rises in both ΔHbO_2 and PbtO_2 are seen, as both increase with a rise in oxygenation of the blood. Negative correlation is seen between trends of ΔHb and PbtO_2 . (bottom) Relative CBF and ΔTHC during the same hyperoxia event (left hemisphere probe only). Both $r\text{CBF}$ and ΔTHC decrease with rise of FiO_2 .

6.2.3 Discussion

Our hybrid optical monitor was tested during a period of induced hyperoxia, where the FiO_2 was increased to 100% for 2 minutes. In the neurocritical care unit, this intervention is used in times of respiratory distress or hemodynamic compromise, or as a simple way of testing the brain tissue oxygen partial pressure monitor. During the 2-minute period of hyperoxia, both the brain tissue oxygen and DOS monitors observed increases in oxygenation as a population, but the relative changes differed. DOS found much smaller relative changes in oxy- and deoxyhemoglobin than the brain tissue oxygen monitor's changes in PbtO_2 . In general, however, the two different quantities may not necessarily be well correlated due to the inverse S-shape of the hemoglobin dissociation curve [2], and due to the fact that different regions of the brain were probed by the two monitors. $rCBF$ (and ΔTHC) fell an average of -4.4% (and $-0.4 \mu\text{M}$).

A study by McLeod et al. also measured blood oxygenation with NIRS in comparison to brain tissue oxygen tension in eight patients with head injury [147]. They began at the patient's baseline FiO_2 for 10 minutes, then increased to 100% for 30 minutes. Although the duration of induced hyperoxia in their study was much longer (and therefore provides an explanation for greater magnitudes of change), their results have a trend similar to ours: $2.80 \mu\text{M}$ increase in ΔHbO_2 , $-5.2 \mu\text{M}$ drop in ΔHb , $-2.4 \mu\text{M}$ drop in ΔTHC , 117.5 mmHg increase in PbtO_2 , and no significant change in MAP or ICP.

Numerous studies on healthy subjects have found a varying magnitude of CBF decrease with induced hyperoxia, ranging from -27% to -10.8% as reviewed by Johnston et al. [113].

Also on healthy individuals, Floyd et al. measured an even larger drop in $rCBF$ (-33%) with continuous arterial spin-labeled perfusion MRI [72]. For those with severe head injury, the typical response is as yet unsubstantiated. Menzel et al. used stable xenon-CT to measure six patients with severe traumatic brain injury, with 35% inspired oxygen for baseline scan and 60% for second scan [153]. They found a global CBF decrease of -9%, and for an undamaged region of interest (as determined by noncontrast CT), a regional decrease of -19.3%. This may support results found by DCS in that the magnitude of decrease found in a head injured population is less than those reported in healthy subject literature. However, caution must be taken in directly comparing results from DCS (where FiO_2 was increased from baseline value to 100%, not 35 to 60%).

Another study by Rosenthal et al. on fourteen TBI patients also observed a decrease in $rCBF$ (-22.6%) using a thermal diffusion probe, but with greater magnitude than that found by Menzel et al. and by our study [195]. This differential may be explained by the fact that they maintained 100% inspired oxygen for 20 minutes as compared to our 2 minutes.

The results of this pilot study suggest hybrid diffuse optical devices utilizing DCS/DOS technology has the potential to be implemented as a bedside monitor of CBF and blood oxygenation in the neuro-intensive care unit. When brain-injured patients underwent periods of induced hyperoxia, DCS/DOS detected changes in frontal cortical microvascular CBF and blood oxygenation that were in general agreement with vitals measurements provided by invasive intraparenchymal monitoring devices. Further studies are warranted to examine

the utility of DCS/DOS continuous bedside monitoring in the neurocritical care unit.

6.3 Conclusion

In this chapter, we demonstrated feasibility of a hybrid diffuse optical device as a continuous, non-invasive bedside monitor for severely brain-injured patients in the neurocritical care unit. We had already shown that DCS measurements of relative CBF were shown to correlate with relative CBF values measured by a "gold-standard" CBF technique: xenon-enhanced CT. Thus, following this validation, we demonstrated the hybrid diffuse optical device can also monitor significant changes in CBF and blood oxygenation during two common clinical interventions: head-of-bed elevation change and induced hyperoxia. This opens the door for DCS/DOS add to the array of bedside monitors currently used in the neurocritical care unit to give clinicians additional information on cerebral hemodynamics during various interventions. Future studies include long-time monitoring (>24 hours) to investigate the effects of other types of interventions such as drug administration or suctioning.

Chapter 7

Use of DCS at High Altitudes

High altitude has profound cerebrovascular effects on those that work, live, or are stationed at heights greater than 2400 m (8000 ft above sea level). For them, high altitude cerebral edema (HACE), or the swelling of brain tissue from fluid leakage, is a common cause of death; the only treatment for HACE in current use is immediate descent. But because edema is also found frequently in severe brain injury, it has been hypothesized that methods proven to successfully treat patients in the neurocritical care unit could also help those with altitude sickness, i.e., without forcing them to descend. For instance, treatments like oxygen administration and some medications have proven themselves useful as temporary relief until descent [86].

High altitude scientists would likely benefit greatly from a portable and continuous monitor of CBF in order to investigate therapies and their effect on blood flow in such an environment. Currently, near-infrared spectroscopy (NIRS) and transcranial Doppler (TCD) are options, but these techniques are surrogate measures of CBF. Diffuse correla-

tion spectroscopy (DCS) could provide a compact, continuous technique for monitoring changes in CBF at high altitudes.

This chapter describes a first attempt to use DCS as a monitor of relative CBF at high altitude. We utilize a hyperventilation intervention. Hyperventilation is the simplest of the treatments for high intracranial pressure (ICP) used in the neurocritical care unit, but it is also known to decrease CBF at sea level. Its use at high altitude could lead to possible ischemia, since those at altitude already suffer from respiratory alkalosis (high blood pH) [86]. However, we wanted to directly measure the effects on CBF of hyperventilation at high altitude, to determine whether blood flow indeed decreases as a result, as it does at sea level. Also note that this work is currently being prepared for publication.

7.1 Effects of High Altitude

Due to lower atmospheric pressure, high altitudes affect humans because of a lowered partial pressure of oxygen. Acute exposure to high altitude hypoxia can cause pathophysiological changes that manifest as a spectrum of disorders ranging from the relatively benign high-altitude headache to life-threatening high-altitude cerebral edema. One study that looked at trekkers in Nepal found that the incidence of HACE was 21%, and that there were 8 altitude illness-related deaths for every 100,000 trekkers [129].

In addition, the potential long-term neurological sequelae from travel to high-altitude are beginning to be appreciated with magnetic resonance imaging (MRI) evidence of cortical atrophy, white matter changes and enlargement of Virchow-Robin spaces [66], and

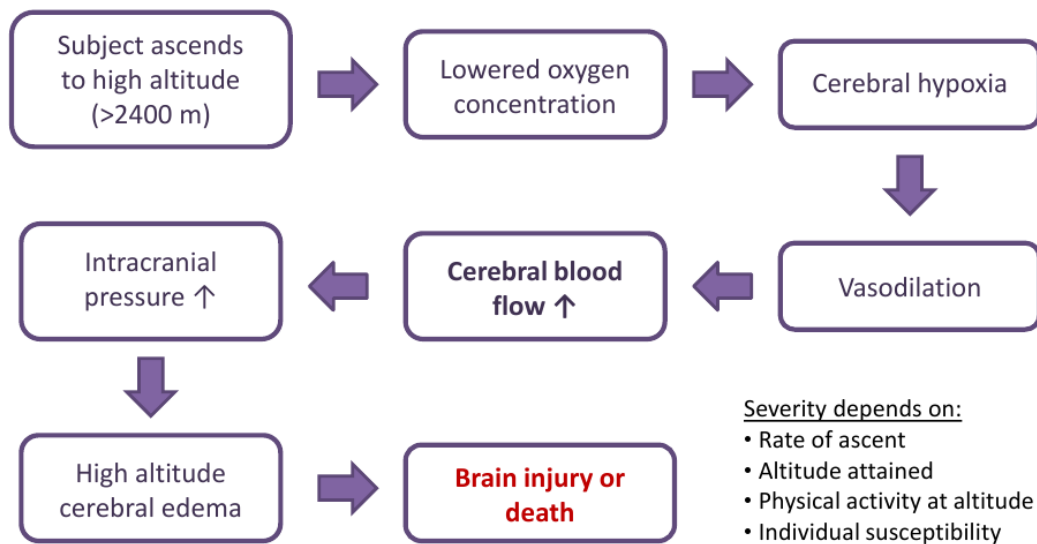


Figure 7.1: One possible train of effects of high altitude on humans. Ascent to altitude can cause a number of disorders ranging from altitude sickness to life-threatening high-altitude cerebral edema.

persistent cognitive impairment [29]. While these changes seem to be related to cerebral hypoxemia [245], the underlying pathophysiology remains elusive with the cerebrovascular response to altitude incompletely characterized. Cerebral oxygenation is determined by arterial oxygen content, oxygen consumption and CBF. In turn, CBF is subject to different regulatory mechanisms than peripheral blood flow and is known to be particularly reactive to changes in arterial carbon dioxide (CO₂).

High altitude illness begins with mild to moderate acute mountain sickness (AMS), characterized by symptoms such as headache, nausea, fatigue, and sleep disturbance [10]. Severe AMS, if left untreated, may develop into life-threatening HACE. The exact mechanism causing these syndromes is unknown, but raised ICP found in those with moderate to severe AMS has led to one proposed chain of events shown in Figure 7.1 [190, 85]. First,

a subject ascends to high altitude (>2400 m) where the oxygen concentration is low due to low atmospheric pressure. This causes cerebral hypoxia, or a reduced supply of oxygen to the brain, which in turn then leads to a dilation of the blood vessels in the body's attempt to increase oxygen supply by increasing blood flow. It is also thought that the blood-brain barrier decreases in permeability [10]. The increased CBF and blood volume in the brain can lead to an increase in ICP, and can cause the brain to swell.

Severity of injury depends on rate of ascent (faster \rightarrow more dangerous), maximum altitude attained, and amount of physical activity at altitude. There also seems to be an individual's own susceptibility to altitude, i.e. some people are more susceptible to AMS than others. Individual susceptibility is due, in part, to how familiar one is with being at altitude (e.g. sherpas, experienced trekkers, or those raised and living at high altitudes versus visitors to high altitude). For instance, one study looked at over 3000 adult tourists who traveled to the Rocky Mountains of Colorado and found that the biggest factor influencing those who developed AMS was a permanent residence below 900 m (3000 ft) [99].

Another theory in line with the cascade of events shown in Figure 7.1 is that those who have "tight brains", i.e., a smaller ratio of cranial cerebrospinal fluid to brain volume, are more susceptible to AMS [85]. This is because they are less able to tolerate brain swelling through the displacement of cerebrospinal fluid than those with higher ratios. Some recent imaging evidence has supported this "tight-fit" hypothesis [253, 116].

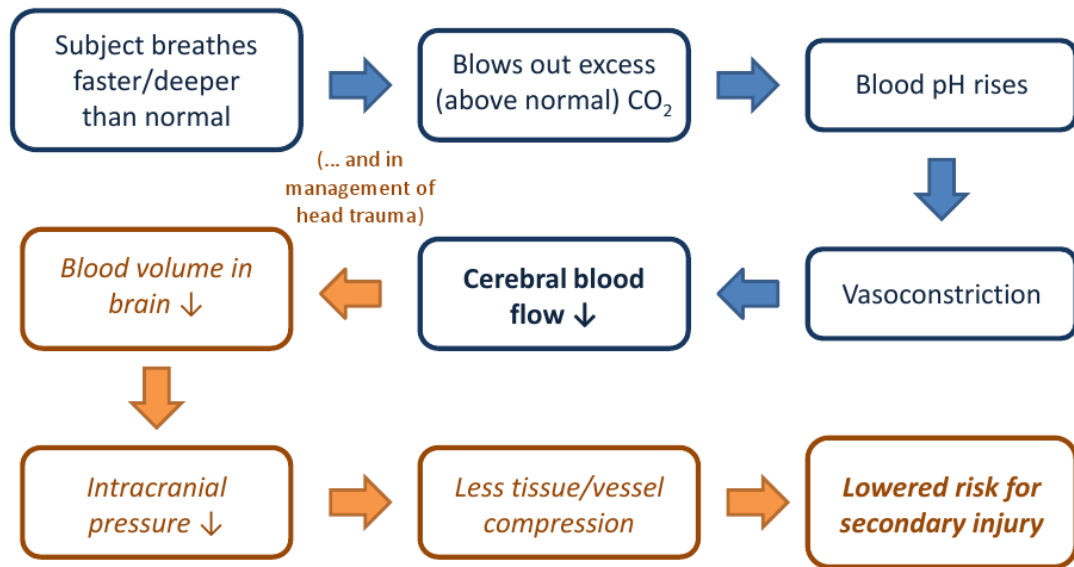


Figure 7.2: Effects of hyperventilation on humans at sea level. Hyperventilation is the state of breathing faster or deeper than normal, causing excessive expulsion of carbon dioxide and ultimately a decrease in cerebral blood flow.

7.2 Hyperventilation as Possible Treatment

As mentioned in Section 1.3, hyperventilation is one simple procedure that can be employed to decrease ICP in severely brain-injured patients. Hyperventilation is defined as a state of breathing faster or deeper than normal. Hyperventilation can cause the excessive expulsion of CO_2 . Figure 7.2 shows the cascade of events that result from hyperventilation at sea level, and its cerebrovascular effects. The subject begins to breath faster and deeper than normal, blowing out excessive CO_2 . This causes the blood pH to rise, making it more alkaline, and leading to vasoconstriction and a drop in CBF. In the case of head trauma management, this drop in cerebral blood volume would cause a subsequent and relieving decrease in ICP, possibly reducing the risk for secondary injury.

However, it is unknown what happens to CBF when humans hyperventilate at high altitudes. One study used NIRS on 20 healthy subjects at sea level, 2770 m, 3560 m, and 4680 m [106]. They found that hyperventilation caused end-tidal carbon dioxide (EtCO_2) to reduce to approximately 50% of baseline level, while cerebral tissue oxygen saturation (StO_2) decreased with hyperventilation for sea level and 2770 m. However, interestingly, StO_2 remained unchanged at 3560 m and increased at 4680 m.

Other studies have used TCD-measured cerebral blood flow velocity as a CBF surrogate during hyperventilation. One study looked at cerebral blood flow velocity (CBFV) in the middle cerebral artery (MCA) of 43 subjects without AMS, 17 subjects with AMS, and 20 sherpas [110]. All were at an altitude of 4243 m, and after hyperventilation, all three groups saw decreases in MCA flow velocity. But the AMS subjects saw a greater decrease in flow velocity than the non-AMS subjects and the sherpas. There was no difference in CBFV change between the non-AMS subjects and the sherpas. Another TCD study saw a similar decrease of -34% in CBFV after being at an altitude of 4559 m for about a day [138].

7.3 Study Motivation

Studies of cerebral hemodynamics at altitude have been hampered by the lack of an effective method to monitor intracranial microvascular perfusion. DCS has the ability to fill this niche, as it provides a non-invasive, portable way to measure relative cortical blood flow. Importantly, it does not rely on the principles of tracer clearance and is a continuous

measure of CBF changes. DCS modules are simple to build (see Section 3.2.5), and can be made both compact and sturdy enough to survive ascent to high altitudes.

Hyperventilation will naturally cause a decrease in CBF at sea level, but may cause an increase in CBF after ascent. If this is the case, hyperventilation (or any physical activity causing heavy breathing) could aggravate altitude-related illness rather than reduce it. If this is not the case, hyperventilation could be explored as a method to help alleviate altitude-related illness.

Using our lab-built DCS device with concurrent measurements of StO_2 from a commercial diffuse optical spectroscopy (DOS; otherwise known as near-infrared spectroscopy) module, we sought to elucidate the effects of altitude and acclimatization on cerebral hemodynamics and oxygenation during hyperventilation. We also used TCD measurements of CBFV to see whether the microvascular changes in CBF seen by DCS would match commonly measured large-vessel CBFV.

7.4 Methods

Approval for this study was obtained from the ethics committees of the University of Turin and University College London. All participants underwent medical screening and written informed consent was obtained after the possible risks of the study were explained. Twelve subjects ranging in age from 22 to 80 years, with varying degrees of experience at altitude were recruited from the 2010 Xtreme Alps Medical Research Expedition. None had traveled to altitude during the previous three months, nor had any history of cardio-

vascular, respiratory or neurological disease. Subjects were initially studied in London, UK at a baseline altitude of 75 m above sea level prior to the expedition. High altitude measurements took place at the Capanna Regina Margherita¹ at 4559 m.

The presence of AMS symptoms was collected using a self-reported Lake Louise scoring system questionnaire at approximately 6 a.m. daily. Subjects with symptoms of AMS severe enough to require treatment with dexamethasone or acetazolamide were excluded from further participation in the study after they began treatment.

7.4.1 Optical Instrumentation

We used a house-built, two-channel multi-wavelength DCS module modified specifically for this study (see Section 3.3.3). The module includes 785 nm and 830 nm long-coherence length continuous-wave lasers, two single-channel avalanche photodiodes, and a 2-channel hardware correlator. The probe had a source-detector separation of 2.5 cm, and we used a 2-to-1 detector fiber bundle to increase signal-to-noise. Relative cerebral blood flow ($rCBF$) data is calculated every 3 seconds.

A commercial DOS device, the Fore-sight Absolute Cerebral Oximeter (Casmed; Branford, CT, USA), uses 4 wavelengths of near-infrared light (690, 780, 805, and 850 nm) to calculate absolute cerebral tissue oxygen saturation (StO_2). The probe has two source-detector separations, and measurements of absolute StO_2 are obtained once every two seconds. A wool cap was then placed over the probe to minimize interference from ambient

¹The Capanna Regina Margherita is a hut built on the top of Punta Gnifetti (4559 m) in the Italian Alps with an observatory for scientific studies beside it.

light and to apply a constant, even pressure.

The DOS device provided absolute StO_2 at both baseline (resting) and during hyper-ventilation, and those values were used in conjunction with measurements of intensity changes from both lasers of the multi-wavelength DCS module. Using these intensity changes, we used the differential pathlength method (see Section 2.1.4) to calculate changes in oxy- and deoxyhemoglobin concentrations (ΔHbO_2 , ΔHb). With this information, we could then find values of absolute oxy- (HbO_2), deoxy- (Hb), and total hemoglobin concentrations (THC). Changes in absorption were calculated and used in fitting the temporal intensity autocorrelation functions to extract blood flow index (BFI). Scattering was assumed to remain constant.

7.4.2 Transcranial Doppler Ultrasound

Transcranial Doppler ultrasound was assessed using the Sonosite MicroMaxx™ (Sonosite; Bothell, WA, USA), a handheld ultrasound device [252]. A 5-1 MHz transducer was used to insonate the subject's MCA via the right temporal window. The clinoid process of the sphenoid bone, the Circle of Willis and the distal internal carotid artery were initially located, and then the identification of the M1 segment of the MCA was characterized by flow towards the transducer. An optimal portion of the MCA without branches and with laminar flow was then selected and the depth recorded. Once identified, the center of the artery was insonated resulting in values of peak systolic velocity (PSV). On subsequent studies, every effort was made to insonate the same depth (to within 1 mm).

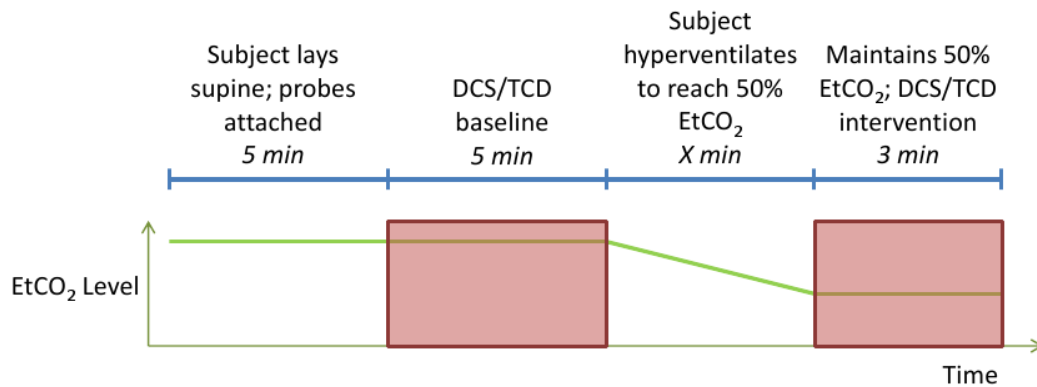


Figure 7.3: Hyperventilation protocol. Subject lays supine with DCS/DOS probes attached and relaxes. During this time, baseline values are recorded for 5 minutes. The subject then hyperventilates until their end tidal carbon dioxide (EtCO₂) level reaches 50% of baseline. This EtCO₂ level is maintained and a second set of data is taken.

7.4.3 Systemic Vitals

An in-line capnograph (EMMA Capnometer, Phasein Medical Technologies; Danderyd, Sweden) was used to record end-tidal CO₂ (EtCO₂) values via a tight-fitting face mask both at pre-study baseline and throughout the hyperventilation protocol. Peripheral arterial oxygen saturation (SpO₂) was monitored by a near-infrared pulse oximetry probe (Nonin, Onyx model 9500; MN, USA) placed on the finger.

7.4.4 Hyperventilation Protocol

Figure 7.3 outlines the hyperventilation protocol. Subjects were positioned supine and asked to relax. DCS/DOS probes (one per subject) were affixed above the brow overlying the left/right hemispheres, being careful to avoid the frontal and superior sagittal sinuses. Baseline values of PSV from the MCA were obtained by the TCD operator, and once

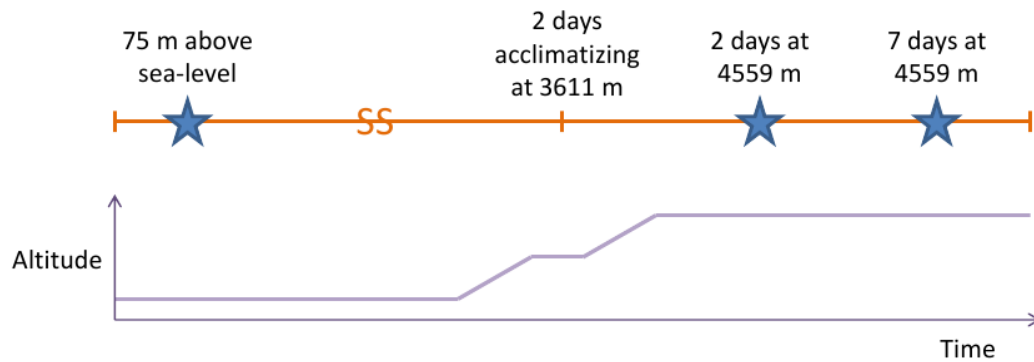


Figure 7.4: Study protocol. The hyperventilation experiment is repeated at on the same subjects at 3 different timepoints: 1) 75 m above sea level, 2) 4559 m above sea level after 2 days at altitude, 3) 4559 m above sea level after 7 days at altitude. Subjects ascended first to 3611 m for two days, then proceeded to 4559 m.

proper DCS/DOS signal had been confirmed, $rCBF$ and StO_2 baseline data were taken for 5 minutes. Subjects were then asked to hyperventilate to 50% of their baseline $EtCO_2$, with verbal feedback and instruction given to the subject regarding depth and rate of respiration based on readings from the capnograph. After achieving this target, the subject maintained the level of $EtCO_2$ for 3 minutes, an additional set of DCS/DOS/TCD measurements were obtained.

This hyperventilation protocol was to be repeated on the same subjects at three different time-points (see Figure 7.4): 1) 75 m above sea level, 2) 4559 m above sea level after 2 days of being at altitude, 3) 4559 m above sea level after 7 days of being at altitude. Ascent was by cable car and on foot, with two days spent acclimatizing at 3611 m.

7.4.5 Statistical Analysis

Mean changes in each cerebral and systemic physiological parameter due to hyperventilation and each timepoint were computed from continuous time-series data by taking the average ($\langle \rangle$) during the 5-minute time period (t_{BL}) of rest as baseline for comparison against the 3-minute hyperventilation time period (t_{HV}). Periods were defined as those data measured after the optical signal had stabilized, with all data during the hyperventilation transition and all motion artifacts excluded from the analysis. Differential values for DOS data as well as for systemic vitals were defined as

$$\Delta Y = \langle Y(t_{0^\circ}) \rangle - \langle Y(t_{30^\circ}) \rangle, \quad (7.1)$$

with Y representing the parameter of interest. For DCS/TCD data, a percentage change from baseline was employed to compute $rCBF$ /relative PSV (rPSV), as follows:

$$rCBF = \frac{\langle BFI(t_{HV}) \rangle - \langle BFI(t_{BL}) \rangle}{\langle BFI(t_{BL}) \rangle}, \quad (7.2)$$

and

$$rPSV = \frac{\langle PSV(t_{HV}) \rangle - \langle PSV(t_{BL}) \rangle}{\langle PSV(t_{BL}) \rangle}. \quad (7.3)$$

Data are expressed as mean \pm standard deviation (SD). We wanted to test for four different hypotheses. First, we used a one-way ANOVA test to determine whether there was evidence of differences between baseline (resting) means of the physiological parameters

Table 7.1: Number of subjects included in each timepoint.

Timepoint	Altitude	No. of Subjects
1	Sea Level	N = 12
2	Day 2 at 4559 m	N = 9
3	Day 7 at 4559 m	N = 7

measured at each of the three timepoints: sea level, 2 days and 7 days at altitude. Second, we again used a one-way ANOVA test to see if induced changes from hyperventilation are different among the three timepoints. Third, a two-tailed Student's t-test was used to determine whether the induced changes themselves were significant. Lastly, correlations between parameters were performed using Spearman's correlation. Statistical significance was defined as a P-value smaller than 0.05.

7.5 Results

Out of twelve initial subjects, data were collected on nine subjects at the second timepoint (2 days at altitude) and seven at the third timepoint (7 days at altitude). Incomplete data were a result of two subjects that had developed severe AMS before the second timepoint, who then required treatment with dexamethasone or acetazolamide; these subjects contributed data only to the sea level, or first, timepoint. One subject was left the study right after the sea level measurement, and another was excluded prior to the third timepoint. Finally, a subject was unable to tolerate maximal hyperventilation on day 7 at altitude and was thus excluded. Table 7.1 outlines the number of subjects included in each timepoint of the study.

Table 7.2: Baseline (resting) physiology at sea level, 2 days at altitude, and 7 days at altitude.

Parameter	Sea Level	Day 2 at Altitude	Day 7 at Altitude	P-value
EtCO_2 , kPa	4.5 ± 0.8	3.3 ± 0.4 †	3.2 ± 0.4 †	<0.001
SpO_2 , %	98.0 ± 1.5	80.5 ± 4.3 †	84.4 ± 5.8 †	<0.001
StO_2 , %	69.5 ± 4.4	65.0 ± 5.4	62.2 ± 4.1 †	0.005
THC , μM	71.4 ± 28.4	61.8 ± 13.1	63.9 ± 10.2	0.502
HbO_2 , μM	49.2 ± 18.5	40.0 ± 8.7	39.6 ± 6.0	0.172
Hb , μM	22.2 ± 10.5	21.9 ± 5.5	24.3 ± 5.3	0.779
PSV , cm/s	82.4 ± 15.6	100.9 ± 32.4	84.6 ± 27.8	0.203

Values listed as mean ± SD; P-values from one-way ANOVA test; † Significantly different from sea level; ‡ Significantly different from 2 days at altitude.

7.5.1 Effects of Altitude on Baseline Physiology

Baseline (resting) values of both systemic and cerebral parameters are shown in Table 7.2, with significant differences between timepoints noted. EtCO_2 decreased from 4.5 kPa ± 0.8 kPa at sea level to 3.3 kPa ± 0.4 kPa after 2 days at altitude. The change in EtCO_2 between days 2 and 7 at altitude was not significant. Baseline SpO_2 decreased from 98.0% ± 1.5% at sea level to 80.5% ± 4.3% at day 2 at altitude. At day 7 at altitude, baseline SpO_2 was 84.4% ± 5.8% – still significantly lower than sea level, but not different than day 2.

In contrast to peripheral oxygen saturation, baseline cerebral oxygen saturation continued to decline throughout each of the three timepoints, although the drop was only significant between sea level and day 7 at altitude. StO_2 decreased from 69.5% ± 4.4% at sea level to 65.0% ± 5.4% after 2 days at altitude, and further to 62.2% ± 4.1% on day 7. All the other baseline cerebral oxygenation parameters (THC , HbO_2 , Hb) did not change among the three timepoints.

Table 7.3: Effects of hyperventilation at sea level, 2 days at altitude, and 7 days at altitude.

Parameter	Sea Level	Day 2 at Altitude	Day 7 at Altitude	P-value
ΔSpO_2 , %	0.9 ± 1.4	15.9 ± 6.7 *†	13.9 ± 5.2 *†	<0.001
ΔStO_2 , %	-5.1 ± 2.0 *	5.2 ± 3.3 *†	2.5 ± 5.4 †	<0.001
ΔTHC , μM	-5.1 ± 10.4	-3.1 ± 3.1 *	-1.5 ± 2.3	0.473
ΔHbO_2 , μM	-7.1 ± 6.2 *	0.9 ± 3.3 †	0.3 ± 3.1 †	0.001
ΔHb , μM	2.0 ± 5.1	-3.9 ± 2.3 *†	-1.7 ± 4.0	0.006
rPSV, %	-33.1 ± 12.8 *	-32.6 ± 21.4 *	-34.0 ± 9.7 * †	0.980
rCBF, %	-20.9 ± 13.2 *	-25.7 ± 16.3 *	-31.2 ± 24.9 *	0.440

Values listed as mean ± SD; * Significant change with hyperventilation; P-values from one-way ANOVA test; † Significantly different from sea level; ‡ Day 7 significantly different from day 2 at altitude.

Baseline PSV also did not change significantly from sea level to either day at altitude.

7.5.2 Effects of Altitude on Response to Hyperventilation

Table 7.3 summarizes changes in systemic and cerebral parameters induced by hyperventilation at all three timepoints.

The study cohort's peripheral and cerebral oxygen saturation responses to hyperventilation are shown in Figure 7.5. Hyperventilation increased SpO_2 at altitude, but remained unchanged at sea level. After 2 days at altitude, hyperventilation induced an increase in SpO_2 of $15.9\% \pm 6.7\%$, and after 7 days, $13.9\% \pm 5.2\%$.

Following hyperventilation, StO_2 decreased $-5.1\% \pm 2.0\%$ at sea level. But after 2 days at altitude, hyperventilation resulted in an increase in cerebral oxygen saturation of $5.2\% \pm 3.3\%$. After 7 days at altitude, hyperventilation did not induce a significant change in StO_2 . Changes in total hemoglobin concentration were not affected by altitude, but changes in oxy- and deoxyhemoglobin concentration at 2 days after being at altitude were different from sea level. ΔHbO_2 decreased $-7.1 \mu\text{M} \pm 6.2\mu\text{M}$ at sea level, but did not change with

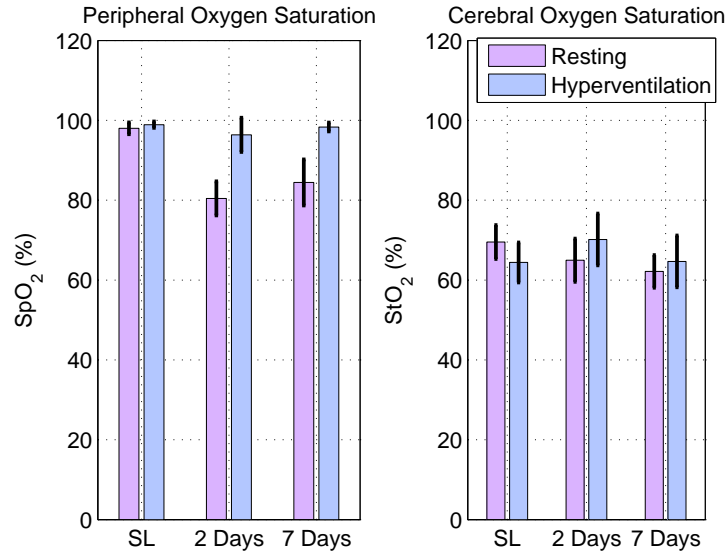


Figure 7.5: Bar plot showing peripheral and cerebral oxygen saturation changes with hyperventilation. The hyperventilation protocol was performed at three timepoints: 1) approximately sea level (SL), 2) 4559 m above sea level after 2 days at altitude, 3) 4559 m above sea level after 7 days at altitude.

hyperventilation at either altitude timepoints. On the other hand, ΔHb saw no change at sea level or 7 days at altitude, but dropped $-3.9 \mu\text{M} \pm 2.3 \mu\text{M}$ after 2 days at altitude.

Figure 7.6 shows changes in PSV and CBF with hyperventilation, and the effects of high altitude on cohort response. $r\text{PSV}$ dropped with hyperventilation at all three timepoints, with no significant difference in magnitude between sea level and high altitude. $r\text{PSV}$ at sea level decreased $-33.1\% \pm 12.8\%$, $-32.6\% \pm 21.4\%$ after 2 days at altitude, and $-34.0\% \pm 9.7\%$.

DCS measured a decrease in $r\text{CBF}$ of $-20.9\% \pm 13.2\%$ at sea level, $-25.7\% \pm 16.3\%$ after 2 days at altitude, and $-31.2\% \pm 24.9\%$ after 7 days. There was a trend towards more pronounced decreases in CBF with hyperventilation with increasing time at altitude, but it did not reach significance.

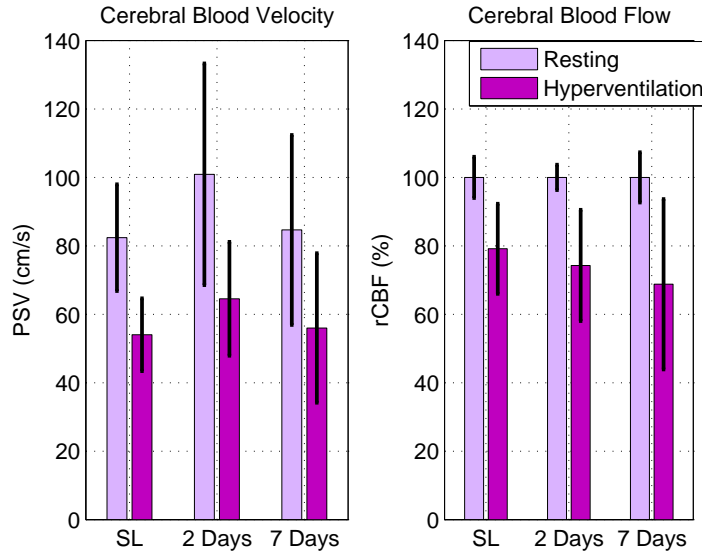


Figure 7.6: Bar plot showing cerebral blood flow changes with hyperventilation. The hyperventilation protocol was performed at three timepoints: 1) approximately sea level (SL), 2) 4559 m above sea level after 2 days at altitude, 3) 4559 m above sea level after 7 days at altitude.

7.5.3 Correlations Between Parameters

Baseline SpO_2 was correlated with baseline StO_2 ($\rho = 0.52$, $P = 0.003$). Baseline PSV correlated significantly with baseline StO_2 ($R = -0.52$, $P = 0.003$) as well as with SpO_2 ($R = -0.37$, $P = 0.039$). However, as seen in Figure 7.7, no association was found between changes in $rCBF$ and $rPSV$ with hyperventilation ($\rho = -0.02$, $P = 0.91$). $rCBF$ was also not correlated with changes in any of the DOS parameters.

7.6 Discussion

We have reported the changing, dynamic relationship between peripheral oxygenation, cerebral oxygenation, and cerebral blood flow that occurs with hyperventilation after as-

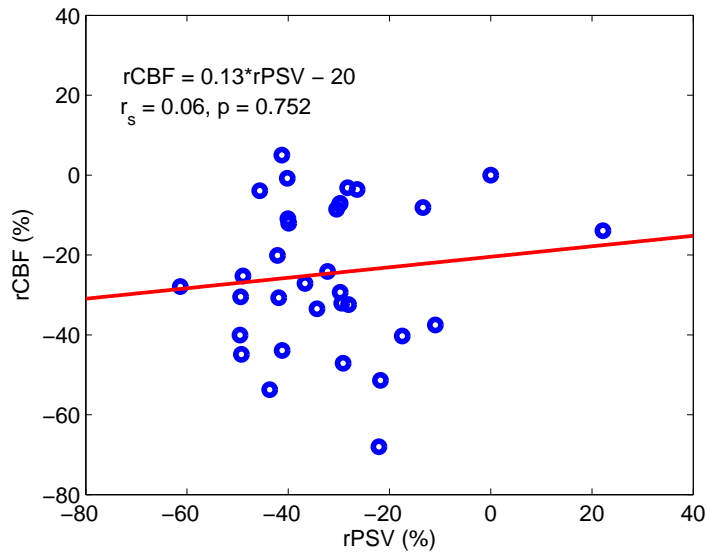


Figure 7.7: Scatter plot illustrating the correlation between $rCBF$ (as measured by DCS) and $rPSV$ (as measured by TCD). The fit line has a slope of 0.13 and an offset of -20%. No significant correlation was found between the two modalities.

cent to altitude and following partial acclimatization. There are several novel findings in this study. Firstly, we have demonstrated the feasibility of using DCS to measure cortical blood flow with a high temporal resolution in an austere environment. We have also documented the effects of voluntary hyperventilation on cerebral oxygenation and cerebral blood flow over time spent at high altitude. And lastly, on an instrumentation front, we have successfully implemented multi-wavelength DCS in a compact, rugged module for monitoring both cerebral blood flow and oxygenation changes simultaneously.

Peripheral oxygen saturation decreased after 2 days at altitude and then rebounded partially after 7 days at altitude, but still remained lower than sea level. Cerebral oxygen saturation, on the other hand, continued to decrease from 2 to 7 days, and the difference from sea level reached significance after 7 days. This demonstrates a differential effect

of acclimatization on peripheral and cerebral oxygenation. This divergence may be attributable to the differences in the vascular response to arterial CO₂ between the periphery and the central nervous system. Interestingly, at simulated extreme altitudes, Hornbein *et al* found a significant correlation between subjects with a more pronounced hypoxic ventilatory response (HVR) and increased impairment on a variety of cognitive tasks [102].

This contrasts with other reports demonstrating improved climbing performance in subjects with a higher HVR [144, 167, 202]. This dichotomy between athletic and cognitive performance parallels the divergence between peripheral and cerebral oxygenation seen in the present study. Subjects with a more pronounced HVR are better able to increase peripheral oxygenation. However, this also results in hypocapnia which leads to cerebral vasoconstriction, exacerbating cerebral hypoxia. Thus, those travellers to very high altitudes that are most adapted to deal with the physical rigors of altitude may be most susceptible to cerebral hypoxia and the associated structural and functional changes.

This study is the first of its kind to utilize the absolute cerebral oximeter in the assessment of cerebral oxygen saturation. Previous studies have relied on examining regional cerebral saturation trends making direct comparisons with peripheral saturation difficult. However, the inherent weakness of cerebral DOS technology remain [174]. DOS monitors measure the saturation of oxy- and deoxyhemoglobin in all biological material beneath the probe (arterioles, capillaries, tissue, and veins) and assumes a stable ratio of arterial-to-venous compartment volumes. Therefore, relative changes in these compartment volumes could also lead to changes in StO₂ [94]. This is particularly relevant given the putative role

of venous hypertension in the in the pathogenesis of AMS/HACE [254, 250, 252].

Hyperventilation on day 2 at 4559 m caused both peripheral and cerebral oxygen saturation to return to sea level values. In the non-acclimatized subject, the normalization of peripheral oxygenation probably overcomes the negative effects of hypocapnic cerebral vasoconstriction to increase cerebral oxygenation. The situation after acclimatization, however, is harder to explain. After hyperventilation on day 7 at 4559 m, peripheral oxygen saturation again returned to its sea level value whereas cerebral oxygenation did not. Thus, acclimatization abolished the initial improvement in cerebral oxygenation seen with hyperventilation.

The ideal modality to measure CBF at high altitudes would provide a real-time, non-invasive, portable quantification of absolute blood flow. While various techniques have been used to approximate cerebral blood flow at altitude, all have important shortcomings [180]. Severinghaus applied the Kety-Schmidt nitrous oxide technique [119] at altitude, demonstrating an initial increase in CBF of 24% 6 to 12 hours after ascent, declining to 13% above baseline after 3 to 5 days of acclimatization [207]. However, this modality requires that CBF be at steady state and is not appropriate for dynamic studies as the temporal resolution is poor.

Transcranial Doppler ultrasound is currently the most common method for estimating CBF at altitude. The accuracy of this measurement is predicated on the assumption that MCA diameter remains constant at altitude and assumes no regional variation. An increase in measured CBFV may reflect either a decrease in MCA diameter and thus a net decrease

in CBF, or an increase in diameter of smaller arteries and arterioles downstream from the MCA and thus a net increase in CBF. Although several studies have demonstrated that MCA diameter changes less than smaller intracranial vessels with small, acute changes in blood pressure or CO₂ [76, 206], a more recent study demonstrated that MCA diameter changes significantly with altitude [251]. More recently, it has been shown that intact or partially intact cerebral vascular responses to CO₂ are associated with poor correlation between CBFV and CBF [200].

Diffuse correlation spectroscopy was successfully used for the first time in a high altitude environment. We modified a module specifically for this study – added an additional wavelength of laser, made the instrument rugged and portable, and used our DCS device in conjunction with a commercial DOS device to get absolute optical properties of tissue. Both probes and software were made user-friendly – enough so to be operated solely by a medical doctor with no prior training in optics for use on all this study’s experiments. Future versions of the device could be improved in various ways for further implementation at high altitudes.

In this study, DCS measured a consistent reduction in CBF with hyperventilation at all timepoints. There was a trend towards a larger drop in CBF with hyperventilation with increasing time at altitude, but it was not significant. This potential exaggeration of the hypocapnic vasoconstrictive response with increasing time at altitude is in agreement with the findings of Lucas *et al* [135]. It also may explain why the initial improvement in cerebral oxygen saturation via hyperventilation is abolished with increasing time at altitude.

The larger decrease in CBF overcomes the increase in peripheral oxygen saturation, leading to an overall no change in cerebral oxygenation.

Although DCS signals consistently demonstrated the expected reduction in rCBF following hyperventilation, there was considerable inter-subject variability that may reflect physiological differences in reaction to altitude and acclimatization (see Section 7.1). Larger studies and further refinements in technique are necessary to reduce inter-subject variability.

There was no correlation between relative changes in CBFV as measured by TCD and CBF as measured by DCS. The two techniques differ considerably in what they are measuring, and thus this lack of correlation is not completely surprising. TCD measures flow velocity through the MCA and thus is a global indicator of changes in flow dynamics, reflecting changes to a large region of the concerned hemisphere and measures velocity of flow rather than flow. It is thus susceptible to misinterpretation when the diameter of the measured vessel changes. DCS measures regional cortical perfusion in a small portion of tissue and reflects changes in a focal region of brain parenchyma.

7.7 Conclusion

Hyperventilation induced lowered cerebral blood flow and velocity both at sea level and at altitude. Diffuse correlation spectroscopy was shown to be a promising technology with the potential to increase our understanding of changes in cerebral blood flow at altitude. Larger studies and further refinements in technique are necessary to reduce inter-subject

variability.

Chapter 8

Conclusions and Future Work

This dissertation has emphasized the translation of hybrid diffuse optics, i.e., the combination of diffuse optical spectroscopy (DOS) and diffuse correlation spectroscopy (DCS), to the neurocritical care unit. Prior to this work, hybrid diffuse optics had been tested on animal brain and to some extent in human applications (e.g. healthy subjects, neonates, ischemic stroke patients). But DCS/DOS had not been used to investigate a severely brain-injured population before.

Neurocritical care patients could benefit from a continuous cerebral blood flow and oxygenation monitor. They are in danger of secondary injury while residing in the intensive care unit, e.g., following a severe primary insult such as traumatic brain injury or ruptured aneurysm. Clinicians now routinely monitor intracranial pressure (ICP), which has led to lower mortality rates, but ICP can only serve as a surrogate measure of perfusion. Additional information about the state of their cerebral physiology could help prevent further brain damage and even death. My work suggests that DCS/DOS should add significantly

to the existing monitoring tools.

In Chapter 4, we described the first successful validation of DCS-measured cerebral blood flow in adults, against gold-standard method stable xenon-enhanced computed tomography. This experiment showed good agreement between the two techniques, and since the study cohort was comprised of brain-injured patients, it took first steps towards establishing that DCS could serve as a blood flow monitor in the neurointensive care unit.

The study outlined in Chapter 5 stemmed from the need to understand the normative response of head-of-bed manipulation. We had looked at the response of brain-injured patients, and wanted to know what DCS/DOS would measure in healthy controls. From that need, it was decided that an entire study could be born out of this idea – the effects of age on normative responses to not just head-of-bed manipulation, but a supine-to-standing posture change. Results showed that healthy subjects across the age spectrum experience significant postural declines in frontal cortical blood flow. This study also showed that hybrid diffuse optics is easily implemented for studying cerebral hemodynamics in healthy subjects across the age spectrum.

Chapter 6 explored experiments done with DCS/DOS monitoring during two simple and common interventions performed regularly in the neurointensive care unit: head-of-bed manipulation and induced hyperoxia. This was an exercise in identifying what issues might fall upon us while monitoring cerebral hemodynamics in this type of patient population. We also wanted to see if hybrid diffuse optics could provide additional information about patient condition. DCS/DOS was able to detect differences in cerebral hemodynamic

responses of brain-injured patients versus healthy controls during posture change. During induced hyperoxia, both the invasive brain tissue oxygen and DOS monitors observed increases in oxygenation, but the relative changes differed. Overall, knowing real-time, continuous, unpredictable trends in blood flow and oxygenation gives clinicians extra valuable information, particularly in situations and interventions by the bedside where they would ordinarily be somewhat steering blindly.

Lastly, we took our lab-built instrumentation to the heights of the Italian Alps for a unique opportunity to measure cerebral hemodynamics on adults at high altitude. Many of the issues seen in those afflicted by severe altitude-related illness are similar to those of neurocritical care patients. Thus, we investigated whether hybrid diffuse optics could help those in danger of high altitude cerebral edema, which can lead to death if left untreated. This represented the first time DCS was used in such an environment, and its successful implementation led us to believe that it could be used as a much-needed high altitude blood flow monitor.

The use of DCS continues to spread outside of our group, e.g., as other laboratories find even more applications and uses. The main hurdles that prevent its eventual widespread acceptance by clinicians include: 1) need for better probe interface engineering, 2) issues with going through hair, 3) relative rather than absolute blood flow measurements. Groups including ours are in the midst of tackling these challenges.

The trend in neurocritical care continues to move towards individualized medicine, and to do so, clinicians must utilize multimodal monitoring. DCS/DOS, being non-invasive

and relatively inexpensive, has the ability to easily fit in with other monitoring techniques with little cost and potentially great benefit to patient outcome. Future work should involve long-term (>12 hours) monitoring and looking at possible vasospasm detection.

Bibliography

- [1] B. J. Ackerson, R. L. Dougherty, N. M. Reguigui, and U. Nobbmann. Correlation transfer - Application of radiative transfer solution methods to photon correlation problems. *Journal of Thermophysics and Heat Transfer*, 6(4):577–588, January 1992.
- [2] G. S. Adair. The Oxygen Dissociation Curve of Hemoglobin. *The Journal of Biological Chemistry*, January 1925.
- [3] P. D. Adelson, E. Nemoto, A. Colak, and M. Painter. The use of near infrared spectroscopy (NIRS) in children after traumatic brain injury: a preliminary report. *Acta neurochirurgica. Supplement*, 71:250–254, 1998.
- [4] P. G. Al-Rawi. Near infrared spectroscopy in brain injury: today’s perspective. *Acta neurochirurgica. Supplement*, 95:453–457, 2005.
- [5] Noam Alperin, Sang H. Lee, Anusha Sivaramakrishnan, and Stephen G. Hushek. Quantifying the effect of posture on intracranial physiology in humans by MRI flow studies. *J. Magn. Reson. Imaging*, 22(5):591–596, November 2005.
- [6] Peter J. Andrews and Giuseppe Citerio. Intracranial pressure. Part one: historical overview and basic concepts. *Intensive care medicine*, 30(9):1730–1733, September 2004.

- [7] B. Asgeirsson, P. O. Grände, and C. H. Nordström. A new therapy of post-trauma brain oedema based on haemodynamic principles for brain volume regulation. *Intensive care medicine*, 20(4):260–267, 1994.
- [8] P. J. Aucoin, H. R. Kotilainen, N. M. Gantz, R. Davidson, P. Kellogg, and B. Stone. Intracranial pressure monitors. Epidemiologic study of risk factors and infections. *The American journal of medicine*, 80(3):369–376, March 1986.
- [9] M. Balestreri, M. Czosnyka, D. A. Chatfield, L. A. Steiner, E. A. Schmidt, P. Smielewski, B. Matta, and J. D. Pickard. Predictive value of Glasgow coma scale after brain trauma: change in trend over the past ten years. *Journal of Neurology, Neurosurgery & Psychiatry*, 75(1):161–162, January 2004.
- [10] Buddha Basnyat and David R. Murdoch. High-altitude illness. *Lancet*, 361(9373):1967–1974, June 2003.
- [11] J. B. Bederson, I. M. Germano, and L. Guarino. Cortical blood flow and cerebral perfusion pressure in a new noncraniotomy model of subarachnoid hemorrhage in the rat. *Stroke*, 26(6), June 1995.
- [12] J. M. Bland and D. G. Altman. Statistical methods for assessing agreement between two methods of clinical measurement. *Lancet*, 1(8476):307–310, February 1986.
- [13] D. A. Boas, L. E. Campbell, and A. G. Yodh. Scattering and Imaging with Diffusing Temporal Field Correlations. *Physical Review Letters*, 75(9):1855+, 1995.
- [14] D. A. Boas, M. A. O’Leary, B. Chance, and A. G. Yodh. Scattering and wavelength transduction of diffuse photon density waves. *Physical Review E*, 47:R2999–R3002, May 1993.

- [15] D. A. Boas and A. G. Yodh. Spatially varying dynamical properties of turbid media probed with diffusing temporal light correlation. *J. Opt. Soc. Am. A*, 14(1):192–215, January 1997.
- [16] David A. Boas. *Diffuse Photon Probes of Structural and Dynamical Properties of Turbid Media: Theory and Biomedical Applications*. PhD thesis, University of Pennsylvania, 1996.
- [17] David A. Boas, Tom Gaudette, Gary Strangman, Xuefeng Cheng, John J. A. Marota, and Joseph B. Mandeville. The Accuracy of Near Infrared Spectroscopy and Imaging during Focal Changes in Cerebral Hemodynamics. *NeuroImage*, 13(1):76–90, January 2001.
- [18] P. Bolognese, J. I. Miller, I. M. Heger, and T. H. Milhorat. Laser-Doppler flowmetry in neurosurgery. *Journal of neurosurgical anesthesiology*, 5(3):151–158, July 1993.
- [19] Brain Trauma Foundation, American Association of Neurological Surgeons, Congress of Neurological Surgeons, Joint Section on Neurotrauma and Critical Care, AANS/CNS, Susan L. Bratton, Randall M. Chestnut, Jamshid Ghajar, Flora F. McConnell Hammond, Odette A. Harris, Roger Hartl, Geoffrey T. Manley, Andrew Nemecek, David W. Newell, Guy Rosenthal, Joost Schouten, Lori Shutter, Shelly D. Timmons, Jamie S. Ullman, Walter Videtta, Jack E. Wilberger, and David W. Wright. Guidelines for the management of severe traumatic brain injury. VIII. Intracranial pressure thresholds. *Journal of neurotrauma*, 24 Suppl 1, 2007.
- [20] David J. Brenner and Eric J. Hall. Computed Tomography An Increasing Source of Radiation Exposure. *N Engl J Med*, 357(22):2277–2284, November 2007.

- [21] J. P. Broderick, T. G. Brott, J. E. Duldner, T. Tomsick, and A. Leach. Initial and recurrent bleeding are the major causes of death following subarachnoid hemorrhage. *Stroke; a journal of cerebral circulation*, 25(7):1342–1347, July 1994.
- [22] K. Büchner, J. Meixensberger, J. Dings, and K. Roosen. Near-infrared spectroscopy— not useful to monitor cerebral oxygenation after severe brain injury. *Zentralblatt für Neurochirurgie*, 61(2):69–73, 2000.
- [23] Erin M. Buckley. *Cerebral Hemodynamics in High-risk Neonates Probed by Diffuse Optical Spectroscopies*. PhD thesis, University of Pennsylvania, 2011.
- [24] Erin M. Buckley, Noah M. Cook, Turgut Durduran, Meeri N. Kim, Chao Zhou, Regine Choe, Guoqiang Yu, Susan Schultz, Chandra M. Sehgal, Daniel J. Licht, Peter H. Arger, Mary E. Putt, Hallam H. Hurt, and Arjun G. Yodh. Cerebral hemodynamics in preterm infants during positional intervention measured with diffuse correlation spectroscopy and transcranial Doppler ultrasound. *Opt. Express*, 17(15):12571–12581, July 2009.
- [25] Erin M. Buckley, Dalton Hance, Thomas Pawlowski, Jennifer Lynch, Felice B. Wilson, Rickson C. Mesquita, Turgut Durduran, Laura K. Diaz, Mary E. Putt, Daniel J. Licht, Mark A. Fogel, and Arjun G. Yodh. Validation of diffuse correlation spectroscopic measurement of cerebral blood flow using phase-encoded velocity mapping magnetic resonance imaging. *Journal of biomedical optics*, 17(3), March 2012.
- [26] Brian J. Carey, Ronney B. Panerai, and John F. Potter. Effect of Aging on Dynamic Cerebral Autoregulation During Head-Up Tilt. *Stroke*, 34(8):1871–1875, August 2003.
- [27] S. A. Carp, G. P. Dai, D. A. Boas, M. A. Franceschini, and Y. R. Kim. Validation of diffuse correlation spectroscopy measurements of rodent cerebral blood flow with

simultaneous arterial spin labeling MRI; towards MRI-optical continuous cerebral metabolic monitoring. *Biomed. Opt. Express*, 1(2):553–565, September 2010.

- [28] Kenneth M. Case and P. F. Zweifel. *Linear transport theory*. Addison-Wesley Pub. Co., 1967.
- [29] G. Cavaletti, P. Garavaglia, G. Arrigoni, and G. Tredici. Persistent memory impairment after high altitude climbing. *International journal of sports medicine*, 11(3):176–178, June 1990.
- [30] W. F. Cheong, S. A. Prael, and A. J. Welch. A review of the optical properties of biological tissues. *Quantum Electronics, IEEE Journal of*, 26(12):2166–2185, December 1990.
- [31] R. M. Chesnut, L. F. Marshall, M. R. Klauber, B. A. Blunt, N. Baldwin, H. M. Eisenberg, J. A. Jane, A. Marmarou, and M. A. Foulkes. The role of secondary brain injury in determining outcome from severe head injury. *The Journal of trauma*, 34(2):216–222, February 1993.
- [32] R. M. Chesnut, S. B. Marshall, J. Piek, B. A. Blunt, M. R. Klauber, and L. F. Marshall. Early and late systemic hypotension as a frequent and fundamental source of cerebral ischemia following severe brain injury in the Traumatic Coma Data Bank. *Acta neurochirurgica. Supplementum*, 59:121–125, 1993.
- [33] Randall M. Chesnut, Nancy Temkin, Nancy Carney, Sureyya Dikmen, Carlos Rondina, Walter Videtta, Gustavo Petroni, Silvia Lujan, Jim Pridgeon, Jason Barber, Joan Machamer, Kelley Chaddock, Juanita M. Celix, Marianna Cherner, and Terence Hendrix. A Trial of Intracranial-Pressure Monitoring in Traumatic Brain Injury. *New England Journal of Medicine*, 367(26):2471–2481, December 2012.

- [34] C. Cheung, J. P. Culver, K. Takahashi, J. H. Greenberg, and A. G. Yodh. In vivo cerebrovascular measurement combining diffuse near-infrared absorption and correlation spectroscopies. *Physics in Medicine and Biology*, pages 2053–2065, 2001.
- [35] Chierigato, Arturo, Tanfani, Alessandra, Compagnone, Christian, Turrini, Claudia, Sarpieri, Federica, Ravaldini, Maurizio, Targa, Luigi, Fainardi, and Enrico. Global cerebral blood flow and CPP after severe head injury: a xenon-CT study. *Intensive Care Medicine*, 33(5):856–862, May 2007.
- [36] Regine Choe. *Diffuse Optical Tomography and Spectroscopy of Breast Cancer and Fetal Brain*. PhD thesis, University of Pennsylvania, 2005.
- [37] JeeHyun Choi, Martin Wolf, Vladislav Toronov, Ursula Wolf, Chiara Polzonetti, Dennis Hueber, Larisa P. Safonova, Rajarsi Gupta, Antonios Michalos, William Mantulin, and Enrico Gratton. Noninvasive determination of the optical properties of adult brain: near-infrared spectroscopy approach. *Journal of Biomedical Optics*, 9(1):221+, 2004.
- [38] J. P. Coles. Imaging after brain injury. *British journal of anaesthesia*, 99(1):49–60, July 2007.
- [39] M. Cope and D. T. Delpy. System for long-term measurement of cerebral blood and tissue oxygenation on newborn infants by near infra-red transillumination. *Medical & biological engineering & computing*, 26(3):289–294, May 1988.
- [40] Manuela Cormio, Claudia S. Robertson, and Raj K. Narayan. Secondary insults to the injured brain. *Journal of Clinical Neuroscience*, 4(2):132–148, April 1997.
- [41] Olaf L. Cremer, Gert W. van Dijk, Erik van Wensen, Geert J. Brekelmans, Karel G. Moons, Loek P. Leenen, and Cor J. Kalkman. Effect of intracranial pressure mon-

itoring and targeted intensive care on functional outcome after severe head injury. *Critical care medicine*, 33(10):2207–2213, October 2005.

- [42] J. Cruz. Cerebral oxygenation. Monitoring and management. *Acta neurochirurgica. Supplementum*, 59:86–90, 1993.
- [43] J. Cruz, J. L. Jaggi, and O. J. Hoffstad. Cerebral blood flow, vascular resistance, and oxygen metabolism in acute brain trauma: redefining the role of cerebral perfusion pressure? *Critical care medicine*, 23(8):1412–1417, August 1995.
- [44] S. C. CULLEN and E. G. GROSS. The anesthetic properties of xenon in animals and human beings, with additional observations on krypton. *Science (New York, N.Y.)*, 113(2942):580–582, May 1951.
- [45] M. Czosnyka, P. Smielewski, S. Piechnik, L. A. Steiner, and J. D. Pickard. Cerebral autoregulation following head injury. *J Neurosurg*, 95(5):756–763, November 2001.
- [46] B. Davison. *Neutron transport theory*. Clarendon Press, 1957.
- [47] C. De Deyne. Jugular bulb oximetry: the link between cerebral and systemic management of severe head injury. *Intensive care medicine*, 25(5):430–431, May 1999.
- [48] D. T. Delpy, M. Cope, P. van der Zee, S. Arridge, S. Wray, and J. Wyatt. Estimation of optical pathlength through tissue from direct time of flight measurement. *Physics in Medicine and Biology*, 33(12):1433+, December 2000.
- [49] P. D. Dernbach, J. R. Little, S. C. Jones, and Z. Y. Ebrahim. Altered cerebral autoregulation and CO₂ reactivity after aneurysmal subarachnoid hemorrhage. *Neurosurgery*, 22(5):822–826, May 1988.
- [50] Mamadou Diop, Kyle Verdecchia, Ting-Yim Lee, and Keith St Lawrence. Calibration of diffuse correlation spectroscopy with a time-resolved near-infrared tech-

nique to yield absolute cerebral blood flow measurements. *Biomed. Opt. Express*, 2(7):2068–2081, July 2011.

- [51] E. M. Doppenberg, A. Zauner, R. Bullock, J. D. Ward, P. P. Fatouros, and H. F. Young. Correlations between brain tissue oxygen tension, carbon dioxide tension, pH, and cerebral blood flow—a better way of monitoring the severely injured brain? *Surgical neurology*, 49(6):650–654, June 1998.
- [52] A. Duncan, J. H. Meek, M. Clemence, C. E. Elwell, P. Fallon, L. Tyszczuk, M. Cope, and D. T. Delpy. Measurement of cranial optical path length as a function of age using phase resolved near infrared spectroscopy. *Pediatric research*, 39(5):889–894, May 1996.
- [53] Ian F. Dunn, Dilantha B. Ellegala, Zachary N. Litvack, and Dong H. Kim. Neuromonitoring in neurological critical care. *Neurocritical Care*, 4(1):83–92, February 2006.
- [54] T. Durduran. *Non-Invasive Measurements of Tissue Hemodynamics with Hybrid Diffuse Optical Methods*. PhD thesis, University of Pennsylvania, 2004.
- [55] T. Durduran, R. Choe, W. B. Baker, and A. G. Yodh. Diffuse optics for tissue monitoring and tomography. *Reports on Progress in Physics*, 73(7):076701+, June 2010.
- [56] Turgut Durduran, David L. Minkoff, Meeri N. Kim, Dalton Hance, Erin M. Buckley, Mari Tobita, Jiongjiong Wang, Joel H. Greenberg, John A. Detre, and Arjun G. Yodh. Concurrent MRI and Diffuse Correlation and Near-Infrared Spectroscopic Measurement of Cerebral Hemodynamic Response to Hypercapnia and Hyperoxia. OSA Technical Digest (CD), pages BTuB2+. Optical Society of America, April 2010.

- [57] Turgut Durduran, Guoqiang Yu, Mark G. Burnett, John A. Detre, Joel H. Greenberg, Jiongjiong Wang, Chao Zhou, and Arjun G. Yodh. Diffuse optical measurement of blood flow, bloodoxygenation, and metabolism in a human brain during sensorimotorcortex activation. *Opt. Lett.*, 29(15):1766–1768, 2004.
- [58] Turgut Durduran, Chao Zhou, Erin M. Buckley, Meeri N. Kim, Guoqiang Yu, Regine Choe, J. William Gaynor, Thomas L. Spray, Suzanne M. Durning, Stefanie E. Mason, Lisa M. Montenegro, Susan C. Nicolson, Robert A. Zimmerman, Mary E. Putt, Jiongjiong Wang, Joel H. Greenberg, John A. Detre, Arjun G. Yodh, and Daniel J. Licht. Optical measurement of cerebral hemodynamics and oxygen metabolism in neonates with congenital heart defects. *Journal of Biomedical Optics*, 15(3):037004+, 2010.
- [59] Turgut Durduran, Chao Zhou, Brian L. Edlow, Guoqiang Yu, Regine Choe, Meeri N. Kim, Brett L. Cucchiara, Mary E. Putt, Qaisar Shah, Scott E. Kasner, Joel H. Greenberg, Arjun G. Yodh, and John A. Detre. Transcranial optical monitoring of cerebrovascular hemodynamics in acute stroke patients. *Opt. Express*, 17(5):3884–3902, March 2009.
- [60] Q. J. Durward, A. L. Amacher, R. F. Del Maestro, and W. J. Sibbald. Cerebral and cardiovascular responses to changes in head elevation in patients with intracranial hypertension. *Journal of neurosurgery*, 59(6):938–944, December 1983.
- [61] Brian L. Edlow, Meeri N. Kim, Turgut Durduran, Chao Zhou, Mary E. Putt, Arjun G. Yodh, Joel H. Greenberg, and John A. Detre. The effects of healthy aging on cerebral hemodynamic responses to posture change. *Physiological Measurement*, 31(4):477+, April 2010.

- [62] E. M. Enevoldsen and F. T. Jensen. Autoregulation and CO₂ responses of cerebral blood flow in patients with acute severe head injury. *Journal of neurosurgery*, 48(5):689–703, May 1978.
- [63] D. H. Evans and W. N. McDicken. *Doppler ultrasound : physics, instrumentation, and signal processing*, volume 2nd. Wiley, 2000.
- [64] J. Y. Fan. Effect of backrest position on intracranial pressure and cerebral perfusion pressure in individuals with brain injury: a systematic review. *The Journal of neuroscience nursing : journal of the American Association of Neuroscience Nurses*, 36(5):278–288, October 2004.
- [65] M. Faul, L. Xu, M. M. Wald, and V. G. Coronado. Traumatic brain injury in the United States: Emergency department visits, hospitalizations and deaths 2002–2006. *Atlanta, GA: Centers for Disease Control and Prevention, National Center for Injury Prevention and Control*, 2010.
- [66] Nicolás Fayed, Pedro J. Modrego, and Humberto Morales. Evidence of brain damage after high-altitude climbing by means of magnetic resonance imaging. *The American journal of medicine*, 119(2):168.e1–168.e6, February 2006.
- [67] Z. Feldman, M. J. Kanter, C. S. Robertson, C. F. Contant, C. Hayes, M. A. Sheinberg, C. A. Villareal, R. K. Narayan, and R. G. Grossman. Effect of head elevation on intracranial pressure, cerebral perfusion pressure, and cerebral blood flow in head-injured patients. *Journal of neurosurgery*, 76(2):207–211, February 1992.
- [68] Eric A. Finkelstein, Phaedra S. Corso, and Ted R. Miller. *The Incidence and Economic Burden of Injuries in the United States*. Oxford University Press US, 2006.

- [69] F. A. FINNERTY, L. WITKIN, and J. F. FAZEKAS. Cerebral hemodynamics during cerebral ischemia induced by acute hypotension. *The Journal of clinical investigation*, 33(9):1227–1232, September 1954.
- [70] C. M. Fisher, J. P. Kistler, and J. M. Davis. Relation of cerebral vasospasm to subarachnoid hemorrhage visualized by computerized tomographic scanning. *Neurosurgery*, 6(1):1–9, January 1980.
- [71] Joshua B. Fishkin and Enrico Gratton. Propagation of photon-density waves in strongly scattering media containing an absorbing semi-infinite plane bounded by a straight edge. *J. Opt. Soc. Am. A*, 10(1):127–140, January 1993.
- [72] Thomas F. Floyd, James M. Clark, Robert Gelfand, John A. Detre, Sarah Ratcliffe, Dimitri Guvakov, Christian J. Lambertsen, and Roderic G. Eckenhoff. Independent cerebral vasoconstrictive effects of hyperoxia and accompanying arterial hypocapnia at 1 ATA. *J Appl Physiol*, 95(6):2453–2461, December 2003.
- [73] Louis Gagnon, Michèle Desjardins, Julien Jehanne-Lacasse, Louis Bherer, and Frédéric Lesage. Investigation of diffuse correlation spectroscopy in multi-layered media including the human head. *Opt. Express*, 16(20):15514–15530, September 2008.
- [74] T. J. Germon, P. D. Evans, N. J. Barnett, P. Wall, A. R. Manara, and R. J. Nelson. Cerebral near infrared spectroscopy: emitter-detector separation must be increased. *British Journal of Anaesthesia*, 82(6):831–837, June 1999.
- [75] J. Ghajar. Traumatic brain injury. *Lancet*, 356(9233):923–929, September 2000.
- [76] C. A. Giller, G. Bowman, H. Dyer, L. Mootz, and W. Krippner. Cerebral arterial diameters during changes in blood pressure and carbon dioxide during craniotomy. *Neurosurgery*, 32(5), May 1993.

- [77] C. A. Giller, P. Purdy, and W. W. Lindstrom. Effects of inhaled stable xenon on cerebral blood flow velocity. *AJNR Am J Neuroradiol*, 11(1):177–182, January 1990.
- [78] W. F. Good and D. Gur. Xenon-enhanced CT of the brain: effect of flow activation on derived cerebral blood flow measurements. *AJNR. American journal of neuroradiology*, 12(1):83–85, 1991.
- [79] Cecile B. Grandin, Thierry P. Duprez, Anne M. Smith, Catherine Oppenheim, Andre Peeters, Annie R. Robert, and Guy Cosnard. Which MR-derived Perfusion Parameters are the Best Predictors of Infarct Growth in Hyperacute Stroke? Comparative Study between Relative and Quantitative Measurements. *Radiology*, pages 2232010673+, March 2002.
- [80] Brian Gribbin, Thomas G. Pickering, Peter Sleight, and Richard Peto. Effect of Age and High Blood Pressure on Baroreflex Sensitivity in Man. *Circulation Research*, 29(4):424–431, October 1971.
- [81] Brigham Women’s Hospital Neurosurgery Group. Neuromonitoring in Neurological Critical Care. *Neurocritical Care*, 8(2):310, April 2008.
- [82] Thomas C. Gualtieri. *Brain Injury and Mental Retardation: Psychopharmacology and Neuropsychiatry*. Lippincott Williams & Wilkins, 2002.
- [83] D. Gur, H. Yonas, and W. F. Good. Local cerebral blood flow by xenon-enhanced CT: current status, potential improvements, and future directions. *Cerebrovascular and brain metabolism reviews*, 1(1):68–86, 1989.
- [84] R. C. Gur, P. D. Mozley, S. M. Resnick, G. L. Gottlieb, M. Kohn, R. Zimmerman, G. Herman, S. Atlas, R. Grossman, and D. Berretta. Gender differences in age effect on brain atrophy measured by magnetic resonance imaging. *Proceedings of the National Academy of Sciences*, 88(7):2845–2849, April 1991.

- [85] P. H. Hackett. The cerebral etiology of high-altitude cerebral edema and acute mountain sickness. *Wilderness & environmental medicine*, 10(2):97–109, 1999.
- [86] Peter H. Hackett and Robert C. Roach. High altitude cerebral edema. *High altitude medicine & biology*, 5(2):136–146, 2004.
- [87] I. K. Haitisma and A. I. Maas. Monitoring cerebral oxygenation in traumatic brain injury. *Progress in brain research*, 161:207–216, 2007.
- [88] David Hargroves, Raymond Tallis, Valerie Pomeroy, and Ajay Bhalla. The influence of positioning upon cerebral oxygenation after acute stroke: a pilot study. *Age Ageing*, 37(5):581–585, September 2008.
- [89] M. P. M. Harms, W. N. J. M. Colier, W. Wieling, J. W. M. Lenders, N. H. Secher, and J. J. van Lieshout. Orthostatic Tolerance, Cerebral Oxygenation, and Blood Velocity in Humans With Sympathetic Failure. *Stroke*, 31(7):1608–1614, July 2000.
- [90] A. Hartmann, C. Dettmers, F. J. Schuier, H. D. Wassmann, and H. W. Schumacher. Effect of stable xenon on regional cerebral blood flow and the electroencephalogram in normal volunteers. *Stroke*, 22(2):182–189, February 1991.
- [91] K. Haselsberger, R. Pucher, and L. M. Auer. Prognosis after acute subdural or epidural haemorrhage. *Acta neurochirurgica*, 90(3-4):111–116, 1988.
- [92] Richard C. Haskell, Lars O. Svaasand, Tsong-Tseh Tsay, Ti-Chen Feng, Matthew S. McAdams, and Bruce J. Tromberg. Boundary conditions for the diffusion equation in radiative transfer. *J. Opt. Soc. Am. A*, 11(10):2727–2741, October 1994.
- [93] C. Haubrich, A. Wendt, R. R. Diehl, and C. Klötzsch. Dynamic Autoregulation Testing in the Posterior Cerebral Artery. *Stroke*, 35(4):848–852, April 2004.

- [94] Martin Heine, Andrew W. Subudhi, and Robert C. Roach. Effect of ventilation on cerebral oxygenation during exercise: insights from canonical correlation. *Respiratory physiology & neurobiology*, 166(2):125–128, April 2009.
- [95] Hans J. Hennes, Carsten Lott, Michael Windirsch, Daniel F. Hanley, Stephan Boor, Ansgar Brambrink, and Wolfgang Dick. Noninvasive detection of intracerebral hemorrhage using near-infrared spectroscopy (NIRS). volume 3194, pages 42–54. SPIE, 1998.
- [96] Elizabeth M. C. Hillman. Optical brain imaging in vivo: techniques and applications from animal to man. *Journal of Biomedical Optics*, 12(5):051402+, 2007.
- [97] R. Hlatky, Y. Furuya, A. B. Valadka, J. Gonzalez, A. Chacko, Y. Mizutani, C. F. Contant, and C. S. Robertson. Dynamic autoregulatory response after severe head injury. *Journal of neurosurgery*, 97(5):1054–1061, November 2002.
- [98] M. Holzschuh, C. Woertgen, C. Metz, and A. Brawanski. Dynamic changes of cerebral oxygenation measured by brain tissue oxygen pressure and near infrared spectroscopy. *Neurological research*, 19(3):246–248, June 1997.
- [99] B. Honigman, M. K. Theis, J. Koziol-McLain, R. Roach, R. Yip, C. Houston, L. G. Moore, and P. Pearce. Acute mountain sickness in a general tourist population at moderate altitudes. *Annals of internal medicine*, 118(8):587–592, April 1993.
- [100] J. W. Hop, G. J. Rinkel, A. Algra, and J. van Gijn. Case-fatality rates and functional outcome after subarachnoid hemorrhage: a systematic review. *Stroke; a journal of cerebral circulation*, 28(3):660–664, March 1997.
- [101] Peter Horn, Peter Vajkoczy, Claudius Thome, Elke Muench, Lothar Schilling, and Peter Schmiedek. Xenon-Induced Flow Activation in Patients with Cerebral Insult

- Who Undergo Xenon-Enhanced CT Blood Flow Studies. *AJNR Am J Neuroradiol*, 22(8):1543–1549, September 2001.
- [102] T. F. Hornbein, B. D. Townes, R. B. Schoene, J. R. Sutton, and C. S. Houston. The cost to the central nervous system of climbing to extremely high altitude. *The New England journal of medicine*, 321(25):1714–1719, December 1989.
- [103] Katharine Hunt, Ilias Tachtsidis, Katharine Bleasdale-Barr, Clare Elwell, Christopher Mathias, and Martin Smith. Changes in cerebral oxygenation and haemodynamics during postural blood pressure changes in patients with autonomic failure. *Physiological Measurement*, 27(9):777–785, June 2006.
- [104] W. E. Hunt and R. M. Hess. Surgical risk as related to time of intervention in the repair of intracranial aneurysms. *Journal of neurosurgery*, 28(1):14–20, January 1968.
- [105] Ben P. M. Imholz, Wouter Wieling, Gert A. van Montfrans, and Karel H. Wesseling. Fifteen years experience with finger arterial pressure monitoring:. *Cardiovascular Research*, 38(3):605–616, June 1998.
- [106] C. H. Imray, S. Brearey, T. Clarke, D. Hale, J. Morgan, S. Walsh, and A. D. Wright. Cerebral oxygenation at high altitude and the response to carbon dioxide, hyperventilation and oxygen. The Birmingham Medical Research Expeditionary Society. *Clinical science (London, England : 1979)*, 98(2):159–164, February 2000.
- [107] T. J. Ingall, J. P. Whisnant, D. O. Wiebers, and W. M. O’Fallon. Has there been a decline in subarachnoid hemorrhage mortality? *Stroke*, 20(6):718–724, June 1989.
- [108] A. Jackowski, A. Crockard, G. Burnstock, R. R. Russell, and F. Kristek. The time course of intracranial pathophysiological changes following experimental subarach-

- noid haemorrhage in the rat. *Journal of cerebral blood flow and metabolism : official journal of the International Society of Cerebral Blood Flow and Metabolism*, 10(6):835–849, November 1990.
- [109] Matthias Jaeger, Martin U. Schuhmann, Martin Soehle, Christoph Nagel, and Jürgen Meixensberger. Continuous Monitoring of Cerebrovascular Autoregulation After Subarachnoid Hemorrhage by Brain Tissue Oxygen Pressure Reactivity and Its Relation to Delayed Cerebral Infarction. *Stroke*, 38(3):981–986, March 2007.
- [110] G. F. Jansen, A. Krins, and B. Basnyat. Cerebral vasomotor reactivity at high altitude in humans. *Journal of applied physiology (Bethesda, Md. : 1985)*, 86(2):681–686, February 1999.
- [111] R. W. Jansen, J. W. Lenders, T. Thien, and W. H. Hoefnagels. The influence of age and blood pressure on the hemodynamic and humoral response to head-up tilt. *Journal of the American Geriatrics Society*, 37(6):528–532, June 1989.
- [112] Frans F. Jobsis-vanderVliet. Discovery of the Near-Infrared Window into the Body and the Early Development of Near-Infrared Spectroscopy. *Journal of Biomedical Optics*, 4(4):392+, 1999.
- [113] A. J. Johnston, L. A. Steiner, A. K. Gupta, and D. K. Menon. Cerebral oxygen vasoreactivity and cerebral tissue oxygen reactivity. *Br J Anaesth*, 90(6):774–786, June 2003.
- [114] P. A. Jones, P. J. Andrews, S. Midgley, S. I. Anderson, I. R. Piper, J. L. Tocher, A. M. Housley, J. A. Corrie, J. Slattery, and N. M. Dearden. Measuring the burden of secondary insults in head-injured patients during intensive care. *Journal of neurosurgical anesthesiology*, 6(1):4–14, January 1994.

- [115] N. Juul, G. F. Morris, S. B. Marshall, and L. F. Marshall. Intracranial hypertension and cerebral perfusion pressure: influence on neurological deterioration and outcome in severe head injury. The Executive Committee of the International Selfotel Trial. *Journal of neurosurgery*, 92(1):1–6, January 2000.
- [116] Kai Kallenberg, Damian M. Bailey, Stefan Christ, Alexander Mohr, Robin Roukens, Elmar Menold, Thorsten Steiner, Peter Bärtzsch, and Michael Knauth. Magnetic resonance imaging evidence of cytotoxic cerebral edema in acute mountain sickness. *Journal of cerebral blood flow and metabolism*, 27(5):1064–1071, May 2007.
- [117] N. F. Kassell, J. C. Torner, J. A. Jane, E. C. Haley, and H. P. Adams. The International Cooperative Study on the Timing of Aneurysm Surgery. Part 2: Surgical results. *Journal of neurosurgery*, 73(1):37–47, July 1990.
- [118] E. Keller, A. Nadler, H. G. Imhof, P. Niederer, P. Roth, and Y. Yonekawa. New methods for monitoring cerebral oxygenation and hemodynamics in patients with subarachnoid hemorrhage. *Acta neurochirurgica. Supplement*, 82:87–92, 2002.
- [119] Seymour S. Kety. The theory and applications of the exchange of inert gas at the lungs and tissues. *Pharmacological Reviews*, 3(1):1–41, March 1951.
- [120] Meeri Kim, Turgut Durduran, Suzanne Frangos, Brian Edlow, Erin Buckley, Heather Moss, Chao Zhou, Guoqiang Yu, Regine Choe, Eileen Maloney-Wilensky, Ronald Wolf, M. Grady, Joel Greenberg, Joshua Levine, Arjun Yodh, John Detre, and W. Kofke. Noninvasive Measurement of Cerebral Blood Flow and Blood Oxygenation Using Near-Infrared and Diffuse Correlation Spectroscopies in Critically Brain-Injured Adults. *Neurocritical Care*, 12(2):173–180, April 2010.
- [121] Meeri N. Kim, Brian L. Edlow, Turgut Durduran, Suzanne Frangos, Rickson C. Mesquita, Joshua M. Levine, Joel H. Greenberg, Arjun G. Yodh, and John A. De-

- tre. Continuous Optical Monitoring of Cerebral Hemodynamics during Head-of-Bed Manipulation in Brain-Injured Adults. *Neurocritical Care*, (forthcoming), 2013.
- [122] Yu-Sok Kim, Lysander W. J. Bogert, Rogier V. Immink, Mark P. M. Harms, Willy N. J. M. Colier, and Johannes J. van Lieshout. Effects of aging on the cerebrovascular orthostatic response. *Neurobiology of Aging*, 32(2):344–353, February 2011.
- [123] P. J. Kirkpatrick, P. Smielewski, M. Czosnyka, D. K. Menon, and J. D. Pickard. Near-infrared spectroscopy use in patients with head injury. *Journal of neurosurgery*, 83(6):963–970, December 1995.
- [124] P. J. Kirkpatrick, P. Smielewski, M. Czosnyka, and J. D. Pickard. Continuous monitoring of cortical perfusion by laser Doppler flowmetry in ventilated patients with head injury. *Journal of Neurology, Neurosurgery & Psychiatry*, 57(11):1382–1388, November 1994.
- [125] Karsten Krakow, Stefan Ries, Michael Daffertshofer, and Michael Hennerici. Simultaneous Assessment of Brain Tissue Oxygenation and Cerebral Perfusion during Orthostatic Stress. *European Neurology*, 43(1):39–46, 2000.
- [126] J. Krejza, Z. Mariak, J. Walecki, P. Szydlak, J. Lewko, and A. Ustymowicz. Transcranial color Doppler sonography of basal cerebral arteries in 182 healthy subjects: age and sex variability and normal reference values for blood flow parameters. *American Journal of Roentgenology*, 172(1):213–218, January 1999.
- [127] E. W. Lang, R. R. Diehl, and H. M. Mehdorn. Cerebral autoregulation testing after aneurysmal subarachnoid hemorrhage: the phase relationship between arterial blood pressure and cerebral blood flow velocity. *Critical care medicine*, 29(1):158–163, January 2001.

- [128] J. A. Langlois, W. Rutland-Brown, and K. E. Thomas. Traumatic Brain Injury in the United States: Emergency Department Visits, Hospitalizations, and Deaths. *Centers for Disease Control and Prevention, National Center for Injury Prevention and Control*, 2006.
- [129] Eyal Leshem, Prativa Pandey, David R. Shlim, Kazuko Hiramatsu, Yechezkel Sidi, and Eli Schwartz. Clinical Features of Patients With Severe Altitude Illness in Nepal. *Journal of Travel Medicine*, 15(5):315–322, September 2008.
- [130] Jun Li, Gregor Dietsche, Diana Iftime, Sergey E. Skipetrov, Georg Maret, Thomas Elbert, Brigitte Rockstroh, and Thomas Gisler. Noninvasive detection of functional brain activity with near-infrared diffusing-wave spectroscopy. *Journal of Biomedical Optics*, 10(4), 2005.
- [131] Xingde Li. *Fluorescence and Diffusive Wave Diffraction Tomographic Probes in Turbid Media*. PhD thesis, University of Pennsylvania, 1998.
- [132] Lewis A. Lipsitz, Seiji Mukai, Jason Hamner, Margaret Gagnon, and Viken Babikian. Dynamic Regulation of Middle Cerebral Artery Blood Flow Velocity in Aging and Hypertension. *Stroke*, 31(8):1897–1903, August 2000.
- [133] Linda R. Littlejohns, Mary K. Bader, and Karen March. Brain Tissue Oxygen Monitoring in Severe Brain Injury, I: Research and Usefulness in Critical Care. *Crit Care Nurse*, 23(4):17–25, August 2003.
- [134] A. Losiniecki and M. Zuccarello. Subarachnoid hemorrhage: effect on cerebral blood flow and cerebral metabolism. *Frontiers in bioscience : a journal and virtual library*, 13:1845–1856, 2008.
- [135] Samuel J. Lucas, Keith R. Burgess, Kate N. Thomas, Joseph Donnelly, Karen C. Peebles, Rebekah A. Lucas, Jui-Lin L. Fan, James D. Cotter, Rishi Basnyat, and

- Philip N. Ainslie. Alterations in cerebral blood flow and cerebrovascular reactivity during 14 days at 5050 m. *The Journal of physiology*, 589(Pt 3):741–753, February 2011.
- [136] N. Lundberg, H. Troupp, and H. Lorin. Continuous recording of the ventricular-fluid pressure in patients with severe acute traumatic brain injury. A preliminary report. *Journal of neurosurgery*, 22(6):581–590, June 1965.
- [137] Niels Lynnerup. Cranial thickness in relation to age, sex and general body build in a Danish forensic sample. *Forensic Science International*, 117(1-2):45–51, March 2001.
- [138] Christopher Lysakowski, Erik Von Elm, Lionel Dumont, Jean-Daniel D. Junod, Edömer Tassonyi, Bengt Kayser, and Martin R. Tramèr. Effect of magnesium, high altitude and acute mountain sickness on blood flow velocity in the middle cerebral artery. *Clinical science (London, England : 1979)*, 106(3):279–285, March 2004.
- [139] A. I. Maas, W. Fleckenstein, D. A. de Jong, and H. van Santbrink. Monitoring cerebral oxygenation: experimental studies and preliminary clinical results of continuous monitoring of cerebrospinal fluid and brain tissue oxygen tension. *Acta neurochirurgica. Supplementum*, 59:50–57, 1993.
- [140] A. I. R. Maas, N. Stocchetti, and R. Bullock. Moderate and severe traumatic brain injury in adults. *The Lancet Neurology*, 7(8), 2008.
- [141] Amar J. Majmundar, Nicolas Skuli, Rickson C. Mesquita, Meeri N. Kim, Arjun G. Yodh, Michelle Nguyen-McCarty, and M. Celeste Simon. O₂ Regulates Skeletal Muscle Progenitor Differentiation through Phosphatidylinositol 3-Kinase/AKT Signaling. *Molecular and Cellular Biology*, 32(1):36–49, January 2012.

- [142] G. Maret and P. E. Wolf. Multiple light scattering from disordered media. The effect of Brownian motion of scatterers. *Zeitschrift für Physik B Condensed Matter*, 65(4):409–413, 1987.
- [143] Lawrence F. Marshall, Theresa Gautille, Melville R. Klauber, Howard M. Eisenberg, John A. Jane, Thomas G. Luerssen, Anthony Marmarou, and Mary A. Foulkes. The outcome of severe closed head injury. *Journal of Neurosurgery*, 75(1S):28+, 1991.
- [144] S. Masuyama, H. Kimura, T. Sugita, T. Kuriyama, K. Tatsumi, F. Kunitomo, S. Okita, H. Tojima, Y. Yuguchi, and S. Watanabe. Control of ventilation in extreme-altitude climbers. *Journal of applied physiology (Bethesda, Md. : 1985)*, 61(2):500–506, August 1986.
- [145] H. Matsuda, T. Maeda, M. Yamada, L. X. Gui, N. Tonami, and K. Hisada. Age-matched normal values and topographic maps for regional cerebral blood flow measurements by Xe-133 inhalation. *Stroke*, 15(2):336–342, March 1984.
- [146] C. G. Mayhall, N. H. Archer, V. A. Lamb, A. C. Spadora, J. W. Baggett, J. D. Ward, and R. K. Narayan. Ventriculostomy-related infections. A prospective epidemiologic study. *The New England journal of medicine*, 310(9):553–559, March 1984.
- [147] Andrew D. Mcleod, Farrell Igielman, Clare Elwell, Mark Cope, and Martin Smith. Measuring Cerebral Oxygenation During Normobaric Hyperoxia: A Comparison of Tissue Microprobes, Near-Infrared Spectroscopy, and Jugular Venous Oximetry in Head Injury. *Anesth Analg*, 97(3):851–856, September 2003.
- [148] D. J. Mehagnoul-Schipper, W. N. J. M. Colier, and R. W. M. M. Jansen. Reproducibility of orthostatic changes in cerebral oxygenation in healthy subjects aged 70 years or older. *Clinical Physiology*, 21(1):77–84, 2001.

- [149] D. Jannet Mehagnoul-Schipper, Lilian C. M. Vloet, Willy N. J. M. Colier, Willibrord H. L. Hoefnagels, and René W. M. M. Jansen. Cerebral Oxygenation Declines in Healthy Elderly Subjects in Response to Assuming the Upright Position. *Stroke*, 31(7):1615–1620, July 2000.
- [150] Chandrakala Menon, Glenn M. Polin, Indira Prabakaran, Alex Hsi, Cecil Cheung, Joseph P. Culver, James F. Pingpank, Chandra S. Sehgal, Arjun G. Yodh, Donald G. Buerk, and Douglas L. Fraker. An Integrated Approach to Measuring Tumor Oxygen Status Using Human Melanoma Xenografts as a Model. *Cancer Res*, 63(21):7232–7240, November 2003.
- [151] David K. Menon, Jonathan P. Coles, Arun K. Gupta, Tim D. Fryer, Peter Smielewski, Doris A. Chatfield, Franklin Aigbirhio, Jeremy N. Skepper, Pawan S. Minhas, Peter J. Hutchinson, T. Adrian Carpenter, John C. Clark, and John D. Pickard. Diffusion limited oxygen delivery following head injury. *Critical care medicine*, 32(6):1384–1390, June 2004.
- [152] M. Menzel, E. M. Doppenberg, A. Zauner, J. Soukup, M. M. Reinert, and R. Bullock. Increased inspired oxygen concentration as a factor in improved brain tissue oxygenation and tissue lactate levels after severe human head injury. *Journal of neurosurgery*, 91(1):1–10, July 1999.
- [153] M. Menzel, E. M. Doppenberg, A. Zauner, J. Soukup, M. M. Reinert, T. Clausen, P. B. Brockenbrough, and R. Bullock. Cerebral oxygenation in patients after severe head injury: monitoring and effects of arterial hyperoxia on cerebral blood flow, metabolism and intracranial pressure. *Journal of neurosurgical anesthesiology*, 11(4):240–251, October 1999.

- [154] Rickson C. Mesquita, Turgut Durduran, Guoqiang Yu, Erin M. Buckley, Meeri N. Kim, Chao Zhou, Regine Choe, Ulas Sunar, and Arjun G. Yodh. Direct measurement of tissue blood flow and metabolism with diffuse optics. *Philosophical Transactions of the Royal Society A: Mathematical, Physical and Engineering Sciences*, 369(1955):4390–4406, November 2011.
- [155] Rickson C. Mesquita, Steven S. Schenkel, Turgut Durduran, Christopher G. Favilla, Meeri N. Kim, David L. Minkoff, Michael Mullen, Joel H. Greenberg, John A. Detre, Scott E. Kasner, and Arjun G. Yodh. Diffuse Correlation Spectroscopy for Flow Assessment & Management of Acute Ischemic Stroke. OSA Technical Digest, pages BW4B.4+. Optical Society of America, April 2012.
- [156] Rickson C. Mesquita, Nicolas Skuli, Meeri N. Kim, Jiaming Liang, Steve Schenkel, Amar J. Majmundar, M. Celeste Simon, and Arjun G. Yodh. Hemodynamic and metabolic diffuse optical monitoring in a mouse model of hindlimb ischemia. *Biomed. Opt. Express*, 1(4):1173–1187, November 2010.
- [157] Rickson C. Mesquita and Arjun G. Yodh. Diffuse optics: Fundamentals and tissue applications. *Proceedings of the International School of Physics "Enrico Fermi" Course CLXXIII "Nano Optics and Atomics: Transport of Light and Matter Waves*, 173:51–74, 2011.
- [158] J. S. Meyer, L. A. Hayman, M. Yamamoto, F. Sakai, and S. Nakajima. Local cerebral blood flow measured by CT after stable xenon inhalation. *Am. J. Roentgenol.*, 135(2):239–251, August 1980.
- [159] P. Miranda, A. Lagares, J. Alen, A. Perez-Nuñez, I. Arrese, and R. D. Lobato. Early transcranial Doppler after subarachnoid hemorrhage: clinical and radiological correlations. *Surgical neurology*, 65(3), March 2006.

- [160] J. J. Moraine, J. Berré, and C. Mélot. Is cerebral perfusion pressure a major determinant of cerebral blood flow during head elevation in comatose patients with severe intracranial lesions? *Journal of neurosurgery*, 92(4):606–614, April 2000.
- [161] D. G. M. Murphy, C. DeCarli, M. B. Schapiro, S. I. Rapoport, and B. Horwitz. Age-Related Differences in Volumes of Subcortical Nuclei, Brain Matter, and Cerebrospinal Fluid in Healthy Men as Measured With Magnetic Resonance Imaging. *Archives of Neurology*, 49(8):839–845, August 1992.
- [162] C. J. L. Murray, A. D. Lopez, and Others. Global mortality, disability, and the contribution of risk factors: Global Burden of Disease Study. *Lancet*, 349(9063), 1997.
- [163] Alexandra Nagel, Daniela Graetz, Tania Schink, Katja Frieler, Oliver Sakowitz, Peter Vajkoczy, and Asita Sarrafzadeh. Relevance of intracranial hypertension for cerebral metabolism in aneurysmal subarachnoid hemorrhage. Clinical article. *Journal of neurosurgery*, 111(1):94–101, July 2009.
- [164] Raj K. Narayan, Mary Ellen E. Michel, Beth Ansell, Alex Baethmann, Anat Biegon, Michael B. Bracken, M. Ross Bullock, Sung C. Choi, Guy L. Clifton, Charles F. Contant, William M. Coplin, W. Dalton Dietrich, Jamshid Ghajar, Sean M. Grady, Robert G. Grossman, Edward D. Hall, William Heetderks, David A. Hovda, Jack Jallo, Russell L. Katz, Nachshon Knoller, Patrick M. Kochanek, Andrew I. Maas, Jeannine Majde, Donald W. Marion, Anthony Marmarou, Lawrence F. Marshall, Tracy K. McIntosh, Emmy Miller, Noel Mohberg, J. Paul Muizelaar, Lawrence H. Pitts, Peter Quinn, Gad Riesenfeld, Claudia S. Robertson, Kenneth I. Strauss, Graham Teasdale, Nancy Temkin, Ronald Tuma, Charles Wade, Michael D. Walker, Michael Weinrich, John Whyte, Jack Wilberger, A. Byron Young, and Lorraine

- Yurkewicz. Clinical trials in head injury. *Journal of neurotrauma*, 19(5):503–557, May 2002.
- [165] Walter D. Obrist, Howard K. Thompson, Hsioh S. H. A. N. Wang, and William E. Wilkinson. Regional Cerebral Blood Flow Estimated by ¹³³Xenon Inhalation. *Stroke*, 6(3):245–256, May 1975.
- [166] Walter D. Obrist, Zihong Zhang, and Howard Yonas. Effect of Xenon-Induced Flow Activation on Xenon-Enhanced Computed Tomography Cerebral Blood Flow Calculations. *J Cereb Blood Flow Metab*, 18(11):1192–1195, November 1998.
- [167] O. Oelz, H. Howald, P. E. Di Prampero, H. Hoppeler, H. Claassen, R. Jenni, A. Bühlmann, G. Ferretti, J. C. Brückner, and A. Veicsteinas. Physiological profile of world-class high-altitude climbers. *Journal of applied physiology (Bethesda, Md. : 1985)*, 60(5):1734–1742, May 1986.
- [168] Eiji Okada and David T. Delpy. Near-Infrared Light Propagation in an Adult Head Model. II. Effect of Superficial Tissue Thickness on the Sensitivity of the Near-Infrared Spectroscopy Signal. *Appl. Opt.*, 42(16):2915–2922, June 2003.
- [169] M. A. O’Leary, D. A. Boas, B. Chance, and A. G. Yodh. Refraction of diffuse photon density waves. *Physical Review Letters*, 69(18):2658–2661, November 1992.
- [170] Yasuomi Ouchi, Hiroyuki Okada, Etsuji Yoshikawa, Shuji Nobezawa, and Masami Futatsubashi. Brain activation during maintenance of standing postures in humans. *Brain*, 122(2):329–338, February 1999.
- [171] J. Overgaard, C. Mosdal, and W. A. Tweed. Cerebral circulation after head injury. Part 3: Does reduced regional cerebral blood flow determine recovery of brain function after blunt head injury? *Journal of neurosurgery*, 55(1):63–74, July 1981.

- [172] J. Overgaard and W. A. Tweed. Cerebral circulation after head injury. 1. Cerebral blood flow and its regulation after closed head injury with emphasis on clinical correlations. *Journal of neurosurgery*, 41(5):531–541, November 1974.
- [173] Ronney B. Panerai. Assessment of cerebral pressure autoregulation in humans - a review of measurement methods. *Physiological Measurement*, 19(3):305–338, August 1998.
- [174] K. T. Pattinson, C. H. Imray, and A. D. Wright. What does cerebral oximetry measure? *British journal of anaesthesia*, 94(6):863–864, June 2005.
- [175] Lawrence H. Phillips, Jack P. Whisnant, Michael W. O’Fallon, and Thoralf M. Sundt. The unchanging pattern of subarachnoid hemorrhage in a community. *Neurology*, 30(10):1034+, October 1980.
- [176] Ronda R. Pindzola and Howard Yonas. The Xenon-enhanced Computed Tomography Cerebral Blood Flow Method. *Neurosurgery*, 43(6):1488–1492, December 1998.
- [177] D. J. Pine, D. A. Weitz, P. M. Chaikin, and E. Herbolzheimer. Diffusing wave spectroscopy. *Physical Review Letters*, 60(12):1134–1137, March 1988.
- [178] José C. Pinheiro and Douglas M. Bates. *Mixed-Effects Models in S and S-Plus*. Springer, 2000.
- [179] G. F. Prunell, T. Mathiesen, and N. A. Svendgaard. Experimental subarachnoid hemorrhage: cerebral blood flow and brain metabolism during the acute phase in three different models in the rat. *Neurosurgery*, 54(2), February 2004.
- [180] Jordan S. Querido and A. William Sheel. Regulation of cerebral blood flow during exercise. *Sports medicine (Auckland, N.Z.)*, 37(9):765–782, 2007.

- [181] Alejandro A. Rabinstein, Stephen Weigand, John L. D. Atkinson, and Eelco F. M. Wijdicks. Patterns of Cerebral Infarction in Aneurysmal Subarachnoid Hemorrhage. *Stroke*, 36(5):992–997, May 2005.
- [182] K. Rajamani and M. Gorman. Transcranial Doppler in stroke. *Biomedicine & Pharmacotherapy*, 55(5):247–257, June 2001.
- [183] T. Rätsep and T. Asser. Cerebral hemodynamic impairment after aneurysmal subarachnoid hemorrhage as evaluated using transcranial doppler ultrasonography: relationship to delayed cerebral ischemia and clinical outcome. *Journal of neurosurgery*, 95(3):393–401, September 2001.
- [184] Matthias Reinhard, Elisabeth Wehrle-Wieland, Daniel Grabiak, Markus Roth, Brigitte Guschlbauer, Jens Timmer, Cornelius Weiller, and Andreas Hetzel. Oscillatory cerebral hemodynamicsthe macro- vs. microvascular level. *Journal of the Neurological Sciences*, 250(1-2):103–109, December 2006.
- [185] Maryam E. Rettmann, Michael A. Kraut, Jerry L. Prince, and Susan M. Resnick. Cross-sectional and Longitudinal Analyses of Anatomical Sulcal Changes Associated with Aging. *Cerebral Cortex*, 16(11):1584–1594, November 2006.
- [186] S. O. Rice. Mathematical Analysis of Random Noise. *Bell Systems Technical Journal*, 23:282–332, 1944.
- [187] M. Rijdsdijk, I. C. van der Schaaf, B. K. Velthuis, M. J. Wermer, and G. J. Rinkel. Global and focal cerebral perfusion after aneurysmal subarachnoid hemorrhage in relation with delayed cerebral ischemia. *Neuroradiology*, 50(9):813–820, September 2008.
- [188] R. W. Rimel, B. Giordani, J. T. Barth, T. J. Boll, and J. A. Jane. Disability caused by minor head injury. *Neurosurgery*, 9(3):221–228, September 1981.

- [189] Jorge Ripoll. *Light Diffusion in Turbid Media with Biomedical Application*. PhD thesis, Universidad Autónoma de Madrid, 2000.
- [190] R. C. Roach and P. H. Hackett. Frontiers of hypoxia research: acute mountain sickness. *The Journal of experimental biology*, 204(Pt 18):3161–3170, September 2001.
- [191] Nadège Roche-Labarbe, Stefan A. Carp, Andrea Surova, Megha Patel, David A. Boas, P. Ellen Grant, and Maria A. Franceschini. Noninvasive optical measures of CBV, StO₂, CBF index, and rCMRO₂ in human premature neonates' brains in the first six weeks of life. *Hum. Brain Mapp.*, 31(3):341–352, March 2010.
- [192] Sarah B. Rockswold, Gaylan L. Rockswold, David A. Zaun, Xuewei Zhang, Carla E. Cerra, Thomas A. Bergman, and Jiannong Liu. A prospective, randomized clinical trial to compare the effect of hyperbaric to normobaric hyperoxia on cerebral metabolism, intracranial pressure, and oxygen toxicity in severe traumatic brain injury. *Journal of neurosurgery*, 112(5):1080–1094, May 2010.
- [193] A. H. Ropper, D. O'Rourke, and S. K. Kennedy. Head position, intracranial pressure, and compliance. *Neurology*, 32(11):1288–1291, November 1982.
- [194] David S. Rosen and R. Loch Macdonald. Subarachnoid hemorrhage grading scales. *Neurocritical Care*, 2(2):110–118, April 2005.
- [195] Guy Rosenthal, J. Claude Hemphill, Marco Sorani, Christine Martin, Diane Morabito, Walter D. Obrist, and Geoffrey T. Manley. Brain tissue oxygen tension is more indicative of oxygen diffusion than oxygen delivery and metabolism in patients with traumatic brain injury. *Critical care medicine*, 36(6):1917–1924, June 2008.
- [196] M. J. Rosner, S. D. Rosner, and A. H. Johnson. Cerebral perfusion pressure: management protocol and clinical results. *Journal of neurosurgery*, 83(6):949–962, December 1995.

- [197] R. D. Rothoerl, R. Faltermeier, R. Burger, C. Woertgen, and A. Brawanski. Dynamic correlation between tissue PO₂ and near infrared spectroscopy. *Acta neurochirurgica. Supplement*, 81:311–313, 2002.
- [198] R. L. Sacco, P. A. Wolf, N. E. Bharucha, S. L. Meeks, W. B. Kannel, L. J. Charette, P. M. McNamara, E. P. Palmer, and R. D’Agostino. Subarachnoid and intracerebral hemorrhage: natural history, prognosis, and precursive factors in the Framingham Study. *Neurology*, 34(7):847–854, July 1984.
- [199] Rachael I. Scahill. A Longitudinal Study of Brain Volume Changes in Normal Aging Using Serial Registered Magnetic Resonance Imaging. *Archives of Neurology*, 60(7):989–994, July 2003.
- [200] Bawarjan Schatlo, Sven Gläsker, Alois Zauner, B. Gregory Thompson, Edward H. Oldfield, and Ryszard M. Pluta. Continuous neuromonitoring using transcranial Doppler reflects blood flow during carbon dioxide challenge in primates with global cerebral ischemia. *Neurosurgery*, 64(6), June 2009.
- [201] J. M. Schmitt, A. Knüttel, and J. R. Knutson. Interference of diffusive light waves. *J. Opt. Soc. Am. A*, 9(10):1832–1843, October 1992.
- [202] R. B. Schoene, S. Lahiri, P. H. Hackett, R. M. Peters, J. S. Milledge, C. J. Pizzo, F. H. Sarnquist, S. J. Boyer, D. J. Graber, and K. H. Maret. Relationship of hypoxic ventilatory response to exercise performance on Mount Everest. *Journal of applied physiology: respiratory, environmental and exercise physiology*, 56(6):1478–1483, June 1984.
- [203] G. A. Schubert and C. Thome. Cerebral blood flow changes in acute subarachnoid hemorrhage. *Frontiers in bioscience : a journal and virtual library*, 13:1594–1603, 2008.

- [204] H. W. Schytz, T. Wienecke, L. T. Jensen, J. Selb, D. A. Boas, and M. Ashina. Changes in cerebral blood flow after acetazolamide: an experimental study comparing near-infrared spectroscopy and SPECT. *European Journal of Neurology*, 16(4):461–467, April 2009.
- [205] J. M. Seelig, D. P. Becker, J. D. Miller, R. P. Greenberg, J. D. Ward, and S. C. Choi. Traumatic acute subdural hematoma: major mortality reduction in comatose patients treated within four hours. *The New England journal of medicine*, 304(25):1511–1518, June 1981.
- [206] J. M. Serrador, P. A. Picot, B. K. Rutt, J. K. Shoemaker, and R. L. Bondar. MRI measures of middle cerebral artery diameter in conscious humans during simulated orthostasis. *Stroke; a journal of cerebral circulation*, 31(7):1672–1678, July 2000.
- [207] J. W. Severinghaus, H. Chiodi, E. I. Eger, B. Brandstater, and T. F. Hornbein. Cerebral blood flow in man at high altitude. Role of cerebrospinal fluid pH in normalization of flow in chronic hypocapnia. *Circulation research*, 19(2):274–282, August 1966.
- [208] Yu Shang, Youquan Zhao, Ran Cheng, Lixin Dong, Daniel Irwin, and Guoqiang Yu. Portable optical tissue flow oximeter based on diffuse correlation spectroscopy. *Opt. Lett.*, 34(22):3556–3558, November 2009.
- [209] H. A. Shenkin and W. G. Scheuerman. Effect of change of position upon the cerebral circulation of man. *Journal of applied physiology*, 2(6):317–326, December 1949.
- [210] Cyndya Shibao, Carlos G. Grijalva, Satish R. Raj, Italo Biaggioni, and Marie R. Griffin. Orthostatic Hypotension-Related Hospitalizations in the United States. *The American Journal of Medicine*, 120(11):975–980, November 2007.

- [211] P. J. Sioutos, J. A. Orozco, L. P. Carter, M. E. Weinand, A. J. Hamilton, and F. C. Williams. Continuous regional cerebral cortical blood flow monitoring in head-injured patients. *Neurosurgery*, 36(5), May 1995.
- [212] Nicolas Skuli, Amar J. Majmundar, Bryan L. Krock, Rickson C. Mesquita, Lijoy K. Mathew, Zachary L. Quinn, Anja Runge, Liping Liu, Meeri N. Kim, Jiaming Liang, Steven Schenkel, Arjun G. Yodh, Brian Keith, and M. Celeste Simon. Endothelial HIF-2 regulates murine pathological angiogenesis and revascularization processes. *The Journal of clinical investigation*, 122(4):1427–1443, April 2012.
- [213] Peter Smielewski, Peter Kirkpatrick, Paven Minhas, John D. Pickard, and Marek Czosnyka. Can Cerebrovascular Reactivity Be Measured With Near-Infrared Spectroscopy? *Stroke*, 26(12):2285–2292, December 1995.
- [214] Martin Soehle, Marek Czosnyka, John D. Pickard, and Peter J. Kirkpatrick. Continuous Assessment of Cerebral Autoregulation in Subarachnoid Hemorrhage. *Anesth Analg*, 98(4):1133–1139, April 2004.
- [215] Louis Sokoloff. The effects of carbon dioxide on the cerebral circulation. *Anesthesiology*, 21(6):664–673, November 1960.
- [216] N. J. Solenski, E. C. Haley, N. F. Kassell, G. Kongable, T. Germanson, L. Truskowski, and J. C. Torner. Medical complications of aneurysmal subarachnoid hemorrhage: a report of the multicenter, cooperative aneurysm study. Participants of the Multicenter Cooperative Aneurysm Study. *Critical care medicine*, 23(6):1007–1017, June 1995.
- [217] Gregory A. Sorensen. What Is the Meaning of Quantitative CBF? *AJNR Am J Neuroradiol*, 22(2):235–236, February 2001.

- [218] Farzaneh A. Sorond, Rose Khavari, Jorge M. Serrador, and Lewis A. Lipsitz. Regional Cerebral Autoregulation During Orthostatic Stress: Age-Related Differences. *The Journals of Gerontology Series A: Biological Sciences and Medical Sciences*, 60(11):1484–1487, November 2005.
- [219] Jean F. Soustiel, Eli Levy, Menashe Zaaroor, Roni Bibi, Sergei Lukaschuk, and Dan Manor. A New Angle-Independent Doppler Ultrasonic Device for Assessment of Blood Flow Volume in the Extracranial Internal Carotid Artery. *Journal of Ultrasound in Medicine*, 21(12):1405–1412, December 2002.
- [220] M. R. Stankovic, D. Maulik, W. Rosenfeld, P. G. Stubblefield, A. D. Kofinas, S. Drexler, R. Nair, M. A. Franceschini, D. Hueber, E. Gratton, and S. Fantini. Real-time optical imaging of experimental brain ischemia and hemorrhage in neonatal piglets. *Journal of perinatal medicine*, 27(4):279–286, 1999.
- [221] L. A. Steiner and P. J. Andrews. Monitoring the injured brain: ICP and CBF. *British journal of anaesthesia*, 97(1):26–38, July 2006.
- [222] Nino Stocchetti, Francesca Pagan, Emiliana Calappi, Katia Canavesi, Luigi Beretta, Giuseppe Citerio, Manuela Cormio, and Angelo Colombo. Inaccurate early assessment of neurological severity in head injury. *Journal of neurotrauma*, 21(9):1131–1140, September 2004.
- [223] Gary Strangman, Maria A. Franceschini, and David A. Boas. Factors affecting the accuracy of near-infrared spectroscopy concentration calculations for focal changes in oxygenation parameters. *NeuroImage*, 18(4):865–879, April 2003.
- [224] Jose I. Suarez, Robert W. Tarr, and Warren R. Selman. Aneurysmal subarachnoid hemorrhage. *The New England journal of medicine*, 354(4):387–396, January 2006.

- [225] Ulas Sunar, Sosina Makonnen, Chao Zhou, Turgut Durduran, Guoqiang Yu, Hsing-Wen Wang, William M. Lee, and Arjun G. Yodh. Hemodynamic responses to antivasular therapy and ionizing radiation assessed by diffuse optical spectroscopies. *Opt. Express*, 15(23):15507–15516, November 2007.
- [226] Ilias Tachtsidis, Clare E. Elwell, Terence S. Leung, Chuen-Wai Lee, Martin Smith, and David T. Delpy. Investigation of cerebral haemodynamics by near-infrared spectroscopy in young healthy volunteers reveals posture-dependent spontaneous oscillations. *Physiological Measurement*, 25(2):437–445, February 2004.
- [227] A. Talacchi. Sequential measurements of cerebral blood flow in the acute phase of subarachnoid hemorrhage. *Journal of neurosurgical sciences*, 37(1):9–18, March 1993.
- [228] R Core Development Team. *A Language and Environment for Statistical Computing*. R Core Development Team, 2008.
- [229] G. Teasdale and B. Jennett. Assessment of coma and impaired consciousness. A practical scale. *Lancet*, 2(7872):81–84, July 1974.
- [230] G. M. Teasdale and D. I. Graham. Craniocerebral trauma: protection and retrieval of the neuronal population after injury. *Neurosurgery*, 43(4), October 1998.
- [231] L. L. Teunissen, G. J. Rinkel, A. Algra, and J. van Gijn. Risk factors for subarachnoid hemorrhage: a systematic review. *Stroke; a journal of cerebral circulation*, 27(3):544–549, March 1996.
- [232] D. Thurman. The epidemiology and economics of head trauma. *Head trauma: basic, preclinical, and clinical directions*. New York (NY): Wiley and Sons, 2001.

- [233] Bruce J. Tromberg, Lars O. Svaasand, Tsong-Tseh Tsay, and Richard C. Haskell. Properties of photon density waves in multiple-scattering media. *Appl. Opt.*, 32(4):607–616, February 1993.
- [234] Miles Tsuji, Adre Duplessis, George Taylor, Robert Crocker, and Joseph J. Volpe. Near Infrared Spectroscopy Detects Cerebral Ischemia during Hypotension in Piglets. *Pediatric Research*, 44(4):591–595, October 1998.
- [235] P. Vajkoczy, H. Roth, P. Horn, T. Lucke, C. Thomé, U. Hubner, G. T. Martin, C. Zapletal, E. Klar, L. Schilling, and P. Schmiedek. Continuous monitoring of regional cerebral blood flow: experimental and clinical validation of a novel thermal diffusion microprobe. *Journal of neurosurgery*, 93(2):265–274, August 2000.
- [236] Arenda H. E. A. van Beek, Jurgen A. H. R. Claassen, Marcel G. M. Rikkert, and Rene W. M. M. Jansen. Cerebral autoregulation: an overview of current concepts and methodology with special focus on the elderly. *Journal of Cerebral Blood Flow & Metabolism*, 28(6):1071–1085, March 2008.
- [237] J. van Gijn and G. J. Rinkel. Subarachnoid haemorrhage: diagnosis, causes and management. *Brain : a journal of neurology*, 124(Pt 2):249–278, February 2001.
- [238] J. van Gijn and K. J. van Dongen. Computerized tomography in subarachnoid hemorrhage. *Neurology*, 30(5):538, May 1980.
- [239] H. van Santbrink, A. I. Maas, and C. J. Avezaat. Continuous monitoring of partial pressure of brain tissue oxygen in patients with severe head injury. *Neurosurgery*, 38(1):21–31, January 1996.
- [240] H. J. van Staveren, C. J. Moes, J. van Marie, S. A. Prahl, and M. J. van Gemert. Light scattering in Intralipid-10% in the wavelength range of 400-1100 nm. *Applied optics*, 30(31):4507–4514, November 1991.

- [241] B. K. Velthuis, G. J. Rinkel, L. M. Ramos, T. D. Witkamp, J. W. Berkelbach van der Sprenkel, W. P. Vandertop, and M. S. van Leeuwen. Subarachnoid hemorrhage: aneurysm detection and preoperative evaluation with CT angiography. *Radiology*, 208(2):423–430, August 1998.
- [242] B. H. Verweij, G. J. Amelink, and J. P. Muizelaar. Current concepts of cerebral oxygen transport and energy metabolism after severe traumatic brain injury. *Progress in brain research*, 161:111–124, 2007.
- [243] Paul Vespa. What is the optimal threshold for cerebral perfusion pressure following traumatic brain injury? *Neurosurgical focus*, 15(6), December 2003.
- [244] Arno Villringer and Britton Chance. Non-invasive optical spectroscopy and imaging of human brain function. *Trends in Neurosciences*, 20(10):435–442, October 1997.
- [245] Jaap Vuyk, Jan Van Den Bos, Kees Terhell, Rene De Bos, Ad Vletter, Pierre Valk, Martie Van Beuzekom, Jack Van Kleef, and Albert Dahan. Acetazolamide improves cerebral oxygenation during exercise at high altitude. *High altitude medicine & biology*, 7(4):290–301, 2006.
- [246] Siegbert Warkentin, Ulla Passant, Lennart Minthon, Siv Karlson, Lars Edvinsson, Roger Fäldt, Lars Gustafson, and Jarl Risberg. Redistribution of blood flow in the cerebral cortex of normal subjects during head-up postural change. *Clinical Autonomic Research*, 2(2):119–124, April 1992.
- [247] Katja E. Wartenberg, J. Michael Schmidt, and Stephan A. Mayer. Multimodality Monitoring in Neurocritical Care. *Critical Care Clinics*, 23(3):507–538, July 2007.
- [248] Christian Waydhas. Equipment review: Intrahospital transport of critically ill patients. *Critical Care*, 3(5):R83–R89, 1999.

- [249] Hayden White and Andrew Baker. Continuous jugular venous oximetry in the neurointensive care unit - a brief review: [L'oxymetrie continue de la veine jugulaire a l' unite des soins intensifs neurologiques - une breve revue]. *Can J Anesth*, 49(6):623–629, June 2002.
- [250] Mark H. Wilson, Indran Davagnanam, Graeme Holland, Raj S. Dattani, Alexander Tamm, Shashivadan P. Hirani, Nicky Kolfschoten, Lisa Strycharczuk, Cathy Green, John S. Thornton, Alex Wright, Mark Edsell, Neil D. Kitchen, David J. Sharp, Timothy E. Ham, Andrew Murray, Cameron J. Holloway, Kieran Clarke, Mike P. Grocott, Hugh Montgomery, Chris Imray, and Birmingham Medical Research Expeditionary Society and Caudwell Xtreme Everest Research Group. Cerebral venous system and anatomical predisposition to high-altitude headache. *Annals of neurology*, November 2012.
- [251] Mark H. Wilson, Mark E. Edsell, Indran Davagnanam, Shashivadan P. Hirani, Dan S. Martin, Denny Z. Levett, John S. Thornton, Xavier Golay, Lisa Strycharczuk, Stanton P. Newman, Hugh E. Montgomery, Mike P. Grocott, Christopher H. Imray, and Caudwell Xtreme Everest Research Group. Cerebral artery dilatation maintains cerebral oxygenation at extreme altitude and in acute hypoxia—an ultrasound and MRI study. *Journal of cerebral blood flow and metabolism*, 31(10):2019–2029, October 2011.
- [252] Mark H. Wilson, Christopher H. Imray, and Alan R. Hargens. The headache of high altitude and microgravity—similarities with clinical syndromes of cerebral venous hypertension. *High altitude medicine & biology*, 12(4):379–386, 2011.
- [253] Mark H. Wilson and James Milledge. Direct measurement of intracranial pressure at high altitude and correlation of ventricular size with acute mountain sickness:

- Brian Cummins' results from the 1985 Kishtwar expedition. *Neurosurgery*, 63(5), November 2008.
- [254] Mark H. Wilson, Stanton Newman, and Chris H. Imray. The cerebral effects of ascent to high altitudes. *Lancet neurology*, 8(2):175–191, February 2009.
- [255] C. Winkelman. Effect of backrest position on intracranial and cerebral perfusion pressures in traumatically brain-injured adults. *American journal of critical care : an official publication, American Association of Critical-Care Nurses*, 9(6), November 2000.
- [256] M. Wintermark, M. Sesay, E. Barbier, K. Borbély, W. P. Dillon, J. D. Eastwood, T. C. Glenn, C. B. Grandin, S. Pedraza, J. F. Soustiel, T. Nariai, G. Zaharchuk, J. M. Caillé, V. Dousset, and H. Yonas. Comparative overview of brain perfusion imaging techniques. *Journal of neuroradiology. Journal de neuroradiologie*, 32(5):294–314, December 2005.
- [257] Alan T. Yam, Erhard W. Lang, Jim Lagopoulos, Kwok Yip, Jane Griffith, Yugan Mudaliar, and Nicholas W. C. Dorsch. Cerebral autoregulation and ageing. *Journal of Clinical Neuroscience*, 12(6):643–646, August 2005.
- [258] H. Yonas, R. P. Pindzola, and D. W. Johnson. Xenon/computed tomography cerebral blood flow and its use in clinical management. *Neurosurgery clinics of North America*, 7(4):605–616, October 1996.
- [259] Jeffrey S. Young, Osbert Blow, Florence Turrentine, Jeffrey A. Claridge, and Andrew Schulman. Is there an upper limit of intracranial pressure in patients with severe head injury if cerebral perfusion pressure is maintained? *Neurosurgical focus*, 15(6), December 2003.

- [260] Guoqiang Yu, Turgut Durduran, Chao Zhou, Hsing-Wen Wang, Mary E. Putt, Mark H. Saunders, Chandra M. Sehgal, Eli Glatstein, Arjun G. Yodh, and Theresa M. Busch. Noninvasive Monitoring of Murine Tumor Blood Flow During and After Photodynamic Therapy Provides Early Assessment of Therapeutic Efficacy. *Clin Cancer Res*, 11(9):3543–3552, May 2005.
- [261] Guoqiang Yu, Thomas F. Floyd, Turgut Durduran, Chao Zhou, Jiongjiong Wang, John A. Detre, and Arjun G. Yodh. Validation of diffuse correlation spectroscopy for muscle blood flow with concurrent arterial spin labeled perfusion MRI. *Opt. Express*, 15(3):1064–1075, February 2007.
- [262] Z. Zhang. Reliability and error analysis on xenon/CT CBF. *The Keio journal of medicine*, 49 Suppl 1, February 2000.
- [263] Chao Zhou. *In-Vivo Optical Imaging and Spectroscopy of Cerebral Hemodynamics*. PhD thesis, University of Pennsylvania, 2007.
- [264] Chao Zhou, Stephanie A. Eucker, Turgut Durduran, Guoqiang Yu, Jill Ralston, Stuart H. Friess, Rebecca N. Ichord, Susan S. Margulies, and Arjun G. Yodh. Diffuse optical monitoring of hemodynamic changes in piglet brain with closed head injury. *Journal of Biomedical Optics*, 14(3):034015+, 2009.
- [265] Peyman Zirak, Raquel Delgado-Mederos, Joan Martí-Fàbregas, and Turgut Durduran. Effects of acetazolamide on the micro- and macro-vascular cerebral hemodynamics: a diffuse optical and transcranial doppler ultrasound study. *Biomed. Opt. Express*, 1(5):1443–1459, December 2010.